Graduate School ETD Form 9
(Revised 12/07)

# PURDUE UNIVERSITY
## GRADUATE SCHOOL
## Thesis/Dissertation Acceptance

This is to certify that the thesis/dissertation prepared

By Katya M. Casper

Entitled Hypersonic Wind-Tunnel Measurements of Boundary-Layer Pressure Fluctuations

For the degree of Master of Science in Aeronautics and Astronautics

Is approved by the final examining committee:

Steven P. Schneider
Chair

Steven J. Beresh

John P. Sullivan

To the best of my knowledge and as understood by the student in the *Research Integrity and Copyright Disclaimer (Graduate School Form 20)*, this thesis/dissertation adheres to the provisions of Purdue University's "Policy on Integrity in Research" and the use of copyrighted material.

Approved by Major Professor(s): Steven P. Schneider

Approved by: Kathleen C. Howell 7/27/2009
Head of the Graduate Program Date

Graduate School Form 20
(Revised 6/09)

# PURDUE UNIVERSITY
## GRADUATE SCHOOL

## Research Integrity and Copyright Disclaimer

Title of Thesis/Dissertation:
Hypersonic Wind-Tunnel Measurements of Boundary-Layer Pressure Fluctuations

For the degree of Master of Science in Aeronautics and Astronautics

I certify that in the preparation of this thesis, I have observed the provisions of *Purdue University Executive Memorandum No. C-22,* September 6, 1991, *Policy on Integrity in Research.**

Further, I certify that this work is free of plagiarism and all materials appearing in this thesis/dissertation have been properly quoted and attributed.

I certify that all copyrighted material incorporated into this thesis/dissertation is in compliance with the United States' copyright law and that I have received written permission from the copyright owners for my use of their work, which is beyond the scope of the law. I agree to indemnify and save harmless Purdue University from any and all claims that may be asserted or that may arise from any copyright violation.

Katya M. Casper
Printed Name and Signature of Candidate

07/29/2009
Date (month/day/year)

*Located at http://www.purdue.edu/policies/pages/teach_res_outreach/c_22.html

# HYPERSONIC WIND-TUNNEL MEASUREMENTS OF BOUNDARY-LAYER PRESSURE FLUCTUATIONS

A Thesis

Submitted to the Faculty

of

Purdue University

by

Katya M. Casper

In Partial Fulfillment of the

Requirements for the Degree

of

Master of Science in Aeronautics and Astronautics

August 2009

Purdue University

West Lafayette, Indiana

To my family and loved ones.

# ACKNOWLEDGMENTS

This work could not have been completed without the help and support of many individuals. Thanks first to my family for all their love and support. They truly have made me who I am today. Thanks also to my advisors Dr. Steven Schneider and Dr. Steven Beresh for guiding me the past two years. Also, thank you to Dr. John Sullivan for being on my committee. The Ludwieg Tube Group provided advice and suggestions throughout my time at Purdue. The ASL machine shop—Madeline Chadwell, Jerry Hahn, Robin Snodgrass, and Jim Younts also provided much needed design advice and help. John Phillips helped with the headaches of wiring and fixed many malfunctioning sensors. Also, thanks go out to the Sandia wind-tunnel group: John Henfling, Rusty Spillers, and Brian Pruett. I would not have any HWT measurements without them. Tom Grasser and Roger Harmon also aided in the model design. Funding was provided in part by the National Defense Science and Engineering Graduate Fellowship, Sandia National Laboratories, and AFOSR.

TABLE OF CONTENTS

# LIST OF TABLES

# LIST OF FIGURES

Figure Page

# SYMBOLS

| | |
|---|---|
| $\delta$ | boundary-layer thickness |
| $\delta^*$ | boundary-layer displacement thickness |
| $\epsilon_T$ | compressibility factor |
| $\gamma$ | specific heat ratio |
| $\phi$ | cone azimuthal angle, also cone roll angle |
| $\rho_1$ | boundary layer density at location of maximum noise generation |
| $\rho_e$ | boundary-layer edge density |
| $\tau_w$ | nozzle-wall shear stress |
| $a_1$ | constant in Houbolt correlation |
| $a_2$ | constant in Houbolt correlation |
| $A$ | parameter |
| $c$ | constant, also tunnel test-section circumference in Pate's correlation |
| $\overline{c}$ | aerodynamic-noise-transition correlation size parameter |
| $c_1$ | test-section circumference of a $0.305 \times 0.305$-m tunnel |
| $C_{F_{II}}$ | mean turbulent skin-friction coefficient calculated using method of Van-Driest II |
| $C_F$ | mean turbulent skin-friction coefficient |
| $K_1$ | constant |
| $K_2$ | constant |
| $K_n$ | velocity power law parameter |
| $m$ | Sutherland viscosity power law coefficient |
| $M$ | freestream Mach number |
| $M_e$ | Mach number at boundary-layer edge |
| $MF$ | Mangler Factor |

| | |
|---|---|
| $n$ | velocity power law exponent, also temperature ratio exponent |
| $\tilde{p}$ | root-mean-square pressure |
| $p_e$ | boundary-layer edge pressure |
| $p_p$ | surface Pitot probe pressure |
| $P_0$ | tunnel stagnation pressure |
| $P_{02}$ | stagnation pressure behind normal shock |
| $\tilde{P}_{02}$ | root-mean-square stagnation pressure behind normal shock |
| $q_e$ | dynamic pressure at boundary-layer edge |
| $r$ | recovery factor |
| $r_1$ | recovery type factor at boundary-layer location of maximum noise generation |
| $r_e$ | recovery factor at boundary-layer edge |
| $Re/m$ | freestream unit Reynolds number |
| $Re_{t_\delta}$ | transition Reynolds number based on boundary-layer edge conditions |
| $t$ | time into run |
| $T^*$ | Eckert reference temperature |
| $T_0$ | tunnel stagnation temperature |
| $T_1$ | boundary-layer temperature at location of maximum noise generation |
| $T_{aw}$ | adiabatic wall temperature |
| $T_e$ | boundary-layer edge temperature |
| $T_w$ | wall temperature |
| $U$ | freestream velocity |
| $U_1$ | boundary-layer velocity at location of maximum noise generation |
| $U_e$ | boundary-layer edge velocity |
| $x$ | axial model coordinate measured from sharp nosetip |
| $x_{tr}$ | axial model transition location measured from sharp nosetip |
| $z$ | axial tunnel coordinate measured from throat |

# ABBREVIATIONS

| | |
|---|---|
| BAM6QT | Boeing/AFOSR Mach-6 Quiet Tunnel |
| HWT | Sandia Hypersonic Wind Tunnel |
| HWT-5 | Sandia Hypersonic Wind Tunnel with Mach 5 nozzle |
| HWT-8 | Sandia Hypersonic Wind Tunnel with Mach 8 nozzle |
| PSD | power spectral density |
| RMS | root-mean-square |
| TSP | temperature-sensitive paint |

# ABSTRACT

Casper, Katya M. M.S.A.A.E., Purdue University, August, 2009. Hypersonic Wind-Tunnel Measurements of Boundary-Layer Pressure Fluctuations. Major Professor: Steven P. Schneider.

During atmospheric reentry, hypersonic vehicles are subjected to high levels of boundary-layer pressure fluctuations. To improve understanding and prediction of these fluctuations, measurements of surface pressure fluctuations on a seven-degree sharp cone at zero angle of attack were conducted in Sandia's Hypersonic Wind Tunnel under noisy flow and in Purdue University's Boeing/AFOSR Mach-6 Quiet Tunnel under noisy and quiet flow.

Fluctuations under laminar boundary layers reflected tunnel noise levels. Laminar boundary-layer measurements under quiet flow were an order of magnitude lower than under noisy flow. Transition on the model only occurred under noisy flow, and fluctuations peaked during transition. The transition location, marked by the peak, depended on tunnel noise parameters. Turbulent boundary-layer fluctuations were lower than transitional fluctuations and also reflected tunnel noise levels. Measurements of second-mode waves showed the waves started to grow under a laminar boundary layer, saturated, and then broke down near the peak in transitional pressure fluctuations.

A physics-based model of transitional fluctuations is sought by relating them to the development and growth of turbulent spots. Hot-film traces indicated the possible presence of turbulent spots. The kurtosis and skewness also peaked during transition, indicating impulsiveness of the flow. However, turbulent spots could not be easily identified in the pressure traces. More work is needed to characterize the pressure fluctuations in the transition region.

# 1. INTRODUCTION AND OUTLINE OF EXPERIMENTS

## 1.1 Introduction

Hypersonic reentry vehicles are subjected to high levels of fluctuating pressures. These intense fluctuations can cause vibration of internal components and can lead to structural fatigue. There is a need to predict the magnitude and location of the pressure fluctuations to better design reentry vehicles. Current designs often use overly conservative estimates of the fluctuations which can lead to heavier vehicles and degraded flight performance. Some correlations exist for the magnitude of laminar, transitional, and turbulent pressure fluctuations, but these were derived primarily using either incompressible data or conventional (noisy flow) hypersonic wind-tunnel tests [1–8]. These correlations are described in Chapter 2. Correlations of the laminar and turbulent fluctuations are based on physical concepts; however, little work has focused on understanding the physics behind the generation of transitional pressure fluctuations.

Wind-tunnel tests at fixed freestream conditions have shown that transitional pressure fluctuations can be more severe than turbulent pressure fluctuations, making transitional fluctuations of primary interest for this work. The transition process can be described through intermittency and the growth and propagation of turbulent spots in the transitional boundary layer. This work seeks to relate turbulent spot growth to the generation of the pressure fluctuations. A similar idea was proposed by Owen [9, 10] for low speed work. He noted that for hot-film measurements on a flat plate, "the well defined peak voltage fluctuation towards the end of transition, close to the positions of maximum surface temperature and peak surface Pitot pressure, coincides with the point where the turbulent burst frequency is a maximum." This connection was also investigated at higher speeds [11, 12], indicating that the maxi-

mum transitional pressure fluctuations should occur at a point where the turbulent spot frequency is a maximum.

Turbulent spots have a characteristic pressure trace. Joksch and Kleiser [13] recently computed an expected pressure trace for a turbulent spot at Mach 5. The spot has a region of higher mean surface pressure as well as regions of alternating high and low pressure peaks. These fluctuations should be identifiable in surface-mounted pressure transducers. Figure 1.1 shows a schlieren image of turbulent spots on a ballistic-range model that is traveling from left to right through still air. Density fluctuations within the spots as well as radiated noise generated by the spot can be seen. This is similar to the radiated noise from turbulent boundary layers that causes high levels of tunnel noise in conventional hypersonic tunnels. There are also stronger acoustic waves generated in front of the turbulent spots.

There is already a wealth of literature studying turbulent spots [14–18], and recent advances in computations have enabled simulations of their growth and interaction [13, 19–21]. This existing knowledge should be used to predict transitional pressure fluctuations. Turbulent-spot models can be developed to describe the intermittent transition process [22, 23]. By including pressure fluctuations associated with a turbulent spot, the models can be extended to calculate transitional pressure fluctuations. Lauchle [24, 25] developed a similar model for radiated pressure fluctuations during incompressible boundary-layer transition. A similar analysis could be done to model pressure fluctuations transmitted to the wall in hypersonic boundary-layer transition. It is hoped that this description of transitional pressure fluctuations can provide a more physics-based method of understanding and predicting transitional fluctuations.

## 1.2 Outline of Experimental Work

In order to improve prediction of hypersonic pressure fluctuations, experiments were conducted on a 7° sharp cone at zero angle of attack in two hypersonic tunnels

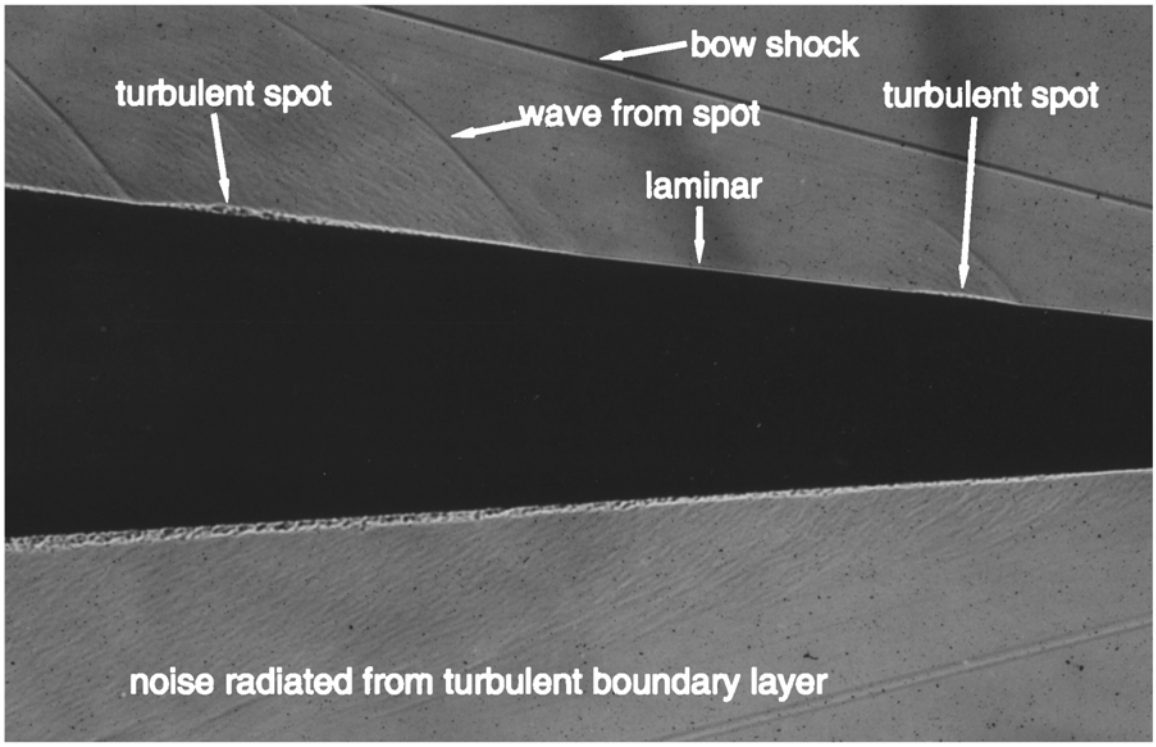


Figure 1.1. Schlieren image of turbulent spots on a 5° sharp cone at Mach 4.3 in NOL Ballistics Range, from Reference 26

under conventional and quiet noise levels. Surface-mounted pressure sensors were used to measure the pressure fluctuations. Experiments under noisy flow were conducted in the Sandia National Laboratories Hypersonic Wind Tunnel (HWT) at Mach 5 and 8 and in the Boeing/AFOSR Mach-6 Quiet Tunnel (BAM6QT) at Purdue University. Measurements under quiet flow were also conducted in the BAM6QT for comparison to noisy-flow measurements and flight data. The BAM6QT is the only operational hypersonic quiet tunnel in the world. It features low noise of about 0.05% (Pitot probe fluctuations divided by the mean), which is similar to flight and an order of magnitude lower than conventional tunnels [27]. This low noise makes the tunnel invaluable for comparing to flight. Research efforts so far have focused on five main points:

1. A comparison of different pressure sensors was conducted to identify which are most appropriate for measuring pressure fluctuations and identifying turbulent spots. The sensor responses to a laminar boundary layer were compared as well as the sensor responses to large turbulent spots on the BAM6QT nozzle wall under quiet-flow conditions.

2. Pressure fluctuations were measured on the surface of a cone in laminar, transitional, and turbulent flow in conventional (noisy) tunnels. These results were compared to previous measurements on cones and existing correlations for the pressure fluctuations. The transition region was identified with surface-mounted pressure transducers.

3. To begin to isolate noise effects on the measurements, tunnel noise measurements were conducted and compared to cone pressure fluctuations. Pressure fluctuations were also measured under noisy and quiet flow in the BAM6QT at similar $Re/m$. This allowed comparison of laminar pressure fluctuations and transition location under noisy and quiet-flow conditions.

4. Attempts were made under noisy flow to identify turbulent spots during transition. The hot film indicated possible turbulent spots; however, the spots could not be clearly identified in any of the pressure transducer traces. A statistical analysis of the pressure traces was used to explore transitional fluctuations, but more work is needed.

5. Measurements of second-mode waves were made in each tunnel. The breakdown of the waves is a useful indicator of transition and was compared to peak transitional pressure-fluctuation measurements between 0 and 50 kHz.

# 2. REVIEW OF LITERATURE

A series of experiments and research efforts were conducted in the 1960's and 1970's to better understand and predict pressure fluctuations. Much of this work was done at subsonic speeds and was summarized by Willmarth [28] in 1975. Limited work was conducted at hypersonic speeds, but it is far from complete. Correlations and underlying assumptions from this previous work are presented here. The reader is referred to the appropriate papers for more details about the development of these correlations.

## 2.1 Turbulent Pressure Fluctuations

Most correlations developed for hypersonic boundary-layer pressure fluctuations focused on turbulent pressure fluctuations. Houbolt [1] and Lowson [2] developed simple correlations of turbulent pressure fluctuations based on subsonic data. Later, others extended this work using hypersonic experiments and new theoretical approaches [3–8].

### 2.1.1 Houbolt

Houbolt [1] developed simple expressions to predict pressure fluctuations in turbulent boundary layers in the 1960's. His approach uses several key assumptions.

1. The turbulent eddy velocities are proportional to the freestream velocity.

2. The significant parameter contributing to the fluctuations is the local mean density in the region of maximum noise generation.

3. The region of maximum noise generation is the point within the boundary layer with the maximum temperature. This corresponds to the location of the maximum velocity gradient and the maximum shear flow.

4. The location of maximum noise generation given by $\delta/\delta^*$ does not vary significantly with Mach number.

The location of maximum noise generation is represented by the subscript 1. Here, a conical boundary layer is assumed. Houbolt's derivation begins with the following equation:

$$\tilde{p} = c\rho_1 U_e^2 = cq_e \frac{\rho_1}{\rho_e} \tag{2.1}$$

The density ratio is obtained by assuming $T_1$ can be obtained using a recovery type factor. This yields:

$$\frac{\rho_1}{\rho_e} = \frac{T_e}{T_1} = \frac{\frac{1}{a_1}}{1 + \frac{a_2}{a_1}\frac{\gamma-1}{2}M_e^2} \tag{2.2}$$

$a_2/a_1$ is found using Crocco's energy equation. Houbolt chooses the ratio to be 0.06 as a conservative estimate. $c/a_1$ is taken as 0.007, from experimental results on a Scout launch vehicle at $M = 1$ [29]. The resulting expression for the pressure fluctuations is:

$$\frac{\tilde{p}}{q_e} = \frac{0.007}{1 + 0.012M_e^2} \tag{2.3}$$

This can be rewritten to relate the pressure fluctuations to the edge pressure:

$$\frac{\tilde{p}}{p_e} = \frac{0.0049}{1 + 0.012M_e^2} \tag{2.4}$$

Houbolt also obtains the same results by assuming the fluctuations are generated by quadripole sources with strength proportional to the Reynolds stress.

Houbolt later revised his method when experimental data showed his correlation overpredicted hypersonic pressure fluctuations. His revision was unpublished but is given by Martellucci et al. [3], Chaump et al. [4], and Laganelli and Howe [7]. The revised equation is:

$$\frac{\tilde{p}}{q_e} = \frac{0.007}{1 + r_e\left(\frac{\gamma-1}{2}\right) M_e^2} \tag{2.5}$$

where

$$r_e = \left[1 - \left(\frac{U_1}{U_e}\right)\right]\left[r_1 + \left(\frac{U_1}{U_e}\right)\right] \tag{2.6}$$

$$r_1 = 2\left[\left(\frac{T_w}{T_e}\right) - 1\right] / \left[M_e^2\left(\gamma - 1\right)\right] \tag{2.7}$$

$$\frac{T_w}{T_e} = 1 + r_1\left(\frac{\gamma - 1}{2}\right) M_e^2 \tag{2.8}$$

and

$$\frac{U_1}{U_e} = 10.5\left[\left(\frac{T_w}{T_e}\right)\left(\frac{C_F}{2}\right)\right]^{1/2} \tag{2.9}$$

### 2.1.2 Lowson

Lowson [2] also developed a correlation for turbulent boundary layers. The correlation is based on a compilation of subsonic experiments that show that the pressure fluctuations equal 0.006 times the freestream dynamic pressure. The source of the pressure fluctuations is assumed to be the wall layer. Like Houbolt, Lowson considers the density at the site of the most intense eddy formation as the most important factor for noise generation. He also assumes an adiabatic wall and uses Crocco's equation (assuming $Pr = 1$) to form an expression for the density relation. A conical boundary layer is also assumed here, giving:

$$\frac{\rho_1}{\rho_e} = \frac{T_e}{T_1} = \frac{1}{1 + \left(1 - \frac{U_1}{U_e}\right)\left(r + \frac{U_1}{U_e}\right)\frac{\gamma-1}{2}M_e^2} \tag{2.10}$$

The recovery factor is taken as 0.9 and the source of the pressure fluctuations is assumed to be at the edge of the laminar sublayer where $U_1 = 0.5U_e$. This leads to the following expression for the pressure fluctuations on a cone:

$$\frac{\tilde{p}}{q_e} = \frac{0.006}{1 + 0.14M_e^2} \tag{2.11}$$

Written in terms of the edge pressure, this becomes:

$$\frac{\tilde{p}}{p_e} = \frac{0.0042}{1 + 0.14M_e^2} \tag{2.12}$$

### 2.1.3 Chaump and Martellucci

Chaump and Martellucci [3,4] extended the early work of Houbolt and Lowson. A review of existing experiments was completed, and a series of new tests on a 7.2° cone with sharp and blunt nosetips was conducted. The results were used to modify the turbulent prediction of Lowson and Houbolt. Houbolt's unpublished correlation was shown to estimate turbulent pressure fluctuations well. For Mach numbers less than 5, Lowson's equation also worked well. For higher Mach numbers, Lowson's equation was adjusted to:

$$\frac{\tilde{p}}{q_e} = \frac{0.002}{1 + 0.02M_e^2} \tag{2.13}$$

### 2.1.4 Laganelli

Laganelli [6, 7] continued previous work on pressure fluctuations. He analyzed Lowson and Houbolt's work and investigated some of their assumptions that may not have been applicable. These assumptions included:

1. The constants used in both Lowson's and Houbolt's work were based on subsonic experiments.

2. Compressibility was taken into account only through density. The change in viscosity due to higher temperature changes in compressible flow was not considered.

3. Crocco's linear temperature-velocity relationship was used, but this is questionable for turbulent flow.

4. The assumed velocity ratio at the edge of the laminar sublayer can vary.

5. Adiabatic wall assumptions do not always hold, especially in hypersonic wind-tunnel tests.

Laganelli based the development of a new correlation on Lilley's work [30, 31] that showed that the pressure fluctuations normalized by the wall shear stress are bounded both at M = 0 and as M goes to infinity. Others showed that the ratio was only weakly dependent on Reynolds number and Mach number [3, 5, 32], so the ratio is set equal to the parameter A:

$$\frac{\tilde{p}}{\tau_w} = A \tag{2.14}$$

where

$$\tau_w = 2q_e \left( \frac{C_F}{2} \right) \tag{2.15}$$

This gives:

$$\frac{\tilde{p}}{q_e} = 2A\left(\frac{C_F}{2}\right) \tag{2.16}$$

The Blasius skin friction form generalized for a variable power law is used for the skin-friction coefficient. Here $MF$ is the Mangler factor and $K(n)$ is a parameter related to the velocity power law. A compressibility factor $\epsilon_T$ that includes both density and viscosity is introduced. This differs from Houbolt and Lowson, who only introduced compressibility through density.

$$\frac{C_F}{2} = MF\,K(n)\,\epsilon_T\,(\mathrm{Re}_x)^{\frac{-2}{3+n}} \tag{2.17}$$

To match Lowson's empirical constant of 0.006 for incompressible flow, the parameter A is set to 2 since it is an average of the incompressible results. The Reynolds number term is assumed near 20 for typical experiments. A Mangler Factor of one (corresponding to a flat plate) is used. The result is a simplified expression for the pressure fluctuations where an incompressible result (0.006) is converted to compressible form using the compressibility factor. The final correlation is:

$$\left(\frac{\tilde{p}}{q_e}\right)_c = \left(\frac{\tilde{p}}{q_e}\right)_i \epsilon_T \tag{2.18}$$

$$\left(\frac{\tilde{p}}{q_e}\right)_i = 0.006 \tag{2.19}$$

$$\epsilon_T = \left(\frac{T^*}{T_e}\right)^{\frac{2m-(1+n)}{3+n}} \tag{2.20}$$

where the temperature ratio comes from the Eckert reference temperature method:

$$\frac{T^*}{T_e} = \frac{1}{2}\left(1 + \frac{T_w}{T_e}\right) + 0.22r\frac{\gamma-1}{2}M_e^2 \tag{2.21}$$

and m is the power in the Sutherland viscosity power law (temperature in English units):

$$m = \frac{3}{2} + \frac{\ln\left(\frac{T_e+198.6}{T_w+198.6}\right)}{\ln\left(\frac{T_w}{T_e}\right)} \tag{2.22}$$

For fully-developed turbulent flow, $n = 7$. However, many wind-tunnel experiments do not reach fully-developed turbulent boundary layers. For the turbulence just after boundary-layer transition, $n = 9$ is more appropriate [7].

## 2.2 Transitional Pressure Fluctuations

Several experiments and flight data have shown that pressure fluctuations peak during transition and have indicated the usefulness of surface mounted pressure transducers for transition detection [3, 4, 33–37]. The surface pressure fluctuations show a distinct peak near the end of transition. That peak has been shown to correspond to the point of maximum heat transfer often used to define the end of transition [3,37]. In this paper, transition will be defined in this manner; the peak pressure fluctuations occur near the end of transition. However, Owen and Horstman [11] and Martellucci [3] point out that there is still a region of non-similar flow after the peak in heat transfer that should still be considered part of the transitional region, though it is traditionally defined as turbulent. Despite the peak in transitional fluctuations, few correlations or experiments exist for transitional pressure fluctuations. Two are presented here and later compared to experiments.

### 2.2.1 Chaump and Martellucci

Chaump and Martellucci [3, 4] did an extensive review of hypersonic boundary-layer pressure fluctuations. They did not find any transitional pressure-fluctuation correlations even though the fluctuations peak during transition and should be of

interest for vehicle design. Using new experiments and those by Pate and Brown [33] and Johnson et al. [34], they developed an empirical correlation for transitional fluctuations:

$$\frac{\tilde{p}}{q_e} = \frac{0.0041}{1 + 0.013M_e^2} \tag{2.23}$$

However, as with existing turbulent correlations, this estimate was based on results from noisy tunnels. Their experiments suggested that the velocity power-law coefficient (normally 7 for fully-developed turbulent flow) changed during transition. This pointed to the possibility of predicting both turbulent and transitional pressure fluctuations with a similar formulation that would take the change in the power-law coefficient into account. Their work also showed that the peak in transitional pressure fluctuations occurred at the same time as the peak in heat transfer during transition. This relationship between the peak transitional fluctuations and other common methods of locating transition was explored further by Pate [37].

### 2.2.2 Laganelli

Laganelli [7] developed a correlation for transitional flow by taking into account the change in the velocity power-law coefficient as suggested by Chaump and Martellucci [3, 4]. Laganelli's turbulent correlation discussed above was used for transition. However, instead of using the typical $n = 7$ or $n = 9$ for turbulent flow, $n$ was found to vary between 2 to 6 for transitional flow [38]. Laganelli states that $n = 4$ should be used for the beginning to middle of transition, and $n = 6$ should be used to estimate peak transitional fluctuations. However, this seems inconsistent as $n = 4$ predicts higher pressure fluctuations than when using $n = 6$. Laganelli's experiments did show that $n = 6$ agreed better with the measured peak transitional fluctuations [7], so this higher value of $n = 6$ was used for comparison to the present results.

## 2.3 Tunnel Noise Considerations

Existing correlations were all developed using experiments from conventional wind tunnels. However, these conventional wind tunnels have a high level of freestream noise that can influence not only the transition location on the model but also the measured pressure fluctuations. This tunnel noise must be taken into account when comparing wind-tunnel experiments to flight.

Extensive work was done to study freestream noise in wind tunnels, particularly during the 1960's and 1970's. Laufer [39] discovered that although the dominant source of tunnel disturbances at low speeds was freestream vorticity disturbances, at Mach numbers higher than 3, the acoustic noise radiated from turbulent boundary layers on the walls was the dominant disturbance. This noise increases with increasing Mach number. The noise level in conventional hypersonic tunnels, defined as the root-mean-square (RMS) Pitot pressure divided by the mean Pitot pressure, can be near 1% and sometimes as high as 2–5% [40]. Noise levels can be even higher if the wall boundary layer is transitioning. These conventional tunnel noise levels are an order of magnitude higher than flight [41, 42].

Pate [43, 44] and Stainback [45], among others, investigated the relationship between tunnel noise and transition location on models and found they were related. The higher the tunnel noise level, the earlier transition occurred on the model. High noise levels have also been shown to cause transition on models much earlier than in flight [41, 42, 46]. To address this issue, quiet tunnels have been developed to better simulate flight noise levels [26,47]. Quiet tunnels maintain laminar boundary layers on the tunnel wall to avoid the noise radiation from turbulent boundary layers. However, they are still not common as it is difficult and costly to maintain laminar boundary layers on the nozzle wall for long distances and high Reynolds number. Most research is still done in conventional tunnels, making it important to understand the effect of noise on the results.

### 2.3.1 Pate's Correlation for Transition Location in Noisy Tunnels

Pate conducted extensive research into transition in several different conventional hypersonic wind tunnels in the 1970's [37]. He was able to show that tunnel noise dominates the transition process for flat plates and sharp cones at zero angle of attack. This had been suspected in previous work by Laufer [48] and others. Pate developed a correlation to predict the transition location on flat plates and sharp cones at zero angle of attack based on tunnel noise parameters: the tunnel wall turbulent boundary layer mean parameters ($C_{F_{II}}$ and $\delta^*$) and the test-section circumference ($c$). The correlation for sharp slender cones (Equation 2.24) gives the transition location, defined as the end of transition corresponding to the peak RMS in surface Pitot probe measurements. The test-section circumference of a 0.305 × 0.305-m tunnel is given by $c_1$.

$$\begin{aligned} &[(\mathrm{Re}_t)_\delta]_{cone} = \frac{\left(C_{F_{II}}\right)^{-1.40}(\overline{c})}{\left[\frac{\delta^*}{c}\right]^{\frac{1}{2}}} \\ &\overline{c} = 0.8 + 0.2\left(\tfrac{c_1}{c}\right) \;\; for \;\tfrac{c_1}{c} < 1.0 \\ &\overline{c} = 1.0 \; for \; \tfrac{c_1}{c} > 1.0 \end{aligned} \tag{2.24}$$

Pate wrote a Fortran code to perform the necessary computations. The code requires the input of the length of the nozzle (or length to the model leading edge), tunnel circumference at the model leading edge, the wall temperature, and the tunnel conditions ($M$, $P_0$, $T_0$). The code then computes the displacement thickness using experimental correlations and the mean turbulent skin-friction coefficient for the nozzle wall using the method of Van Driest-II. These are entered into the correlation to predict transition location. A detailed explanation of the equations and methods used by Pate can be found in Reference 37.

The output of the correlation and Fortran code is the transition location on the model, defined as the end of transition corresponding to the peak RMS in surface Pitot probe measurements. However, the transition location is not a single point on the model, but rather a transitional region. The transition location varies based on

which transition detection method is used. To correlate transition measurements from different tunnels and different transition detection methods, Pate compared different transition detection methods from a variety of experiments. Figure 2.1 shows a summary of those comparisons. From this data, Pate developed recommended correction curves to convert transition measurements to the corresponding location measured by surface Pitot probes (Pate's primary means of transition detection). Figure 2.2 shows the resulting correlations based on Pate's limited data set. Comparison of Pate's correlation to the present work is discussed in Section 4.2.7.

### 2.3.2 Stainback's Correlation for Transition Onset Location

Pate's correlation used only tunnel parameters to predict transition because at the time, few measurements of tunnel noise were available. In the years following Pate's work, measurements of tunnel noise were conducted in many tunnels. Stainback [45, 49] took those measurements of tunnel noise and compared them directly to the transition location on the model. He developed the following simple correlation for transition onset location based on laminar boundary layer pressure fluctuations measured on the surface of a sharp cone:

$$\mathrm{Re}_{st} = 1.41 \times 10^5 \Big/ \left(\tilde{p}/p_e\right)^{0.87} \tag{2.25}$$

The correlation was first given with a power of 0.9 in Reference 45; however, the correlation was later revised for a power of 0.87 [49]. A power of 0.87 was used for comparison to the present work (Section 4.2.8).

## 2.4 Laminar Boundary Layer Pressure Fluctuations

Early work suggested that pressure fluctuations measured on the surface of a sharp cone under a laminar boundary layer were equal to the freestream pressure fluctuations [12,45,49,50]. Stainback et al. [49] conducted experiments that suggested

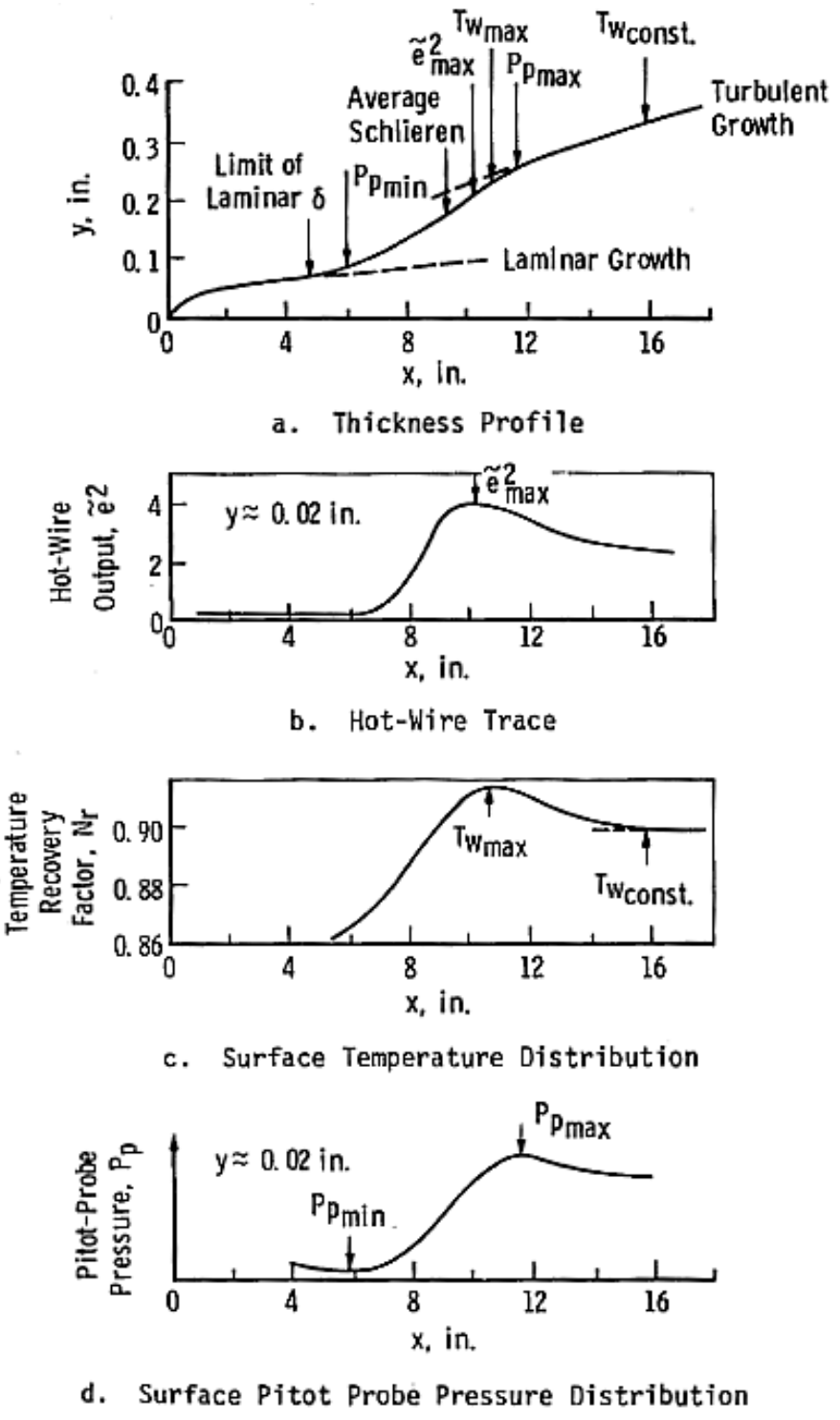


Figure 2.1. Comparison of transition location for various detection methods, from Reference 37

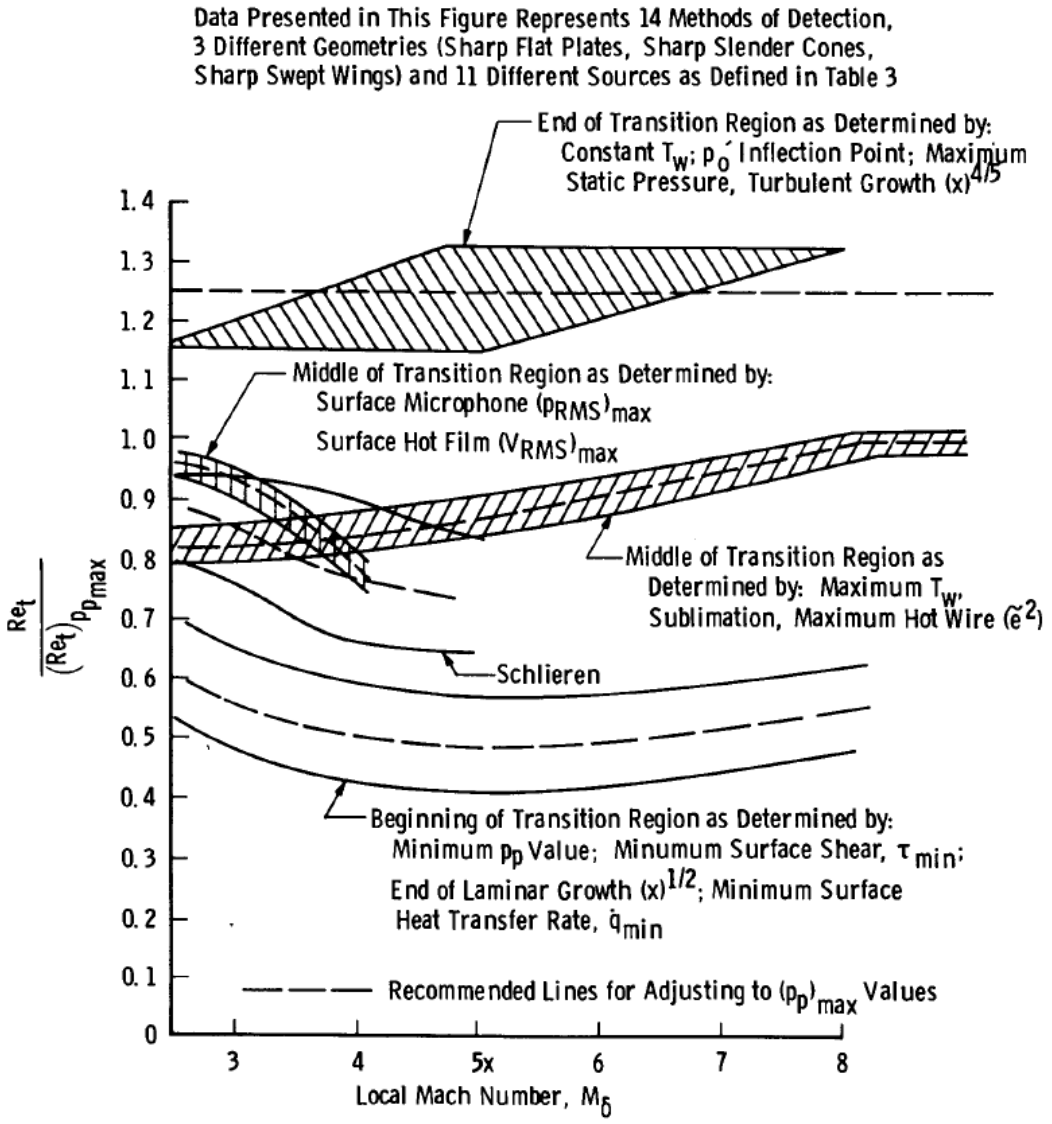


Figure 2.2. Correlations of transition detection methods, from Reference 37

that the freestream tunnel noise was not attenuated through the cone shock. This meant that the acoustic disturbances in the tunnel freestream entered the model laminar boundary layer and remained constant.

### 2.4.1 Stainback's Correlation for Freestream Noise Levels in Conventional Tunnels

Stainback and Rainey [50] developed a correlation for freestream pressure disturbances in conventional tunnels, assuming that the freestream pressure fluctuations equal the cone surface pressure fluctuations under a laminar boundary layer. The correlation could be applied to hot-wire data as well as cone surface pressure-transducer data under a laminar boundary layer. The correlation begins from the following identity:

$$\frac{\tilde{p}}{p} \equiv \frac{\tau_w}{p} \frac{\tilde{p}}{\tilde{p}_w} \frac{\tilde{p}_w}{\tau_w} \tag{2.26}$$

The first term is computed from turbulent boundary-layer theory, using freestream conditions and the distance from the nozzle throat to the acoustic origin. The ratio of freestream to nozzle-wall pressure fluctuations is taken from a curve fit to experimental data. The curve is based on few data points and needs to be modified to take into account new data.

$$\frac{\tilde{p}}{\tilde{p}_w} = f_2(M) = 4.0\times10^{-5}M^3 - 2.478\times10^{-3}M^2 + 4.125\times10^{-2}M - 1.234\times10^{-2} \tag{2.27}$$

A relationship for the ratio of the wall pressure fluctuations to the wall shear stress was developed. Similar to Laganelli, it is based on Lilley's theory [30, 31] that the ratio is limited both at $M = 0$ and as M goes to infinity. Experimental data supports this theory [51]. The following equation is used to fit Lilley's theory for adiabatic walls:

$$\frac{\tilde{p}_w}{\tau_{w,aw}} = f_1(M) = 2.2 + 4.1\left(1 - e^{-0.1M^2}\right) \tag{2.28}$$

The volume of the boundary layer that is radiating noise is added with the ratio $\frac{A_s}{A}$. This term is the ratio of the nozzle surface area from the throat to the most downstream acoustic origin of disturbances detectable by a probe divided by the nozzle cross-sectional area at the acoustic origin. Wall and fluid temperature effects are accounted for with the term $\left(\frac{T_0}{T_w}\right)^n$. The resulting correlation is:

$$\frac{\tilde{p}}{p} = K_1\left[\frac{\tau_w}{p}\frac{A_s}{A}\left(\frac{T_0}{T_w}\right)^n f_1(M)\, f_2(M)\right] + K_2 \tag{2.29}$$

Using this correlation with hot-wire data, $K_1$ becomes 0.0513, $K_2$ is 0.0017, and n = 0.25. Using cone surface pressure-transducer data, $K_1$ is 0.0355, $K_2$ is 0.0033, and n remains 0.25.

### 2.4.2 Amplification of Freestream Noise in Laminar Boundary Layers

In the mid 1970's, a series of papers broke with the understanding that freestream pressure fluctuations remain constant through the model shock and boundary layer [40]. Beckwith [47], Kendall [52], and Pate [53] showed experimental results that freestream noise could be amplified within the laminar boundary layer. This phenomenon was consistent with Mack's [54] forcing theory, developed near the same time. The theory explained the interaction of low-frequency freestream noise components with a laminar boundary layer and allowed for the amplification of freestream noise without an instability, sometimes by factors as high as 5–20.

Schopper [55] complemented Mack's forcing theory by studying the interaction of the higher-frequency freestream noise with a laminar boundary layer. The refraction and focusing of weak shocks in the upper half of the boundary layer (termed the caustic layer) was shown to increase disturbances by factors of 2–6. High-frequency

components were low-pass filtered by the caustic layer. Schopper could not find experimental confirmation of the caustic layer, and it is not known if this theory was ever experimentally verified. The question of whether the freestream noise is amplified in the laminar boundary layer as described by either Mack's or Schopper's theories remains unanswered.

Fischer and Weinstein [56] also noted that the edge of the boundary layer can be transitional or turbulent while the surface remains laminar. Disturbances spread to the wall at a constant angle. Surface pressure measurements upstream of the surface transition location might be influenced by transition or turbulence in the outer portions of the boundary layer [3].

## 2.5 Summary

Boundary-layer pressure fluctuations have been of interest for many years. Early work focused on predicting turbulent-boundary-layer pressure fluctuations, particularly at low speeds. Over the years, those correlations have been extended to hypersonic Mach numbers. Several correlations exist for hypersonic turbulent boundary layers. Only a few exist for transitional boundary layers. Laminar boundary layer correlations exist, but are based on the concept of laminar pressure fluctuations being equal to the freestream tunnel noise. This idea was first questioned in the 1970's with the development of Mack's forcing theory and experimental data to support it. Much work remains to isolate the effects of tunnel noise on existing work and to understand how the fluctuations are generated, particularly during transition.

# 3. EXPERIMENTAL METHODS AND SETUP

## 3.1 Wind-Tunnel Facilities

### 3.1.1 Sandia Hypersonic Wind Tunnel

The Sandia Hypersonic Wind Tunnel (HWT) is a blowdown-to-vacuum facility (Figure 3.1). Interchangeable nozzle and heater sections allow the tunnel to be run at Mach 5, 8, or 14 (Figure 3.2). Mach 5 tests use air as the driver gas while Mach 8 and Mach 14 run with nitrogen. Tests were only conducted at Mach 5 and 8 for this study because the Mach-14 heater was down for repairs. Run times were typically 15–30 s.

HWT-5 has a $P_0$ range of 345–1380 kPa and a $T_0$ range of 330–890 K, giving a $Re/m$ range of 3.3–26 $\times 10^6$. The HWT-5 operating map can be seen in Figure 3.3. The test-section diameter is 0.459 m at the nozzle exit, and the nozzle is 3.251 m long, from the throat to the test-section end.

HWT-8 uses 689 MPa nitrogen supplied from a bottle farm. It has a $P_0$ range of 1720–6890 kPa, $T_0$ range of 500–890 K, and $Re/m$ can be varied from 3.3–20 $\times 10^6$ (Figure 3.4). The Mach 8 test-section diameter is 0.359 m at the nozzle exit, and the nozzle is 2.807 m long.

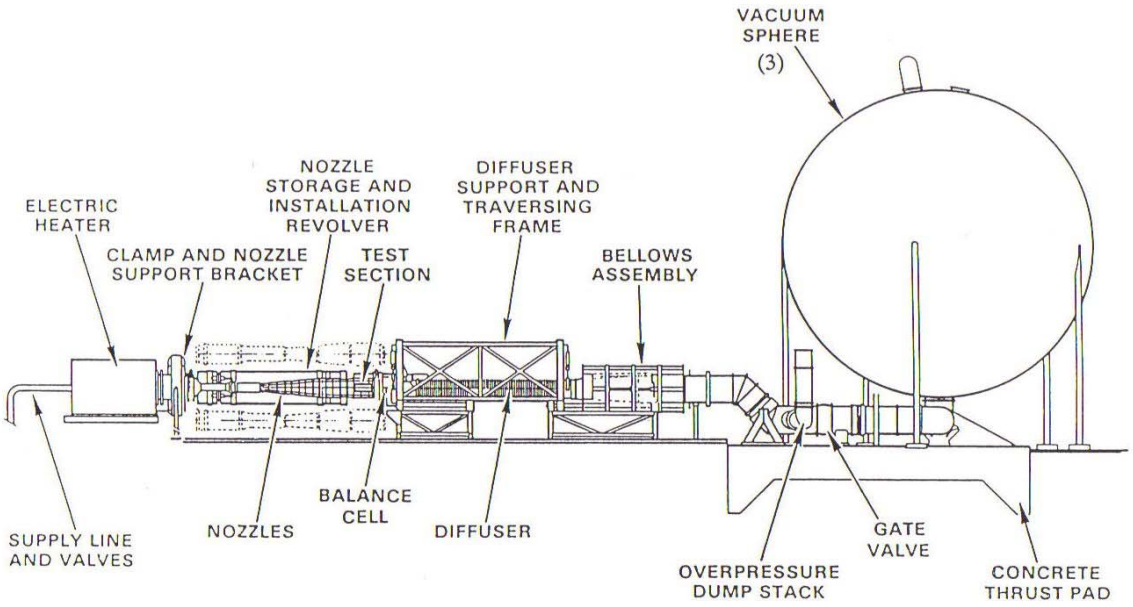


Figure 3.1. Sandia Hypersonic Wind Tunnel

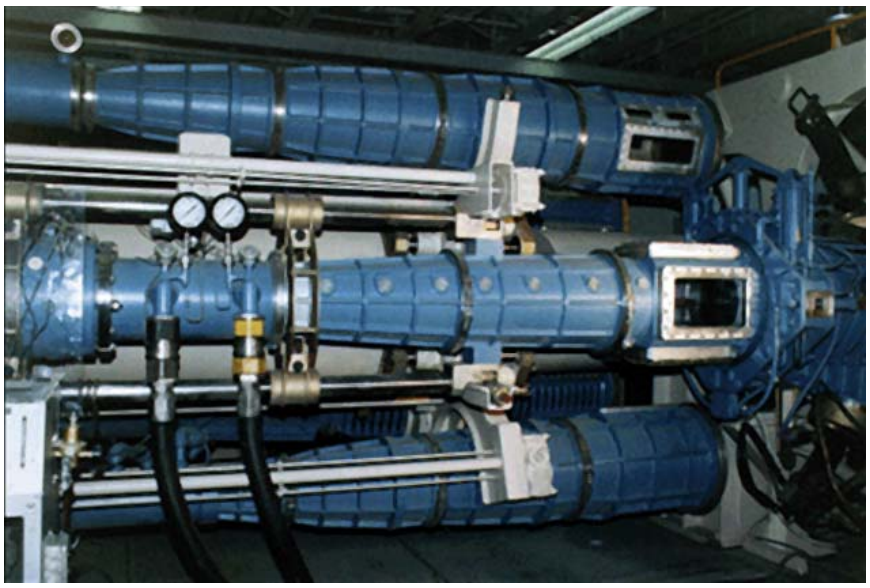

Figure 3.2. Interchangeable HWT nozzles

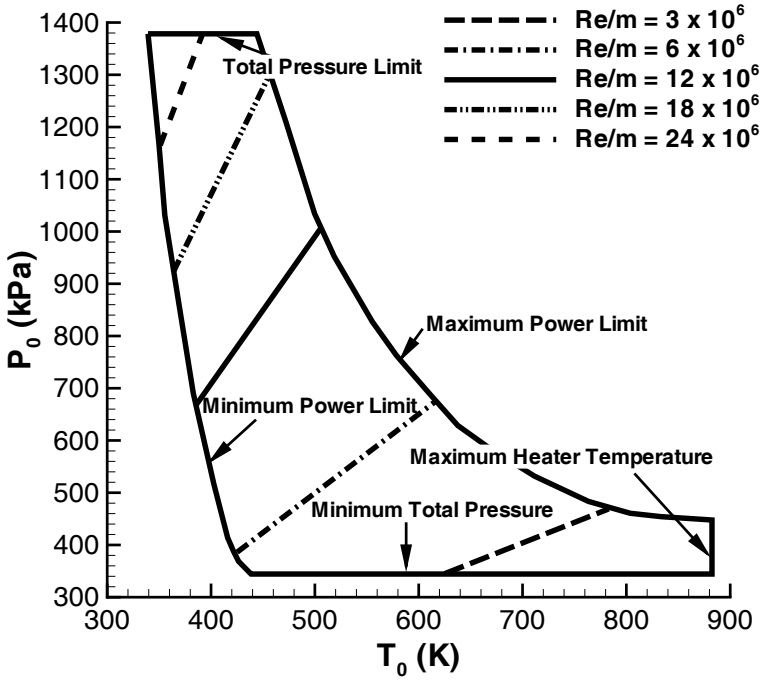


Figure 3.3. HWT-5 operating map

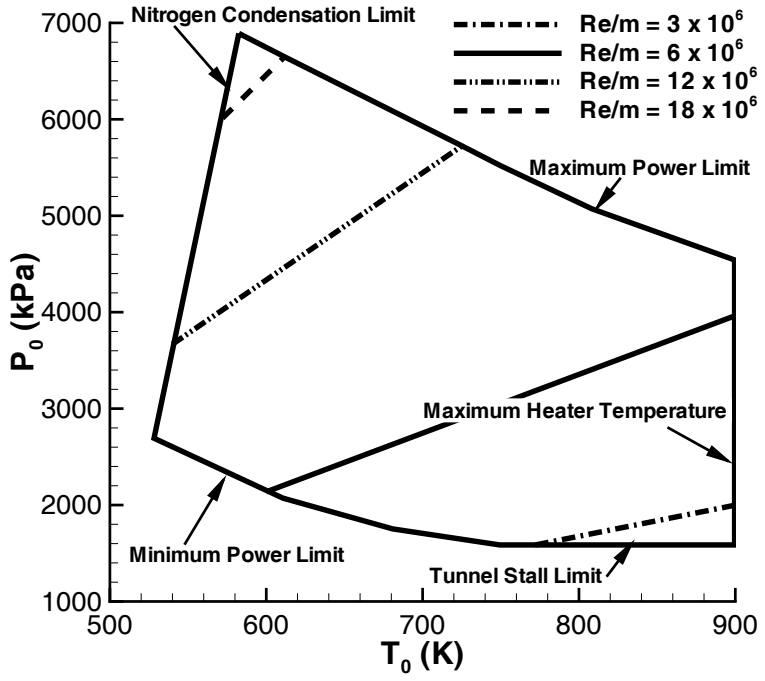


Figure 3.4. HWT-8 operating map

### 3.1.2 Boeing/AFOSR Mach-6 Quiet Tunnel

The BAM6QT (Figures 3.5 and 3.6) can be operated as a conventional noisy tunnel or as a quiet tunnel. The BAM6QT is currently the only operational hypersonic quiet tunnel in the world. This makes it unique for boundary-layer transition studies. The tunnel is a Ludwieg tube, a long tube with a converging-diverging nozzle on the end. The flow passes from the driver tube, through the test section, diffuser, a second throat, and finally to the vacuum tank. Flow is initiated by bursting a double diaphragm that is located downstream of the diffuser. When the flow begins, an expansion wave travels upstream and then reflects between the upstream end of the driver tube and the contraction. The total pressure and temperature drop with each reflection cycle (every 200 ms) until the tunnel unstarts. Run times of 3–5 s are typical at present. The tunnel uses air as the test gas and operates with an initial $P_0$ of 34–2070 kPa and an initial $T_0$ of 430 K, giving a $Re/m$ range of 0.4–$18.3 \times 10^6$. The current maximum quiet pressure ($P_0$) is 1130 kPa which corresponds to $Re/m = 10.5 \times 10^6$. The test-section diameter is 0.241 m at the nozzle exit, and the nozzle is 2.590 m long.

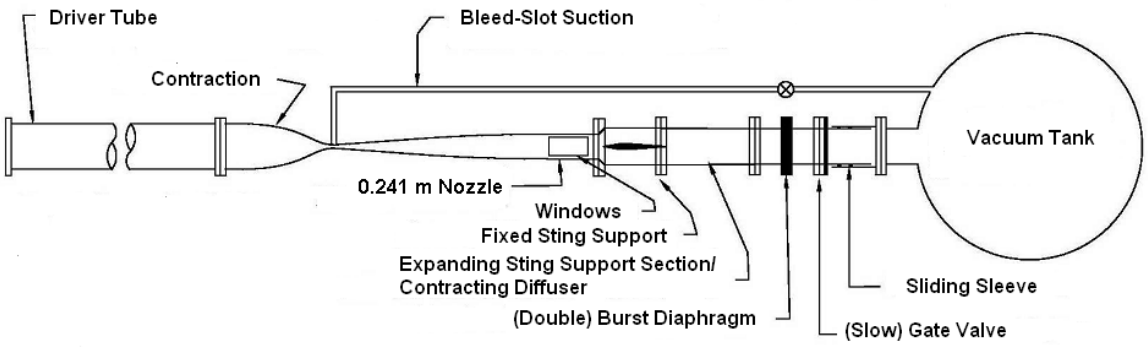


Figure 3.5. Boeing/AFOSR Mach-6 Quiet Tunnel

It is difficult to obtain quiet flow in a hypersonic tunnel. The nozzle is polished to a mirror finish to avoid roughness-induced transition. The contraction boundary

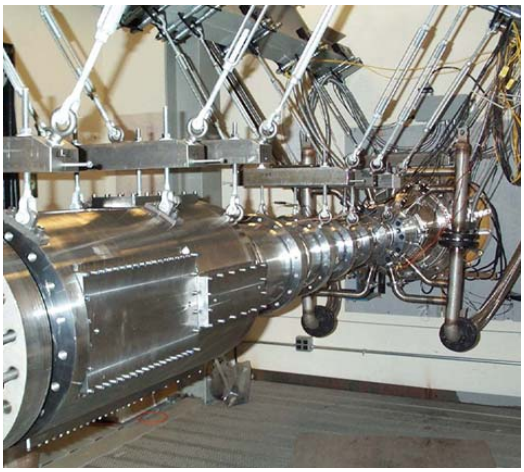

Figure 3.6. BAM6QT nozzle and test section (flow from right to left)

layer is also removed by bleed slots at the throat, for quiet runs. A new laminar boundary layer begins just upstream of the nozzle throat and is maintained through the test section. The air is filtered to remove dust or other particles above 0.01 microns that may damage the nozzle or trip the boundary layer. More details about the development of the BAM6QT can be found in Reference 26.

### 3.2 Pressure-Fluctuation Cone

The Pressure-Fluctuation Cone was used for all wind-tunnel tests (Figure 3.7). The model is a 7° half-angle stainless-steel cone. It has many interchangeable parts that allow flexibility for use in a variety of tunnels and experiments (Figure 3.8). A complete set of drawings and parts list can be found in Appendix B.

The cone has four sections. The first section is the nosetip. Four different nosetips were tested; two sharp nosetips with maximum 0.05-mm radius, a 0.5-mm-radius blunt nose, and a 1.5-mm-radius blunt nose. The different nosetips allow the transition location at a given freestream Reynolds number to be shifted. These blunt nosetips delay the transition location compared to the sharp nosetips [57]. Pictures of these nosetips under a microscope at 20× magnification can be seen in Figures

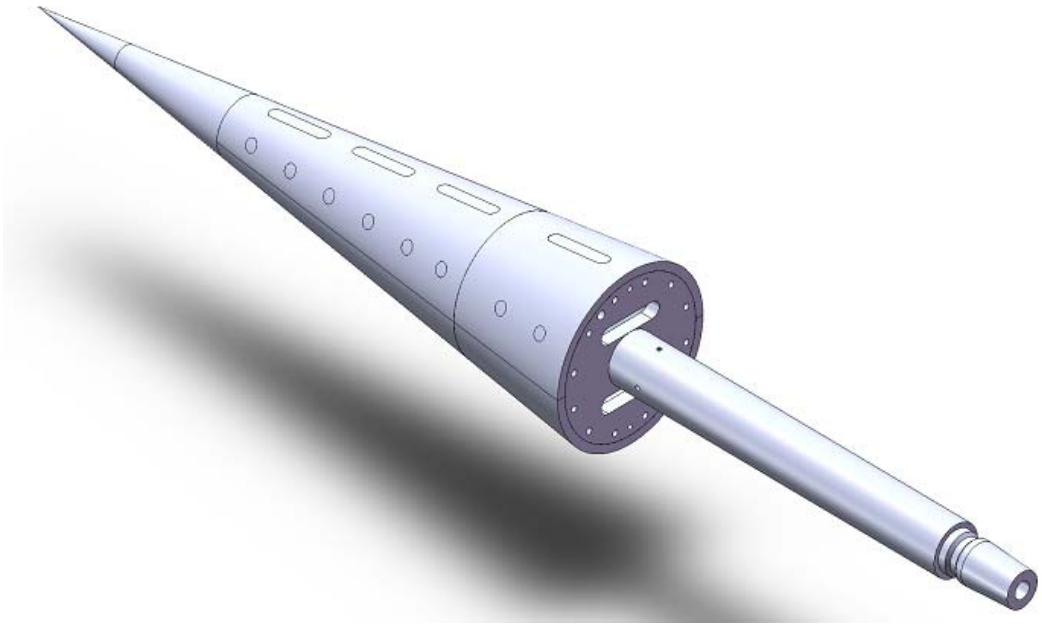

Figure 3.7. Fully assembled Pressure-Fluctuation Cone

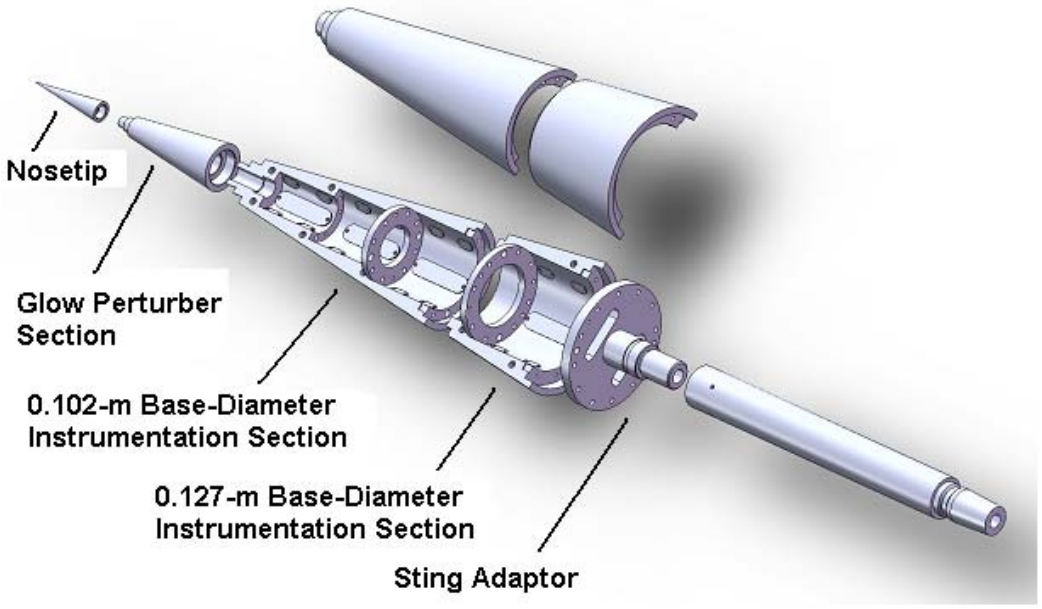


Figure 3.8. Exploded view of Pressure-Fluctuation Cone

3.9(a) through 3.9(d). The sharp nosetips are shown next to a strand of human hair. One of the sharp nosetips was bent during testing and had to be fixed. The nosetip was straightened using rosewood and a lathe, but some imperfection remains. A picture of the straightened nosetip at 40× magnification is shown in Figure 3.9(e).

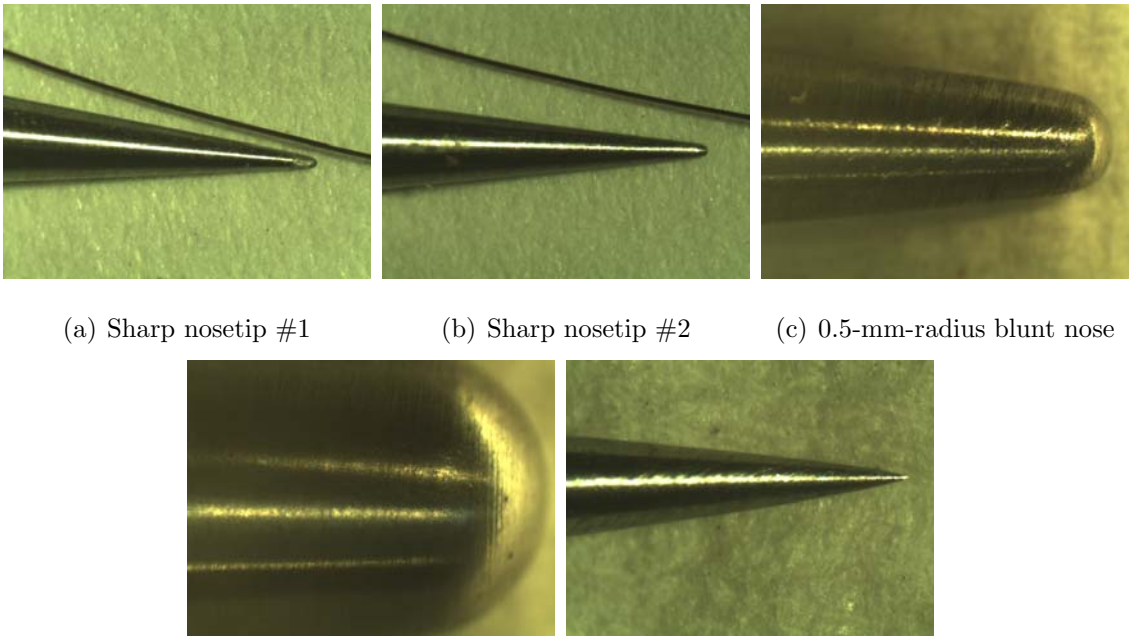

(a) Sharp nosetip #1 (b) Sharp nosetip #2 (c) 0.5-mm-radius blunt nose

(d) 1.5-mm-radius blunt nose (e) Sharp nosetip #1, as repaired

Figure 3.9. Magnified nosetips

The second section is a blank cone forebody section. It is interchangeable with a glow-perturber section that will allow controlled disturbances to be introduced into the boundary layer in future experiments (Figure 3.10). The glow-perturber section has interchangeable inserts for testing different perturber designs. It is also designed to allow rotation so the glow perturber can be placed at different azimuthal locations with respect to the sensors. Only the blank section of the cone was used for these experiments.

The third and fourth sections of the cone are designed to hold the instrumentation. The model can be run as a 0.102-m base-diameter cone using the third section only, or

Figure 3.10. Glow-perturber section

the fourth section can be added to increase the cone base diameter to 0.127 m. These correspond to model lengths of 0.414 m and 0.517 m, respectively. This option allows a smaller cone to be used in tunnels with a more stringent starting requirement. Both sections split in half axially to allow access to the inside of the cone for instrumentation (Figure 3.11). One side of the cone is a solid section without instrumentation inserts. The other half of the cone is machined to hold a series of four axial inserts as well as two rows of eight individual inserts that are 120 degrees apart. Figure 3.12 shows two individual sensors and one axial sensor pulled out of the cone. The individual inserts were used for all testing so far. Axial inserts will be machined later to allow for closer spacing of the sensors. The 0.127-m base-diameter section of the cone is interchangeable with another section that has an axial insert on one half and a single radial insert on the other half. Radial inserts will also allow close azimuthal spacing of sensors.

The cone was fabricated with a complete set of blank inserts that are machined flush with the surface. The blank inserts can be replaced with inserts that hold four types of pressure sensors, either flush mounted or recessed under a 0.41-mm diameter pinhole for increased spatial resolution (Figures B.20 through B.25). Figure 3.13

Figure 3.11. Cone opened for instrumentation

Figure 3.12. Two individual inserts and one axial insert removed from model

shows the insert locations and Table 3.1 lists the possible sensor mounts currently available at each insert location.

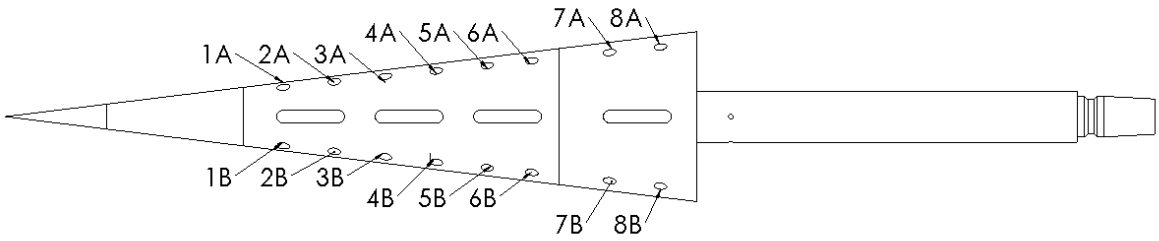


Figure 3.13. Insert locations for individual sensors

## 3.3 Instrumentation

### 3.3.1 Pressure Transducers

Three types of pressure transducers were used during testing. Kulite Mic-062 and XCQ-062-15A sensors were used for frequency measurements between 0 and 50 kHz. Measurements between 11 kHz and 1 MHz were made with PCB132A31 sensors. A summary of pressure transducer specifications is given in Table 3.2.

#### Kulite Pressure Transducers

Kulite pressure transducers use silicon diaphragms as the basic sensing mechanisms. Each diaphragm contains a fully active four-arm Wheatstone bridge. The Kulites have screens to protect the diaphragms from damage. Two types of screens were used. The A-screen (Figure 3.14(a)) has a large central hole. This screen offers only a small amount of diaphragm protection, but the sensor has a flatter frequency response. The sensitive area of the A-screen sensor is the hole size (0.81 $mm^2$). The B-screen (Figure 3.14(b)) has a ring of eight holes around the periphery of a solid screen which offers better diaphragm protection than the A-screen. However, the

| | Axial Distance from Nosetip (m) | | | Pressure Transducer | | | |
|---|---|---|---|---|---|---|---|
| Location | Sharp | 0.5-mm Radius Blunt | 1.5-mm Radius Blunt | XCQ-062 | Mic-062 | PCB132 | PCB105 |
| 1A | 0.208 | 0.204 | 0.197 | flush/recessed | flush/recessed | flush/recessed | flush/recessed |
| 2A | 0.246 | 0.242 | 0.235 | flush | flush | no | no |
| 3A | 0.284 | 0.281 | 0.273 | flush | flush | no | no |
| 4A | 0.322 | 0.319 | 0.311 | flush | flush | no | no |
| 5A | 0.360 | 0.357 | 0.349 | flush | flush | flush | no |
| 6A | 0.398 | 0.395 | 0.387 | flush | flush | no | no |
| 7A | 0.452 | 0.448 | 0.441 | flush | flush | no | no |
| 8A | 0.490 | 0.486 | 0.479 | flush/recessed | flush/recessed | flush/recessed | flush/recessed |
| 1B | 0.208 | 0.204 | 0.197 | flush/recessed | flush/recessed | flush/recessed | flush/recessed |
| 2B | 0.246 | 0.242 | 0.235 | flush | flush | no | no |
| 3B | 0.284 | 0.281 | 0.273 | flush | flush | no | no |
| 4B | 0.322 | 0.319 | 0.311 | flush | flush | no | no |
| 5B | 0.360 | 0.357 | 0.349 | flush | flush | flush | no |
| 6B | 0.398 | 0.395 | 0.387 | flush | flush | no | no |
| 7B | 0.452 | 0.448 | 0.441 | flush | flush | no | no |
| 8B | 0.490 | 0.486 | 0.479 | flush/recessed | flush/recessed | flush/recessed | flush/recessed |

Table 3.1 Individual sensor locations and sensor mount capabilities

Table 3.2 Pressure-transducer comparison

| Sensor | Measurement Range (kPa) | Sensitivity (mV/Pa) | Resonance Frequency (kHz) | Low Frequency Cutoff (kHz) | Diameter (mm) |
|---|---|---|---|---|---|
| Mic-062 | ±7 | 0.207 | 125 | 0 | 1.59 |
| XCQ-062-15A | 0–103 | 0.040 | 225 | 0 | 1.59 |
| PCB105 | 0–690 | 0.007 | > 250 | 0.0005 | 2.51 |
| PCB132A31 | 0–345 | 0.020 | > 1000 | 11 | 3.18 |

frequency response rolls off at a lower frequency than for the A-screens. Frequency-response comparisons are shown in Section 4.1. Each sensor was statically calibrated using a Paroscientific Model 760 Digiquartz Standard with a 103 kPa full scale in HWT and a Model 740 Standard with a 206 kPa full scale in the BAM6QT. The accuracy of the standards is better than 0.008% of full scale. Static calibrations were typically within 1% of the factory calibrations. Dynamic calibrations have not yet been completed because the effort required was outside the scope of the present work. However, future work will include these dynamic calibrations (Section 5.2).

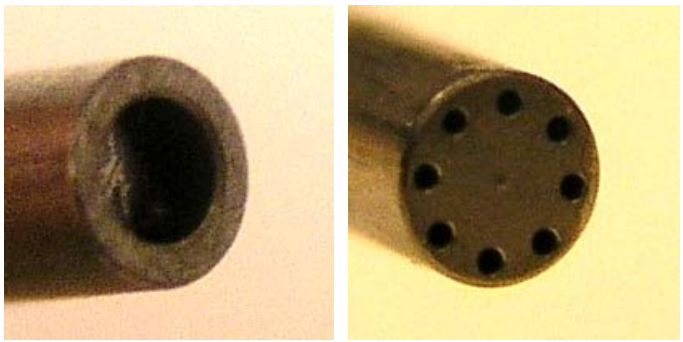

(a) A-screen (b) B-screen

Figure 3.14. Kulite screens

### Mic-062

Both Mic-062 A-screen (Figure 3.15) and B-screen sensors were tested. The microphones measure the pressure differential across a diaphragm, up to ±7 kPa. The back

side of the diaphragm has a pressure reference tube that is approximately 0.05 m long. This tube was bent 90 degrees to fit inside the model and left open to the plenum inside of the model. The plenum gives an approximately steady reference pressure, and high-frequency components of this pressure are filtered by the long reference tube. The diameter of these sensors is 1.59 mm. They have a nominal resonant frequency of 125 kHz and a nominal sensitivity of 0.207 mV/Pa. The quoted repeatability of the sensors is approximately 0.1% of the full scale, or 7 Pa.

Figure 3.15. Mic-062 A-screen installed in individual insert

**XCQ-062-15A**

The XCQ-062-15A sensors are mechanically stopped above 103 kPa to prevent damage to the diaphragms at the high BAM6QT pre-run pressures. Because of their larger measurement range, the sensors are less sensitive than the Mic-062's. However, they have a higher nominal resonant frequency of 225 kHz. The diameter of these sensors is also 1.59 mm. The quoted repeatability of the sensors is approximately 0.1% of the full scale, or 0.1 kPa. Only B-screen XCQ-062's were used in this work, but tests of A-screen sensors are planned.

### PCB Integrated Circuit Piezoelectronic (ICP) Pressure Transducers

PCB piezoelectric pressure sensors operate in a different manner than Kulite pressure sensors. PCB sensors have crystals that release a charge when stressed. Quartz or Tourmaline crystals are typically used for stable, repeatable measurements. The high-impedance charge output of the sensors is converted to a low-impedance voltage output using built-in micro-electronic amplifiers. The charge of these sensors eventually leaks to zero, making only dynamic pressure measurements possible. Dynamic calibrations have not yet been completed.

### PCB105

PCB105 sensors (Figure 3.16) offer another alternate to the Kulite sensors. The diameter of these sensors is 2.51 mm. They have a resonant frequency above 250 kHz and a low-frequency cutoff of 0.5 Hz. The nominal sensitivity of the sensors is approximately 0.007 mV/Pa, and the discharge time constant of the sensors is above 1 second. The resolution of the sensors is 35 Pa, per the manufacturer's specifications. The repeatability of the sensors is not given. The sensors are also rugged—they can measure pressure up to 690 kPa and survive pressures up to 1720 kPa.

Figure 3.16. PCB105 installed in individual insert

**PCB132A31**

The PCB132A31 (Figure 3.17) is a very high frequency piezoelectric time-of-arrival sensor with a pressure resolution of approximately 7 Pa. The nominal sensitivity of the sensors is approximately 0.020 mV/Pa, and the discharge time constant is 0.000045 seconds. The resonant frequency of the sensors is above 1 MHz, but the sensor output is high-pass filtered at 11 kHz, per the manufacturer's specifications. Because the resonant frequency of the PCB132's is high, the sensors can measure high-frequency instabilities leading to transition in hypersonic flows [58,59]. Measurements of these instabilities have typically been made by hot wires [52,60–65]. However, hot-wire measurements in hypersonic flow are difficult, and the sensors frequently break. The PCB132's are rugged and can measure dynamic pressures up to 345 kPa and withstand pressures up to 5516 kPa. They allow a study of instability breakdown to transition, and are useful indicators of transition on the model. However, the sensors have not yet been accurately calibrated for this purpose. The repeatability of the sensors is also not specified by the manufacturer. In addition, the sensors have spatial resolution problems for measuring such high-frequency instabilities. Second-mode waves have a wavelength of approximately twice the boundary-layer thickness (approximately 1–3 mm for this work). The PCB132 diameter (3.18 mm) is larger than half of the instability wavelength. However, the actual sensitive area of the face is unknown, though the piezoelectric sensing elements form a $1 \times 1.6$-mm rectangle below the sensor face. Planned dynamic calibrations of the sensors should better define their behavior and limitations.

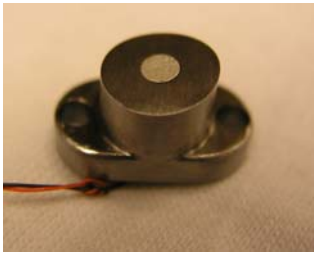

Figure 3.17. PCB132 installed in individual insert

### 3.3.2 Dantec Glue-on Hot-Film Probe

Two Dantec glue-on probes for air (55R47) were pasted on the cone for comparison to the pressure-transducer traces (Figure 3.18). The sensor is glued onto 50 $\mu m$ Kapton foil. The sensor itself is only 0.9 $\times$ 0.1 mm and is oriented perpendicular to the flow. The frequency response of the sensors has not been characterized as it depends on the bonding, model material, and other factors. However, the frequency response is estimated to be near 20 kHz. Bruhn-6 constant temperature anemometers built at Purdue were used to control these sensors. The output of the anemometers is an uncalibrated voltage.

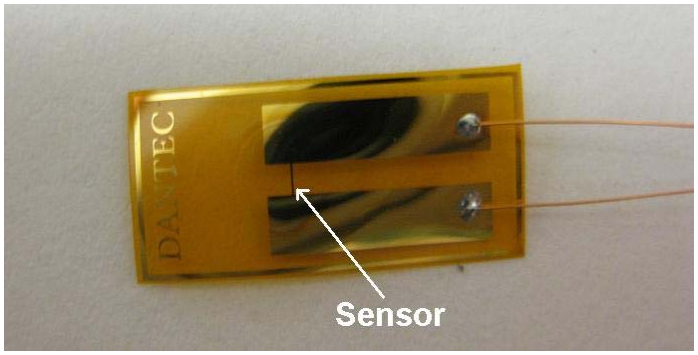


Figure 3.18. Dantec 55R47 glue-on probe for air

### 3.3.3 BAM6QT Senflex Hot-Film Array

An existing Senflex hot-film array [66] on the BAM6QT nozzle wall was used to measure turbulent spots passing by on the nozzle wall. The output of two hot films located at z = 1.918 m and z = 2.070 m were recorded. The hot-film array is also controlled using Bruhn-6 constant temperature anemometers.

## 3.4 Data Acquisition

The data-acquisition systems at each facility (Figure 3.19 and 3.20) are different but provide similar high-speed sampling and anti-aliasing over many channels.

### 3.4.1 Sandia Hypersonic Wind Tunnel

Kulite sensors need an excitation voltage for operation. A 10 V excitation is applied using an Endevco Model 136 DC Amplifier. The amplifier was also used to supply a gain of 100 for Kulite signal output. A Krohn-Hite Model 3384 Tunable Active Filter was used as an anti-aliasing low-pass Bessel filter for the Kulites and hot films. The filter was set at 200 kHz for all 2009 tests, but was set at 50 kHz for 2008 runs. The filter has eight poles and provides 48 dB attenuation per octave. The Kulite sampling frequency was 1 MHz. The PCB132 sensors all run through a PCB 482A22 signal conditioner that provides constant-current excitation to the built-in sensor amplifier. It also decouples the AC signal from the DC bias voltage. The constant current can be varied from 4 to 20 mA; 4 mA was used for all measurements. The output from the signal conditioner is fed through a Krohn-Hite Model 3944 Filter with a 1 MHz low-pass anti-aliasing Bessel filter. This filter has four poles and offers 24 dB of attenuation per octave. The sampling frequency for the PCB132 sensors was 2.5 MHz. Data is acquired using a National Instruments PXI-1042 chassis with 14-bit PXI-6133 modules (10 MHz bandwidth) for data acquisition. A data sample of 0.75 s was acquired during the constant-condition portion of each wind-tunnel run.

### 3.4.2 Boeing/AFOSR Mach-6 Quiet Tunnel

The signal from the Kulite pressure transducers is processed by custom-built electronics, which also supply a 10 V excitation. The output signal is amplified by a gain of 100 with an INA103 instrumentation amplifier chip to give the DC signal.

As in HWT, the output from the PCB sensors is run through a PCB 482A22 signal conditioner.

Two Tektronix DPO7054 and one Tektronix TDS7104 Digital Phosphor Oscilloscopes are used for data acquisition in the BAM6QT. The oscilloscopes have built-in digital filtering. Separate anti-aliasing filters are not required. The DPO7054 has a system bandwidth of 500 MHz and an 8-bit vertical resolution. The resolution can be increased to over 11-bit in Hi-Res mode. Hi-Res mode is used to increase the vertical resolution and reduce random noise. The oscilloscopes average real-time at the maximum sampling rate and then save data at the specified sampling rate. The TDS7104 has similar capabilities, but less memory. Five seconds of data were recorded for each run. The sampling rate was 500 kHz for the Kulites and 5 MHz for the PCB132's.

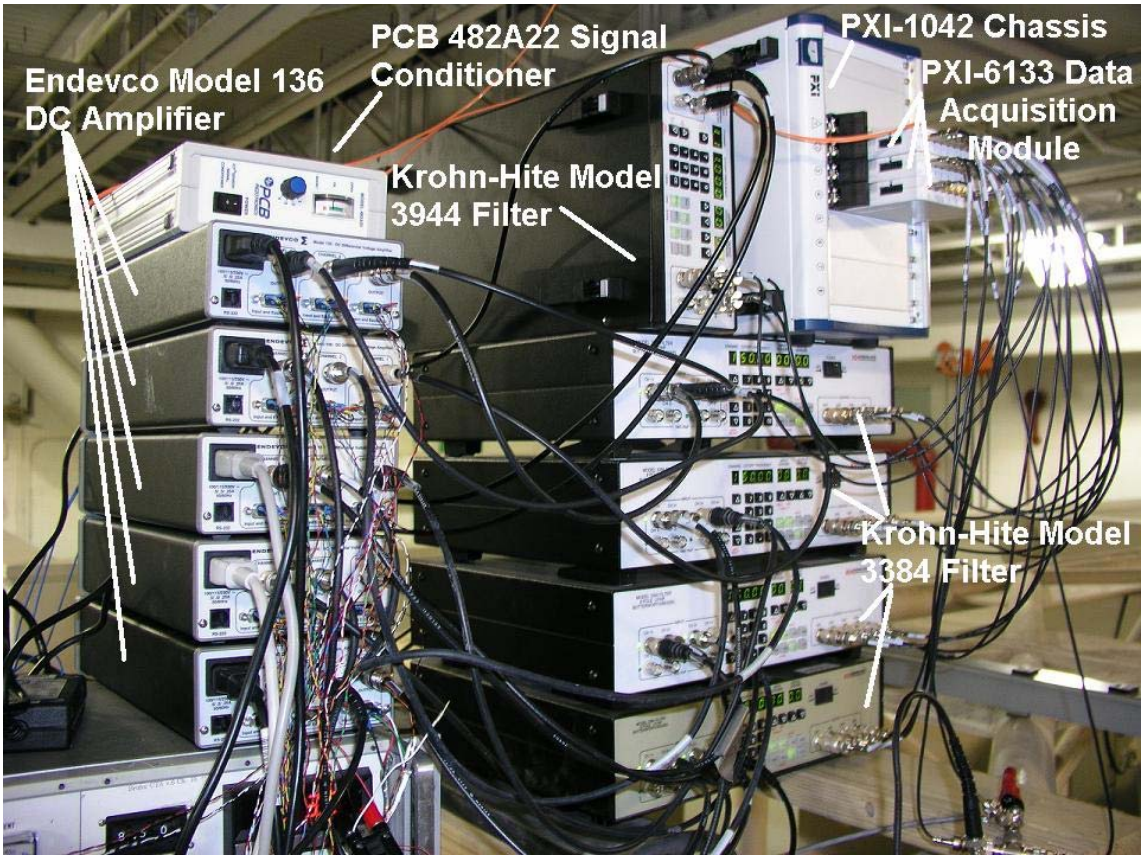


Figure 3.19. HWT data-acquisition system

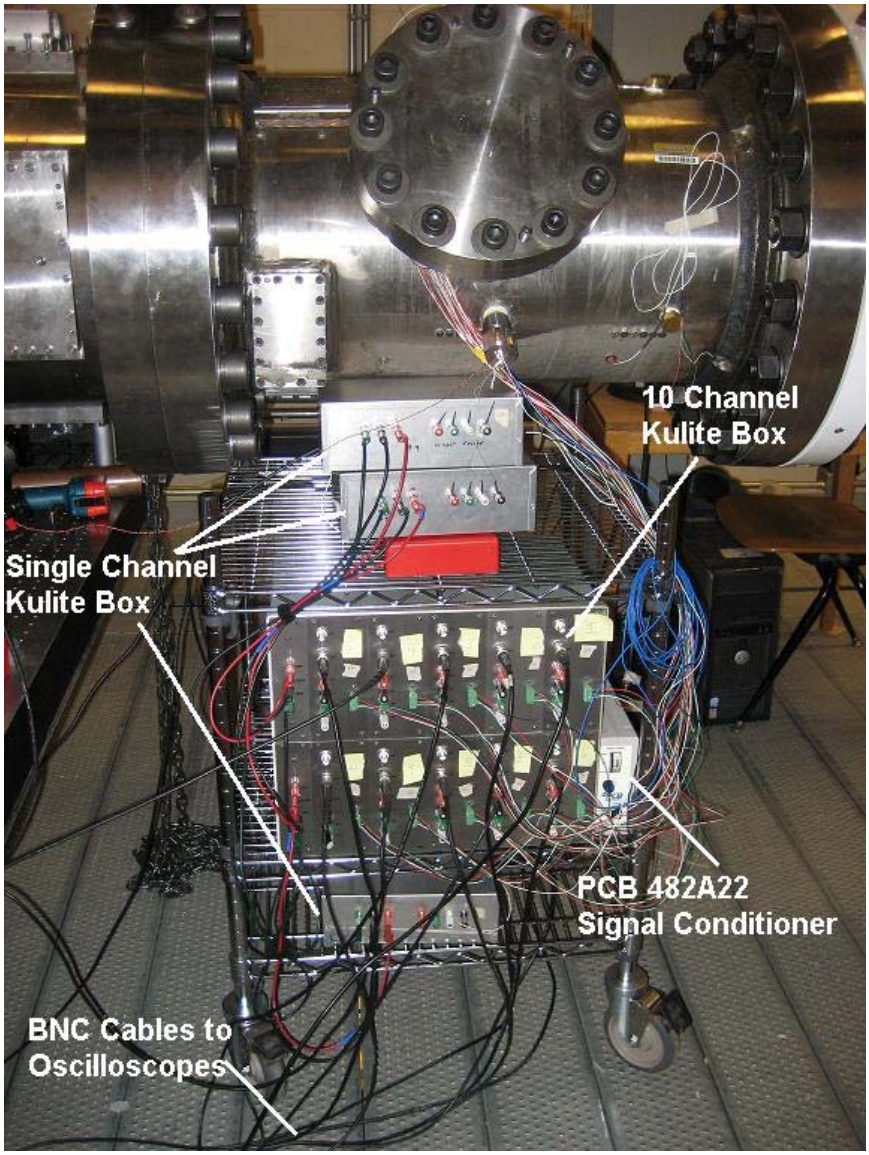


Figure 3.20. BAM6QT data-acquisition system

# 4. EXPERIMENTAL RESULTS

## 4.1 Pressure-Transducer Characterization

### 4.1.1 Sensor Comparison

A variety of pressure transducers were compared to identify which sensor(s) were most appropriate for pressure-fluctuation measurements and the identification of turbulent spots. Three types of Kulite sensors were tested: the Mic-062 A-screen, the Mic-062 B-screen, and the XCQ-062 B-screen. Sensor specifications can be found in Section 3.3. Sensor comparisons were made with two sensors spaced 120 degrees apart at the same axial location. These comparisons were conducted under a laminar boundary layer to reduce any effect of flow nonuniformity that might arise from asymmetric transition on the cone.

Sensors can be installed either flush with the surface of the cone or below a 0.41-mm diameter pinhole. Recessed Kulite sensors have a 0.6 $mm^3$ volume above them (Figure B.21). Flush sensors are installed parallel to the cone surface, but because the sensors are flat, there is still a surface irregularity caused by the sensors. Sensors recessed under a pinhole have better spatial resolution, but their response is attenuated. The pinhole may also cause cavity resonance. Figure 4.1 shows a comparison of the power spectral densities (PSD) from flush and recessed Mic-062 A-screens 120 degrees apart at x = 0.208 m in HWT-5. The recessed sensor shows much lower power across the spectrum than the flush-mounted sensor. Because of their better frequency response, flush-mounted sensors were used for all other measurements.

Figure 4.2 shows a comparison between flush-mounted Kulites in HWT-5. The red lines compare two Mic-062 A-screen sensors at x = 0.322 m. The power spectral densities from the two sensors agree very well, showing that the laminar flow over the cone is fairly axisymmetric. The blue lines show a Mic-062 A-screen and a Mic-062

B-screen at x = 0.398 m. Even though this is the same run, the B-screen sensor rolls off significantly faster than the A-screen sensor. As a result, the B-screen gives a much lower RMS pressure than the A-screen. The green lines show the same results when comparing a Mic-062 A-screen and an XCQ-062 B-screen at x = 0.452 m. Again, the XCQ-062 B-screen sensor rolls off significantly faster than the Mic-062 A-screen sensor and gives a much lower RMS pressure. Similar results were obtained in both the BAM6QT and HWT-8. Additional tests with each type of sensor placed at the same location on the cone for repeat runs confirmed the same results.

The Mic-062 A-screens seem to provide the best dynamic characteristics among the different Kulites. However, the Mic-062 A-screens have large cavities exposed to the flow whereas the B-screens have much smaller holes. PCB105 sensors were tested as an independent verification of the Kulites because they have similar measurement capabilities. They also have a sealed surface so screen effects are not present. Unfortunately, the PCB105 sensors were very susceptible to noise and did not produce reasonable results. Figure 4.3 shows a comparison of a Mic-062 A-screen and PCB105 sensor spaced 120 degrees apart on the cone at x = 0.490 m in the BAM6QT. The PCB105 response is more than an order of magnitude larger than the Kulites. The higher power in the PCB105 spectra is attributed to electrical noise. More tests of the PCB105 are needed to sort through the noise issues. Using an insulated mount may reduce the electrical noise seen by the sensor.

### 4.1.2 Extension of Kulite Spectra to Higher Frequencies using PCB132 Sensors

The PCB132 sensor offers another independent verification of the Kulite pressure sensors. The PCB132's have a frequency response that overlaps with the Kulites between approximately 11 and 50 kHz. The PCB132's also have a sealed surface so any screen or cavity effects are avoided. Figure 4.4 shows a Mic-062 A-screen and a PCB132 spaced 120 degrees apart on the cone at x = 0.360 m in the BAM6QT.

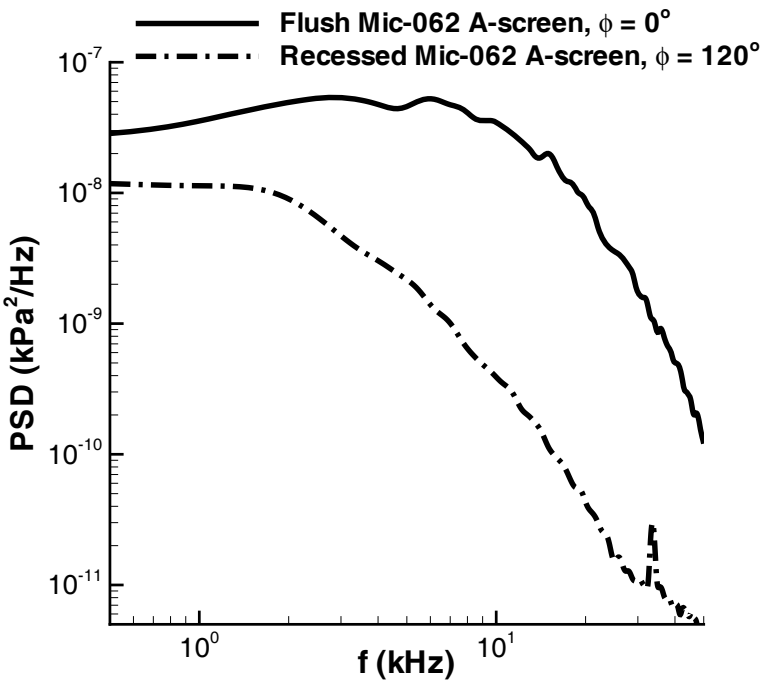


Figure 4.1. Flush and recessed Mic-062 A-screens 120 degrees apart under laminar flow (HWT-5, $Re/m = 6.3 \times 10^6$, x = 0.208 m)

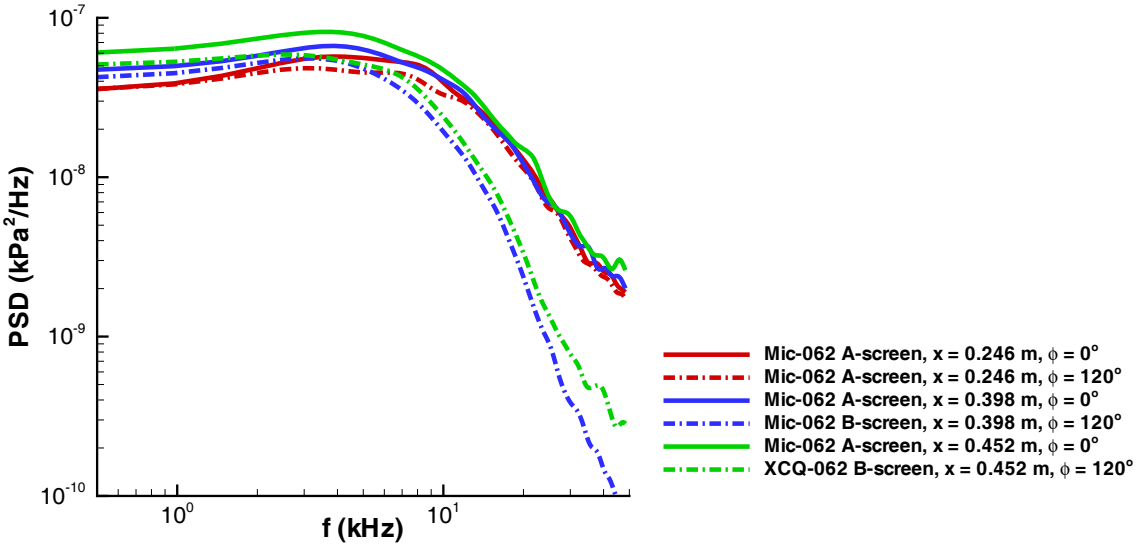


Figure 4.2. Kulite sensors 120 degrees apart on sharp cone under laminar flow (HWT-5, $Re/m = 4.6 \times 10^6$)

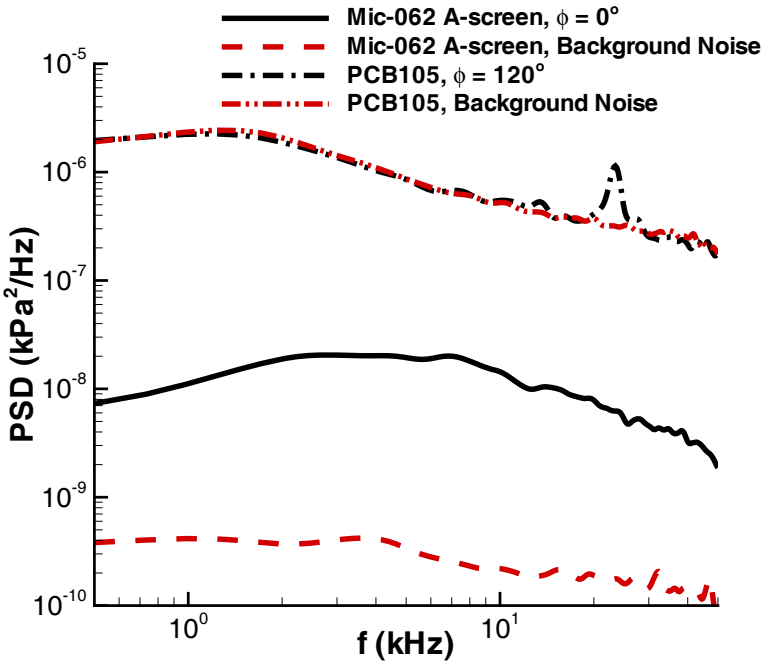


Figure 4.3. Mic-062 A-screen and PCB105 120 degrees apart under laminar flow (BAM6QT, noisy flow, $Re/m = 2.9 \times 10^6$, x = 0.208 m)

At the lowest $Re/m$ when the boundary layer is laminar at both sensors locations, the PCB132 agrees well with the Mic-062 between 11 and 50 kHz. A Mic-062 B-screen would roll off at a much lower frequency than both these sensors. At the next two higher $Re/m$, the cone boundary layer is still laminar. A small second-mode wave can be seen in the PCB132 spectrum near 160 kHz at $Re/m = 2.9 \times 10^6$. A larger second-mode wave near 200 kHz as well as a harmonic of the instability near 400 kHz are present at $Re/m = 5.0 \times 10^6$. In both cases, the PCB132 and the Mic-062 A-screen still show good agreement. The PCB132 also shows many noise spikes. It is unclear why the PCB132's are so sensitive to electrical noise, but the wider bandwidth of the second-mode waves distinguishes them from the narrow noise spikes. More measurements of second-mode waves are discussed in Section 4.3.

At even higher $Re/m$, the second-mode waves break down, and the sensors are under a transitional or turbulent boundary layer. In these latter two cases, the

two sensors no longer agree; the PCB132's have elevated spectra throughout the 11–50 kHz overlap between the sensors. It is unclear why this happens. Perhaps transition is asymmetric over the cone and the sensors are measuring a different part of the transitional region. However, asymmetric transition does not seem to explain the discrepancy seen here. Mic-062 A-screens spaced 120 degrees apart on the cone during transition do not agree as well as under laminar flow, but they do not show the large disagreement between the PCB132 and the Mic-062 A-screen seen here. This discrepancy might instead arise from something not yet understood about the sensors. The PCB132's were designed as time-of-arrival sensors and have not yet been dynamically calibrated. The Mic-062's and PCB132's also have different sensitive areas. Or perhaps this discrepancy stems from a nonlinear response, a spatial resolution issue, or from something else not yet understood about the sensors. More work is needed to investigate this discrepancy including dynamic sensor calibrations. Similar results were obtained in HWT-5 and HWT-8.

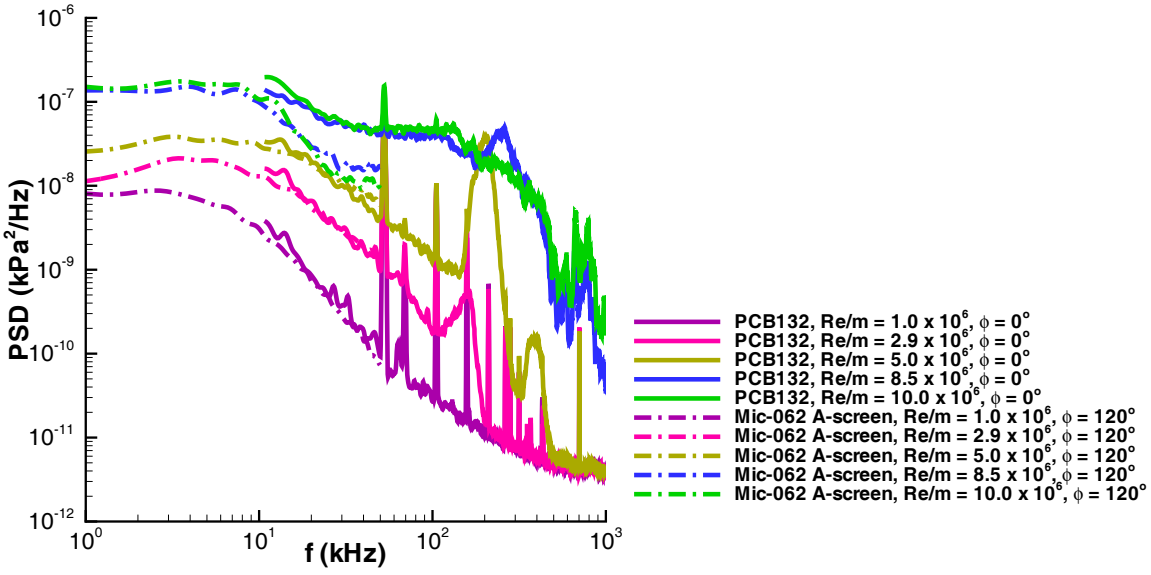


Figure 4.4. Extension of Mic-062 A-screen spectra with a PCB132 120 degrees apart (BAM6QT, noisy flow, x = 0.360 m)

### 4.1.3 Sensor Response to Turbulent Spots on the BAM6QT Nozzle Wall

One of the goals of this work is to measure and understand how turbulent spots and intermittency generate transitional pressure fluctuations. As a test case for sensor response to the passage of turbulent spots, measurements of large turbulent spots on the BAM6QT nozzle wall were conducted. During quiet-flow runs, these spots are randomly generated and grow within the nozzle [67]. The spots are generated well upstream in the nozzle and are large as they pass through the test section. Because of their long duration, they are easily identified. Attempts to measure smaller turbulent spots generated on the model are discussed in Section 4.2.10.

Figure 4.5 shows the passage of a nozzle-wall turbulent spot in hot films on the nozzle wall at z = 1.918 and 2.070 m. A prolonged change in the hot-film voltage as well as higher fluctuations marks the turbulent-spot passage. The front and rear convection speeds of the spot can be calculated from these traces. The front of the spot typically propagates near $0.9U$ whereas the rear of the spot is convected downstream at $0.6U$. These propagation speeds match computations well [21]. The origin of these spots can be estimated using the spot duration and propagation speed. The spot has a duration of approximately 1.2 ms and $U$ = 867 m/s, placing the location of spot generation near the throat. The length of the spot as it passes the hot films is approximately 1 m.

Figure 4.6 shows the passage of a wall turbulent spot in the candidate pressure transducers. An XCQ-062 B-screen is on the nozzle wall at z = 1.918 m, upstream of the model at z = 2.032 m. The nozzle-wall pressure transducer trace (shown $\times 5$ for comparison) shows the passage of the spot; it is marked by a small change in the mean pressure and increased fluctuations. Pressure disturbances are also radiated from the turbulent spot passage on the wall, similar to Figure 1.1. The angle of disturbance radiation can be estimated by assuming a $0.3U$ difference between the freestream velocity and the rear propagation speed of the spot, giving a Mach angle of 34°. The radiated pressures are much larger than the pressure fluctuations measured on the

nozzle wall and are picked up by the model sensors between z = 2.240 and 2.430 m. The radiated pressure is shown clearly by the XCQ-062 and Mic-062 sensors and is also evident in the PCB132 trace. However, because the PCB132 cannot measure frequencies below 11 kHz, the change in the mean pressure is not reflected in the measurements. A second peak in the radiated pressure is also seen. Perhaps this is a stronger acoustic wave generated at the front of the turbulent spot as seen in Figure 1.1. This second peak also appears in Pitot-probe measurements of the turbulent-spot passage [67]. The PCB105 pressure trace (not shown) is dominated by noise, and the turbulent spot cannot be identified.

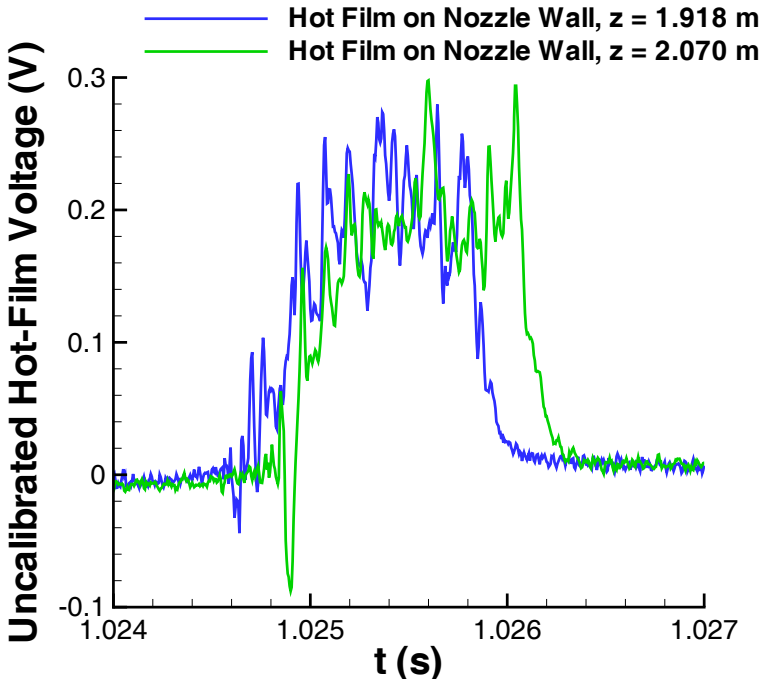


Figure 4.5. Turbulent-spot passage on nozzle wall, measured by hot films (BAM6QT, quiet flow, $Re/m = 8.7 \times 10^6$)

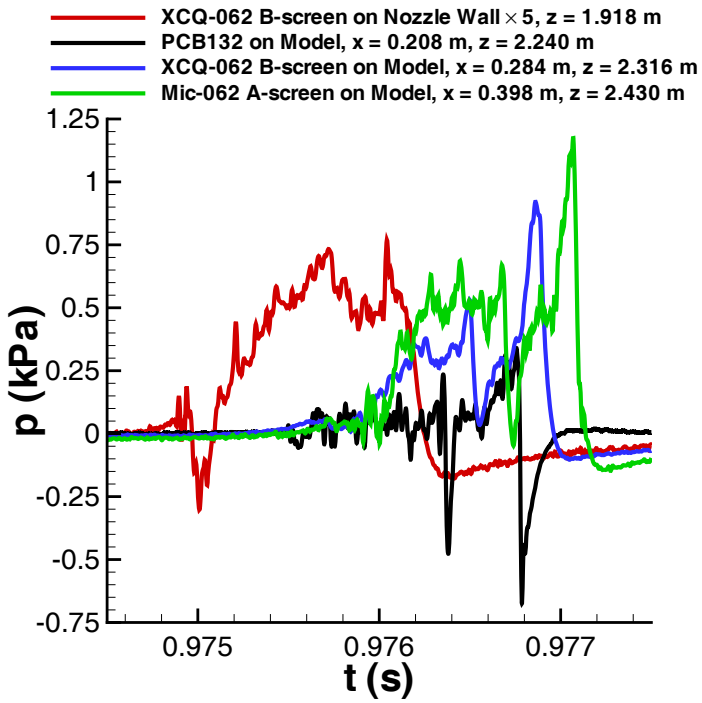


Figure 4.6. Turbulent-spot passage on nozzle wall, measured by pressure transducers (BAM6QT, quiet flow, $Re/m = 9.0 \times 10^6$)

### 4.1.4 Future Sensor Work

Because of their slower roll-off and high sensitivity, the Mic-062 A-screen sensors were chosen for dynamic measurements between 0 and 50 kHz. Higher frequency measurements between 11 and 1 MHz were made with the PCB132 sensors.

There is still work to be done to understand the different sensors. The PCB sensors, especially the PCB105's, experience a high level of electronic noise. Using insulated mounts may reduce electrical noise. Dynamic sensor calibrations have yet to be performed on any sensors. Shock-tube calibrations are planned for both Pitot-mounted sensors as well as side-mounted sensors. A range of shock strengths will be tested to investigate sensor linearity. Calibrations with ultrasonic speakers as well as with shocklets generated by a laser perturber are also planned.

## 4.2 Pressure-Fluctuation Measurements between 0 and 50 kHz

Pressure fluctuations were measured with a series of eight Mic-062 A-screen sensors along row A of the cone. The sensor at position 4A was broken for the tests in HWT-5 and 8. Data from the sensor 120 degrees apart at position 4B were used instead. The row A and row B fluctuations could be compared at position 2. The B row of sensors measured laminar fluctuations that were typically 3% lower than row A in HWT-5 and 2% higher in HWT-8 tests. There was a larger difference in the transitional fluctuations, typically 10% lower fluctuations than row A in HWT-5 and 10% higher in HWT-8. These differences are similar to the observed changes in the measured pressure fluctuations with varying roll angle and small angle of attack, discussed in Section 4.4.

RMS pressure fluctuations are calculated from the power spectral density between 0 and 50 kHz. Run conditions and normalization values are given in Appendix A. Keyes's law was used to calculate viscosity [68] because Sutherland's law is not as accurate at the low freestream temperatures in the tunnels (below 111 K). Real gas effects were neglected. Edge pressure ($p_e$), edge dynamic pressure ($q_e$), and edge Mach number ($M_e$) were calculated using the Taylor-Maccoll solution for a sharp cone. The nozzle-wall shear stress ($\tau_w$) was computed using the method of Van-Driest-II.

### 4.2.1 Pressure Fluctuations along Cone

#### HWT-5

Figure 4.7 shows the unnormalized pressure fluctuations along the cone in HWT-5 for increasing $Re/m$. For the lowest $Re/m$ (marked by squares), the pressure fluctuations remain approximately constant along the cone. The cone boundary layer remains laminar in these cases. At higher $Re/m$, a peak can be seen in the pressure fluctuations. This peak occurs near the end of transition [3, 33, 34, 36, 37]. As $Re/m$ increases further, the peak fluctuations move forward on the cone, showing the up-

stream movement of transition. At the highest $Re/m$ (marked by triangles), the flow is late transitional or turbulent over the rear of the cone.

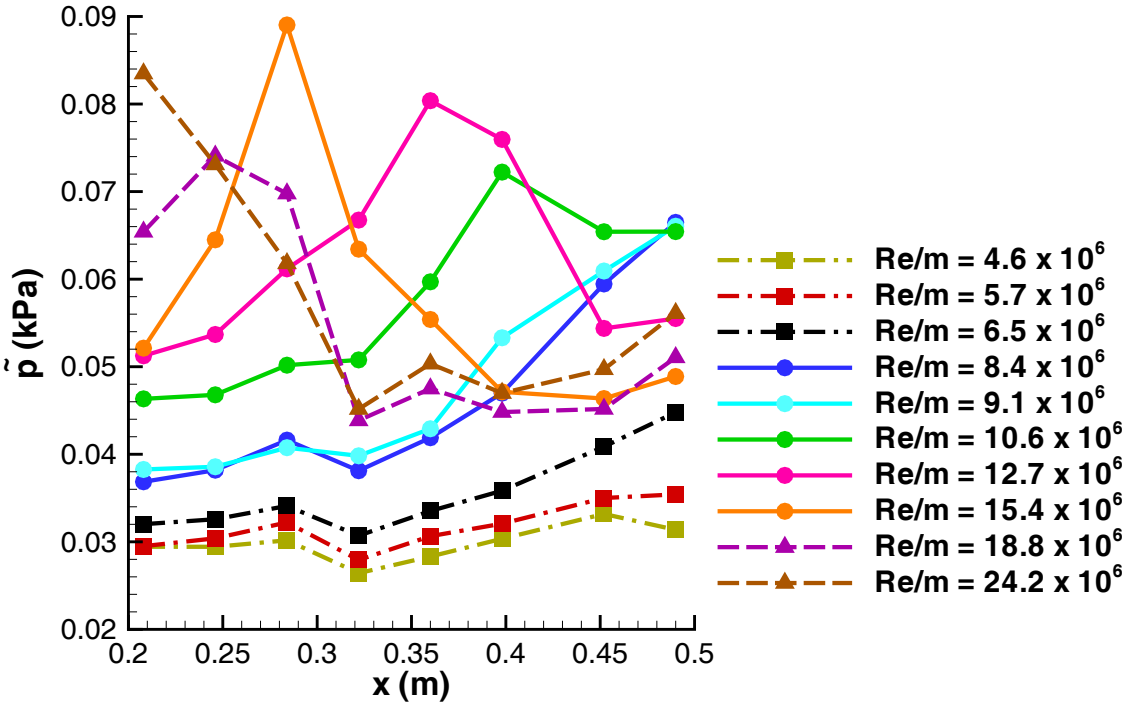


Figure 4.7. Unnormalized RMS pressure along sharp cone in HWT-5

### Normalization of Pressure Fluctuations

The magnitude of the unnormalized pressure fluctuations increases with $Re/m$. A normalization of the fluctuations is desired to collapse data at different freestream conditions. Normalizations of the laminar fluctuations are compared here. Transitional fluctuation peaks are not compared because the sensor spacing was too coarse to fully resolve the transitional peaks. Sufficient turbulent fluctuation data was also not obtained for a full comparison of turbulent fluctuations.

Various parameters have been used in the literature for normalization of pressure fluctuations. The most common are $p_e$ and $q_e$. $\tau_w$ has also been used since this param-

eter is an important factor for tunnel noise generation. Raman [5] and Laderman [40] reviewed various normalizing parameters for freestream tunnel noise and found that the nozzle-wall shear stress worked the best. If the laminar pressure fluctuations are a reflection of tunnel noise, then $\tau_w$ should collapse the pressure fluctuations on the cone.

Figures 4.8 through 4.10 show the RMS pressure fluctuation in HWT-5 normalized by $p_e$, $q_e$, and $\tau_w$, respectively. Laminar fluctuations are seen in the first three sensors below $Re/m = 12.7 \times 10^6$. Both $p_e$ and $q_e$ collapse the laminar fluctuations somewhat, however, there is still scatter in the results. With these normalizations, the peak transitional fluctuations at high $Re/m$ fall in line with the laminar fluctuations at lower $Re/m$. As will be shown later, tunnel noise (when normalized by $p_e$) decreases with increasing $Re/m$, leading to this result.

Normalizing by $\tau_w$ seems to collapse the laminar fluctuations much better, in agreement with Raman and Laderman's results. The peak transitional fluctuations when normalized by $\tau_w$ are also consistently above the laminar fluctuations for all $Re/m$. However, it should be noted that the quoted repeatability of the sensors is approximately 0.1% of the full scale, or 7 Pa. If this uncertainty is taken into account, the laminar fluctuations when normalized by $p_e$, $q_e$, or $\tau_w$ are all within the error bars, and the better normalization seen with $\tau_w$ cannot be stated conclusively. However, repeat tunnel runs did show better repeatability than the manufacturer's quoted repeatability (Section 4.4), suggesting that normalization by $\tau_w$ does collapse the laminar fluctuations best. This collapse with $\tau_w$ is an indication that the laminar pressure fluctuations are a reflection of tunnel noise. The fluctuations following transition fall back towards the laminar level. This seems counter-intuitive, but is likely the result of high levels of tunnel noise. Experiments have also shown that turbulent boundary layers can attenuate tunnel noise [47].

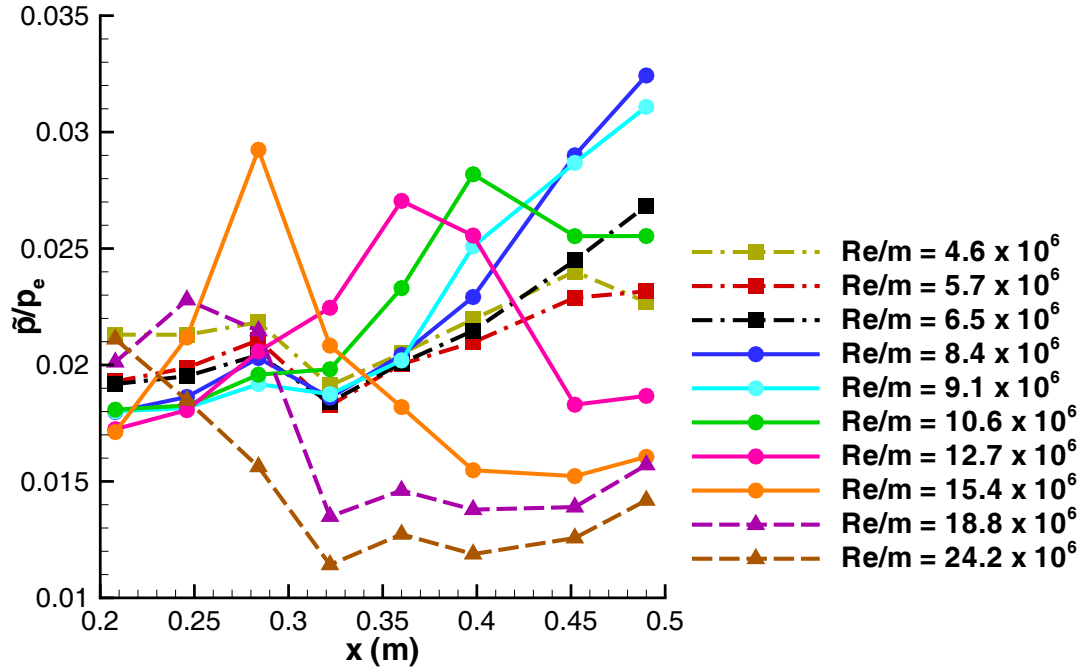


Figure 4.8. RMS pressure normalized by edge pressure along sharp cone in HWT-5

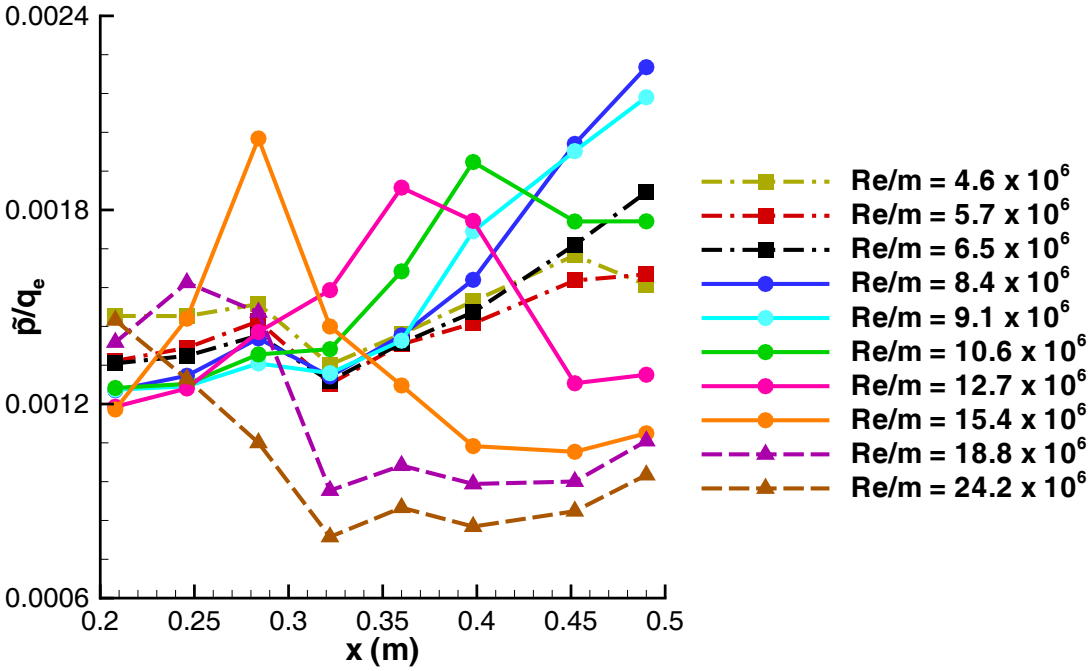


Figure 4.9. RMS pressure normalized by edge dynamic pressure along sharp cone in HWT-5

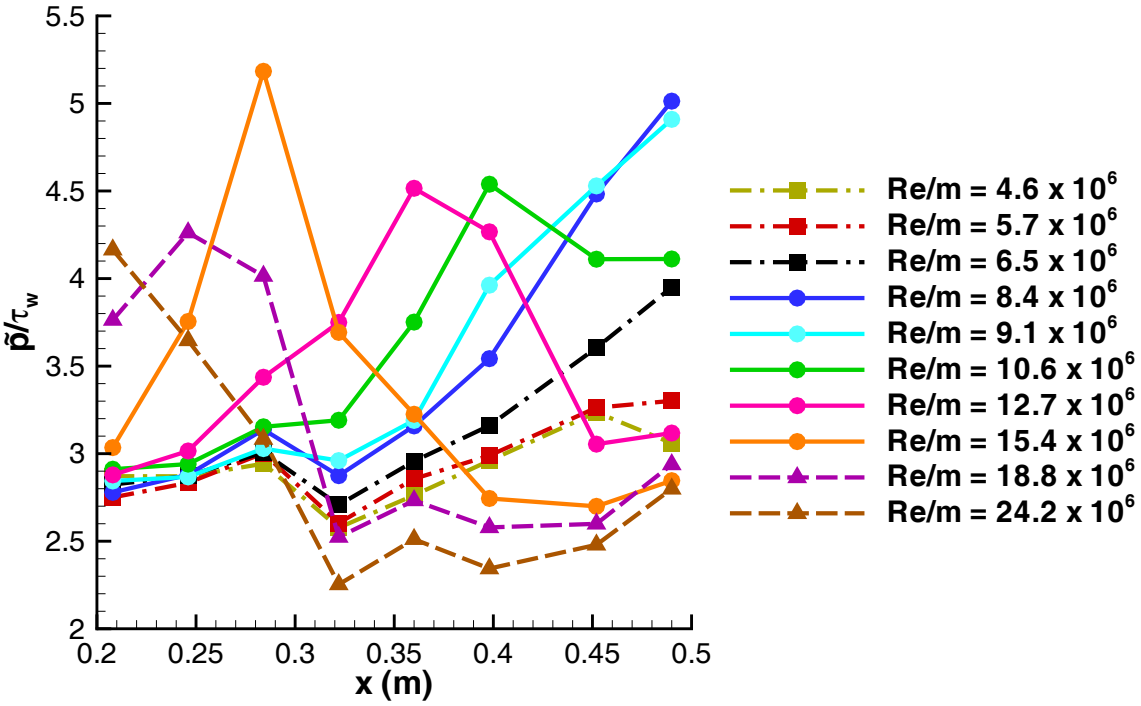


Figure 4.10. RMS pressure normalized by nozzle-wall shear stress along sharp cone in HWT-5

## BAM6QT

Similar results from the BAM6QT under noisy flow are shown in Figures 4.11 through 4.14. A similar trend of transition moving forward with increasing Reynolds number is seen here. Normalization by $p_e$ and $q_e$ again collapses the laminar fluctuations, but not as well as normalization by $\tau_w$. The laminar fluctuations are higher in the BAM6QT which indicates higher noise levels under noisy flow than in HWT-5. This is expected because the Mach number is higher and the test-section diameter is smaller.

At the lower $Re/m$ in the BAM6QT, the normalization does not work as well. The normalized laminar fluctuations are significantly higher than seen at higher $Re/m$.

Tunnel noise when normalized by $p_e$ is highest at the lower $Re/m$, but normalizing by $\tau_w$ should collapse its effect. A likely contribution to this discrepancy is that the signal-to-noise ratio is much lower for these low $Re/m$ cases. The signal-to-noise ratio is above 10 for the highest $Re/m$ cases and reduces to approximately 3 at $Re/m = 1.0 \times 10^6$. At the lower $Re/m$ cases, the normalizing values of $p_e$, $q_e$ and $\tau_w$ are the smallest. Dividing by these small values increases the contribution of the background electronic noise. This effect was not seen in HWT-5 and HWT-8, but the lowest $Re/m$ tested in both tunnels was approximately $5.0 \times 10^6$. The background noise was lower in HWT testing, and the signal-to-noise ratios remained above 10. Also, perhaps the calculation of $\tau_w$ is not as accurate at these lower $Re/m$ in the BAM6QT. There may also be an effect of spillage over the bleed lip. Tunnel noise measurements in the BAM6QT under noisy-flow conditions also show that the noise level at lower $Re/m$ is not constant throughout the test-section, but actually increases further downstream. These changing noise levels indicate that the turbulent boundary layer on the nozzle wall might not be the only contribution to tunnel noise in the BAM6QT.

The transition location marked by the peak in the pressure fluctuations can be compared to temperature-sensitive paint (TSP) data on a 7° sharp cone obtained by Swanson [69]. Swanson shows the temperature and heat-flux variation along the cone at $Re/m = 9.8 \times 10^6$. Transition onset in the TSP data occurs at approximately x = 0.250 m and the peak heating occurs at x = 0.360 m. The pressure-fluctuation variation along the cone at $Re/m = 10.0 \times 10^6$ shows that the onset of transition occurs near x = 0.246 m. The end of transition marked by the peak fluctuations seems to occur between x = 0.284 and 0.322 m, but might occur somewhere between x = 0.322 and 0.360 m. The onset location agrees well with the TSP data, but the end of transition as defined by the peak probably occurs sooner than indicated by the TSP. It may also be that the peak pressure fluctuations do not correspond to the peak in heat transfer, but occur somewhere before. Further comparison of the pressure-fluctuation peak to temperature-sensitive paint and other transition detection methods is desired.

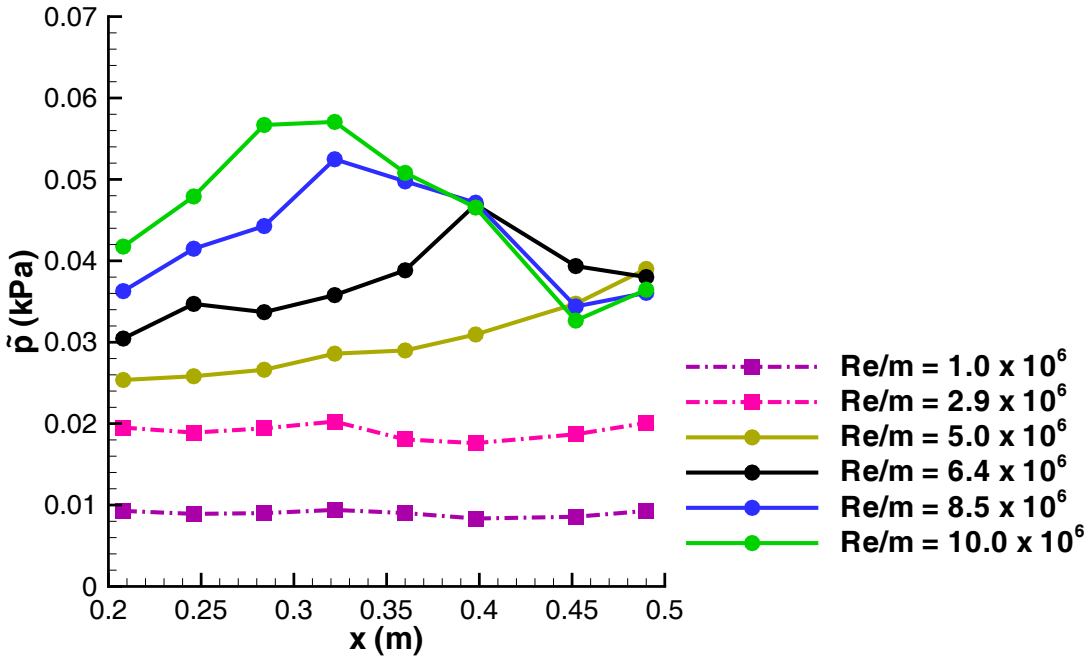


Figure 4.11. Unnormalized RMS pressure along sharp cone in the BAM6QT (noisy flow)

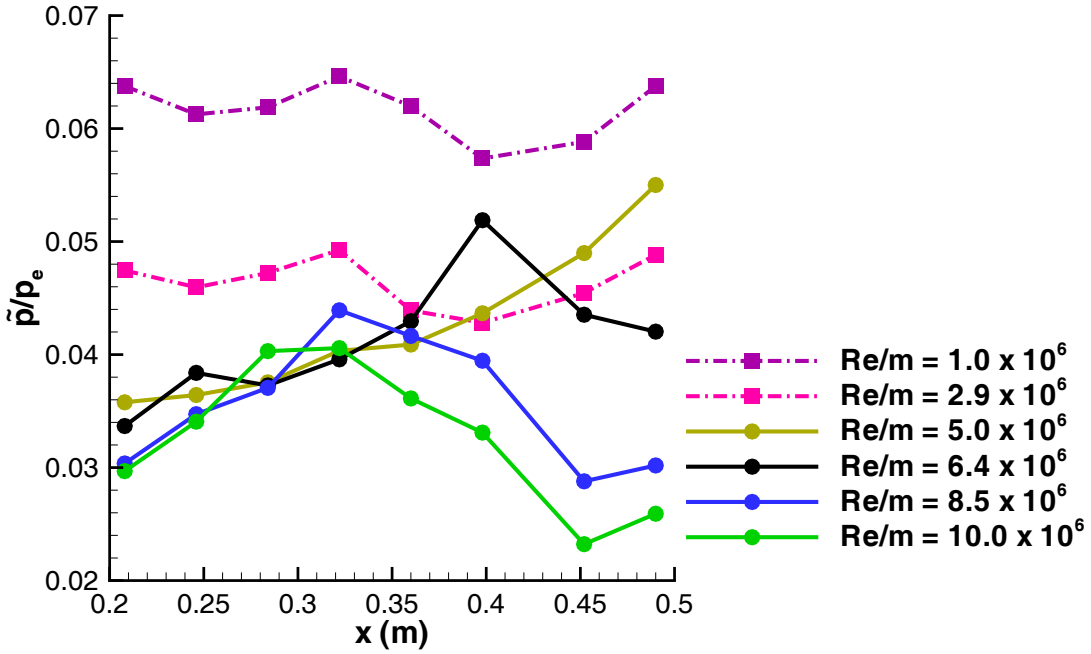


Figure 4.12. RMS pressure normalized by edge pressure along sharp cone in the BAM6QT (noisy flow)

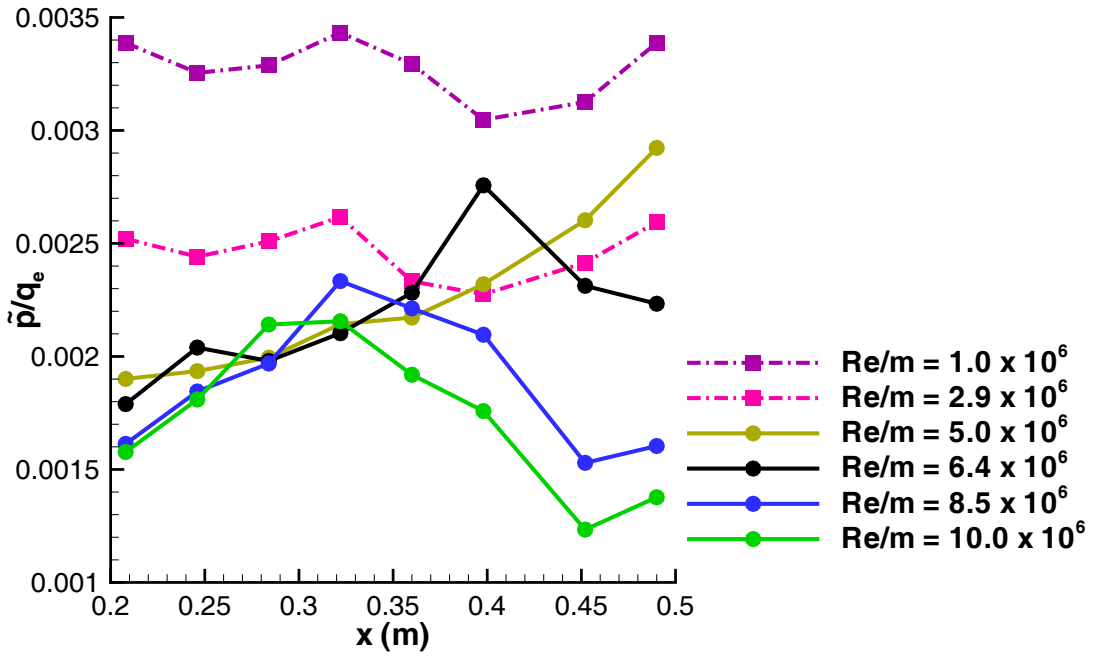


Figure 4.13. RMS pressure normalized by edge dynamic pressure along sharp cone in the BAM6QT (noisy flow)

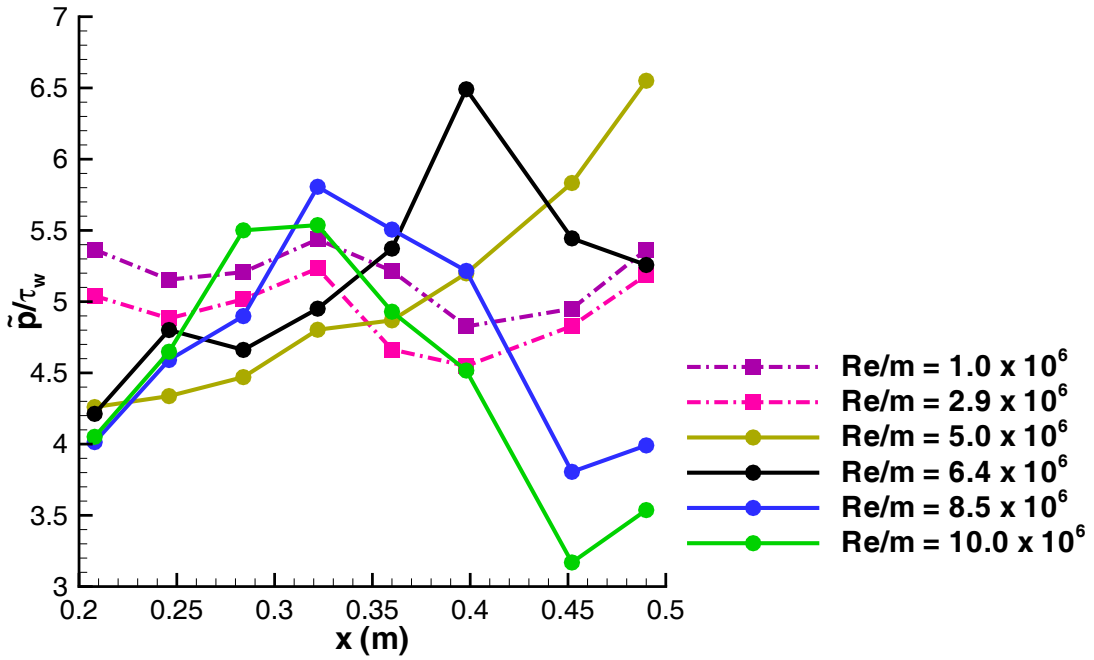


Figure 4.14. RMS pressure normalized by nozzle-wall shear stress along sharp cone in the BAM6QT (noisy flow)

**HWT-8**

Results from HWT-8 are shown in 4.15 through 4.18. The same trends as in HWT-5 and the BAM6QT are seen. Transition again moves further forward with increasing $Re/m$. The nozzle-wall shear stress also seems to collapse the laminar fluctuations better than $p_e$ and $q_e$. However, at the highest $Re/m$, the peak transitional fluctuations when normalized by $\tau_w$ are almost equal to the laminar level, something not seen in HWT-5 or the BAM6QT under noisy-flow conditions. The laminar pressure fluctuations are also higher than in the BAM6QT which indicates even higher levels of tunnel noise in HWT-8. This is expected because of the higher Mach number.

The HWT-8 results also have an anomaly at the first sensor location (x = 0.208 m). This sensor shows a higher pressure-fluctuation level than expected. The sensor seems to be seeing some disturbance not seen by the rest of the sensors. Repeat tests at other roll angles and at small angle of attack did not change the result. This anomaly is not seen with the same setup and same model configuration in HWT-5, indicating that the sensor and data acquisition system are not malfunctioning. Figure 4.34 shows that the sensor consistently sees transition sooner than the next sensor location downstream. This suggests that a local tunnel disturbance in HWT-8 is affecting the sensor. Perhaps there is a Mach wave shimmering off a flaw in the nozzle contour, or maybe a model-based disturbance is affecting the sensor—an effect not seen at lower Mach numbers.

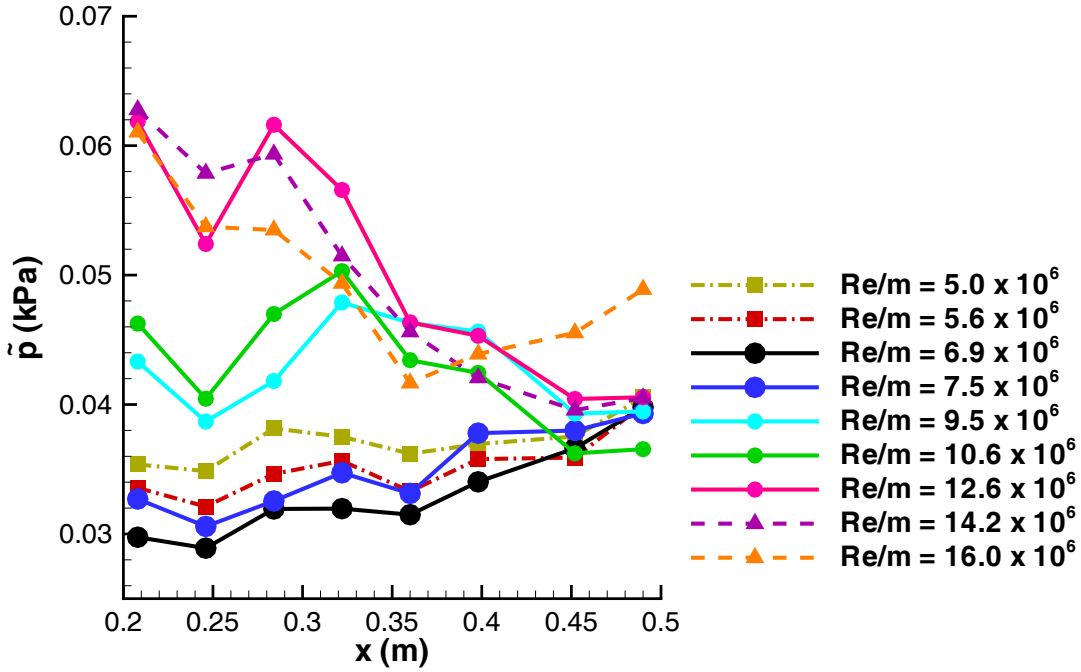


Figure 4.15. Unnormalized RMS pressure along sharp cone in HWT-8

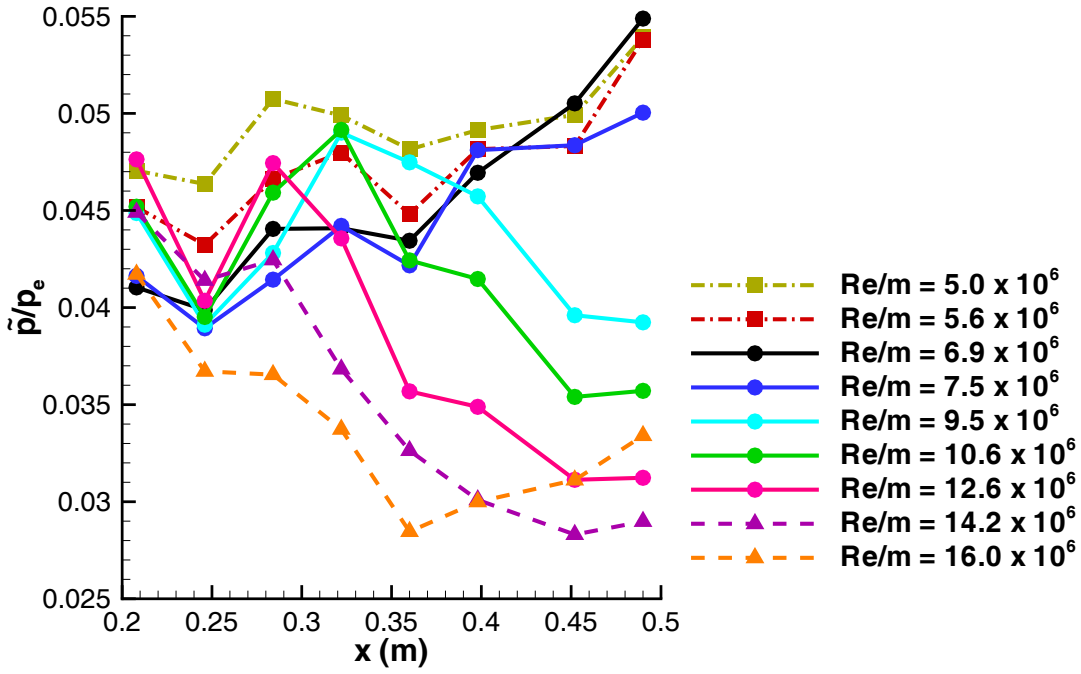


Figure 4.16. RMS pressure normalized by edge pressure along sharp cone in HWT-8

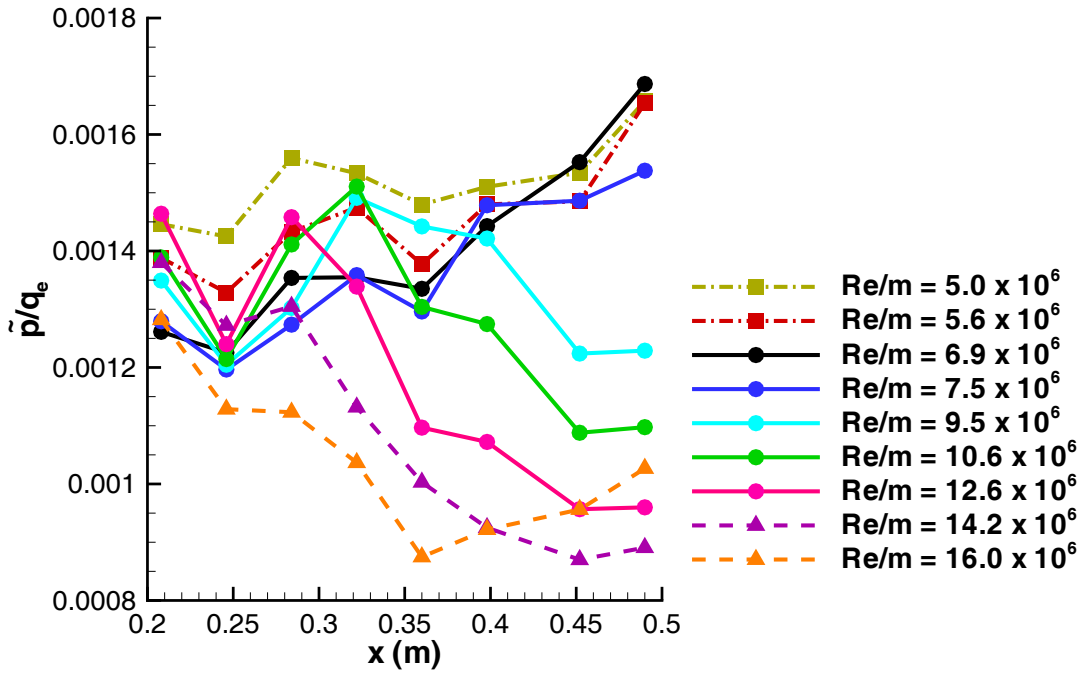


Figure 4.17. RMS pressure normalized by edge dynamic pressure along sharp cone in HWT-8

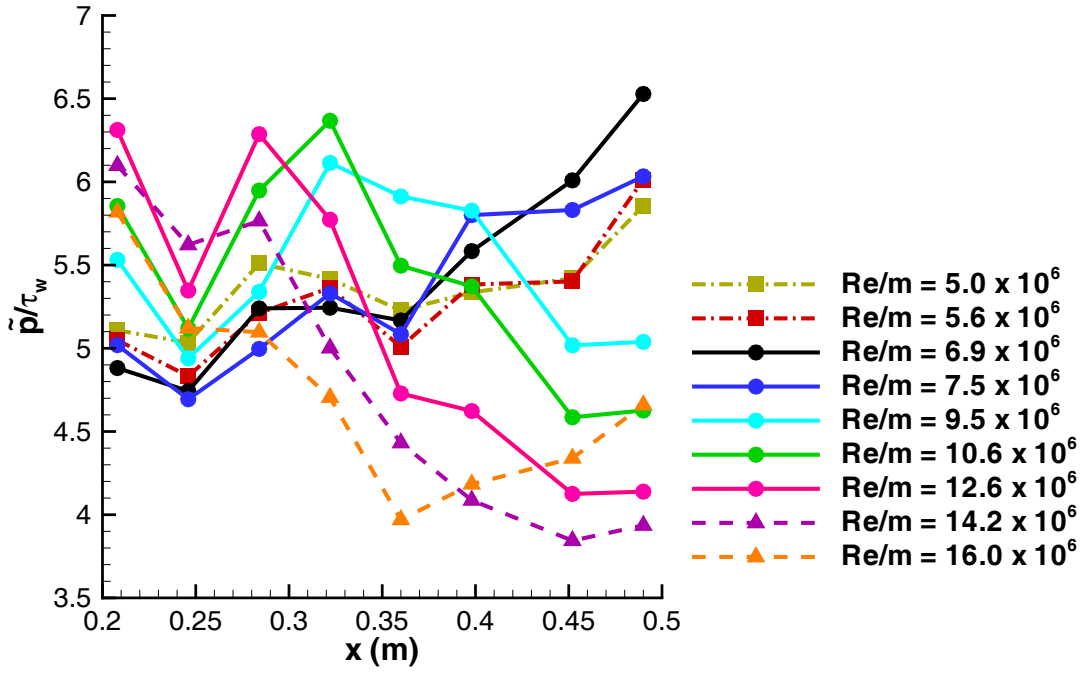


Figure 4.18. RMS pressure normalized by nozzle-wall shear stress along sharp cone in HWT-8

### 4.2.2 Nose-Bluntness Effects

Bluntness effects were observed by testing two blunt nosetips, one with a 0.5-mm radius and the other with a 1.5-mm radius. These bluntnesses delay transition on the cone; they are not blunt enough to reach the transition reversal often seen with large-bluntness nosetips [57, 70]. Figure 4.19 shows the effect of bluntness on the cone in HWT-5 under noisy flow. The peak in pressure fluctuations moves further back with increasing Reynolds number. However, the magnitude of the peak does not seem to be affected by the nose bluntness. This is consistent with observations by Martellucci et al. [3].

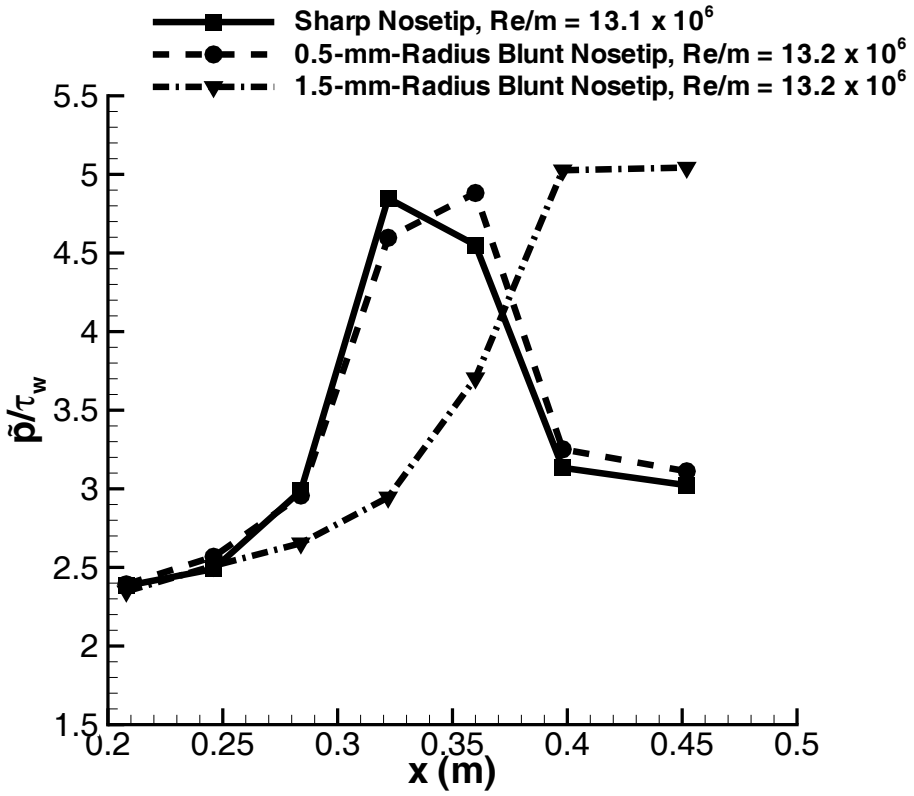


Figure 4.19. RMS pressure normalized by nozzle-wall shear stress for varying nosetip bluntness (HWT-5)

### 4.2.3 Comparison to Existing Pressure-Fluctuation Correlations

Comparisons of the data to existing correlations for transitional and turbulent fluctuations are shown in Figures 4.20 through 4.22. Comparisons to Stainback's correlation [50] for laminar pressure fluctuations (tunnel noise level) have not yet been completed. Details about these correlations are discussed in Chapter 2. All of the correlations shown here use adiabatic-wall assumptions. This assumption gives a lower bound of the fluctuation predictions. Laganelli's correlations were computed using $m = 0.8$.

The measured turbulent pressure fluctuations are compared to the turbulent fluctuation predictions of Houbolt [1], Lowson [2], Martellucci et al. [3, 4], and Laganelli [7]. The agreement between experiments and the correlations is fair. Lowson and Martellucci's correlations for the turbulent boundary layer are the best in each tunnel. Houbolt's adiabatic wall method is somewhat high, but still in good agreement with the present work. Laganelli's prediction of turbulent boundary layers is much higher for all cases.

Transitional pressure fluctuations are compared to the predictions of Martellucci et al. [3, 4] and Laganelli [7]. Correlation estimates are significantly higher than the transitional fluctuations seen in HWT-5 and HWT-8. The BAM6QT results show much better agreement with the correlations though it is not clear why. Although these correlations provide useful checks of the experimental results and simple estimates of fluctuations, they give little insight into the generation of transitional pressure fluctuations. A physics-based method of predicting the pressure fluctuations is still needed.

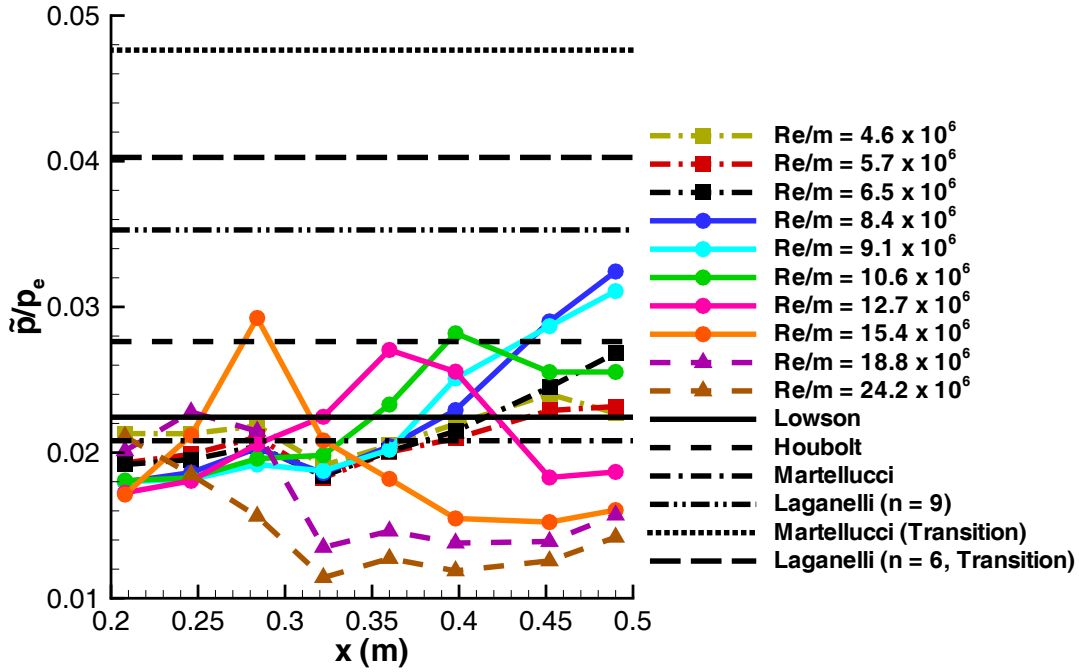


Figure 4.20. Comparison of HWT-5 pressure fluctuations to existing correlations

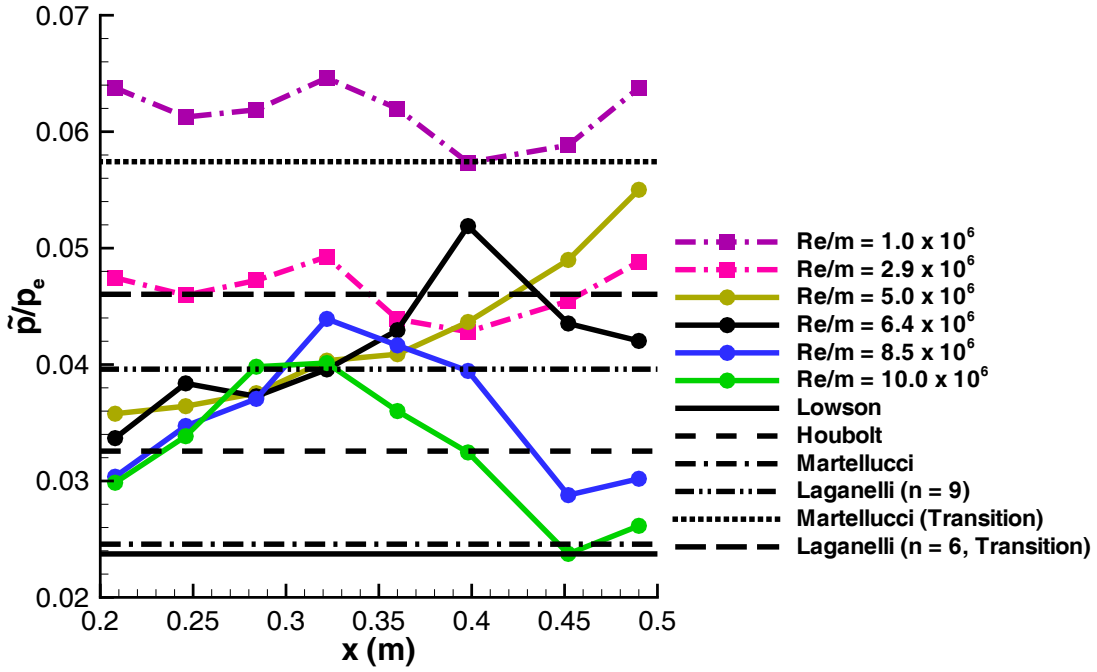


Figure 4.21. Comparison of BAM6QT pressure fluctuations to existing correlations

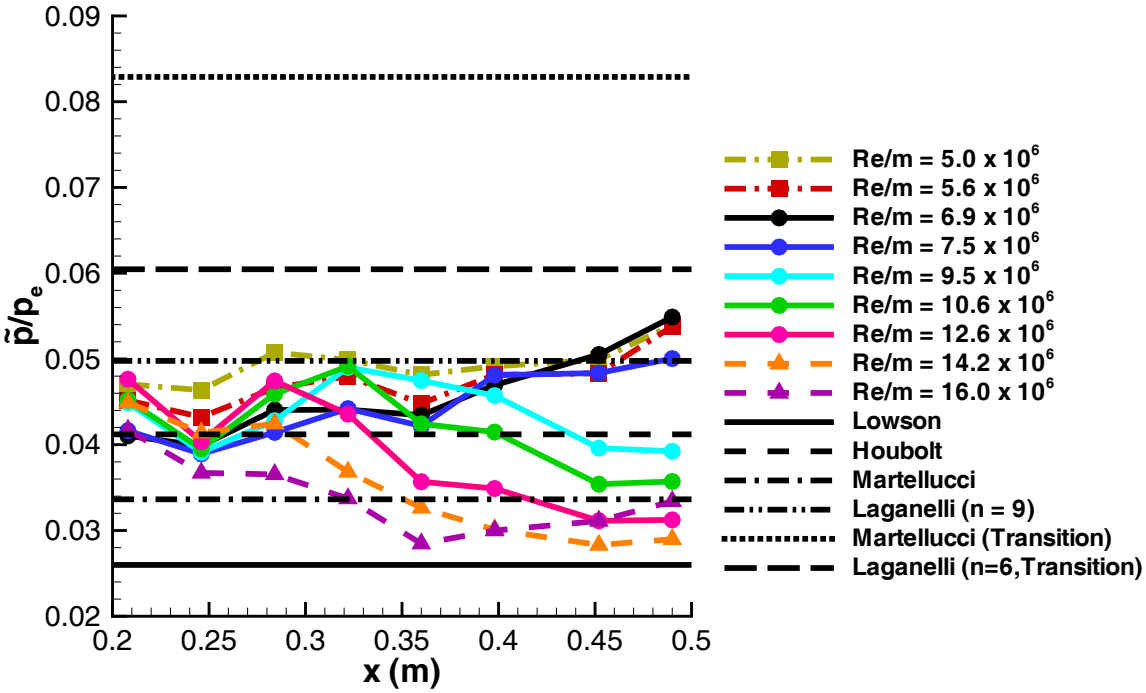


Figure 4.22. Comparison of HWT-8 pressure fluctuations to existing correlations

### 4.2.4 Power Spectral Density during Boundary-Layer Transition

Power spectral densities were calculated for the Kulite data to show the changing frequency contributions to the RMS pressure during transition. The pressure was normalized by $p_e$ to show the strength of the fluctuations relative to the mean. Kulite spectra were calculated for 0.1 s time samples using Welch's method. A Blackman window with 25% overlap was used with a window size of 410 points in the HWT and 205 points in the BAM6QT. Approximately 976 FFT's were averaged.

A typical PSD during transition is shown in Figure 4.23. The first sensor at x = 0.208 m is under a laminar boundary layer. There is still a high level of broadband fluctuations under the laminar boundary layer because of the tunnel noise; the background electrical noise is over an order of magnitude lower. The next two sensors (at

x = 0.246 and 0.322 m) show the onset of transition. There is first an increase in frequency components above 20 kHz, shown by the second sensor. The third sensor shows an increase in frequency components above 15 kHz as well as a rise in lower frequencies. As transition progresses, the pressure fluctuations peak. This peak is marked by a large increase in frequencies below 15 kHz. After the transitional peak, the spectrum drops back towards the laminar level, though there are still some differences in the spectrum. It seems counter-intuitive that the turbulent level is similar to the laminar level, but this may be due to tunnel noise [47]. This same trend was also seen in the BAM6QT and HWT-8 (Figures 4.24 and 4.25). However, both tunnels (particularly in HWT-8) have higher tunnel noise levels which disguise the trends seen in HWT-5.

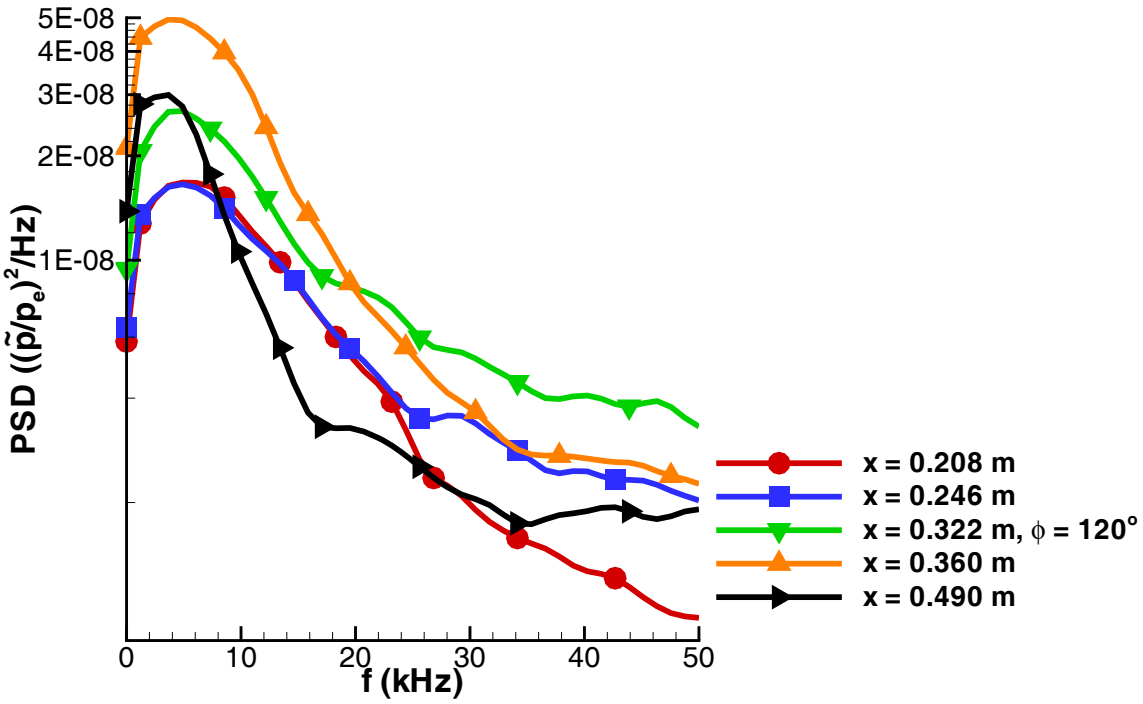


Figure 4.23. Transitional power spectral densities for pressure fluctuations normalized by edge pressure (HWT-5, $Re/m = 12.7 \times 10^6$)

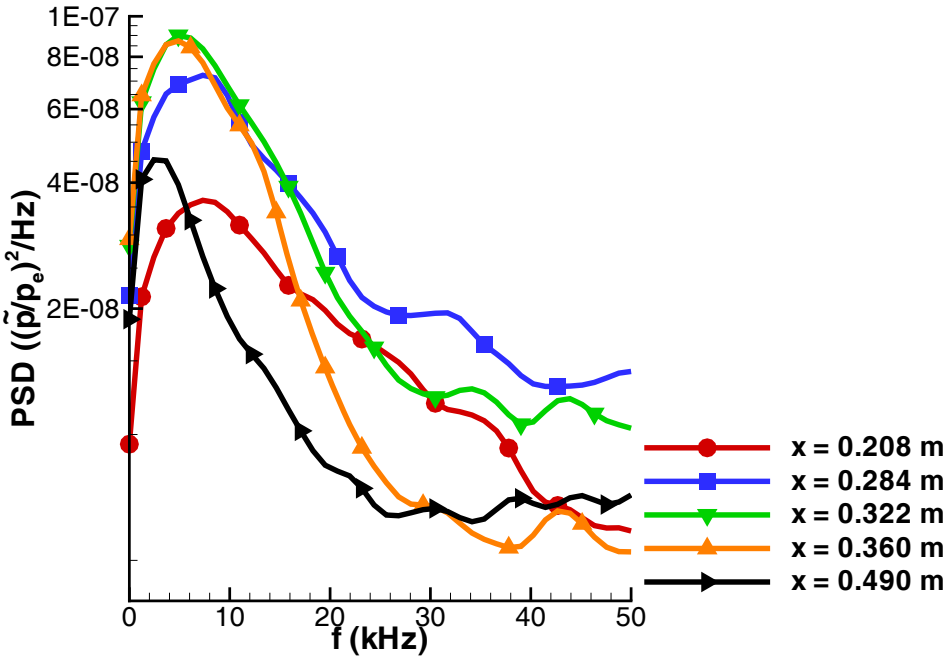


Figure 4.24. Transitional power spectral densities for pressure fluctuations normalized by edge pressure (BAM6QT, noisy flow, $Re/m = 10.0 \times 10^6$)

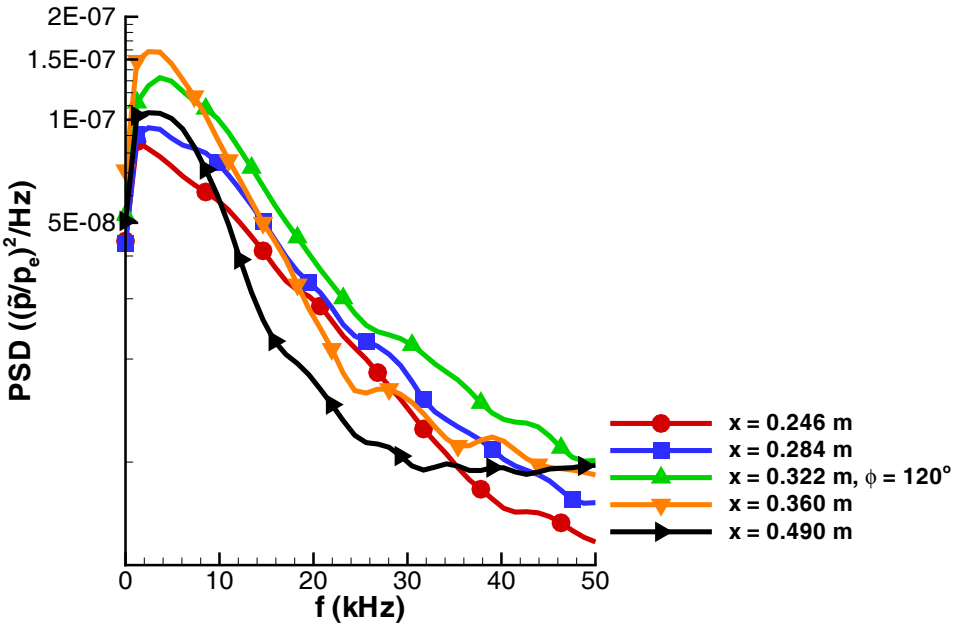


Figure 4.25. Transitional power spectral densities for pressure fluctuations normalized by edge pressure (HWT-8, $Re/m = 9.5 \times 10^6$)

### 4.2.5 Tunnel Noise Measurements

#### HWT

To understand how tunnel noise affected the measured pressure fluctuations, noise measurements were made in HWT-5 and HWT-8. Nozzle-wall fluctuations were measured with a flush-mounted Mic-062 A-screen sensor. Freestream fluctuations were measured with an XCQ-062-25A B-screen sensor mounted in a centerline Pitot probe. Both sensors were located near the same axial location as the nosetip of the Pressure-Fluctuation Cone (z = 2.769 m in HWT-5 and z = 2.324 m in HWT-8).

Figures 4.26 and 4.27 show the noise measurements made in HWT-5 and 8, respectively. Tunnel noise is shown as Pitot pressure fluctuations divided by the mean. Wall pressure fluctuations were normalized by the freestream static pressure. As expected, tunnel noise (when normalized in this manner) decreases with increasing $Re/m$ and increases with increasing Mach number and decreasing test-section diameter. This is expected from tunnel noise studies by Laufer [39, 48] and others.

Comparisons of the spectra from the Pitot probe and measurements under the laminar boundary layer made with a flush-mounted Mic-062 A-screen sensor at x = 0.208 m are shown in Figures 4.28 through 4.29. In both HWT-5 and HWT-8, the low-frequency components of the noise are higher under the cone laminar boundary layer. However, the higher-frequency components of the spectra above approximately 15 kHz are larger in the freestream Pitot spectra. Although Mack's forcing theory [54] allows for large amplification of the freestream noise under a laminar boundary layer, this large amplification is not seen here. Perhaps a smaller effect is responsible for the higher low-frequency amplitudes. Schopper [55] predicts an attenuation of higher frequency components of the spectra below the caustic layer. The caustic layer acts as a low-pass filter to the incoming noise. This may be the reason for the lower amplitude of frequency components above 15 kHz. This might also be due to sensor roll-off at higher frequencies. Dynamic sensor calibrations may help clarify these results.

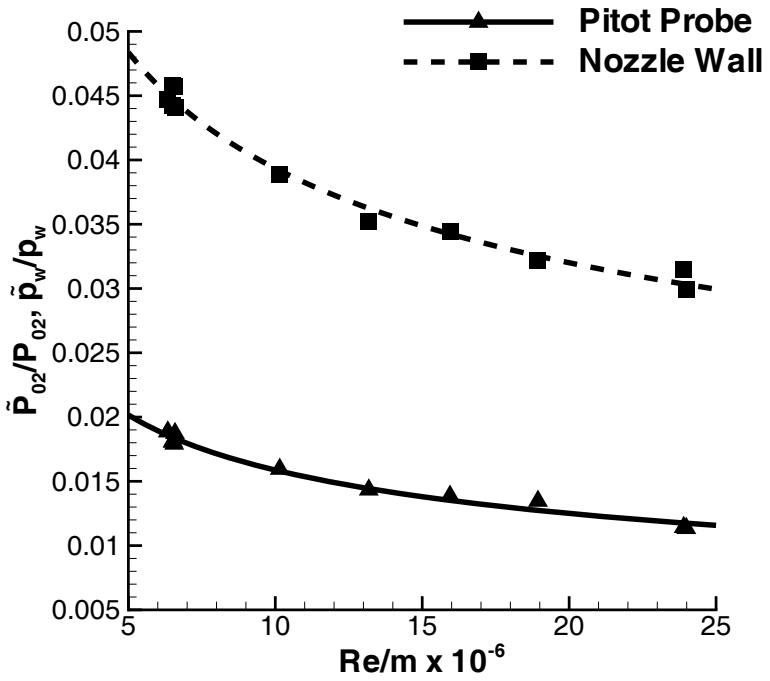


Figure 4.26. Pitot and wall noise measurements in HWT-5 (z = 2.769 m)

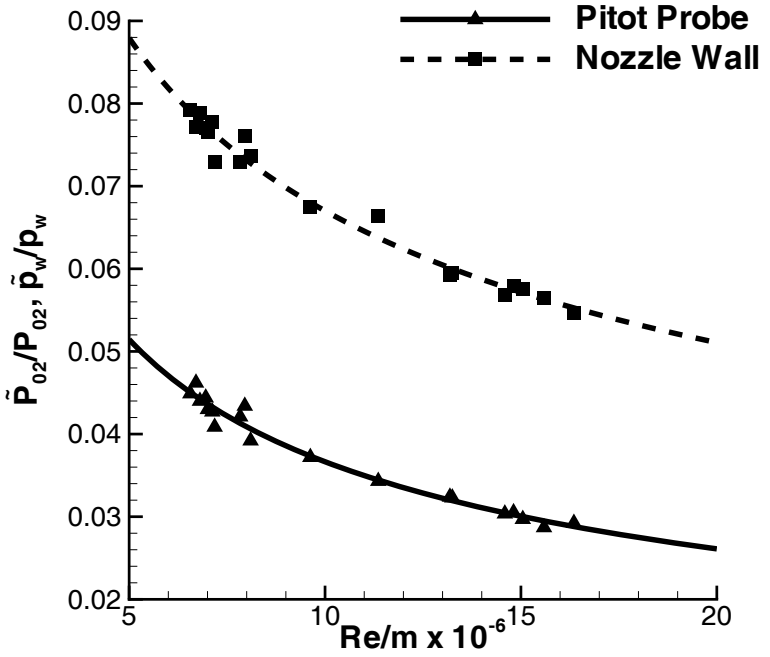


Figure 4.27. Pitot and wall noise measurements in HWT-8 (z = 2.324 m)

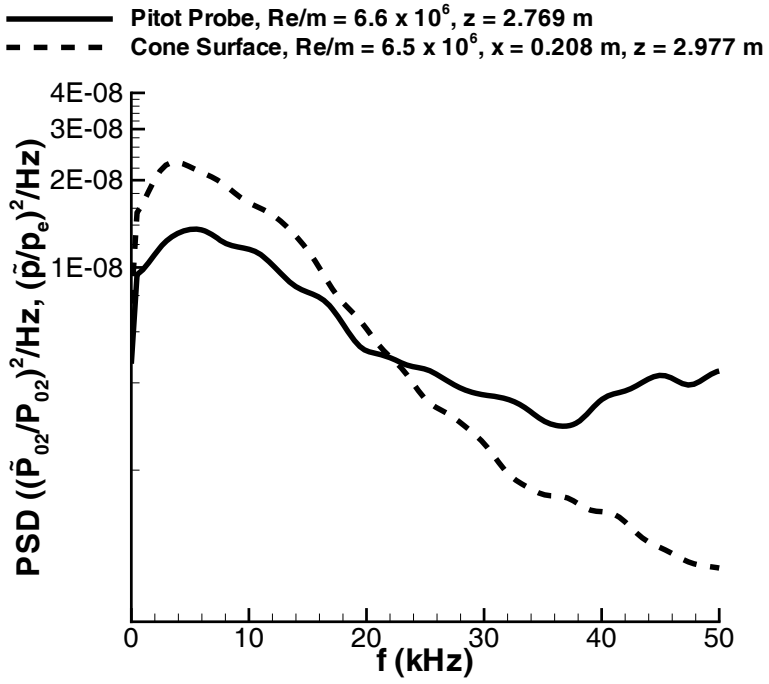


Figure 4.28. Comparison of Pitot spectra with measurements under a sharp cone laminar boundary layer (HWT-5)

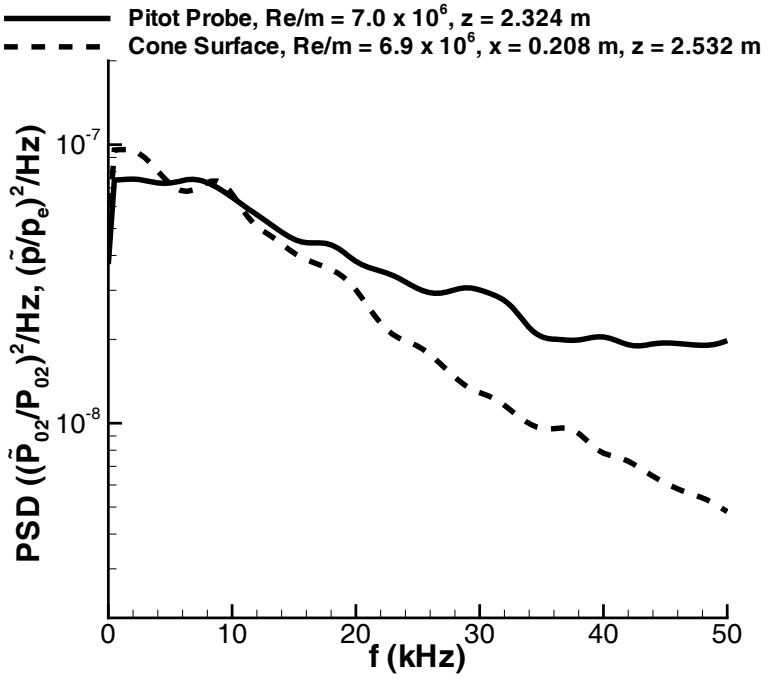


Figure 4.29. Comparison of Pitot spectra with measurements under a sharp cone laminar boundary layer (HWT-8)

**BAM6QT**

Tunnel noise measurements were not conducted in the BAM6QT during this work. Centerline Pitot probe measurements with an XCQ-062-15A were collected from the 2005–2006 work of Juliano [67] and reanalyzed to give an idea of BAM6QT noise levels. Measurements were made at z = 2.155 and 2.385 m under noisy-flow conditions. These measurements were obtained from a variety of runs using both an older aluminum surrogate nozzle as well as the current electroform nozzle. The nozzles were also polished in between separate measurements. Measurements from 2001 at z = 2.141 m fall in between these noise levels [71]. Steen [72] also recently measured tunnel noise at various locations along the centerline, confirming the older noise measurements. Figure 4.30 shows the collected centerline Pitot probe measurements from the BAM6QT under noisy-flow conditions, compared to the noise measurements in HWT-5 and HWT-8. The closed symbols for the BAM6QT are from the work of Juliano [67]. Open symbols are from the work of Steen [72]. The normalized pressure fluctuations decrease with increasing $Re/m$ as expected. Noise levels are higher than HWT-5 but lower than HWT-8. It is also interesting to note that the noise increases significantly with axial distance, especially at the lower $Re/m$. At higher $Re/m$ conditions, the noise levels are nearly constant between z = 2.151 and 2.388 m. For the cone-surface measurements, the sharp nosetip of the model was located at z = 2.134 m. However, Pitot-probe measurements at z = 2.385 m showed better agreement with the present work and are used as representative BAM6QT tunnel noise levels under noisy-flow conditions. Under quiet-flow conditions, the tunnel noise is approximately 0.05% as measured by a centerline Pitot probe [27].

Noisy-flow conditions in the BAM6QT are typically attained with the tunnel bleeds closed. Without bleed-slot suction, turbulent boundary layers grow on the wall of the tunnel. However, at a high enough Reynolds number, the nozzle wall boundary layer can transition even when the bleed slots are open. It was thought that the BAM6QT noise level under noisy-flow conditions might be different with the

bleeds open or closed. To address this question, tunnel noise was compared for four cases where the bleeds slots were open, 1/2 closed, 3/4 closed, and fully closed. The flow is turbulent on the nozzle wall for all cases. Figure 4.31 shows a comparison of the power spectral density for these runs. Despite different amounts of bleed-slot suction, the power spectral density of the noise remains the same, as does the tunnel noise level. This is consistent with 2001 results reported by Schneider and Skoch [71].

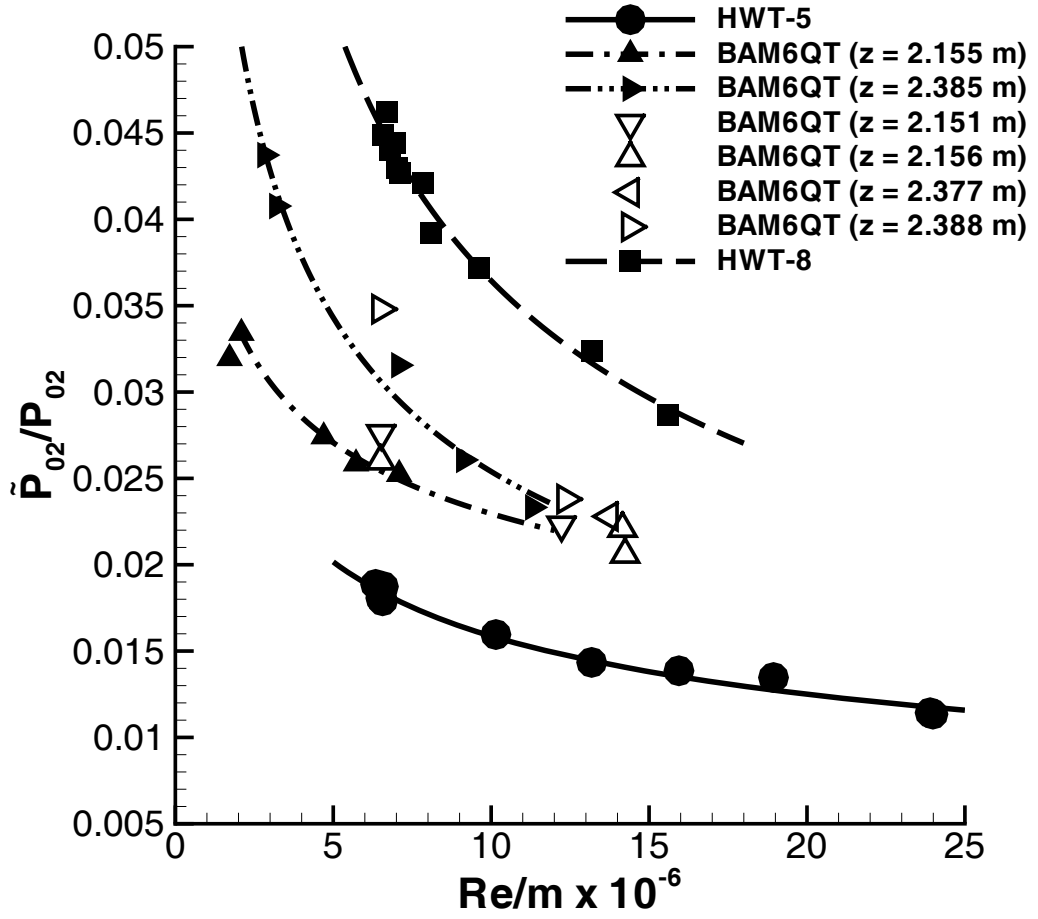


Figure 4.30. Centerline Pitot measurements of freestream noise in BAM6QT (noisy flow) compared to HWT-5 and HWT-8 measurements. BAM6QT closed symbols are from the work of Juliano [67]. Open symbols are from the work of Steen [72].

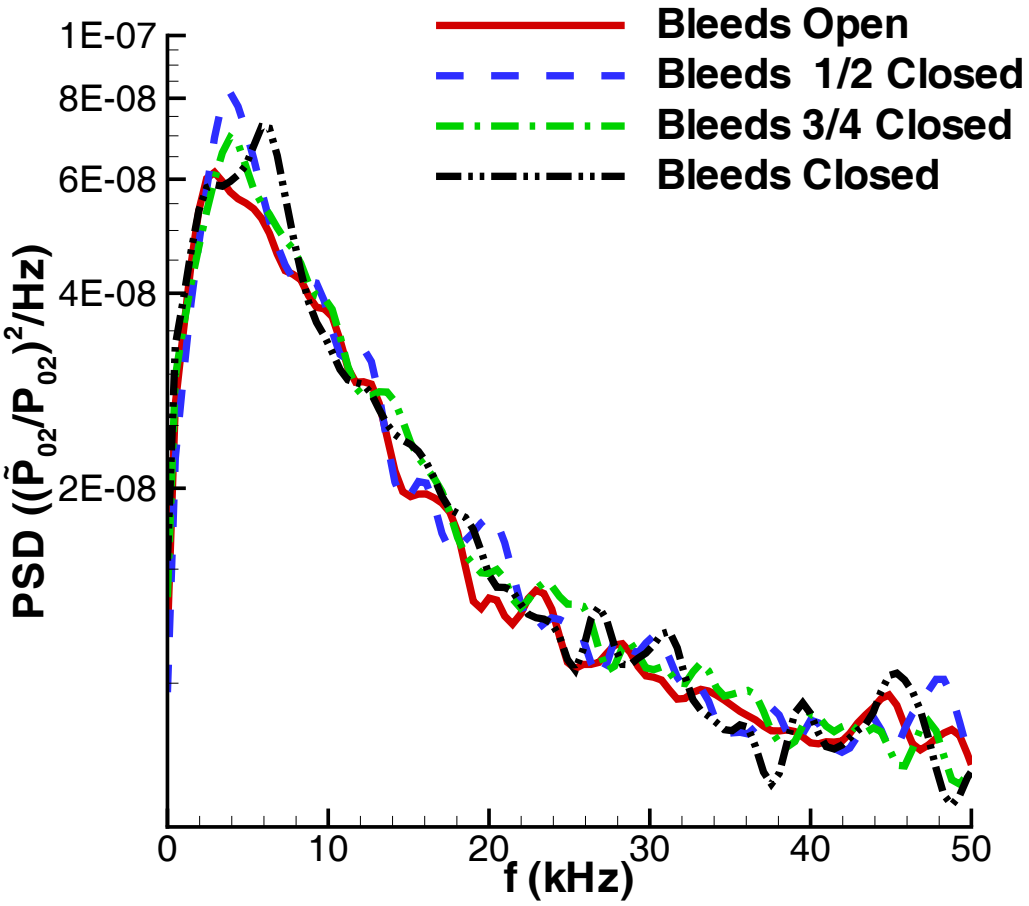


Figure 4.31. Power spectral density of freestream noise in BAM6QT with changing bleed-slot suction (noisy flow, $Re/m = 7.1 \times 10^6$, z = 2.385 m)

### 4.2.6 Pressure-Fluctuation Variation with Freestream Reynolds Number

Pressure fluctuations normalized by $p_e$ along the cone were replotted against $Re/m$ (Figures 4.32 through 4.34). This allows a direct comparison to the tunnel noise measurements. The laminar pressure fluctuations on the cone agree well with the freestream noise level measured by the Pitot probe when normalized by the mean Pitot pressure. Laminar fluctuations are initially close to the tunnel noise level. However, they deviate slightly above the noise level at higher $Re/m$ in HWT-5. The reason for this is unknown. Perhaps there is some amplification of the freestream noise within the laminar boundary layer. Or maybe the boundary layer has already transitioned at the boundary-layer edge but not yet at the surface [56]. A transitional boundary layer at the boundary-layer edge might influence the pressure fluctuations measured on the cone surface [3]. This deviation might also be a part of the transition region. For example, Stainback et al [73] noticed an initial deviation of heat-transfer data on a conical model at low $Re/m$ from the laminar values, but not as great as typically found during transition. This initial deviation is not seen in the BAM6QT or HWT-8, possibly because of higher tunnel noise levels.

As transition progresses, the fluctuations rise above the noise level and peak near the end of transition. Once the flow is late transitional or turbulent, the fluctuations fall back towards the freestream noise level. This is surprising because the turbulent fluctuations would be expected to be higher than the laminar fluctuations. Perhaps the turbulence has a small scale, containing frequencies above 50 kHz. However, this might also be true of the acoustically-induced laminar fluctuations or even the transitional fluctuations. High tunnel noise levels might also cause this result. Beckwith [47] noted a similar result and saw possible attenuation of the freestream disturbances by a turbulent boundary layer.

Because the laminar pressure fluctuations collapsed best with nozzle-wall shear stress, this normalization is again used for the pressure fluctuations plotted against $Re/m$. For comparison to the cone fluctuations, the Pitot pressure fluctuations must

be further multiplied by $p_e/P_{02}$. Figures 4.35 through 4.37 show the pressure fluctuations normalized by $\tau_w$. Normalizing in this manner flattens the laminar and turbulent fluctuation variation with $Re/m$ and also flattens the variation of maximum fluctuation amplitudes, particularly in HWT-5. However, results in the BAM6QT and HWT-8 still decrease with increasing $Re/m$.

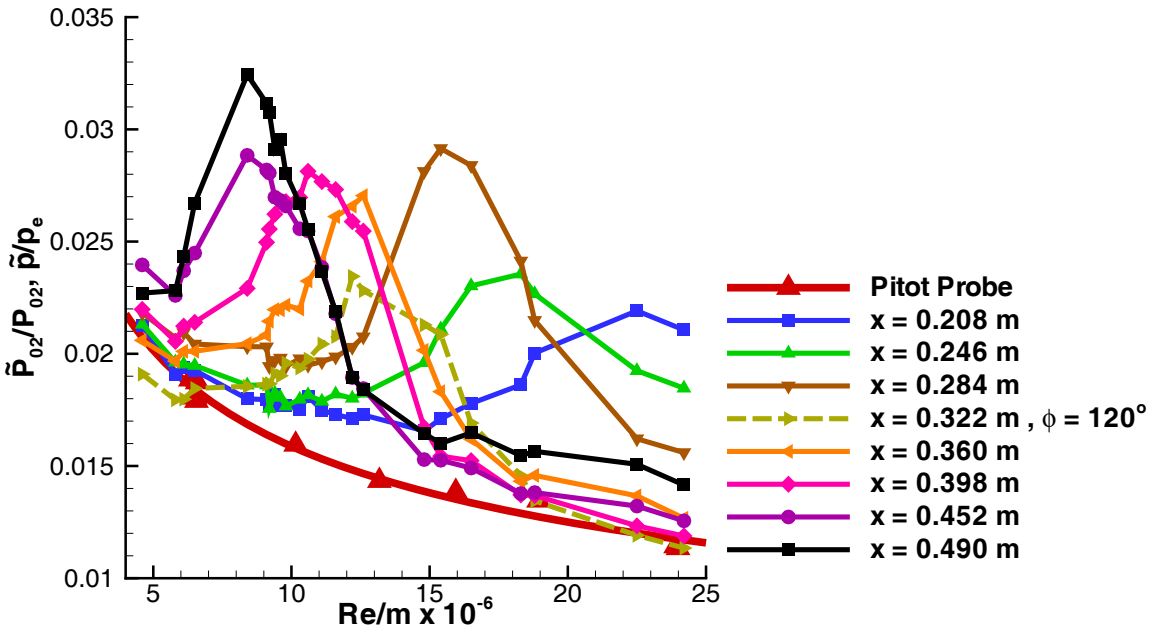


Figure 4.32. Pressure fluctuations normalized by edge pressure as a function of freestream unit Reynolds number (HWT-5)

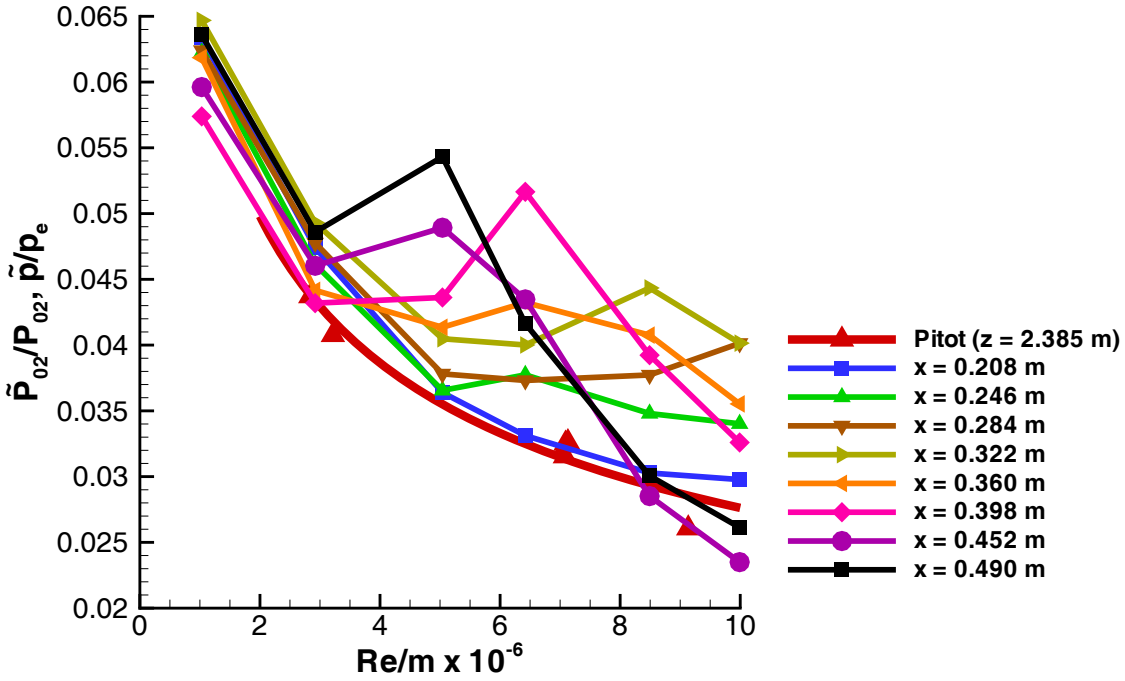


Figure 4.33. Pressure fluctuations normalized by edge pressure as a function of freestream unit Reynolds number (BAM6QT, noisy flow)

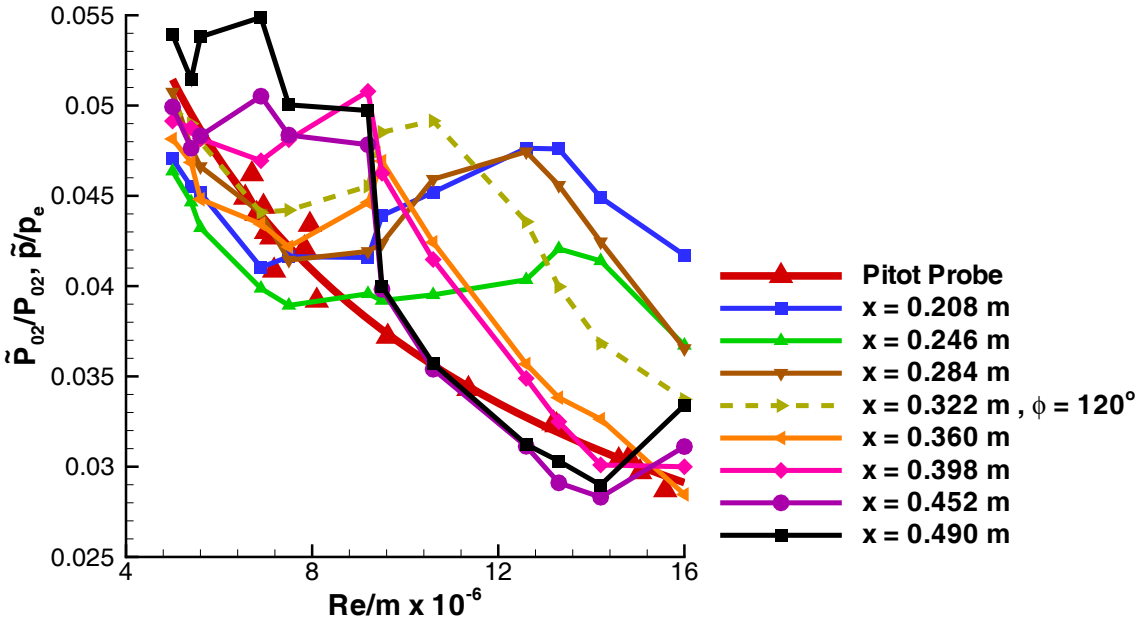


Figure 4.34. Pressure fluctuations normalized by edge pressure as a function of freestream unit Reynolds number (HWT-8)

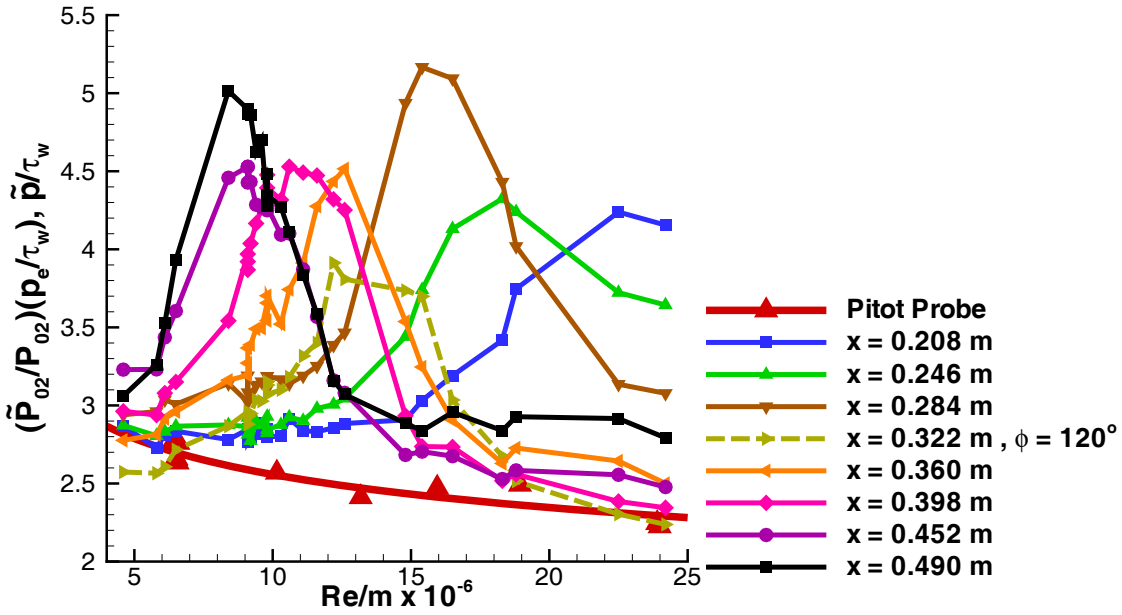


Figure 4.35. Pressure fluctuations normalized by nozzle-wall shear stress as a function of freestream unit Reynolds number (HWT-5)

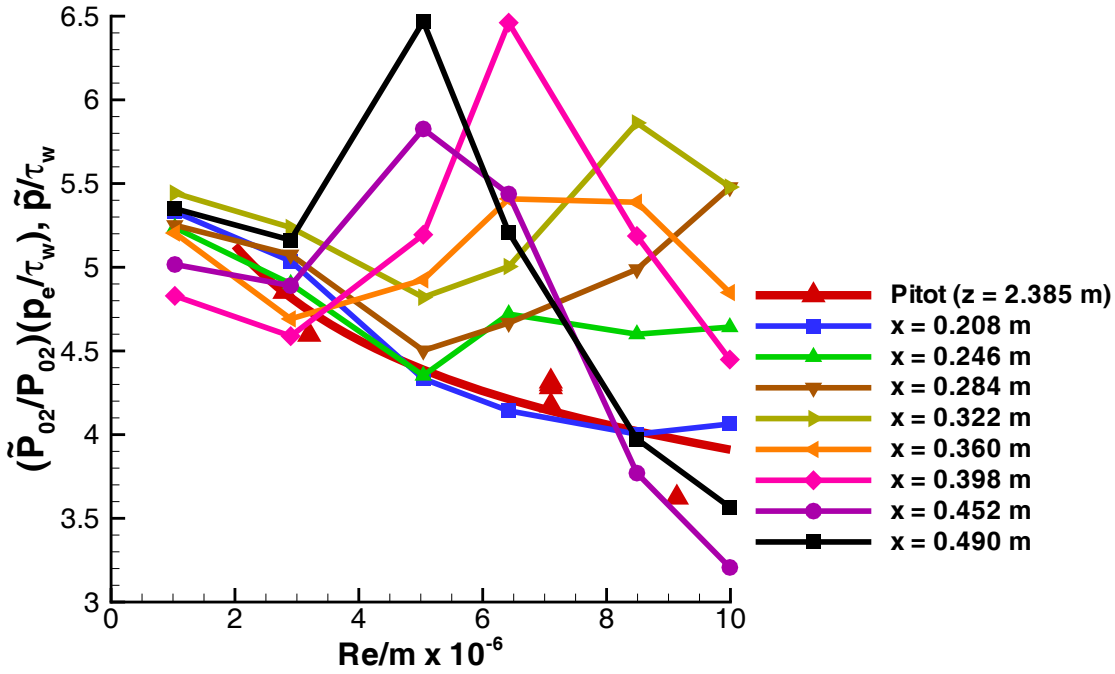


Figure 4.36. Pressure fluctuations normalized by nozzle-wall shear stress as a function of freestream unit Reynolds number (BAM6QT, noisy flow)

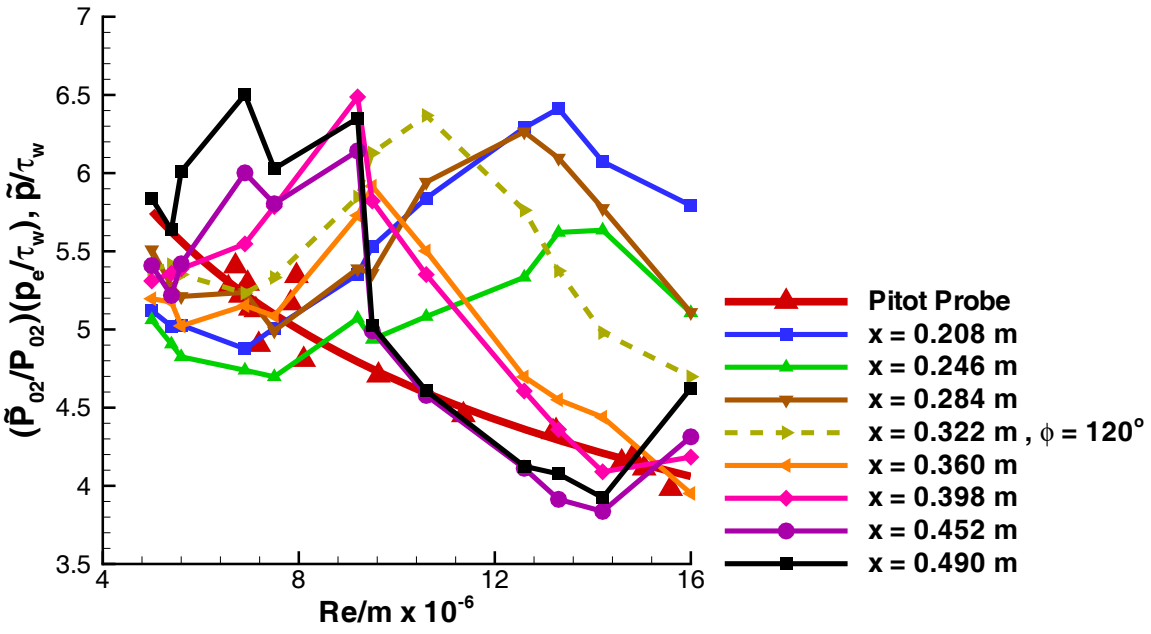


Figure 4.37. Pressure fluctuations normalized by nozzle-wall shear stress as a function of freestream unit Reynolds number (HWT-8)

### 4.2.7 Pate's Correlation for Transition Location in Noisy Tunnels

Pate's correlation for transition location on models in noisy tunnels can be compared to the pressure-fluctuation peaks in the present work. However, the measured transition location varies based on which transition detection method is used. To compare transition measurements obtained with different transition detection methods, Pate correlated different methods to the corresponding location measured by surface Pitot probes (Pate's primary means of transition detection). This correlation (Figure 2.1) was extrapolated to higher Mach numbers using a cubic curve fit that agreed well with Pate's data at lower $M_e$ but also showed good agreement with the present data. This method is arbitrary and more data is needed at higher $M_e$ for comparison. However, applying this correlation to Pate's transition location correlation allows comparison to the surface-microphone pressure fluctuations from the

present work. The correlation values used here are shown plotted along with Pate's correlation of transition detection methods in Figure 4.38.

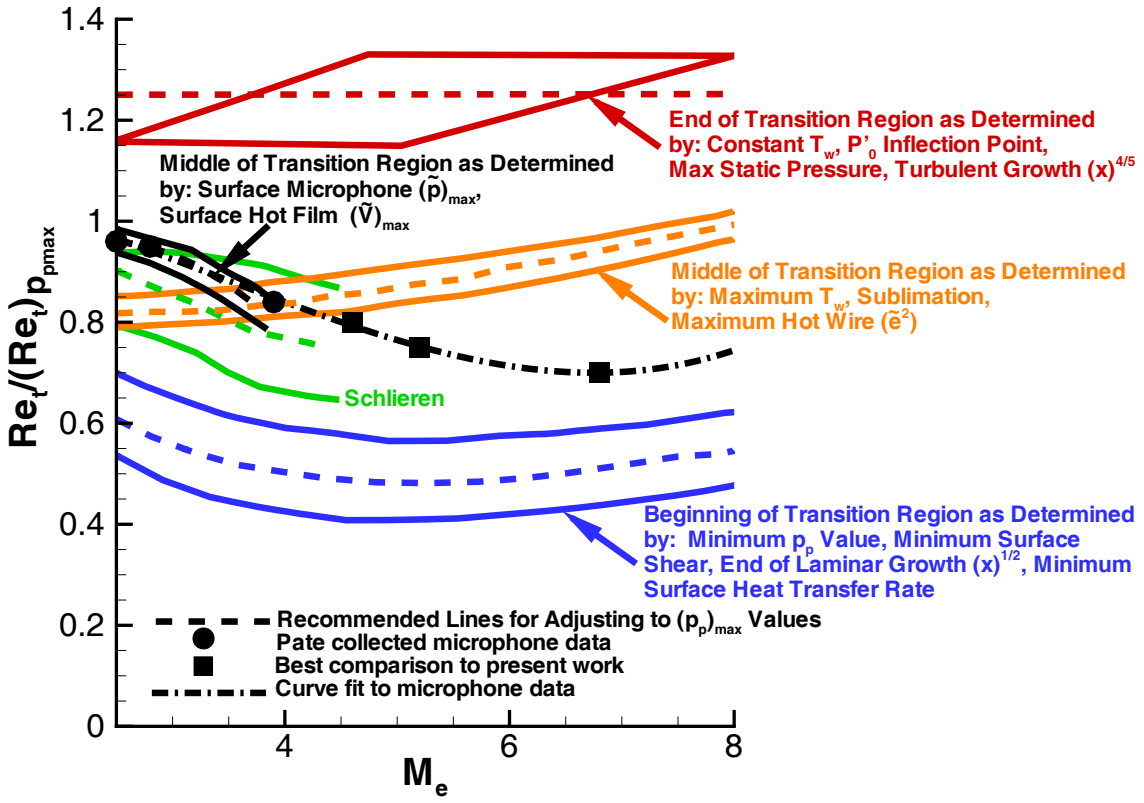


Figure 4.38. Pate's correlation of transition detection methods, replotted from Reference 37

The resulting location of peak surface-microphone fluctuations predicted from Pate's correlation compared to the present work can be seen in Figures 4.39 through 4.41. The error bars for the location of peak surface-microphone fluctuations from the present work are a result of the sensor spacing; the possible error in the peak fluctuation location is one sensor location on either side of the measured peak fluctuation. There is good agreement between experiments and Pate's correlation; the expected trend for movement of transition with increasing $Re/m$ can be seen in all the tunnels. However in HWT-5, the correlation predicts transition after the peak fluctuations

at higher $Re/m$ and before the peak at lower $Re/m$ for unknown reasons. In the BAM6QT, Pate's correlation gives consistent agreement with the transition location. HWT-8 has high levels of freestream fluctuations which make identification of the transition location difficult, but Pate's correlation also shows good agreement with the data. Transition consistently moves further forward on the cone with increasing $Re/m$. A comparison of the location of peak surface-microphone fluctuations between the different tunnels as predicted by Pate's correlation is shown in Figure 4.42. It is interesting to note that even though HWT-8 has the highest levels of tunnel noise, model transition occurs further upstream in the BAM6QT at similar $Re/m$.

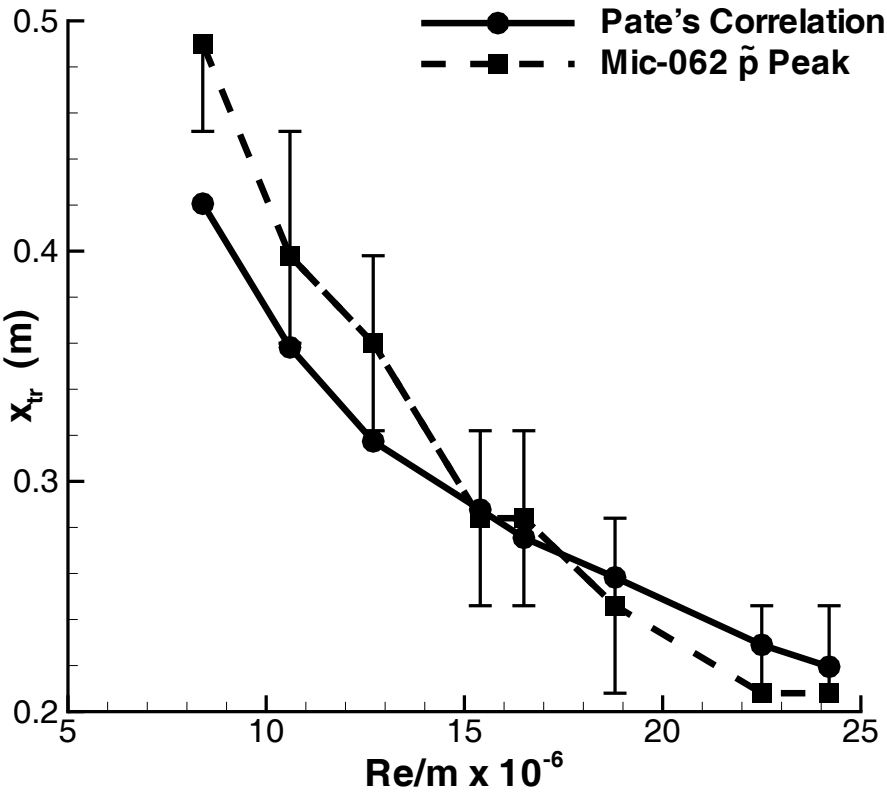


Figure 4.39. Predicted location of maximum surface-microphone fluctuations from Pate's correlation compared to HWT-5 measurements

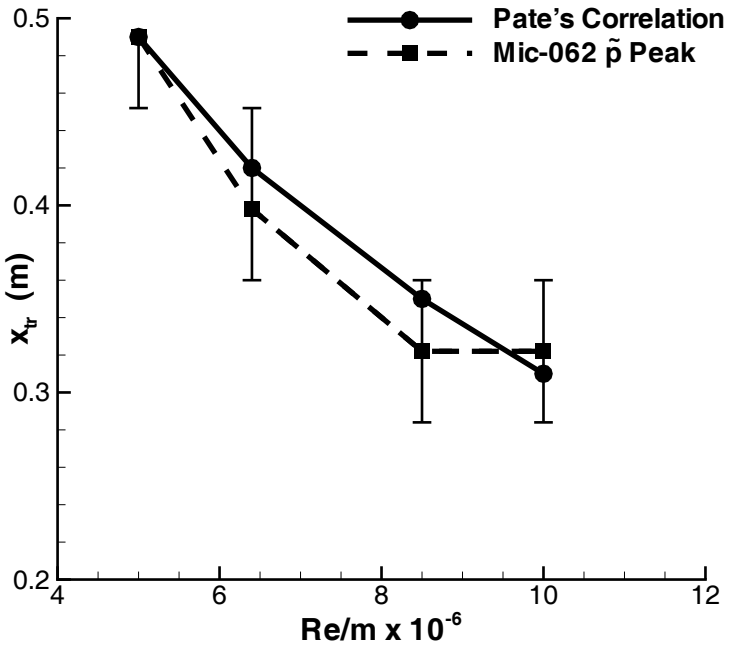


Figure 4.40. Predicted location of maximum surface-microphone fluctuations from Pate's correlation compared to BAM6QT noisy-flow measurements

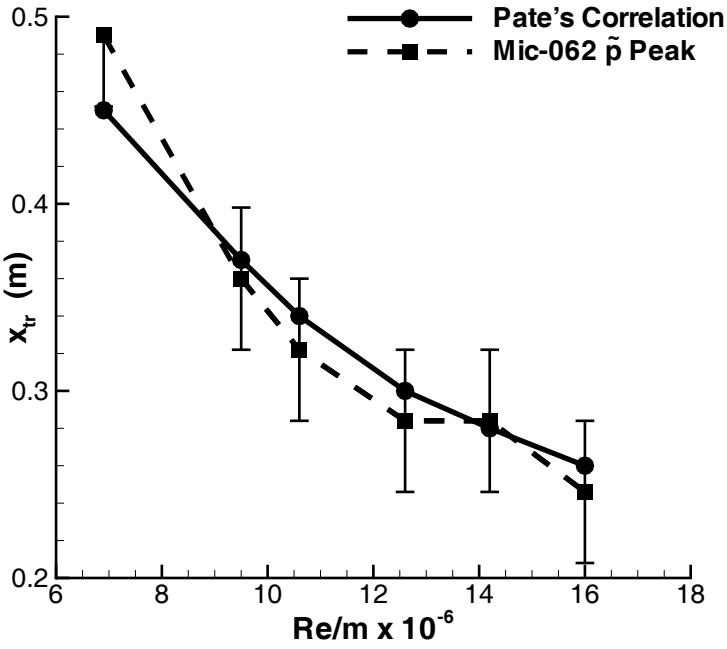


Figure 4.41. Predicted location of maximum surface-microphone fluctuations from Pate's correlation compared to HWT-8 measurements

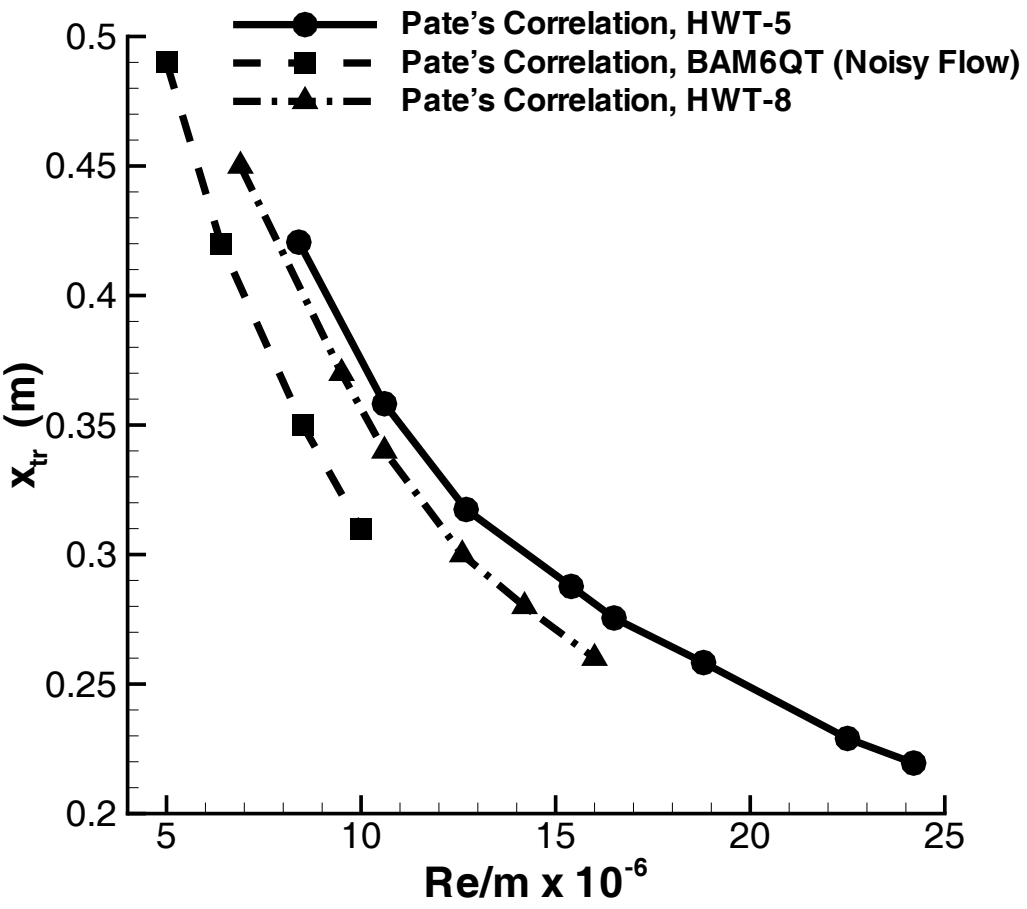


Figure 4.42. Location of peak surface-microphone fluctuations predicted by Pate's correlation in each tunnel

### 4.2.8 Stainback's Correlation for Transition Onset Location

Stainback's correlation [45, 49] for transition onset based on laminar cone fluctuations was compared to experimental results. Transition onset from the present work was defined as the point where fluctuations rose above the laminar fluctuations that collapsed with $\tau_w$. The error bars are one-sided here because the fluctuations are still laminar at the onset location but rise above the laminar fluctuations somewhere before the subsequent sensor location. In HWT-5, Stainback's correlation gave transition onset after the location of peak surface-microphone fluctuations. In the BAM6QT, Stainback's correlation predicts onset at the location of the surface-microphone pressure-fluctuation peak, again not showing agreement with the present work. Only results in HWT-8 showed fair agreement with measured transition onset location (Figure 4.43). However, the onset location defined by the rise in pressure fluctuations above the laminar level may not exactly correspond to Stainback's onset locations (defined by the departure from laminar heating).

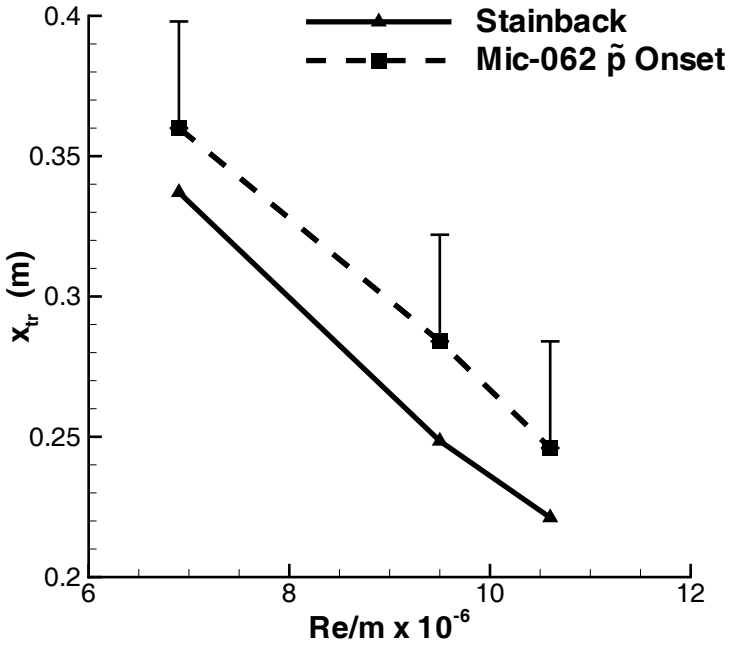


Figure 4.43. Predicted transition onset location from Stainback's correlation compared to HWT-8 measurements

### 4.2.9 Comparison of Pressure Fluctuations under Noisy and Quiet Flow in the BAM6QT

Because the BAM6QT can run with either noisy or quiet flow, the tunnel provides a unique environment to directly show tunnel-noise effects on the measured fluctuations. The cone was run under quiet-flow conditions that matched noisy-flow freestream Reynolds numbers. The Mach number under quiet flow is higher than noisy flow because the laminar boundary layer is thinner: $M = 6.0$ under quiet flow while $M = 5.8$ for noisy-flow runs. As a result, conditions are not exactly matched between quiet and noisy runs.

In all quiet-flow cases, the flow remained laminar over the entire cone, even when transition occurred well forward on the model under noisy flow. Figure 4.44 shows a comparison between noisy and quiet-flow runs at similar $Re/m$. The background noise with no tunnel flow is also shown. The first sensor at x = 0.208 m is seeing the onset of transition under noisy flow and transition occurs downstream. The pressure fluctuations are almost an order of magnitude lower under quiet flow. Figure 4.45 shows the power-spectral density at x = 0.208 m for these runs in the BAM6QT. The noisy-flow spectrum is higher across all frequencies than for quiet flow, though the quiet-flow spectrum shows some low-frequency content. This low-frequency content gives pressure fluctuations higher than those measured in the freestream. This difference indicates that the freestream noise may be interacting with the laminar boundary layer. Further exploration of this interaction is needed.

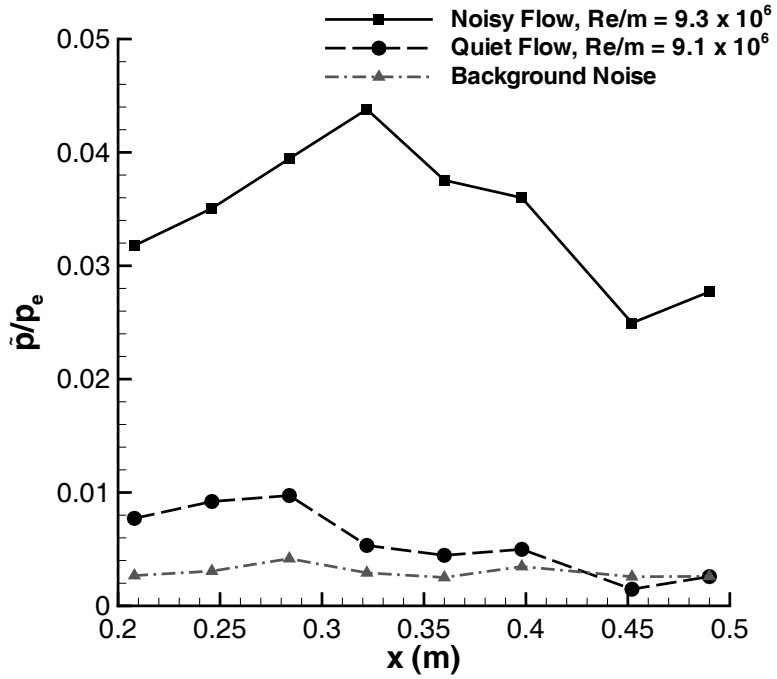


Figure 4.44. RMS pressure normalized by edge pressure along sharp cone under noisy and quiet flow (BAM6QT)

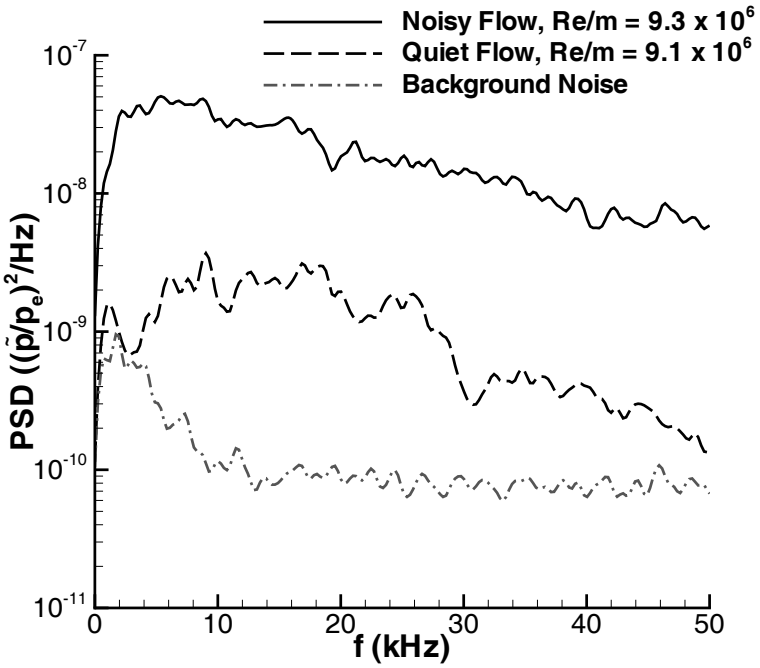


Figure 4.45. Power spectral density normalized by edge pressure along sharp cone under noisy and quiet flow (BAM6QT, x = 0.208 m)

### 4.2.10 Turbulent Spots

One of the goals of the pressure-fluctuation measurements is to identify turbulent spots in the pressure traces. In order to relate transitional pressure fluctuations to spot growth, turbulent spots generated in the transitional boundary layer on the cone must be measured. During transition, the pressure fluctuations peak, which should correspond to peak intermittency and the highest frequency of turbulent spot generation [10–12]. Turbulent spots have been studied before in hypersonic tunnels with thin-films low-pass filtered near 50 kHz [70, 74, 75]. They have also been seen on a larger 7° sharp cone [76] using platinum thin-film sensors sampled at 50 kHz and schlieren imaging. The observed spots in Reference 76 had a duration of 0.1 ms (requiring a frequency of 10 kHz for one data point within the spots) which should be identifiable with pressure sensors.

An estimation of the turbulent-spot size on the model was computed. If the spots are being generated near the beginning of the rise in the pressure fluctuations and grow until the peak in the pressure fluctuations, the transition length from onset to the peak pressure fluctuations will be approximately 50 mm. Assuming the spots have an average propagation speed of $0.75U_e$ (the front of the spot propagates around $0.9U_e$ and the rear of the spot propagates at $0.6U_e$), the length of the spot should be approximately 20 mm. The frequency needed to measure one point during the spot's passage is approximately 32 kHz; however, more points are needed to resolve the spot's passage. The Kulites only measure to 50 kHz whereas the PCB132 sensors filter out frequencies below 11 kHz. This could make identification of the spots difficult, and the current instrumentation may be unable to resolve the spots.

Hot-film traces from the Pressure-Fluctuation Cone in HWT-5 are shown in Figure 4.46(a) and 4.46(b). The first case shows a trace for laminar flow where the voltage fluctuations are small. Figure 4.46(b) shows a higher $Re/m$ case just before the peak pressure fluctuations on the cone (Figure 4.8). The hot-film trace shows many peaks above the nominal laminar level. The presence of these peaks is similar to

Wadhams [76] data showing turbulent spots on the cone. Many of the peaks also have a similar duration of 0.1 ms.

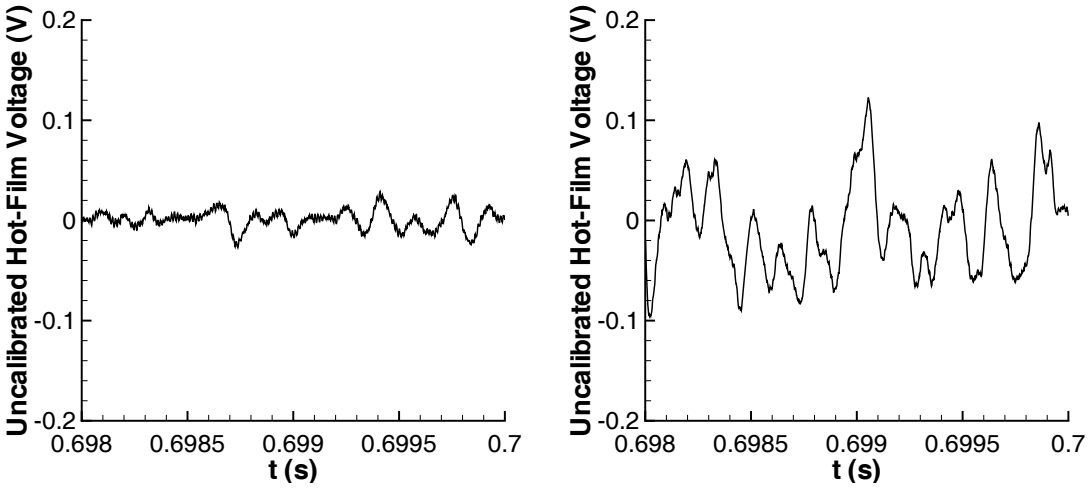


(a) $Re/m = 4.6 \times 10^6$ (b) $Re/m = 8.4 \times 10^6$

Figure 4.46. Hot-film traces under laminar and transitional flow (HWT-5, x = 0.452 m)

Figures 4.47(a) and 4.47(d) show pressure traces on the cone during transition. The traces are low-pass filtered at 75 kHz using a digital Butterworth filter to remove the effect of sensor resonance and are shown with zero mean. The dashed horizontal lines represent the minimum and maximum pressure seen during the 0.1 s time sample. Under laminar flow (x = 0.208 m), there is still a significant amount of pressure fluctuations because of tunnel noise. During transition (x = 0.322 and 0.360 m), there is a higher level of pressure fluctuations and increased impulsiveness is seen in the signal. However, turbulent spots are certainly not clear, especially within the contribution of the tunnel noise. The mean pressure also does not change between laminar and turbulent flow even though the RMS pressure increases. This behavior is unlike the heat transfer which changes value between laminar and turbulent flow. This change in the mean makes turbulent spots more readily identifiable in other types of sensors such as hot films.

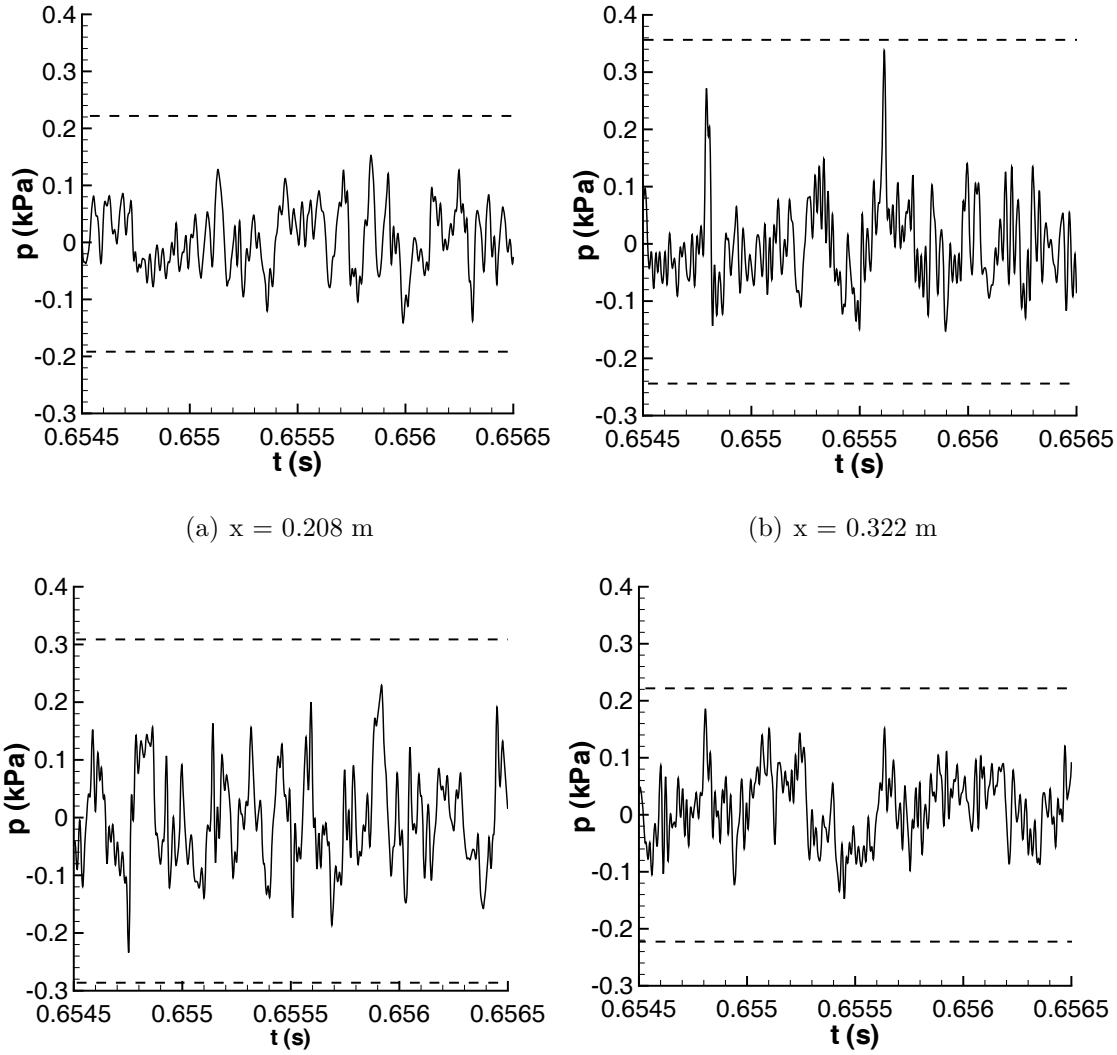


(a) x = 0.208 m

(b) x = 0.322 m

(c) x = 0.360 m

(d) x = 0.490 m

Figure 4.47. Mic-062 A-screen traces during transition (HWT-5, $Re/m = 12.7 \times 10^6$)

Although the turbulent spots are not readily identifiable in the pressure traces, the transitional fluctuations can be studied using statistical methods such as the skewness and kurtosis. Both have been used in the study of turbulent [77, 78] and transitional [70] boundary layers. The skewness is the third moment of the data and represents the asymmetry of the data distribution. A normal distribution has a skewness of zero. A positive skewness means that more of the distribution is concentrated to the left of the mean and there is a longer right tail. A negative skewness is the opposite. Kurtosis is the fourth moment of the data and indicates how peaked the distribution is relative to a Gaussian distribution. Kurtosis is also related to the strength of the tails. A value of three indicates a Gaussian distribution. When the signal begins to show impulsiveness, the kurtosis will rise. Once the impulsiveness increases further, the kurtosis falls as the signal again begins to resemble a normal distribution. The kurtosis has been used to detect impulsiveness in a signal, for example, in detecting bearing failure [79].

Figures 4.48 and 4.49 show the skewness and kurtosis in HWT-5. Both the skewness and kurtosis peak during transition, in agreement with Zanchetta's work [70]. The skewness typically peaks in front of the peak transitional pressure fluctuations. This shows that the distribution is more concentrated to the left and the right tail is strong, indicating many high-amplitude pressure spikes. The kurtosis also peaks one sensor in front of the peak transitional pressure fluctuations (Figure 4.8). When impulses begin to appear, the kurtosis rises. Once many turbulent spots are present and the flow approaches turbulence, the kurtosis declines as the distribution returns towards a Gaussian.

To better identify the characteristics of transitional pressure fluctuations, the HWT-5 case at $Re/m = 12.7 \times 10^6$ is studied in more detail. Figure 4.50 shows the RMS pressure, skewness, and kurtosis along the cone. The skewness and kurtosis peak at x = 0.322 m, while the maximum RMS pressure is at x = 0.360 m. Figures 4.47(a) through 4.47(d) reflect these statistics. At x = 0.208 m (under laminar flow), the pressure fluctuations are centered around the mean. The maximum impulses on

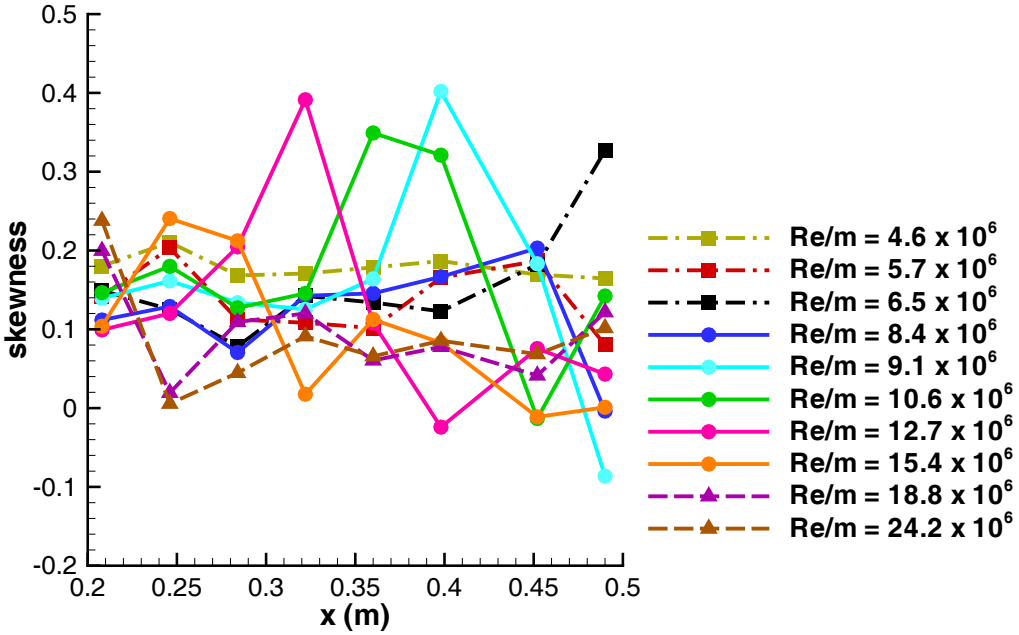


Figure 4.48. Skewness along cone (HWT-5)

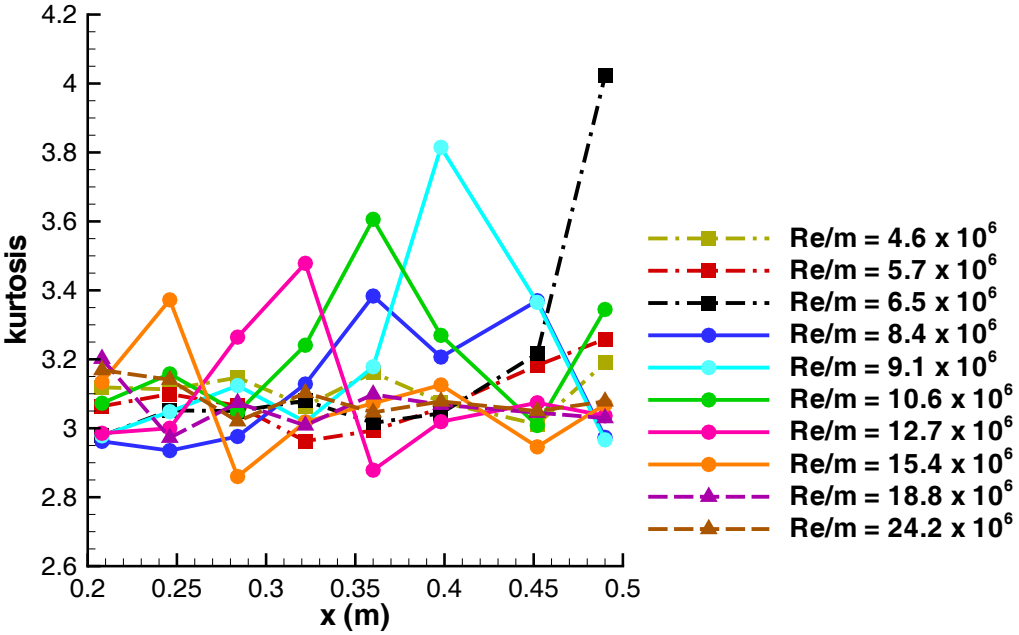


Figure 4.49. Kurtosis along cone (HWT-5)

the cone (given by the dashed lines) are ±0.2 kPa. At x = 0.322 m, large impulses can be seen, and they are asymmetric about the mean. This asymmetry and large-amplitude impulses are reflected in the higher skewness and kurtosis of the signal. At x = 0.360 m, there are more impulses, but they are again centered around the mean. By the end of the cone, the impulses have decreased and the peak amplitudes are again approximately ±2 kPa.

These results can also be seen in the probability density functions as it changes through transition (Figure 4.51). For laminar flow (x = 0.208 m), the density functions are clustered around the mean. There is a small probability of high-amplitude pressure fluctuations. The probability density function agrees well with a Gaussian fit. At x = 0.332 m, one sensor location before the highest transitional pressure fluctuations, both the kurtosis and skewness peak. This can be seen in the probability density function which does not agree with a Gaussian fit. The distribution near the mean is not centered and there is a larger positive tail. The distribution is also more peaked at the center. At x = 0.360 m, during the peak fluctuations on the cone, the probability density function also shows larger tails, indicating higher fluctuations away from the mean. However, there are not high levels of skewness and kurtosis, and the probability density function can be fit well by the Gaussian distribution. This is probably because enough impulses exist in the signal to approach a normal distribution. By x = 0.490 m, the flow is turbulent on the cone. The probability density function is similar to the laminar flow case. There are few large amplitude pressure spikes and the distribution is centered around the mean.

These results point towards the presence of turbulent spots leading to transition. The hot-films seem to indicate turbulent spots on the model, and the skewness and kurtosis both peak prior to the highest transitional fluctuations. However, clear spots are not seen in the pressure transducer traces.

Future work will seek to measure clearly identified turbulent spots in the pressure traces, but the best option for doing so is unclear. Schlieren imaging of the boundary layer can be done in conjunction with pressure fluctuation measurements in HWT

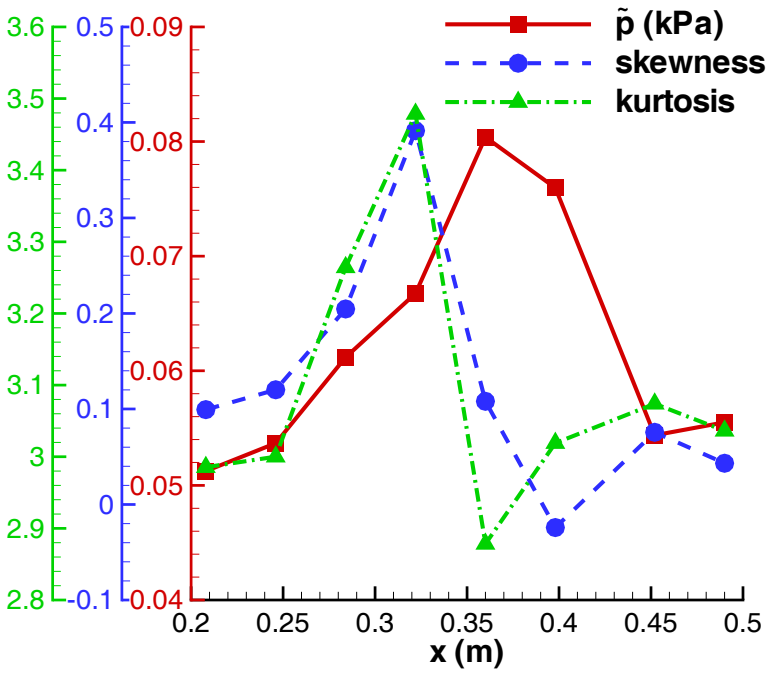


Figure 4.50. RMS pressure, kurtosis, and skewness along sharp cone (HWT-5, $Re/m = 12.7 \times 10^6$)

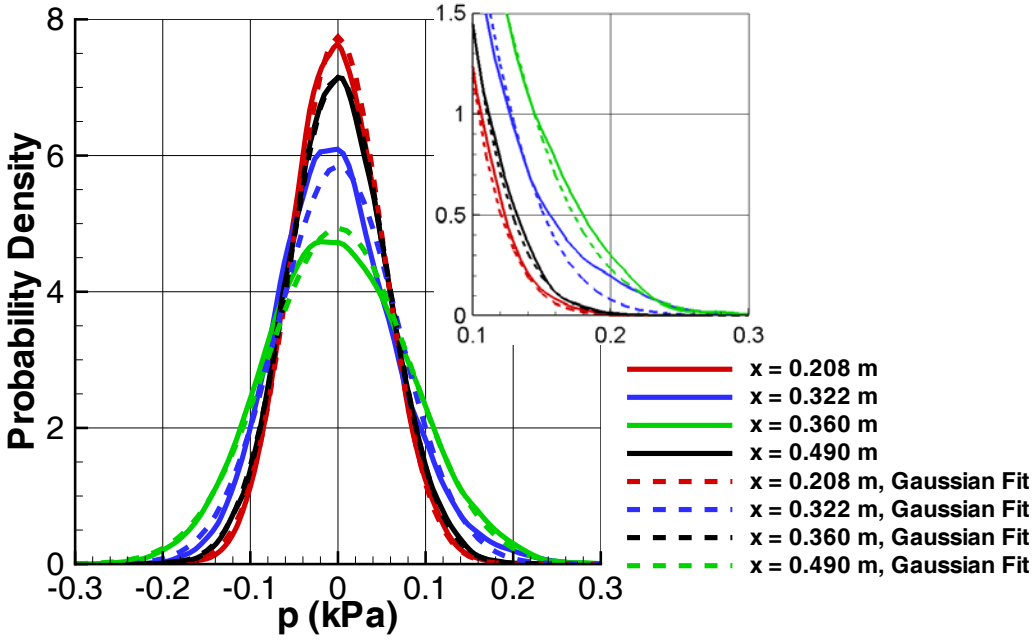


Figure 4.51. Probability density function of pressure fluctuations during transition (HWT-5, $Re/m = 12.7 \times 10^6$)

to aid in the identification of turbulent spots. A glow perturber can also be used to generate controlled spots for study on the model. By generating a controlled disturbance from a known origin, the growth of the spots and their structure can be studied. Inputting these disturbances under quiet-flow conditions should reduce the high laminar fluctuations seen under noisy-flow conditions and allow easier identification of the turbulent spots. Also, introducing the disturbances further upstream on the cone will allow more growth of the spots, making their study easier with the current instrumentation. Dynamic sensor calibrations might also allow the frequency response of the current instrumentation to be extended to higher frequencies. Future work may also include more measurements of turbulent spots on the wall of the BAM6QT under quiet flow to increase understanding of turbulent-spot growth and how the pressure transducers respond to their passage.

### 4.3 Second-Mode Wave Measurements

Second-mode waves are the dominant instability on cones at zero angle of attack for hypersonic $M_e$ [80]. The waves are like trapped acoustic waves that reflect between the wall and the edge of the boundary layer. Initially, the unstable waves grow linearly. Prior to transition, the waves become nonlinear and break down to turbulence. This breakdown should correspond to the point where turbulent spots begin to appear. Flow intermittency increases until the flow eventually becomes fully turbulent. Figure 4.52 shows second-mode dominance in a PCB132 pressure trace low-pass filtered at 1 MHz by the data-acquisition system. The large oscillations of the waves are easily seen.

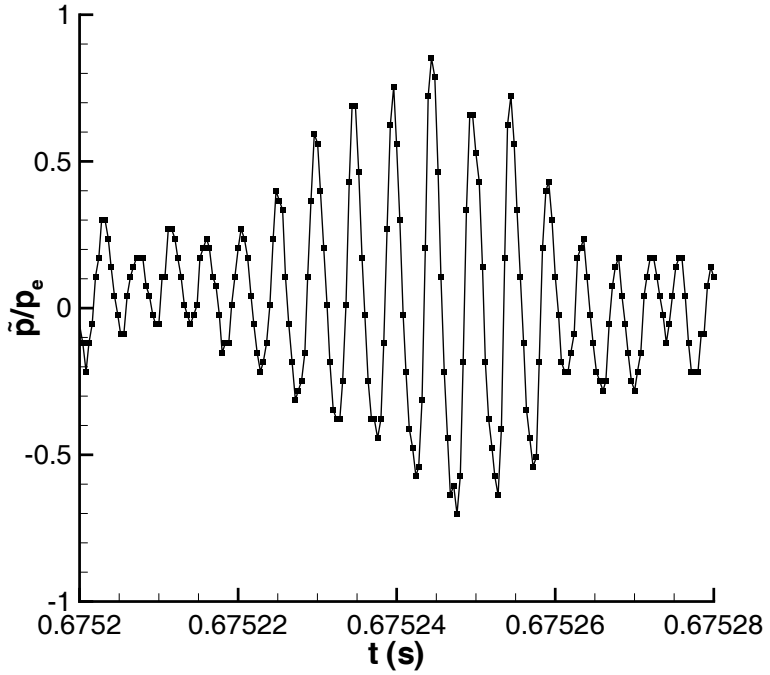


Figure 4.52. PCB132 pressure trace normalized by $p_e$ showing second-mode waves (HWT-8, $Re/m = 6.9 \times 10^6$, x = 0.360 m)

The growth and breakdown of the second-mode wave instability leading to transition was studied for comparison to transition defined by the Kulite pressure fluctuations between 0 and 50 kHz. The second-mode waves were measured with three

PCB132 sensors at positions 1B, 5B, and 8B. Power spectral densities were calculated for 0.1 s samples using Welch's method. A Blackman window with 25% overlap was used with a window size of 1024 points for HWT data and 2048 points for the BAM6QT. Approximately 976 FFT's were averaged. To compare second-mode wave strength prior to breakdown, the normalized power density $((\tilde{p}/p_e)^2/Hz)$ at the most amplified frequency is used. Second-mode wave RMS amplitudes are also compared. The wave power was obtained by integrating the unnormalized PSD over the amplified frequencies. Taking the square root of the power ($\times 100$) and then normalizing by $p_e$ gives the RMS amplitude of the waves as a percentage of the edge pressure. It should be noted that the RMS amplitudes of the amplified frequency bands in all tunnels were reported incorrectly in Reference [81]. RMS amplitudes were also computed over a 4.88 kHz frequency band centered at the most amplified frequency. Comparisons of these second-mode wave measurements to computations are forthcoming [82].

### 4.3.1 HWT-5

Second-mode waves were apparent in HWT-5 prior to transition. This is surprising because $M_e = 4.6$, low for growth of the second-mode instability. Figure 4.53 shows PCB132 power spectral densities when the Kulite pressure fluctuations indicate fully laminar flow along the cone (Figure 4.10). The first two sensors (at x = 0.208 and 0.360 m) show low-frequency fluctuations, but most of the spectra is attributed to electrical noise. The third sensor at x = 0.490 m shows a peak near 200 kHz which is attributed to the growth of the second-mode instability. Further confirmation of this assumption is discussed throughout this section.

Figure 4.54 shows PCB132 power spectral densities for $Re/m = 9.1 \times 10^6$. The Kulite pressure fluctuations indicate peak pressure fluctuations at the rear of the cone (Figure 4.8) for this run. The first PCB132 at x = 0.208 m shows no indication of second-mode waves. This sensor also shows higher electrical noise than the other two sensors for unknown reasons. The second PCB132 at x = 0.360 m shows a second-

mode wave with a peak frequency near 280 kHz. A smaller secondary peak is also evident near 670 kHz. This location on the cone corresponds to the beginning of the rise in Kulite pressure fluctuations. The third PCB132 (x = 0.490 m) is at the rear of the cone where the peak in Kulite fluctuations is seen. The second-mode waves have broken down and are no longer visible. However, the broadband frequency spectrum is higher and significant frequency content is seen up to 650 kHz.

Figure 4.55 shows the PCB132 spectra when the peak Kulite pressure fluctuations occur at or before the first sensor. The cone is seeing late transitional or turbulent flow over all the sensors. The PCB132 spectra confirm these results. Second-mode waves are not seen, and high-frequency content is shown by all the sensors. Small high-frequency peaks are seen in the spectra near 800, 675, and 500 kHz, though it is unclear to what they can be attributed.

The second-mode waves were small in HWT-5. Figure 4.56 shows waves at x = 0.490 m on the cone as they grow and break down with increasing $Re/m$. The frequency of the second-mode waves should be near $\frac{U_e}{2\delta}$. Increasing $Re/m$ should decrease the boundary-layer thickness ($\delta$ is proportional to $\frac{1}{\sqrt{Re_x}}$), increasing the frequency of the waves. However, the frequencies of the second-mode waves seen here do not change much with increasing $Re/m$. This is explained by the changing wall temperature ratio between cases; higher total temperatures are needed to reach the lower $Re/m$ conditions in HWT-5. A decrease in $T_e$ reduces the edge velocity and also decreases the expected frequency of the waves (the opposite effect of the increasing $Re/m$). Near breakdown, the normalized power density of the most amplified frequency is $4.90 \times 10^{-8}/Hz$, and the RMS amplitude of a 4.88 kHz frequency band centered at the most amplified frequency is 1.4%. The RMS amplitude of the entire amplified frequency band is approximately 4.7%. The small amplitude of waves in HWT-5 is probably because of the low $M_e$. Waves in the BAM6QT and HWT-8 are much larger, as seen below. It is also interesting to note that harmonics of the apparent second-mode waves are not seen in HWT-5, though they appear in the BAM6QT and HWT-8 measurements.

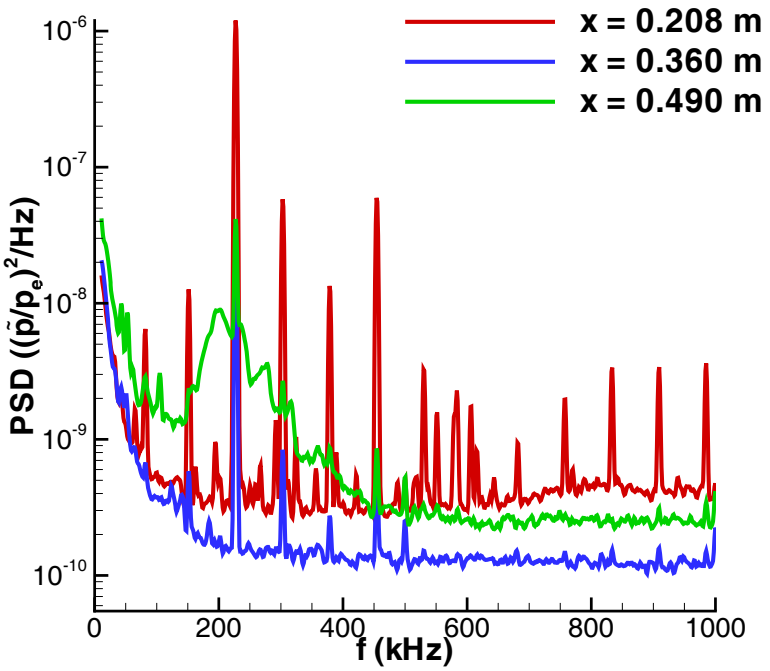


Figure 4.53. PCB132 power spectral density under laminar flow (HWT-5, $Re/m = 5.7 \times 10^6$)

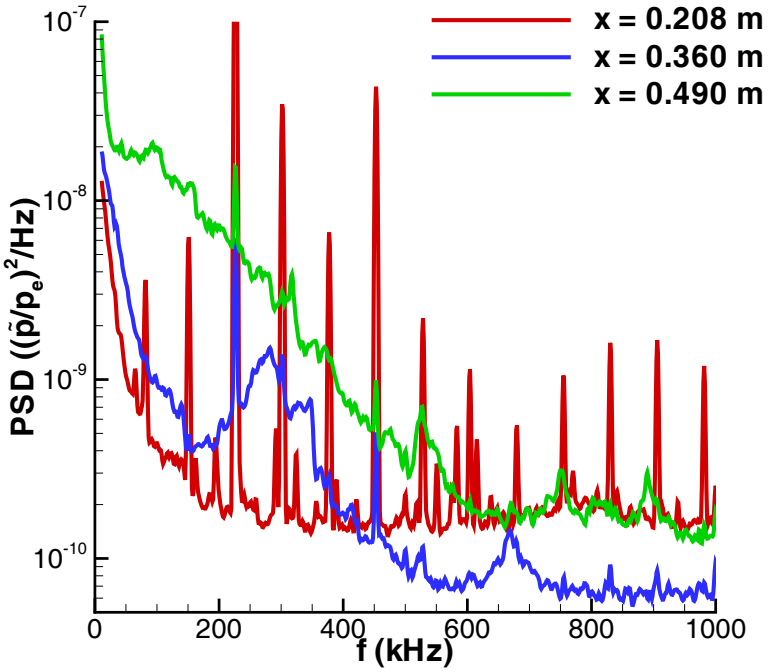


Figure 4.54. PCB132 power spectral density under mostly transitional flow (HWT-5, $Re/m = 9.1 \times 10^6$)

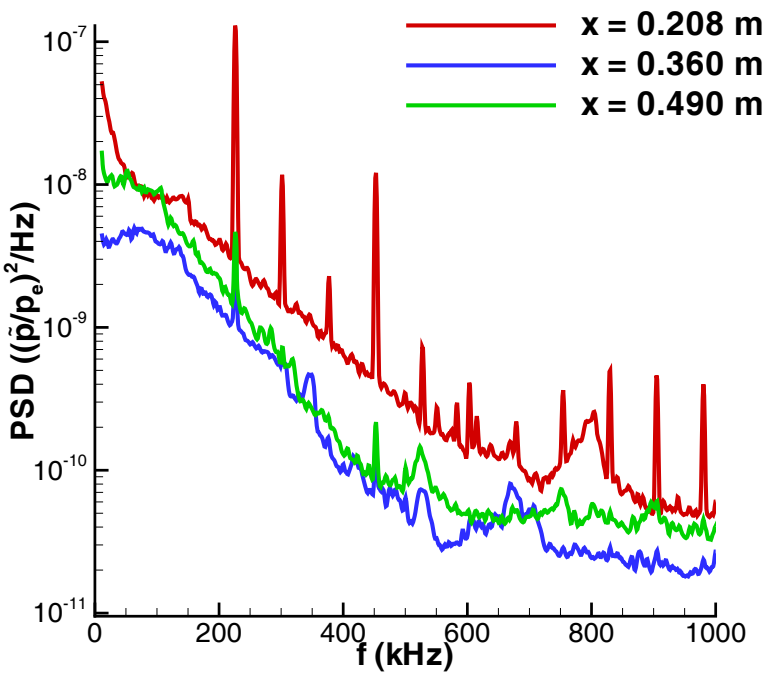


Figure 4.55. PCB132 power spectral density under turbulent flow (HWT-5, $Re/m = 24.2 \times 10^6$)

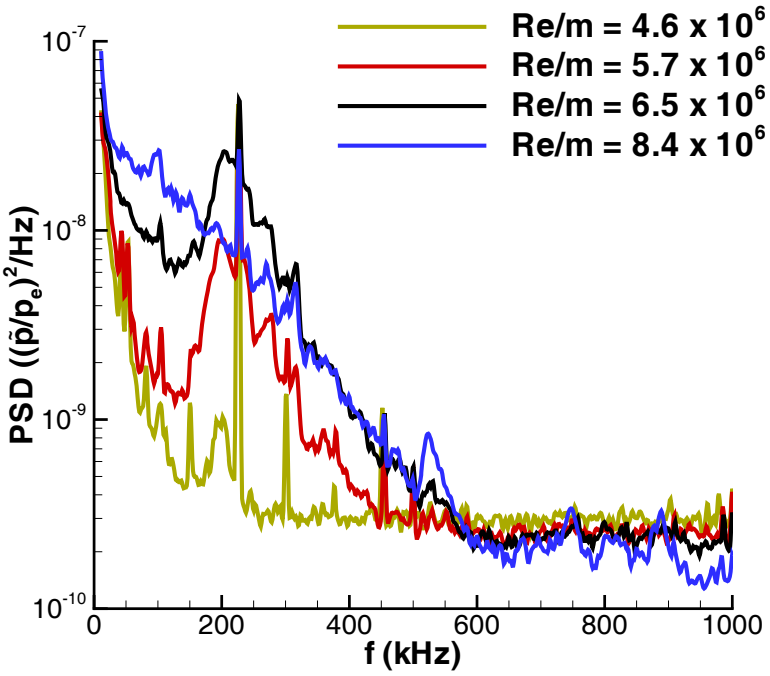


Figure 4.56. Second-mode wave growth and breakdown (HWT-5, x = 0.490 m)

### 4.3.2 BAM6QT

#### Noisy-Flow Measurements

Second-mode waves were also seen in the BAM6QT. Figure 4.57 shows the results for a noisy run with transition over the middle portion of the cone. At x = 0.208 m, a small second-mode wave can be seen centered at 275 kHz. The flow here is still laminar as defined by the Kulite fluctuations (Figure 4.14). By x = 0.360 m, the second-mode waves have grown in amplitude and decreased in frequency to near 205 kHz. A likely harmonic of the wave can also be seen at 410 kHz and there is an increase in broadband frequency content. The Kulite pressure fluctuations indicate transition onset near this location. Rufer [64] measured second-mode waves at 200 kHz with hot wires at this location and at similar freestream conditions. Robarge [83] performed a stability analysis for these conditions and computed a peak second-mode frequency of 200 kHz and an N factor of 4.7. These comparisons form preliminary confirmation that the peaks observed under other conditions are really second-mode waves. Between x = 0.360 and 0.452 m, the Kulite fluctuations peak, indicating the end of transition. Breakdown of the second-mode waves is complete by x = 0.490 m and broadband high-frequencies remain.

The second-mode waves in the BAM6QT have larger amplitudes than in HWT-5. Figure 4.58 shows PCB132 spectra at x = 0.360 m for increasing $Re/m$. Small second-mode waves can be seen near 160 kHz at $Re/m = 2.9 \times 10^6$. As $Re/m$ increases, the waves grow in amplitude. The waves also shift to higher frequencies as the boundary layer thins, and a harmonic becomes visible. At $Re/m = 8.5 \times 10^6$ the wave begins to break down, and breakdown is complete by $Re/m = 10.0 \times 10^6$. The normalized power density of the most amplified frequency is $2.97 \times 10^{-7}/Hz$, and the RMS amplitude of a 4.88 kHz frequency band centered at the most amplified frequency is 3.7% before breakdown. The maximum RMS amplitude of second-mode waves over the amplified frequency band is approximately 12%. This is larger than the waves seen in HWT-5 but smaller than those in HWT-8.

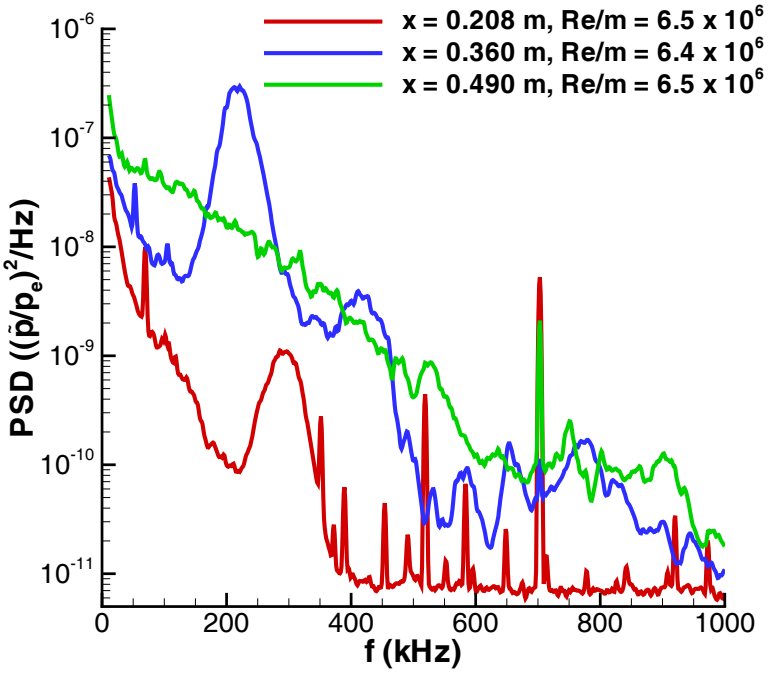


Figure 4.57. PCB132 power spectral density during transition (BAM6QT, noisy flow)

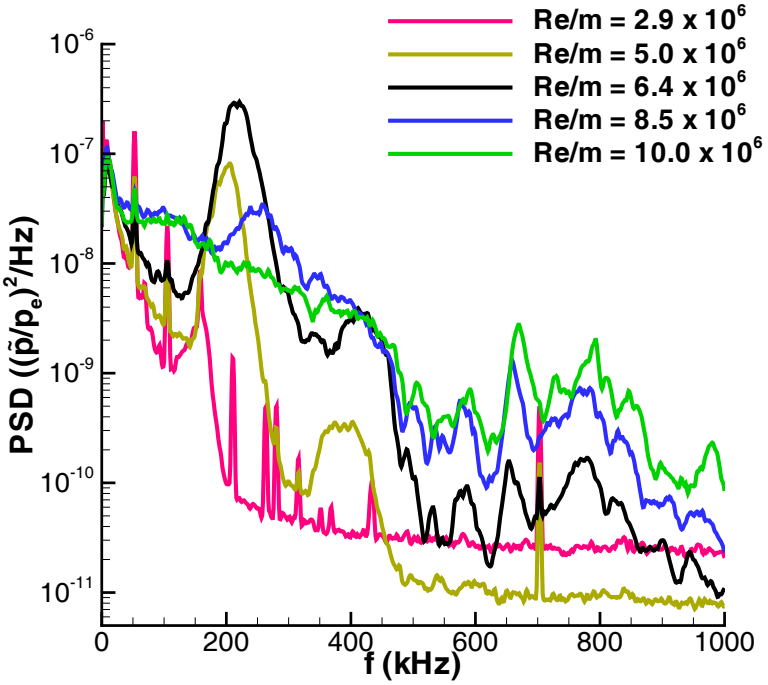


Figure 4.58. Second-mode wave growth and breakdown (BAM6QT, noisy flow, x = 0.360 m)

### Quiet-Flow Measurements

Measurements were repeated under quiet flow. Figure 4.59 shows a comparison of waves measured under quiet flow compared to noisy-flow results. Second-mode waves can be seen at 220 and 235 kHz under quiet flow. Under quiet flow, the RMS amplitude of the amplified frequency band is approximately 0.34%, more than an order of magnitude lower than under noisy flow. Under noisy flow, the waves are centered at 330 and 350 kHz and the RMS amplitude of the amplified frequencies is 5.0%. However, these waves cannot be directly compared. Under quiet flow, the waves are only seen at the last sensor location (x = 0.490 m). The noisy-flow waves appear at the first sensor location (x = 0.208 m) and have broken down by the end of the cone. Further normalization using the edge velocity and the boundary-layer thickness should allow a more direct comparison.

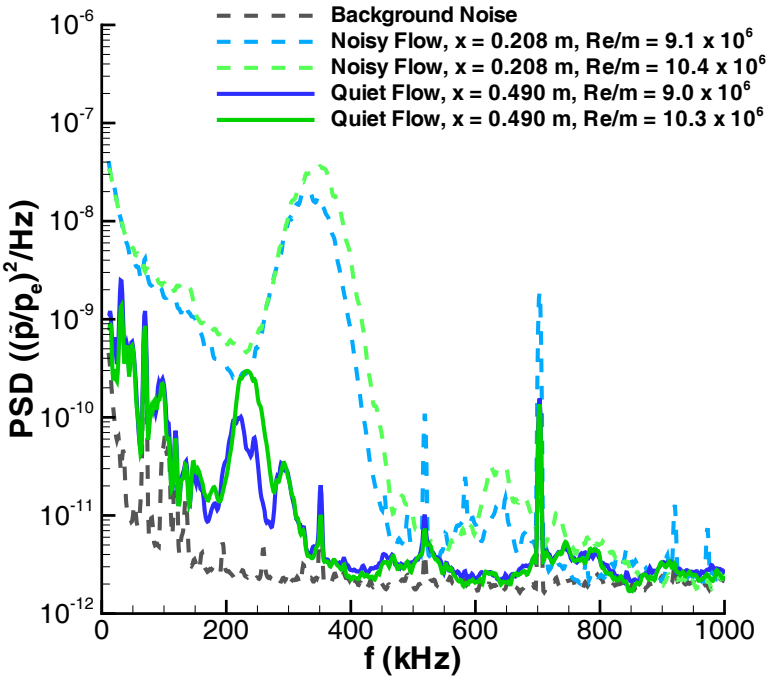


Figure 4.59. PCB132 power spectral densities showing second-mode waves under noisy and quiet flow (BAM6QT)

### 4.3.3 HWT-8

Second-mode waves were largest in HWT-8. This is expected because the edge Mach number is 6.8, higher than in the other tunnels. Figure 4.60 shows PCB132 power spectral densities along the cone for a nominally laminar case. Large second-mode waves are seen at all sensor locations. At x = 0.208 m, a small wave is centered at 295 kHz. By x = 0.360 m, the second-mode wave has grown significantly. The peak frequency of the wave has also decreased to 220 kHz because of the thickening of the boundary layer. Two harmonics appear near 415 kHz and 670 kHz. The third sensor at x = 0.490 m shows an even larger second-mode wave at 180 kHz. The harmonics have also grown in power and decreased in frequency to 350 and 525 kHz, respectively. Despite the presence of the large waves and harmonics, breakdown does not occur and the boundary layer remains laminar as defined by Kulite pressure fluctuations along the cone (Figure 4.18).

Figure 4.61 shows a higher $Re/m$ case where transition occurs over the middle portion of the cone. The first sensor is under fully laminar flow. A large-amplitude second-mode wave at 320 kHz as well as a harmonic at 615 kHz can be seen. The second sensor at x = 0.360 m is in the middle of the peak fluctuations seen by the Kulite sensors (Figure 4.18). In this case, the second-mode wave near 230 kHz has started to break down but is still visible. Higher frequency broadband components are seen throughout the spectrum. The third sensor at x = 0.490 m corresponds to turbulent flow as indicated by Kulite fluctuations. The second-mode waves are no longer visible on the cone, and there are now broadband frequency components.

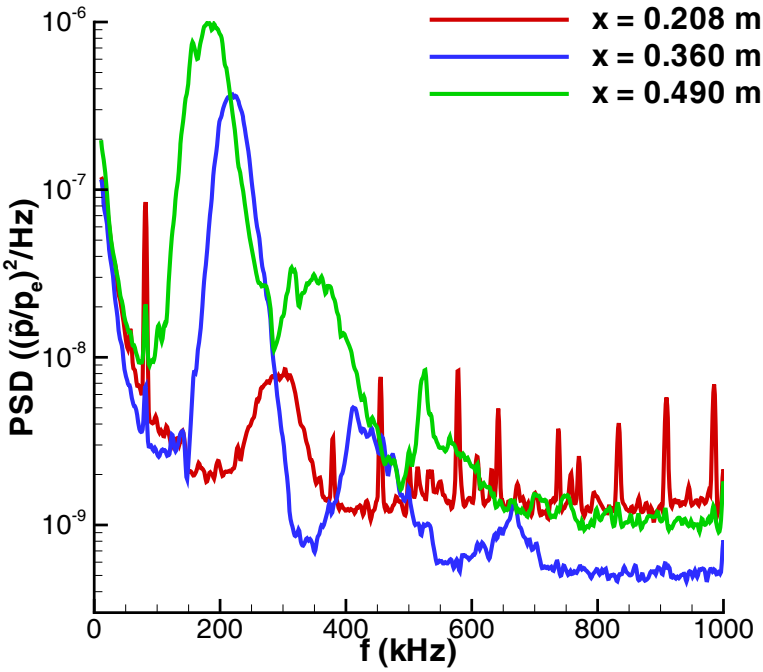


Figure 4.60. PCB132 power spectral density under laminar flow (HWT-8, $Re/m = 5.0 \times 10^6$)

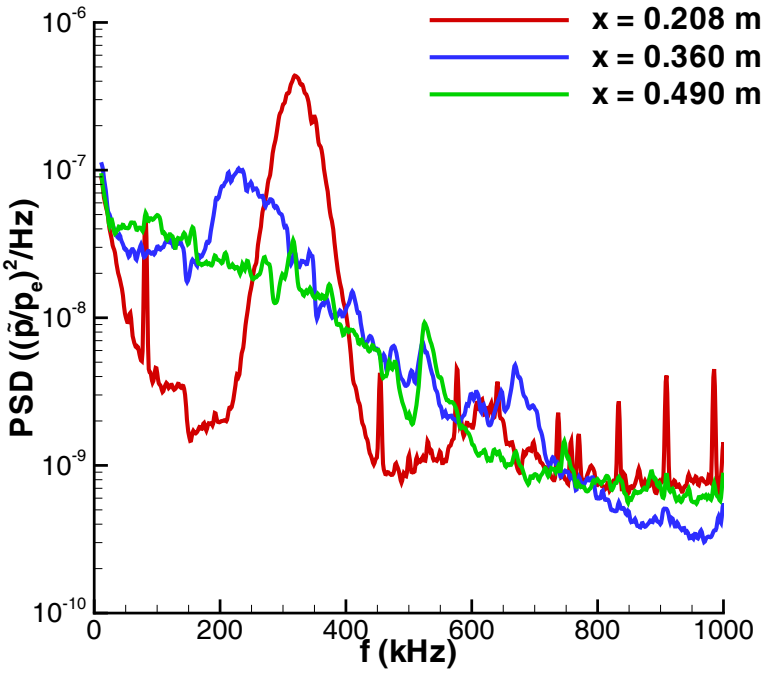


Figure 4.61. PCB132 power spectral density during transition (HWT-8, $Re/m = 9.5 \times 10^6$)

Figure 4.62 shows PCB132 spectra at x = 0.360 m for increasing $Re/m$. Similar growth and breakdown to turbulence as in HWT-5 and the BAM6QT are seen. The frequency of the second-mode waves does not increase with $Re/m$. This is probably because the wall temperature ratio does not remain constant between all cases; to reach the lower $Re/m$ conditions in HWT-8, higher temperature are needed. Before breakdown, the normalized power density of the most amplified frequency is $1.13 \times 10^{-6}/Hz$, and the RMS amplitude of a 4.88 kHz band centered around the most amplified frequency is 7.3%. The RMS amplitude of the amplified second-mode wave frequencies is approximately 24%. These values are higher than in both HWT-5 and the BAM6QT. A sample time trace of the large waves in HWT-8 before breakdown is shown in Figure 4.52. The large waves also show up in Kulite spectra. Figure 4.63 shows second-mode waves measured by an XCQ-062-15A B-screen. The broad peak near 180 kHz is attributed to the second-mode instability whereas the narrow peak at 340 kHz is due to sensor resonance. The amplitude of the waves cannot be used because the sensor dynamic response rolls off above 10 kHz. However, the Kulites are an independent verification of the presence of large second-mode waves.

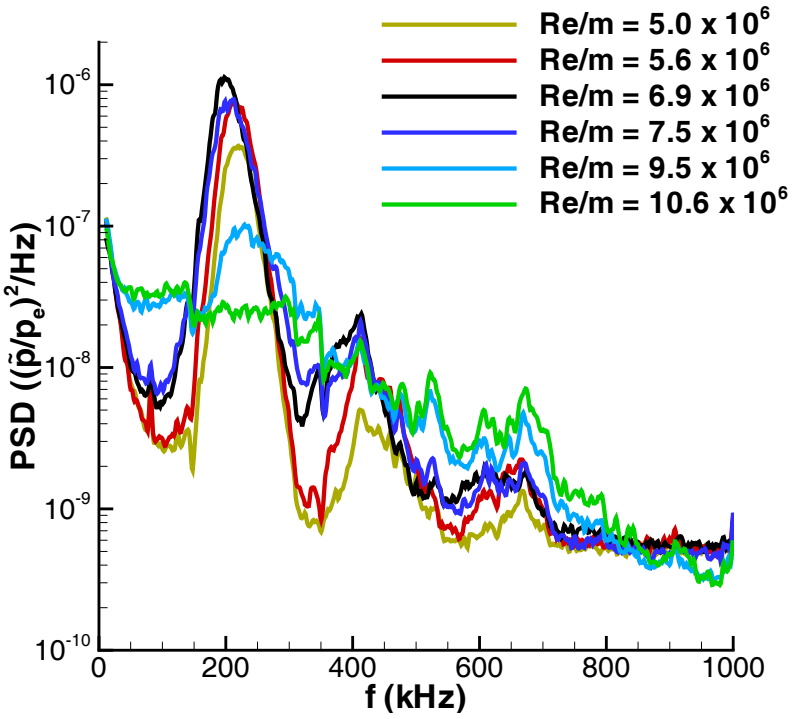


Figure 4.62. Second-mode wave growth and breakdown (HWT-8, x = 0.360 m)

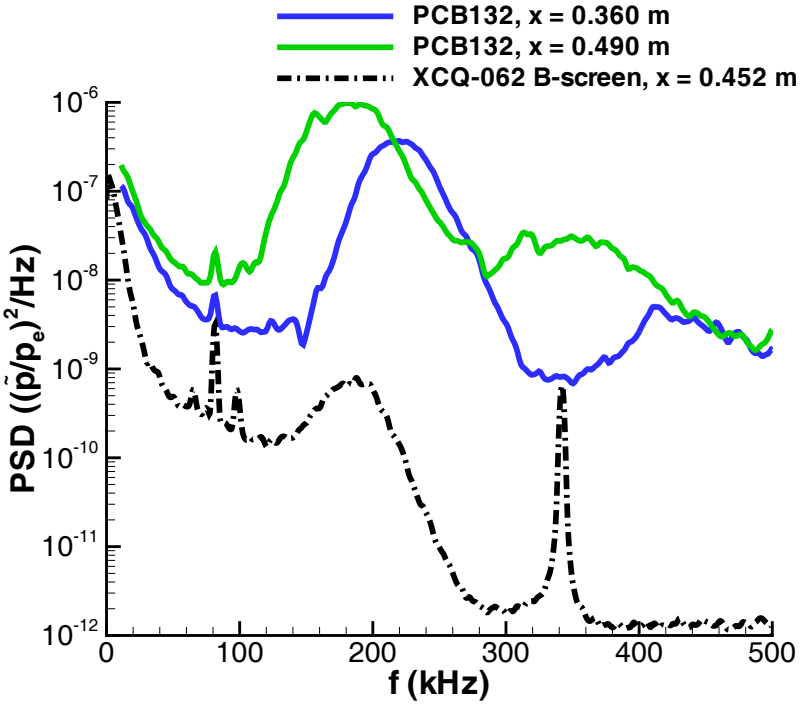


Figure 4.63. Second-mode waves in Kulite spectrum (HWT-8, $Re/m = 5.0 \times 10^6$)

## 4.4 Measurement Uncertainty

There are many possible sources of measurement error including flow nonuniformity and model imperfection effects. Both can affect the pressure fluctuations as well as transition symmetry. Other possible sources include sensor and insert mounting, sensor bias error, spatial resolution, sensor resonance and frequency response, and electrical noise.

Sensor and insert mounting was done carefully to make the sensors and inserts level with the cone surface. Small roughness can trigger early transition on a cone, especially with the thin boundary layers found in hypersonic flow. Sensor inserts were shimmed flush with the surface of the cone. Inserts protruded by a maximum of 20 microns, as measured by a profilometer. Sensors were typically recessed 20–40 microns. The effect of this roughness still needs to be investigated. Also, flat sensors mounted on a cone are never truly flush. If the resulting roughness is too large, this may affect the results [84]. Tests with the sensors and inserts intentionally protruding or recessed by different amounts are needed to define the acceptable tolerance.

Electrical noise was investigated as a possible source of measurement error. Data traces were taken without flow in all tunnels. For all HWT runs, these baseline noise levels were over an order of magnitude lower than the pressure fluctuations measured during a run. The HWT also uses a very high-voltage heater which can be a significant contribution to electrical noise. The RMS pressure fluctuation level during a run was compared before and after the heater was turned on. There was no significant difference in the RMS level. This suggests that the data-acquisition system is well-isolated from the electrical noise generated by the heater. In the BAM6QT, electrical noise was picked up near 200 Hz. Kulite spectra had to be high-pass filtered at 250 Hz. To see the effect this had on the fluctuation levels, this same filtering was done on HWT-5 data. The reduction in unnormalized RMS pressure was typically near 1% of the fluctuations, with a maximum reduction of 3%.

To investigate flow axisymmetry and repeatability, runs were repeated in HWT-5 and 8 by pitching the model up and down by 0.1 degrees and also rolling the cone. Also, because no sharp nosetip is truly sharp, repeat runs with both nosetips were conducted. Figures 4.64 through 4.66 show typical scatter in the Mic-062 A-screen RMS pressure measurements in HWT-5 with these variations. Similar results for small angle of attack and different roll angles were seen in HWT-8. The differences in laminar fluctuation measurements are small; the typical percent difference between runs was 2–3%, with a maximum of approximately 6%. Transition measurements are more sensitive to tiny changes; a small motion of transition location relative to the sensors can appear as a large change in the measured fluctuations. Percent differences in transitional pressure fluctuations were often as low as 2–3% but typically around 8–10%. However, some differences as high as 20% were observed. When comparing separate runs, there is also a scatter in the freestream conditions which can contribute to the observed scatter in results.

Figure 4.67 shows the Mic-062 A-screen power spectral density variation at x = 0.208 m for the runs shown in Figure 4.65. The change in the spectra is small for this case; the sensors are all seeing laminar flow. Figure 4.68 shows the power spectral densities for a case where transition is moving relative to the sensors by simply rolling the model. The spectra show a large change in the results, and the resulting difference in RMS pressure is approximately 20%.

Flow axisymmetry and repeatability can also affect the PCB132 results. Figure 4.69 through 4.71 show typical PCB132 power spectral densities from HWT-5 and HWT-8. Second-mode wave growth does show some sensitivity to small changes in angle of attack, roll angle, and nosetip geometry. There is also a scatter in the freestream conditions between similar runs which probably contributes to this sensitivity.

Although these runs help define the precision of the data, sensor bias errors cannot be traced in this manner. Dynamic calibrations of the sensors will help address the accuracy of the measurements. A complete uncertainty investigation will see future attention.

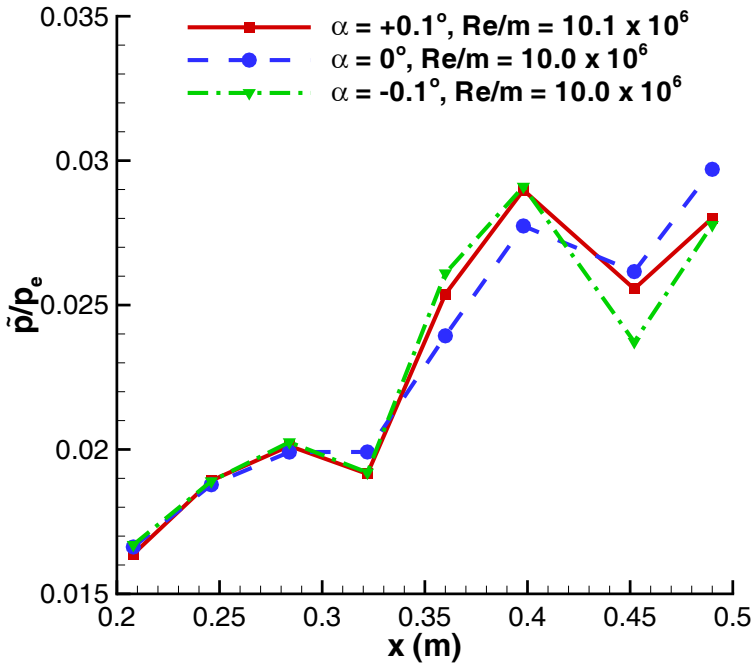


Figure 4.64. Pressure fluctuations along sharp cone for repeat runs at varying angle of attack (HWT-5)

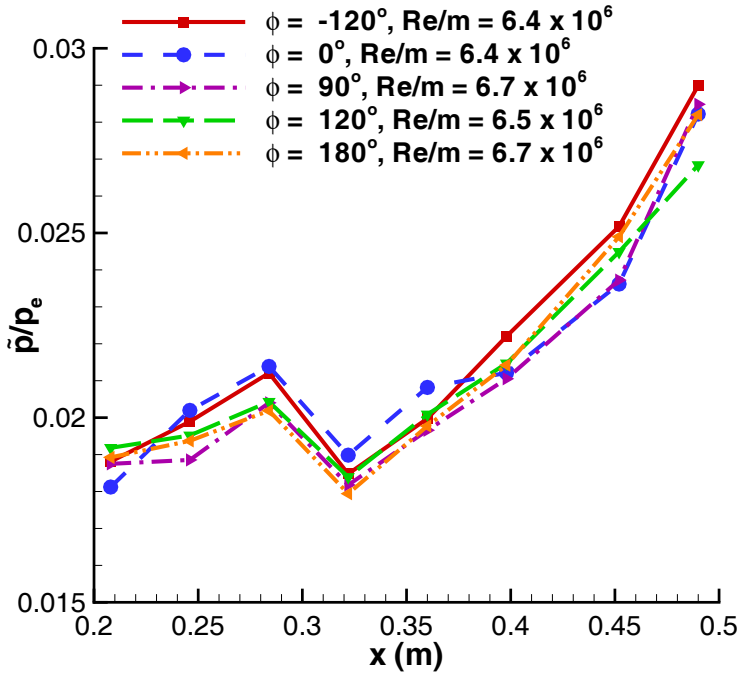


Figure 4.65. Pressure fluctuations along sharp cone for repeat runs at varying roll angles (HWT-5)

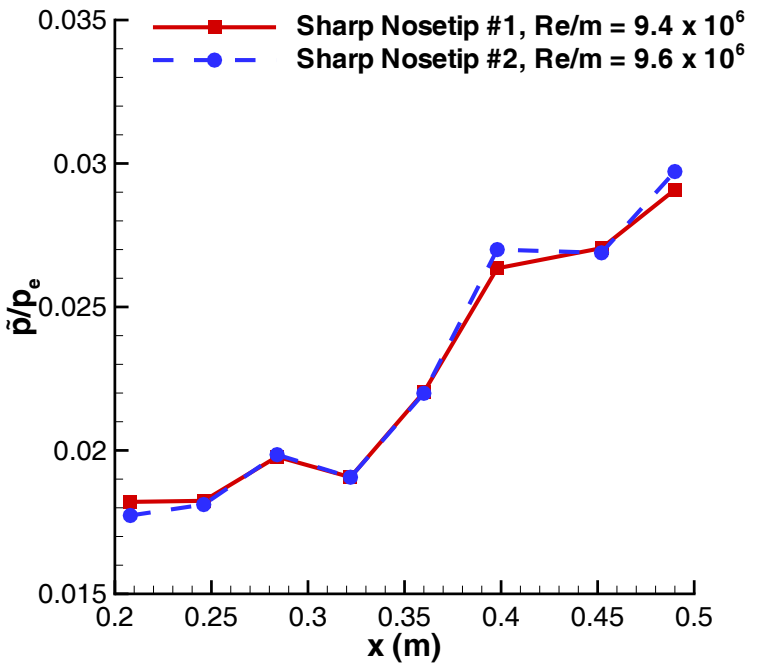


Figure 4.66. Pressure fluctuations along sharp cone for repeat runs with different sharp nosetips (HWT-5)

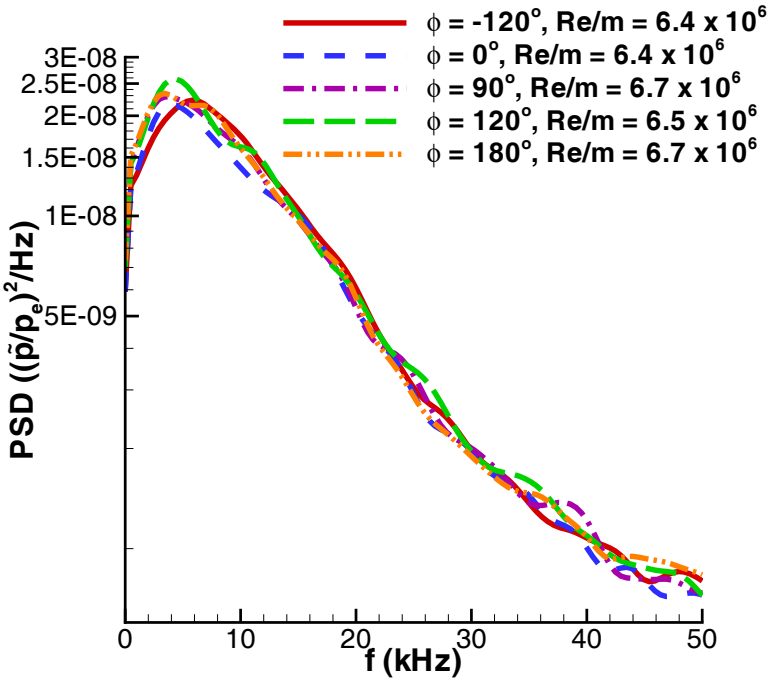


Figure 4.67. Mic-062 A-screen power spectral densities for repeat runs at varying roll angles (HWT-5, x = 0.208 m)

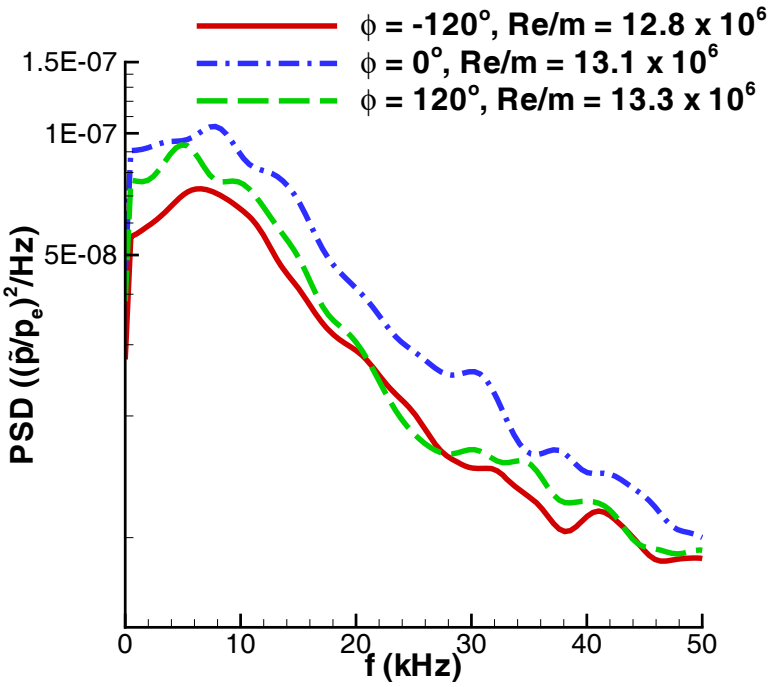


Figure 4.68. Mic-062 A-screen power spectral densities for repeat runs at varying roll angles (HWT-8, x = 0.246 m)

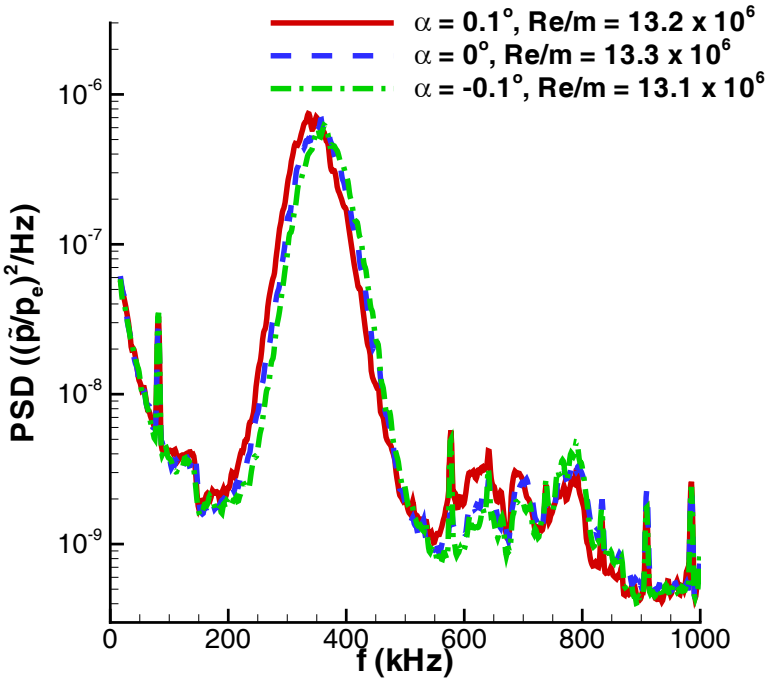


Figure 4.69. PCB132 power spectral densities for repeat runs at varying angle of attack (HWT-8, x = 0.208 m)

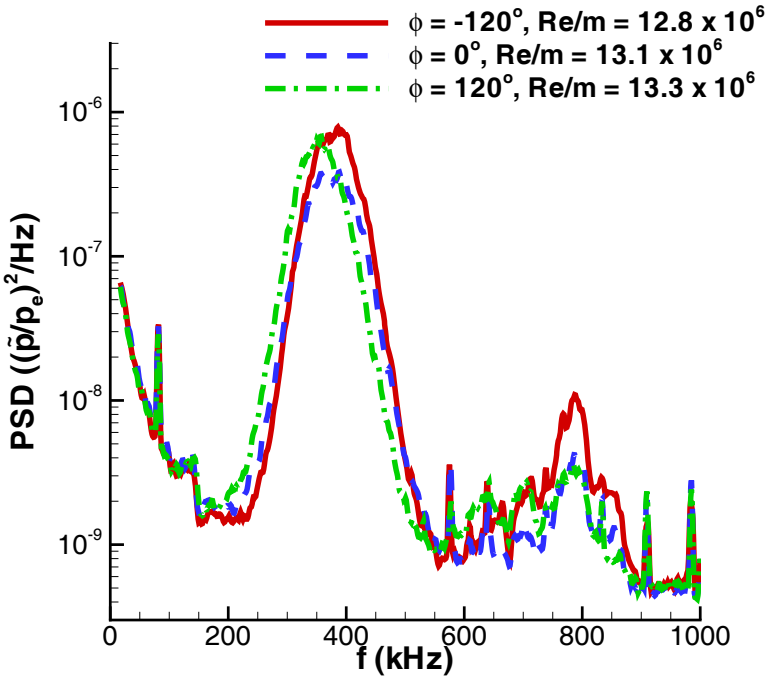


Figure 4.70. PCB132 power spectral densities for repeat runs at varying roll angles (HWT-8, x = 0.208 m)

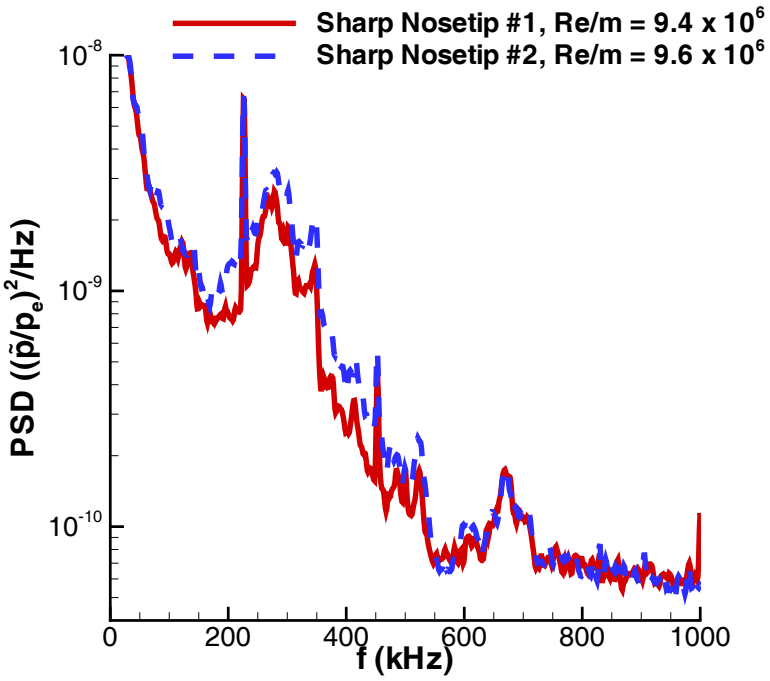


Figure 4.71. PCB132 power spectral densities for repeat runs with varying sharp nosetip (HWT-5, x = 0.360 m)

# 5. CONCLUDING REMARKS

## 5.1 Conclusions

Measurements of pressure fluctuations on a 7° sharp cone at zero angle of attack were conducted in Sandia's Hypersonic Wind Tunnel at Mach 5 and 8. Tests were also conducted in Purdue University's Boeing/AFOSR Mach-6 Quiet Tunnel under noisy and quiet flow. Experiments focused on a characterization of pressure-transducer responses, obtaining new pressure-fluctuation data, attempts to identify turbulent spots in pressure traces, and measurements of second-mode waves.

Comparisons between Mic-062 A-screens, XCQ-062 B-screens and PCB132's were conducted under a laminar boundary layer. The Mic-062 A-screen sensors were found to work best for dynamic measurements below 50 kHz. B-screen sensors rolled off at lower frequencies than the A-screens. PCB132 sensors offered an independent measurement; they could be used for comparison to Kulites between 11 and 50 kHz as well as for higher frequency measurements up to 1 MHz. Good agreement between the Mic-062 A-screens and PCB132's in the overlap region between 11 and 50 kHz was found under laminar boundary layers. Responses under transitional and turbulent boundary layers were higher in the PCB132's.

Pressure fluctuations were measured along the cone at different freestream Reynolds numbers. Mic-062 A-screens showed a peak in the pressure fluctuations during transition. This peak showed fair agreement with transition-location predictions using Pate's correlation. To investigate tunnel-noise effects, freestream noise measurements were made in HWT-5 and 8. Noise levels were reflected in the laminar pressure fluctuations. Fluctuations following transition also approached the tunnel noise level. Quiet-flow measurements confirmed that the laminar pressure fluctuations are primar-

ily due to tunnel noise and that tunnel noise causes early model transition. Transition did not occur on the model under quiet flow.

Even though measurements of transitional pressure fluctuations were made under many different freestream conditions, turbulent spots could not be clearly identified in the Mic-062 A-screen pressure traces. However, hot-film sensors did show possible turbulent spots as in Wadhams [76]. Peaks in the kurtosis and skewness during transition also indicated increased impulsiveness in the flow, and the probability density functions showed higher-amplitude fluctuations. Further analysis should help better characterize the transitional pressure fluctuations, but new measurements and improved instrumentation are needed to clearly identify turbulent spots.

Second-mode waves were apparent in all tunnels. The initial growth of the second mode waves was seen under a laminar boundary layer. The sensors showed wave breakdown near the peak transitional pressure fluctuations measured by Kulites. The maximum observed RMS amplitude of the second-mode waves prior to breakdown increased with $M_e$. After breakdown, the PCB132's showed broadband spectra components up to very high frequency. Small second-mode waves were measured under quiet flow in the BAM6QT, but did not break down at the maximum quiet Reynolds number.

Transitional measurements could only be made under noisy flow because the model boundary layer remained laminar under quiet flow in the BAM6QT. However, both noisy and quiet-flow measurements showed the growth of the second-mode instability. Because of the similar growth of instabilities, further study of noisy-flow measurements should help understand the physics behind transition as well as the generation of boundary-layer pressure fluctuations.

## 5.2 Recommendations for Future Work

Future sensor work will focus on an increased understanding of the dynamic response of the pressure sensors as well as a further characterization of the measurement uncertainty. Dynamic calibrations of all sensors should be performed. Shock-tube calibrations, ultrasonic speaker calibrations, and laser-perturber calibrations are all planned. Dynamics calibrations may also help extend the frequency response of the current instrumentation to higher frequencies. PCB105 sensors also need to be investigated further to understand the cause of the high sensor noise. Insulated mounts for both the PCB105 and PCB132 sensors need to be tested for noise reduction. Better grounding of the data acquisition system or greater amplification of the sensor signals may also improve results. Sensor error also needs to be explored in greater depth. Repeatability of the sensors and tunnel conditions was characterized; however, effects of sensor and insert mounting still need to be tested.

Although a significant amount of pressure-fluctuation data was obtained in these tests, turbulent spots have still not been clearly identified in the pressure traces. Tests can be repeated in HWT-5 and 8 with a schlieren system to aid in the identification of turbulent spots. A glow perturber can also be used to generate controlled spots on the model. Initiating the spots well upstream on the model will allow the spots to grow over a longer distance, hopefully allowing the current instrumentation to resolve the spot passage. These tests can also be done under quiet-flow conditions to reduce the effect of freestream noise on the measurements. Also, because the turbulent spots generated on the wall of the BAM6QT under quiet flow are large, further study of the nozzle wall spots can be conducted with the current instrumentation. This will hopefully increase understanding of turbulent spots and allow better characterization of transitional pressure fluctuations.

# LIST OF REFERENCES

# LIST OF REFERENCES


[1] J. C. Houbolt. On the estimation of pressure fluctuations in boundary layers and wakes. General Electric Technical Information Series 66SD296, April 1966.

[2] M. V. Lowson. Prediction of boundary layer pressure fluctuations. Technical Report AFFDL-TR-67-167, Air Force Flight Dynamics Laboratory, April 1968.

[3] A. Martellucci, L. Chaump, D. Rogers, and D. Smith. Experimental determination of the aeroacoustic environment about a slender cone. *AIAA Journal*, 11(5):635–642, 1973.

[4] L. E. Chaump, A. Martellucci, and A. Monfort. Aeroacoustic loads associated with high beta re-entry vehicles. Technical Report AFFDL-TR-72-138, Air Force Flight Dynamics Laboratory, May 1973. Volume I.

[5] K. R. Raman. Surface pressure fluctuations in hypersonic turbulent boundary layers. AIAA Paper 73-997, October 1973.

[6] A. L. Laganelli, A. Martellucci, and L. Shaw. Prediction of surface pressure fluctuations in hypersonic turbulent boundary layers. AIAA Paper 76-409, July 1976.

[7] A. L. Laganelli and J. R. Howe. Prediction of pressure fluctuations associated with maneuvering reentry vehicles. Technical Report AFFDL-TR-77-59, Air Force Flight Dynamics Laboratory, July 1977.

[8] A. L. Laganelli, A. Martellucci, and L. Shaw. Prediction of turbulent wall pressure fluctuations in attached boundary layer flow. AIAA Paper 81-1227, June 1981.

[9] F. K. Owen. Transition experiments on a flat plate at subsonic and supersonic speeds. AIAA Paper 69-9, January 1969.

[10] F. K. Owen. Transition experiments on a flat plate at subsonic and supersonic speeds. *AIAA Journal*, 8:518–523, 1970.

[11] F. K. Owen and C. C. Horstman. Hypersonic transitional boundary layers. *AIAA Journal*, 10(6):769–775, 1972.

[12] F. K. Owen, C. C. Horstman, P. C. Stainback, and R. D. Wagner. Comparison of wind tunnel transition and freestream disturbance measurements. *AIAA Journal*, 13(3):266–269, 1975.

[13] A. Joksch and L. Kleiser. Growth of turbulent spots in high-speed boundary layers on a flat plate. *International Journal of Heat and Fluid Flow*, 29:1543–1557, 2008.

[14] C. S. James. Observations of turbulent-burst geometry and growth in supersonic flow. Technical Note NACA-TN-4235, NACA, April 1958.

[15] G. B. Schubauer and P. S. Klebanoff. Contributions on the mechanics of boundary-layer transition. Technical Report NACA-TR-1289, NACA, February 1955.

[16] B. Cantwell, D. Coles, and P. Dimotakis. Structure and entrainment in the plane of symmetry of a turbulent spot. *Journal of Fluid Mechanics*, 87(4):641–672, 1977.

[17] O. Savas and D. Coles. Coherence measurements in synthetic turbulent boundary layers. *Journal of Fluid Mechanics*, 160:421–446, May 1985.

[18] R. Narasimha. The laminar-turbulent transition zone in the boundary layer. *Progress in Aerospace Sciences*, 22:29–80, January 1985.

[19] L. Krishnan and N. D. Sandham. On the merging of turbulent spots in a supersonic boundary layer flow. *International Journal of Heat and Fluid Flow*, 27:542–550, March 2006.

[20] L. Krishnan and N. D. Sandham. Turbulent spots in a compressible boundary-layer flow. In R. Govindarajan, editor, *Sixth IUTAM Symposium on Laminar-Turbulent Transition*, pages 329–334. Springer, 2006.

[21] L. Krishnan and N. D. Sandham. Effect of Mach number on the structure of turbulent spots. *Journal of Fluid Mechanics*, 566:225–234, 2006.

[22] T. V. Jones and J. E. Lagraff. Turbulent spot growth rates and generation in a compressible boundary layer. Technical report, United States Air Force Office of Scientific Research, October 1995. Grant Number F49620-92-J-0079.

[23] N. Vinod and R. Govindarajan. Pattern of breakdown of laminar flow into turbulent spots. *Physical Review Letters*, 93(11), 2004.

[24] G. C. Lauchle. Radiated noise due to boundary-layer transition. Technical Memorandum ARL-TM-79-135, Applied Research Laboratory, July 1979.

[25] G. C. Lauchle. On the radiated noise due to boundary-layer transition. *Journal of the Acoustical Society of America*, 67(1):158–168, 1980.

[26] S. P. Schneider. The development of hypersonic quiet tunnels. *Journal of Spacecraft and Rockets*, 45(4):641–664, 2008.

[27] T. Juliano, S. Schneider, S. Aradrag, and D. Knight. Quiet-flow Ludwieg tube for hypersonic transition research. *AIAA Journal*, 46(7):1757–1763, 2008.

[28] W. W. Willmarth. Pressure fluctuations beneath turbulent boundary layers. *Annual Review of Fluid Mechanics*, 7:13–38, 1975.

[29] D. A. Hilton, E. M. Bracalente, and H. H. Hubbard. In-flight aerodynamic noise measurements on a Scout launch vehicle. Technical Note NASA-TN-D-1818, NASA, July 1963.

[30] G. M. Lilley. Wall pressure fluctuations under turbulent boundary layers at subsonic and supersonic speeds. Technical Report 454, Advisory Group for Aeronautical Research and Development, North Atlantic Treaty Organization, April 1963.

[31] G. M. Lilley. A review of pressure fluctuations in turbulent boundary layers at subsonic and supersonic speeds. *Archiwum Mechaniki Stosowanej*, 16(2):301–330, 1964.

[32] A. L. Kistler and W. S. Chen. The fluctuating pressure field in a supersonic turbulent boundary layer. *Journal of Fluid Mechanics*, 16(1):41–64, 1963.

[33] S. R. Pate and M. D. Brown. Acoustic measurements in supersonic transitional boundary layers. Technical Report AEDC-TR-69-182, Arnold Engineering Development Center, October 1969.

[34] R. I. Johnson, M. N. Macourek, and H. Saunders. Boundary layer acoustic measurements in transitional and turbulent flow at $M_\infty = 4.0$. AIAA Paper 69-344, April 1969.

[35] H. H. Heller. Acoustic technique for detection of flow transition on hypersonic re-entry vehicles. *AIAA Journal*, 7(2):2227–2232, 1969.

[36] J. M. Cassanto and D. A. Rogers. An experiment to determine nose tip transition with fluctuating pressure measurements. *AIAA Journal*, 13(10):1257–1258, 1975.

[37] S. R. Pate. Dominance of radiated aerodynamic noise on boundary-layer transition in supersonic/hypersonic wind tunnels. Technical Report AEDC-TR-77-107, Arnold Engineering Development Center, March 1978.

[38] A. L. Laganelli. The effects of mass transfer and angle of attack on hypersonic turbulent boundary layer characteristics. Technical Report AFFDL-TR-75-35, Air Force Flight Dynamics Laboratory, April 1975.

[39] J. Laufer. Some statistical properties of the pressure field radiated by a turbulent boundary layer. *The Physics of Fluids*, 7(8):1191–1197, 1964.

[40] A. J. Laderman. Review of wind-tunnel freestream pressure fluctuations. *AIAA Journal*, 15(4):605–608, 1977.

[41] I. E. Beckwith and C. G. Miller III. Aerothermodynamics and transition in high-speed wind tunnels at NASA Langley. *Annual Review of Fluid Mechanics*, 22:419–439, 1991.

[42] S. P. Schneider. Effects of high-speed tunnel noise on laminar-turbulent transition. *Journal of Spacecraft and Rockets*, 38(3):323–333, 2001.

[43] S. R. Pate and C. J. Schueler. Radiated aerodynamic noise effects on boundary-layer transition in supersonic and hypersonic wind tunnels. *AIAA Journal*, 7(3):450–457, 1969.

[44] S. R. Pate. Measurements and correlations of transition Reynolds numbers on sharp slender cones at high speeds. *AIAA Journal*, 9(6):1082–1090, 1971.

[45] P. C. Stainback. Hypersonic boundary-layer transition in the presence of wind-tunnel noise. *AIAA Journal*, 9(12):2475–2476, 1971.

[46] S. P. Schneider. Flight data for boundary-layer transition at hypersonic and supersonic speeds. *Journal of Spacecraft and Rockets*, 36(1):8–20, 1999.

[47] I. E. Beckwith. Development of a high Reynolds number quiet tunnel for transition research. *AIAA Journal*, 13(3):300–306, 1975.

[48] J. Laufer. Aerodynamic noise in supersonic wind tunnels. *Journal of the Aerospace Sciences*, 28(9):685–692, 1961.

[49] P. C. Stainback, M. C. Fischer, and R. D. Wagner. Effects of wind-tunnel disturbances on hypersonic boundary-layer transition. AIAA Paper 72-181, January 1972.

[50] P. C. Stainback and R. A. Rainey. Correlation of freestream pressure disturbances in supersonic wind tunnels. *AIAA Journal*, 14(2):286–288, 1976.

[51] M. C. Fischer, D. V. Maddalon, L. M. Weinstein, and R. D. Wagner. Boundary-layer surveys on a nozzle wall at $M = 20$ including hot wire fluctuating measurements. AIAA Paper 70-746, June 1970.

[52] J. Kendall. Wind tunnel experiments relating to supersonic and hypersonic boundary-layer transition. *AIAA Journal*, 13(3):290–299, 1975.

[53] S. R. Pate. Effects of wind-tunnel disturbances on boundary-layer transition with emphasis on radiated noise: A review. AIAA Paper 1980-0431, March 1980.

[54] L. M. Mack. Linear stability theory and the problem of supersonic boundary-layer transition. *AIAA Journal*, 13(3):278–289, 1975.

[55] M. R. Schopper. Interaction of aerodynamic noise with laminar boundary layers in supersonic wind tunnels. Contractor Report NASA-CR-3621, NASA, April 1984.

[56] M. C. Fischer and L. M. Weinstein. Cone transitional boundary-layer structure at $M_e = 14$. *AIAA Journal*, 10(5):699–701, 1972.

[57] K. F. Stetson. Nosetip bluntness effects on cone frustrum boundary layer transition in hypersonic flow. AIAA Paper 83-1763, July 1983.

[58] K. Fujii. Experiment of two dimensional roughness effect on hypersonic boundary-layer transition. *Journal of Spacecraft and Rockets*, 43(4):731–738, 2006.

[59] M. Estorf, R. Radespiel, S. P. Schneider, H. Johnson, and S. Hein. Surface-pressure measurements of second-mode instability in quiet hypersonic flow. AIAA Paper 2008-1153, January 2008.

[60] K. F. Stetson, R. Kimmel, E. R. Thompson, J. C. Donaldson, and L. G. Siler. A comparison of planar and conical boundary layer stability at a Mach number of 8. AIAA Paper 91-1639, June 1991.

[61] K. F. Stetson and R. L. Kimmel. Example of second-mode instability dominance at a Mach number of 5.2. *AIAA Journal*, 30(12):2974–2976, 1992.

[62] R. L. Kimmel, A. Demetriades, and J. Donaldson. Space-time correlation measurements in a hypersonic transitional boundary layer. AIAA Paper 95-2292, June 1995.

[63] S. J. Rufer and S. P. Schneider. Hot-wire measurements of instability waves on a blunt cone at Mach 6. AIAA Paper 2005-5137, June 2005.

[64] S. J. Rufer. *Hot-wire Measurements of Instability Waves on Sharp and Blunt Cones at Mach 6*. PhD thesis, Purdue University School of Aeronautics and Astronautics, December 2005.

[65] S. J. Rufer and S. P. Schneider. Hot-wire measurements of instability waves on cones at Mach 6. AIAA Paper 2006-3054, June 2006.

[66] C. R. Skoch. *Disturbances from Shock/Boundary-Layer Interactions Affecting Upstream Hypersonic Flow*. PhD thesis, Purdue University School of Aeronautics and Astronautics, December 2005.

[67] T. Juliano. Nozzle modifications for high-Reynolds-number quiet flow in the Boeing/AFOSR Mach-6 quiet tunnel. Master's thesis, Purdue University School of Aeronautics and Astronautics, December 2006. Available from DTIC as ADA456772.

[68] F. G. Keyes. A summary of viscosity and heat-conduction data for He, A, $H_2, O_2$, CO, $CO_2, H_2O$, and air. *Transactions of the ASME*, 73:589–596, 1951.

[69] E. O. Swanson. *Boundary Layer Transition on Cones at Angle of Attack in a Mach-6 Quiet Tunnel*. PhD thesis, Purdue University School of Aeronautics and Astronautics, August 2008.

[70] M. Zanchetta. *Kinetic Heating and Transition Studies at Hypersonic Speeds*. PhD thesis, Imperial College of Science, Technology, and Medicine, 1996.

[71] S. P. Schneider and C. R. Skoch. Mean flow and noise measurements in the Purdue Mach-6 quiet-flow Ludwieg tube. AIAA Paper 2001-2778, June 2001.

[72] L. E. Steen. Private communication, July 2009.

[73] P. C. Stainback, R.D. Wagner, F.K. Owen, and C.C. Horstman. Experimental studies of hypersonic boundary-layer transition and effects of wind-tunnel disturbances. Technical Note NASA-TN-D-7453, NASA, March 1974.

[74] D. J. Mee and C. P. Goyne. Turbulent spots in boundary layers in a free-piston shock-tunnel flow. In *Shock Waves*, volume 6, pages 337–343. Springer Verlag, June 1996.

[75] A. Fiala, R. Hillier, S. G. Mallinson, and H. S. Wijesinghe. Heat transfer measurement of turbulent spots in a hypersonic blunt-body boundary layer. *Journal of Fluid Mechanics*, 555:81–111, 2006.

[76] T. P. Wadhams, E. Mundy, M. G. MacLean, and M. S. Holden. Ground test studies of the HIFIRE-1 transition experiment part 1:experimental results. *Journal of Spacecraft and Rockets*, 45(6):1134–1148, 2008.

[77] J. Mathieu and J. Scott. *An Introduction to Turbulent Flow*. Cambridge University Press, 2000.

[78] A. J. Smits and J. Dussuage. *Turbulent Shear Layers in Supersonic Flow*. Birkhauser, second edition, 2005.

[79] M. S. Patil, J. Mathew, and P. K. Rejendrakumar. Bearing signature analysis as a medium for fault detection: A review. *Journal of Tribology*, 130, January 2008.

[80] L. M. Mack. Boundary layer linear stability theory. In *Report 709, Special Course on Stability and Transition of Laminar Flow*, pages 1–81. AGARD, March 1984.

[81] K. M. Casper, S. J. Beresh, J. F. Henfling, R. W. Spillers, B. Pruett, and S. P. Schneider. Hypersonic wind-tunnel measurements of boundary-layer pressure fluctuations. AIAA Paper 2009-4054, June 2009.

[82] C. Alba, K. M. Casper, D. Lewis, H. B. Johnson, S. J. Beresh, D. Berridge, and S. P. Schneider. Comparison of experimentally measured and computed second-mode disturbances in hypersonic boundary-layers. Extended abstract submitted to the 48th Aerospace Sciences Meeting, To appear January 2010.

[83] T. W. Robarge. Laminar boundary-layer instabilities on hypersonic cones: Computations for benchmark experiments. Master's thesis, Purdue University School of Aeronautics and Astronautics, August 2005.

[84] D. Heitmann, C. Kahler, R. Radespiel, T. Rodiger, H. Knauss, and E. Kramer. Disturbance-level and transition measurements in a conical boundary layer at Mach 6. AIAA Paper 2008-3951, June 2008.

# APPENDICES

# A. Run Conditions for Chapter 4 Figures

Run conditions for Chapter 4 figures are given in Tables A.1 through A.5. Keyes's law was used to calculate viscosity [68] because Sutherland's law is not as accurate at the low freestream temperatures in the tunnels (below 111 K). Real gas effects were neglected. Edge pressure ($p_e$), edge dynamic pressure ($q_e$), and edge Mach number ($M_e$) were calculated using the Taylor-Maccoll solution for a sharp cone. The nozzle wall shear stress ($\tau_w$) was computed using the method of Van-Driest-II.

Table A.1 Run conditions for Chapter 4 figures

| Chapter 4 Figure Number | Tunnel | Flow | Entry | Run | $Re/m$ | M | $P_0$ | $T_0$ | $p_e$ | $q_e$ | $\tau_w$ | Nosetip | AoA | Roll |
|---|---|---|---|---|---|---|---|---|---|---|---|---|---|---|
| 1 | HWT-5 | Noisy | Jul-08 | 18 | 6.3 | 4.9 | 455 | 470 | N/A | N/A | N/A | Sharp #1 | 0 | 120 |
| 5 | BAM6QT | Quiet | Sep-08 | 9 | 8.7 | 6.0 | 874 | 424 | N/A | N/A | N/A | N/A | N/A | N/A |
| 6 | BAM6QT | Quiet | Nov-08 | 9 | 9.0 | 6.0 | 907 | 427 | N/A | N/A | N/A | Sharp #1 | 0 | 120 |
| 2, 7–10, 20, 32, 35, 46, 48–49, 56 | HWT-5 | Noisy | May-09 | 67 | 4.6 | 4.9 | 391 | 522 | 1.38 | 20.0 | 0.0103 | Sharp #1 | 0 | 120 |
| 7–10, 20, 32, 35, 48–49, 53, 56 | HWT-5 | Noisy | May-09 | 63 | 5.7 | 4.9 | 432 | 483 | 1.53 | 22.1 | 0.0107 | Sharp #1 | 0 | 120 |
| 7–10, 20, 28, 32, 35, 48–49, 56 | HWT-5 | Noisy | May-09 | 54 | 6.5 | 4.9 | 472 | 467 | 1.67 | 24.1 | 0.0113 | Sharp #1 | 0 | 120 |
| 7–10, 20, 32, 35, 46, 48–49, 56 | HWT-5 | Noisy | May-09 | 64 | 8.4 | 4.9 | 582 | 456 | 2.05 | 29.7 | 0.0133 | Sharp #1 | 0 | 120 |
| 7–10, 20, 32, 35, 39, 42, 48–49, 54 | HWT-5 | Noisy | May-09 | 72 | 9.1 | 4.9 | 607 | 442 | 2.12 | 30.7 | 0.0135 | Sharp #1 | 0 | 120 |
| 7–10, 20, 32, 35, 39, 42, 48–49 | HWT-5 | Noisy | May-09 | 61 | 10.6 | 4.9 | 734 | 454 | 2.56 | 37.1 | 0.0159 | Sharp #1 | 0 | 120 |
| 7–10, 20, 32, 35, 39, 48–49 | HWT-5 | Noisy | May-09 | 59 | 11.6 | 4.9 | 800 | 453 | 2.80 | 40.5 | 0.0171 | Sharp #1 | 0 | 120 |
| 7–10, 20, 23, 32, 35, 39, 42, 47–51 | HWT-5 | Noisy | May-09 | 55 | 12.7 | 4.9 | 857 | 444 | 2.97 | 43.0 | 0.0178 | Sharp #1 | 0 | 120 |
| 7–10, 20, 32, 35, 39, 42, 48–49 | HWT-5 | Noisy | May-09 | 56 | 15.4 | 4.9 | 880 | 397 | 3.04 | 44.1 | 0.0172 | Sharp #1 | 0 | 120 |
| 7–10, 20, 32, 35, 39, 42, 48–49 | HWT-5 | Noisy | May-09 | 68 | 18.8 | 5.0 | 945 | 365 | 3.25 | 47.0 | 0.0174 | Sharp #1 | 0 | 120 |
| 7–10, 20, 32, 35, 39, 42, 48–49, 55 | HWT-5 | Noisy | May-09 | 69 | 24.2 | 5.0 | 1153 | 351 | 3.95 | 57.2 | 0.0200 | Sharp #1 | 0 | 120 |
| 4, 11–14, 21, 33, 36 | BAM6QT | Noisy | Feb-09 | 22 | 1.0 | 5.8 | 97 | 430 | 0.15 | 2.7 | 0.0017 | Sharp #2 | 0 | 120 |
| 3–4, 11–14, 21, 33, 36, 58 | BAM6QT | Noisy | Feb-09 | 21 | 2.9 | 5.8 | 274 | 429 | 0.41 | 7.7 | 0.0039 | Sharp #2 | 0 | 120 |
| 4, 11–14, 21, 33, 36, 40, 42, 58 | BAM6QT | Noisy | Feb-09 | 20 | 5.0 | 5.8 | 472 | 429 | 0.71 | 13.3 | 0.0060 | Sharp #2 | 0 | 120 |
| 11–14, 21, 33, 36, 40, 42, 57–58 | BAM6QT | Noisy | Feb-09 | 18 | 6.4 | 5.8 | 602 | 429 | 0.90 | 17.0 | 0.0072 | Sharp #2 | 0 | 120 |
| 4, 11–14, 21, 33, 36, 40, 42, 58 | BAM6QT | Noisy | Feb-09 | 17 | 8.5 | 5.8 | 795 | 429 | 1.19 | 22.5 | 0.0090 | Sharp #2 | 0 | 120 |
| 4, 11–14, 21, 24, 33, 36, 40, 42, 58 | BAM6QT | Noisy | Feb-09 | 19 | 10.0 | 5.8 | 936 | 429 | 1.41 | 26.5 | 0.0103 | Sharp #2 | 0 | 120 |
| 15–18, 22, 34, 37, 60, 62–63 | HWT-8 | Noisy | May-09 | 86 | 5.0 | 7.8 | 2414 | 759 | 0.75 | 24.5 | 0.0069 | Sharp #1 | 0 | 120 |
| 15–18, 22, 34, 37, 62 | HWT-8 | Noisy | May-09 | 84 | 5.6 | 7.8 | 2397 | 704 | 0.74 | 24.2 | 0.0066 | Sharp #1 | 0 | 120 |
| 15–18, 22, 29, 34, 37, 41–43, 52, 62 | HWT-8 | Noisy | May-09 | 76 | 6.9 | 7.8 | 2368 | 602 | 0.72 | 23.6 | 0.0061 | Sharp #1 | 0 | 120 |
| 15–18, 22, 34, 37, 62 | HWT-8 | Noisy | May-09 | 77 | 7.5 | 7.8 | 2579 | 605 | 0.79 | 25.6 | 0.0065 | Sharp #1 | 0 | 120 |
| 15–18, 22, 25, 34, 37, 41–43, 61–62 | HWT-8 | Noisy | May-09 | 78 | 9.5 | 7.9 | 3296 | 606 | 0.99 | 32.1 | 0.0078 | Sharp #1 | 0 | 120 |

Table A.2 Run conditions for Chapter 4 figures, continued

| Chapter 4 Figure Number | Tunnel | Flow | Entry | Run | $Re/m$ $\times 10^{-6}$ | M | $P_0$ (kPa) | $T_0$ (K) | $p_e$ (kPa) | $q_e$ (kPa) | $\tau_w$ (kPa) | Nosetip | AoA | Roll |
|---|---|---|---|---|---|---|---|---|---|---|---|---|---|---|
| 15–18, 22, 34, 37, 41–43, 62 | HWT-8 | Noisy | May-09 | 79 | 10.6 | 7.9 | 3452 | 577 | 1.02 | 33.3 | 0.0079 | Sharp #1 | 0 | 120 |
| 15–18, 22, 34, 37, 41–42 | HWT-8 | Noisy | May-09 | 81 | 12.6 | 7.9 | 4457 | 608 | 1.30 | 42.3 | 0.0098 | Sharp #1 | 0 | 120 |
| 15–18, 22, 34, 37 | HWT-8 | Noisy | May-09 | 80 | 13.3 | 7.9 | 4523 | 589 | 1.31 | 42.6 | 0.0097 | Sharp #1 | 0 | 120 |
| 15–18, 22, 34, 37, 41–42 | HWT-8 | Noisy | May-09 | 82 | 14.2 | 7.9 | 4864 | 593 | 1.40 | 45.5 | 0.0103 | Sharp #1 | 0 | 120 |
| 15–18, 22, 34, 37, 41–42 | HWT-8 | Noisy | May-09 | 83 | 16.0 | 7.9 | 5177 | 568 | 1.46 | 47.6 | 0.0105 | Sharp #1 | 0 | 120 |
| 19 | HWT-5 | Noisy | Jul-08 | 115 | 13.1 | 5.0 | 878 | 439 | 2.94 | 42.6 | 0.0176 | Sharp #1 | 0 | 120 |
| 19 | HWT-5 | Noisy | Jul-08 | 79 | 13.2 | 5.0 | 869 | 433 | 2.91 | 42.1 | 0.0174 | 0.5 mm | 0 | 120 |
| 19 | HWT-5 | Noisy | Jul-08 | 77 | 13.2 | 5.0 | 868 | 432 | 2.91 | 42.0 | 0.0173 | 1.5 mm | 0 | 120 |
| 26, 30, 32, 35 | HWT-5 | Noisy | May-09 | 11 | 6.3 | 4.9 | 468 | 474 | 1.65 | N/A | 0.0113 | N/A | 0 | N/A |
| 26, 30, 32, 35 | HWT-5 | Noisy | May-09 | 3 | 6.5 | 4.9 | 471 | 468 | 1.66 | N/A | 0.0113 | N/A | 1 | N/A |
| 26, 30, 32, 35 | HWT-5 | Noisy | May-09 | 4 | 6.5 | 4.9 | 472 | 468 | 1.66 | N/A | 0.0113 | N/A | -1 | N/A |
| 26, 28, 30, 32, 35 | HWT-5 | Noisy | May-09 | 2 | 6.6 | 4.9 | 474 | 467 | 1.67 | N/A | 0.0113 | N/A | 0 | N/A |
| 26, 30, 32, 35 | HWT-5 | Noisy | May-09 | 1 | 6.6 | 4.9 | 472 | 465 | 1.66 | N/A | 0.0113 | N/A | 0 | N/A |
| 26, 30, 32, 35 | HWT-5 | Noisy | May-09 | 6 | 10.2 | 4.9 | 669 | 438 | 2.33 | N/A | 0.0145 | N/A | 0 | N/A |
| 26, 30, 32, 35 | HWT-5 | Noisy | May-09 | 7 | 13.2 | 5.0 | 875 | 439 | 3.01 | N/A | 0.0179 | N/A | 0 | N/A |
| 26, 30, 32, 35 | HWT-5 | Noisy | May-09 | 8 | 15.9 | 5.0 | 898 | 393 | 3.09 | N/A | 0.0173 | N/A | 0 | N/A |
| 26, 30, 32, 35 | HWT-5 | Noisy | May-09 | 9 | 18.9 | 5.0 | 1026 | 383 | 3.53 | N/A | 0.0191 | N/A | 0 | N/A |
| 26, 30, 32, 35 | HWT-5 | Noisy | May-09 | 5 | 23.9 | 5.0 | 1148 | 354 | 3.95 | N/A | 0.0201 | N/A | 0 | N/A |
| 26, 30, 32, 35 | HWT-5 | Noisy | May-09 | 10 | 24.0 | 5.0 | 1161 | 354 | 3.95 | N/A | 0.0201 | N/A | 0 | N/A |
| 27, 30, 34, 37 | HWT-8 | Noisy | May-09 | 12 | 6.6 | 7.8 | 2296 | 612 | 0.71 | N/A | 0.0060 | N/A | 0 | N/A |
| 27, 30, 34, 37 | HWT-8 | Noisy | May-09 | 19 | 6.7 | 7.8 | 2561 | 649 | 0.79 | N/A | 0.0067 | N/A | 0 | N/A |
| 27, 30, 34, 37 | HWT-8 | Noisy | May-09 | 15 | 6.8 | 7.8 | 2316 | 601 | 0.71 | N/A | 0.0060 | N/A | 1 | N/A |
| 27, 29–30, 34, 37 | HWT-8 | Noisy | May-09 | 14 | 7.0 | 7.8 | 2347 | 597 | 0.72 | N/A | 0.0060 | N/A | 0 | N/A |
| 27, 30, 34, 37 | HWT-8 | Noisy | May-09 | 17 | 7.0 | 7.8 | 2357 | 596 | 0.72 | N/A | 0.0060 | N/A | -1 | N/A |

Table A.3 Run conditions for Chapter 4 figures, continued

| Chapter 4 Figure Number | Tunnel | Flow | Entry | Run | $Re/m$ $\times 10^{-6}$ | M | $P_0$ (kPa) | $T_0$ (K) | $p_e$ (kPa) | $q_e$ (kPa) | $\tau_w$ (kPa) | Nosetip | AoA | Roll |
|---|---|---|---|---|---|---|---|---|---|---|---|---|---|---|
| 27, 30, 34, 37 | HWT-8 | Noisy | May-09 | 13 | 7.1 | 7.8 | 2362 | 590 | 0.72 | N/A | 0.0060 | N/A | 0 | N/A |
| 27, 30, 34, 37 | HWT-8 | Noisy | May-09 | 26 | 7.2 | 7.8 | 2400 | 593 | 0.73 | N/A | 0.0061 | N/A | 0 | N/A |
| 27, 30, 34, 37 | HWT-8 | Noisy | May-09 | 16 | 7.8 | 7.9 | 2475 | 570 | 0.75 | N/A | 0.0061 | N/A | -1 | N/A |
| 27, 30, 34, 37 | HWT-8 | Noisy | May-09 | 25 | 8.0 | 7.9 | 2498 | 568 | 0.76 | N/A | 0.0062 | N/A | 0 | N/A |
| 27, 30, 34, 37 | HWT-8 | Noisy | May-09 | 20 | 8.1 | 7.9 | 2754 | 598 | 0.83 | N/A | 0.0068 | N/A | 0 | N/A |
| 27, 30, 34, 37 | HWT-8 | Noisy | May-09 | 21 | 9.6 | 7.9 | 3303 | 600 | 0.99 | N/A | 0.0078 | N/A | 0 | N/A |
| 27, 30, 34, 37 | HWT-8 | Noisy | May-09 | 28 | 11.4 | 7.9 | 4104 | 618 | 1.21 | N/A | 0.0093 | N/A | 0 | N/A |
| 27, 30, 34, 37 | HWT-8 | Noisy | May-09 | 22 | 13.2 | 7.9 | 4529 | 595 | 1.31 | N/A | 0.0098 | N/A | 0 | N/A |
| 27, 30, 34, 37 | HWT-8 | Noisy | May-09 | 27 | 13.2 | 7.9 | 4374 | 579 | 1.27 | N/A | 0.0094 | N/A | 0 | N/A |
| 27, 30, 34, 37 | HWT-8 | Noisy | May-09 | 24 | 14.6 | 7.9 | 4895 | 584 | 1.40 | N/A | 0.0103 | N/A | 0 | N/A |
| 27, 30, 34, 37 | HWT-8 | Noisy | May-09 | 29 | 14.8 | 7.9 | 4961 | 583 | 1.42 | N/A | 0.0103 | N/A | 0 | N/A |
| 27, 30, 34, 37 | HWT-8 | Noisy | May-09 | 23 | 15.0 | 7.9 | 4732 | 558 | 1.35 | N/A | 0.0097 | N/A | 0 | N/A |
| 27, 30, 34, 37 | HWT-8 | Noisy | May-09 | 18 | 15.6 | 7.9 | 5109 | 573 | 1.45 | N/A | 0.0105 | N/A | 0 | N/A |
| 27, 30, 34, 37 | HWT-8 | Noisy | May-09 | 30 | 16.4 | 7.9 | 5198 | 561 | 1.46 | N/A | 0.0104 | N/A | 0 | N/A |
| 30, 33, 36 | BAM6QT | Noisy | Aug-05 | 2 | 2.091 | 5.8 | 195 | 428 | 0.29 | N/A | 0.0028 | N/A | 0 | N/A |
| 30, 33, 36 | BAM6QT | Noisy | Aug-05 | 2 | 1.718 | 5.8 | 138 | 387 | 0.21 | N/A | 0.0021 | N/A | 0 | N/A |
| 30, 33, 36 | BAM6QT | Noisy | Jan-06 | 15 | 5.721 | 5.8 | 534 | 427 | 0.80 | N/A | 0.0063 | N/A | 0 | N/A |
| 30, 33, 36 | BAM6QT | Noisy | Jan-06 | 15 | 4.698 | 5.8 | 378 | 387 | 0.57 | N/A | 0.0046 | N/A | 0 | N/A |
| 30, 33, 36 | BAM6QT | Noisy | Jan-06 | 8 | 7.087 | 5.8 | 661 | 427 | 0.99 | N/A | 0.0075 | N/A | 0 | N/A |
| 30, 33, 36 | BAM6QT | Noisy | Mar-06 | 1 | 3.215 | 5.8 | 300 | 428 | 0.45 | N/A | 0.0040 | N/A | 0 | N/A |
| 30, 33, 36 | BAM6QT | Noisy | Mar-06 | 1 | 2.839 | 5.8 | 241 | 402 | 0.36 | N/A | 0.0033 | N/A | 0 | N/A |
| 30, 31, 33, 36 | BAM6QT | Noisy | Jun-06 | 2 | 7.08 | 5.8 | 661 | 428 | 0.99 | N/A | 0.0075 | N/A | 0 | N/A |
| 30, 31, 33, 36 | BAM6QT | Noisy | Jun-06 | 3 | 7.13 | 5.8 | 670 | 429 | 1.01 | N/A | 0.0076 | N/A | 0 | N/A |
| 30, 31, 33, 36 | BAM6QT | Noisy | Jun-06 | 4 | 7.09 | 5.8 | 662 | 428 | 0.99 | N/A | 0.0075 | N/A | 0 | N/A |

Table A.4 Run conditions for Chapter 4 figures, continued

| Chapter 4 Figure Number | Tunnel | Flow | Entry | Run | $Re/m$ $\times 10^{-6}$ | M | $P_0$ (kPa) | $T_0$ (K) | $p_e$ (kPa) | $q_e$ (kPa) | $\tau_w$ (kPa) | Nosetip | AoA | Roll |
|---|---|---|---|---|---|---|---|---|---|---|---|---|---|---|
| 30, 31, 33, 36 | BAM6QT | Noisy | Jun-06 | 5 | 7.1 | 5.8 | 667 | 429 | 1.00 | N/A | 0.0076 | N/A | 0 | N/A |
| 30, 33, 36 | BAM6QT | Noisy | Aug-06 | 9 | 9.1 | 5.8 | 852 | 427 | 1.28 | N/A | 0.0092 | N/A | 0 | N/A |
| 30, 33, 36 | BAM6QT | Noisy | Sep-06 | 2 | 11.3 | 5.8 | 1056 | 427 | 1.59 | N/A | 0.0109 | N/A | 0 | N/A |
| 30 | BAM6QT | Noisy | Jun-09 | 2 | 6.7 | 5.8 | 606 | 421 | N/A | N/A | N/A | N/A | 0 | N/A |
| 30 | BAM6QT | Noisy | Jun-09 | 18 | 6.6 | 5.8 | 607 | 423 | N/A | N/A | N/A | N/A | 0 | N/A |
| 30 | BAM6QT | Noisy | Jun-09 | 14 | 6.5 | 5.8 | 605 | 424 | N/A | N/A | N/A | N/A | 0 | N/A |
| 30 | BAM6QT | Noisy | Jun-09 | 5 | 12.6 | 5.8 | 1160 | 424 | N/A | N/A | N/A | N/A | 0 | N/A |
| 30 | BAM6QT | Noisy | Jun-09 | 19 | 12.6 | 5.8 | 1148 | 422 | N/A | N/A | N/A | N/A | 0 | N/A |
| 30 | BAM6QT | Noisy | Jun-09 | 26 | 14.1 | 5.8 | 1329 | 431 | N/A | N/A | N/A | N/A | 0 | N/A |
| 30 | BAM6QT | Noisy | Jun-09 | 27 | 14.2 | 5.8 | 1337 | 430 | N/A | N/A | N/A | N/A | 0 | N/A |
| 30 | BAM6QT | Noisy | Jun-09 | 28 | 13.9 | 5.8 | 1290 | 426 | N/A | N/A | N/A | N/A | 0 | N/A |
| 44–45 | BAM6QT | Noisy | Feb-09 | 19 | 9.3 | 5.8 | 832 | 414 | 1.25 | 23.5 | 0.0092 | Sharp #2 | 0 | 120 |
| 44–45 | BAM6QT | Quiet | Feb-09 | 26 | 9.1 | 6.0 | 923 | 428 | 1.16 | 23.2 | 0.0088 | Sharp #2 | 0 | 120 |
| 57 | BAM6QT | Noisy | Oct-08 | 3 | 6.5 | 5.8 | 608 | 429 | 0.91 | 17.2 | 0.0071 | Sharp #2 | 0 | 120 |
| 59 | BAM6QT | Noisy | Oct-08 | 5 | 9.1 | 5.8 | 814 | 414 | 1.22 | 23.0 | 0.0088 | Sharp #2 | 0 | 120 |
| 59 | BAM6QT | Noisy | Dec-08 | 8 | 10.4 | 5.8 | 937 | 416 | 1.41 | 26.5 | 0.0098 | Sharp #2 | 0 | 120 |
| 59 | BAM6QT | Quiet | Dec-08 | 3 | 9.0 | 6 | 913 | 428 | 1.14 | 22.9 | 0.0084 | Sharp #2 | 0 | 120 |
| 59 | BAM6QT | Quiet | Dec-08 | 7 | 10.3 | 6 | 1043 | 427 | 1.31 | 26.2 | 0.0093 | Sharp #2 | 0 | 120 |
| 64 | HWT-5 | Noisy | May-09 | 37 | 10.0 | 4.9 | 663 | 441 | 2.34 | 33.8 | 0.0145 | Sharp #1 | 0.1 | 120 |
| 64 | HWT-5 | Noisy | May-09 | 36 | 10.1 | 4.9 | 661 | 438 | 2.32 | 33.6 | 0.0144 | Sharp #1 | 0 | 120 |
| 64 | HWT-5 | Noisy | May-09 | 38 | 10.0 | 4.9 | 668 | 443 | 2.35 | 34.0 | 0.0146 | Sharp #1 | -0.1 | 120 |
| 65, 67 | HWT-5 | Noisy | May-09 | 51 | 6.4 | 4.9 | 463 | 471 | 1.64 | 23.7 | 0.0112 | Sharp #1 | 0 | -120 |
| 65, 67 | HWT-5 | Noisy | May-09 | 33 | 6.4 | 4.9 | 462 | 468 | 1.63 | 23.6 | 0.0112 | Sharp #1 | 0 | 0 |
| 65, 67 | HWT-5 | Noisy | May-09 | 53 | 6.7 | 4.9 | 475 | 464 | 1.68 | 24.4 | 0.0114 | Sharp #1 | 0 | 90 |

Table A.5 Run conditions for Chapter 4 figures, end

| Chapter 4 Figure Number | Tunnel | Flow | Entry | Run | $Re/m$ $\times 10^{-6}$ | M | $P_0$ (kPa) | $T_0$ (K) | $p_e$ (kPa) | $q_e$ (kPa) | $\tau_w$ (kPa) | Nosetip | AoA | Roll |
|---|---|---|---|---|---|---|---|---|---|---|---|---|---|---|
| 65, 67 | HWT-5 | Noisy | May-09 | 54 | 6.5 | 4.9 | 472 | 467 | 1.67 | 24.1 | 0.0113 | Sharp #1 | 0 | 120 |
| 65, 67 | HWT-5 | Noisy | May-09 | 52 | 6.7 | 4.9 | 477 | 464 | 1.69 | 24.4 | 0.0114 | Sharp #1 | 0 | 180 |
| 66, 71 | HWT-5 | Noisy | May-09 | 73 | 9.4 | 4.9 | 628 | 441 | 2.19 | 31.7 | 0.0138 | Sharp #1 | 0 | 120 |
| 66, 71 | HWT-5 | Noisy | May-09 | 74 | 9.6 | 4.9 | 647 | 445 | 2.27 | 32.8 | 0.0142 | Sharp #2 | 0 | 120 |
| 68, 70 | HWT-8 | Noisy | May-09 | 88 | 12.8 | 7.9 | 4401 | 595 | 1.28 | 41.6 | 0.0096 | Sharp #1 | 0 | -120 |
| 68, 70 | HWT-8 | Noisy | May-09 | 87 | 13.1 | 7.9 | 4533 | 598 | 1.32 | 42.8 | 0.0098 | Sharp #1 | 0 | 0 |
| 68–70 | HWT-8 | Noisy | May-09 | 80 | 13.3 | 7.9 | 4523 | 589 | 1.31 | 42.6 | 0.0097 | Sharp #1 | 0 | 120 |
| 69 | HWT-8 | Noisy | May-09 | 89 | 13.2 | 7.9 | 4559 | 597 | 1.32 | 43.0 | 0.0099 | Sharp #1 | 0.1 | 120 |
| 69 | HWT-8 | Noisy | May-09 | 90 | 13.1 | 7.9 | 4503 | 595 | 1.31 | 42.5 | 0.0097 | Sharp #1 | -0.1 | 120 |

# B. Drawings of Pressure-Fluctuation Cone

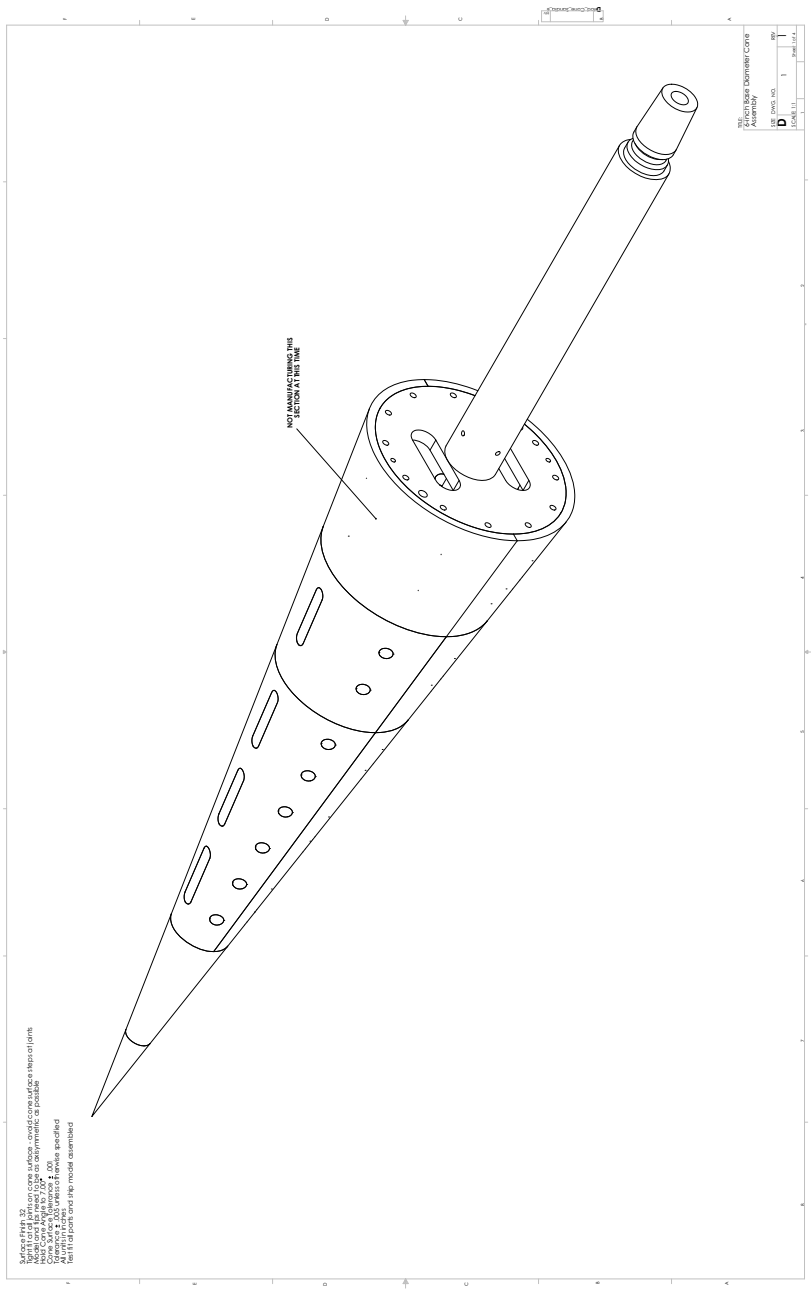


Figure B.1. Cone assembly

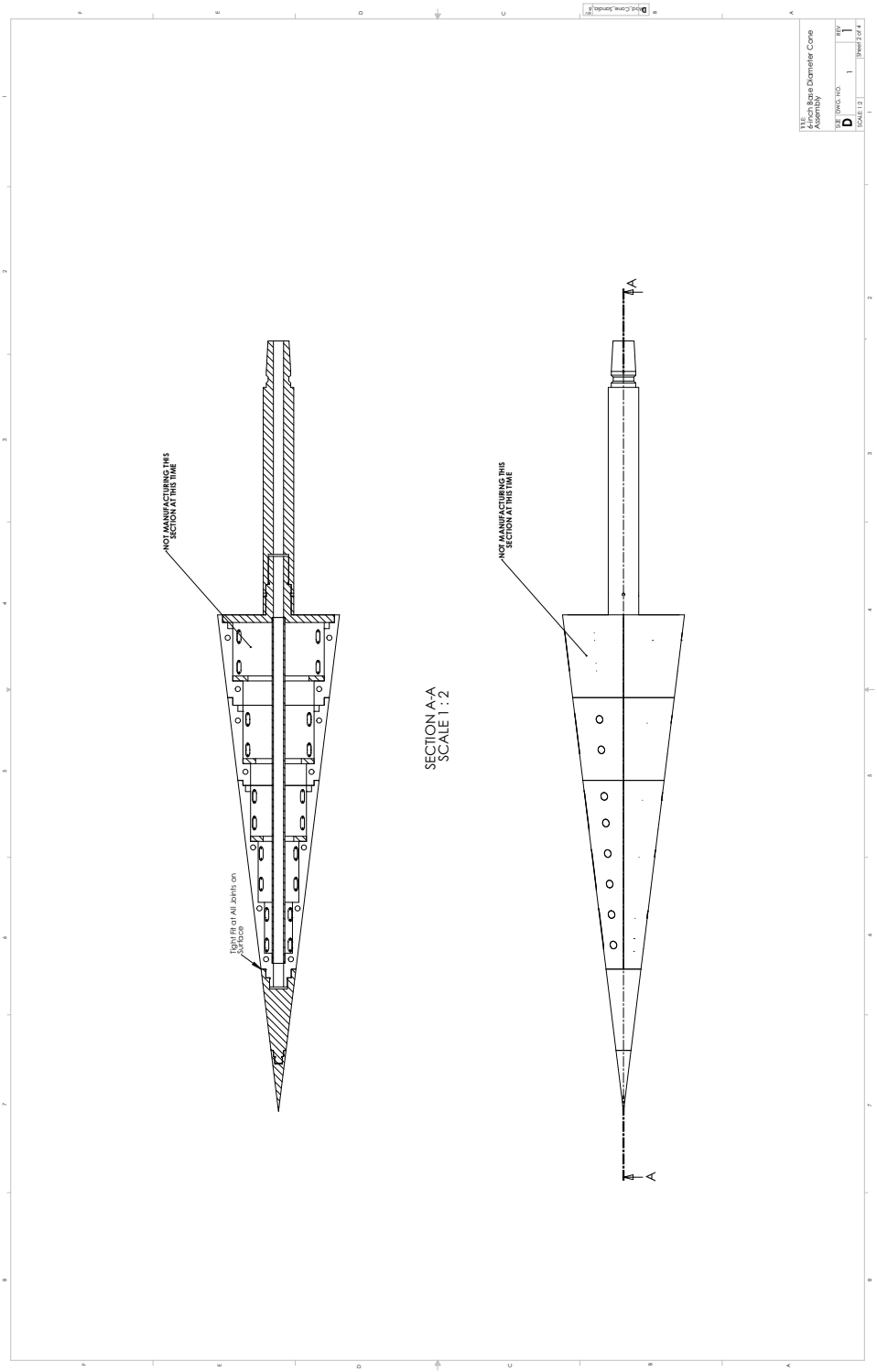


Figure B.2. Section view of cone assembly

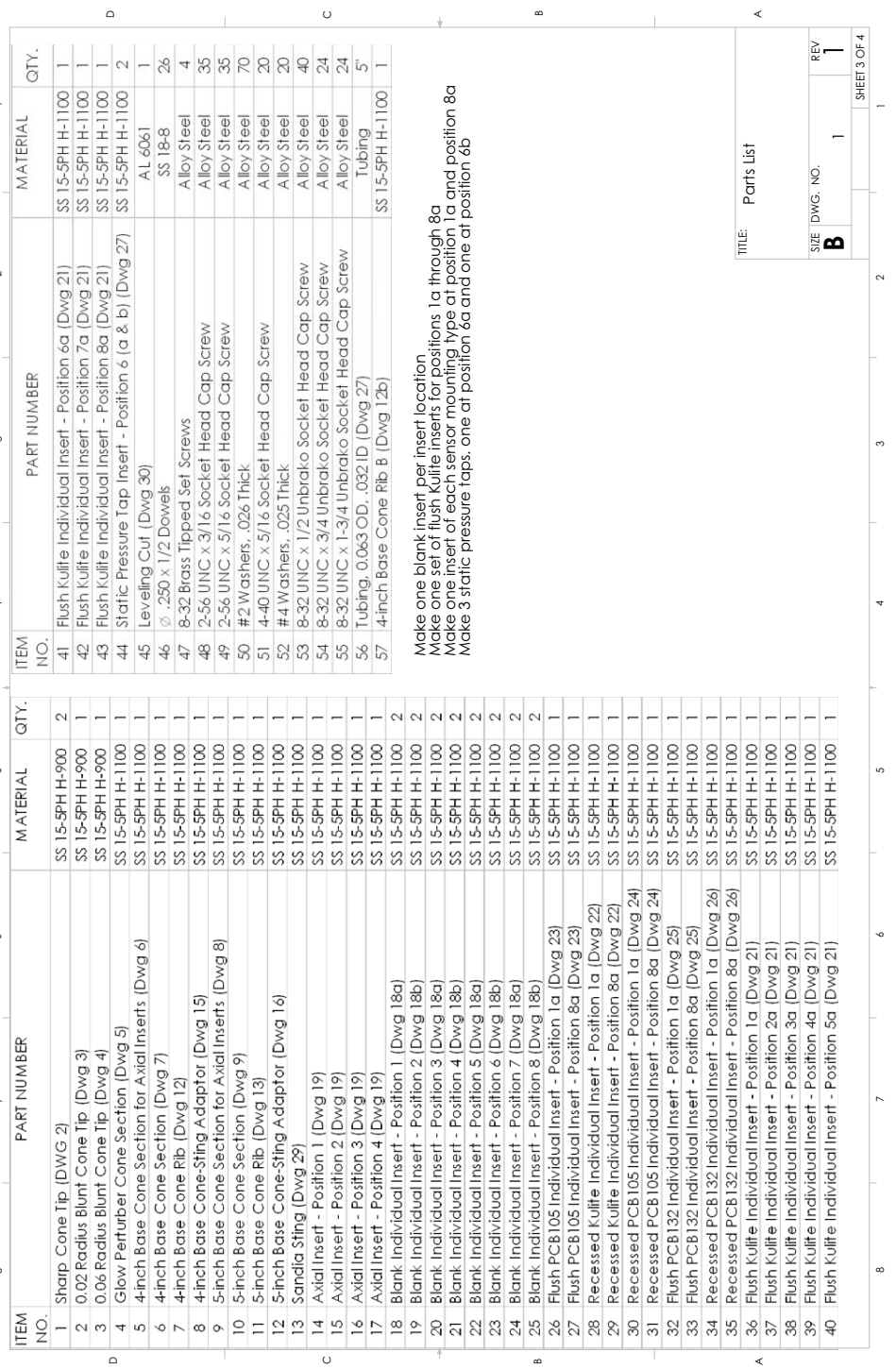

| ITEM NO. | PART NUMBER | MATERIAL | QTY. |
|---|---|---|---|
| 1 | Sharp Cone Tip (DWG 2) | SS 15-5PH H-900 | 2 |
| 2 | 0.02 Radius Blunt Cone Tip (Dwg 3) | SS 15-5PH H-900 | 1 |
| 3 | 0.06 Radius Blunt Cone Tip (Dwg 4) | SS 15-5PH H-900 | 1 |
| 4 | Glow Perturber Cone Section (Dwg 5) | SS 15-5PH H-1100 | 1 |
| 5 | 4-inch Base Cone Section for Axial Inserts (Dwg 6) | SS 15-5PH H-1100 | 1 |
| 6 | 4-inch Base Cone Section (Dwg 7) | SS 15-5PH H-1100 | 1 |
| 7 | 4-inch Base Cone Rib (Dwg 12) | SS 15-5PH H-1100 | 1 |
| 8 | 4-inch Base Cone-Sting Adaptor (Dwg 15) | SS 15-5PH H-1100 | 1 |
| 9 | 5-inch Base Cone Section for Axial Inserts (Dwg 8) | SS 15-5PH H-1100 | 1 |
| 10 | 5-inch Base Cone Section (Dwg 9) | SS 15-5PH H-1100 | 1 |
| 11 | 5-inch Base Cone Rib (Dwg 13) | SS 15-5PH H-1100 | 1 |
| 12 | 5-inch Base Cone-Sting Adaptor (Dwg 16) | SS 15-5PH H-1100 | 1 |
| 13 | Sandia Sting (Dwg 29) | SS 15-5PH H-1100 | 1 |
| 14 | Axial Insert - Position 1 (Dwg 19) | SS 15-5PH H-1100 | 1 |
| 15 | Axial Insert - Position 2 (Dwg 19) | SS 15-5PH H-1100 | 1 |
| 16 | Axial Insert - Position 3 (Dwg 19) | SS 15-5PH H-1100 | 1 |
| 17 | Axial Insert - Position 4 (Dwg 19) | SS 15-5PH H-1100 | 1 |
| 18 | Blank Individual Insert - Position 1 (Dwg 18a) | SS 15-5PH H-1100 | 2 |
| 19 | Blank Individual Insert - Position 2 (Dwg 18b) | SS 15-5PH H-1100 | 2 |
| 20 | Blank Individual Insert - Position 3 (Dwg 18a) | SS 15-5PH H-1100 | 2 |
| 21 | Blank Individual Insert - Position 4 (Dwg 18b) | SS 15-5PH H-1100 | 2 |
| 22 | Blank Individual Insert - Position 5 (Dwg 18a) | SS 15-5PH H-1100 | 2 |
| 23 | Blank Individual Insert - Position 6 (Dwg 18b) | SS 15-5PH H-1100 | 2 |
| 24 | Blank Individual Insert - Position 7 (Dwg 18a) | SS 15-5PH H-1100 | 2 |
| 25 | Blank Individual Insert - Position 8 (Dwg 18b) | SS 15-5PH H-1100 | 2 |
| 26 | Flush PCB105 Individual Insert - Position 1a (Dwg 23) | SS 15-5PH H-1100 | 1 |
| 27 | Flush PCB105 Individual Insert - Position 8a (Dwg 23) | SS 15-5PH H-1100 | 1 |
| 28 | Recessed Kulite Individual Insert - Position 1a (Dwg 22) | SS 15-5PH H-1100 | 1 |
| 29 | Recessed Kulite Individual Insert - Position 8a (Dwg 22) | SS 15-5PH H-1100 | 1 |
| 30 | Recessed PCB105 Individual Insert - Position 1a (Dwg 24) | SS 15-5PH H-1100 | 1 |
| 31 | Recessed PCB105 Individual Insert - Position 8a (Dwg 24) | SS 15-5PH H-1100 | 1 |
| 32 | Flush PCB132 Individual Insert - Position 1a (Dwg 25) | SS 15-5PH H-1100 | 1 |
| 33 | Flush PCB132 Individual Insert - Position 8a (Dwg 25) | SS 15-5PH H-1100 | 1 |
| 34 | Recessed PCB132 Individual Insert - Position 1a (Dwg 26) | SS 15-5PH H-1100 | 1 |
| 35 | Recessed PCB132 Individual Insert - Position 8a (Dwg 26) | SS 15-5PH H-1100 | 1 |
| 36 | Flush Kulite Individual Insert - Position 1a (Dwg 21) | SS 15-5PH H-1100 | 1 |
| 37 | Flush Kulite Individual Insert - Position 2a (Dwg 21) | SS 15-5PH H-1100 | 1 |
| 38 | Flush Kulite Individual Insert - Position 3a (Dwg 21) | SS 15-5PH H-1100 | 1 |
| 39 | Flush Kulite Individual Insert - Position 4a (Dwg 21) | SS 15-5PH H-1100 | 1 |
| 40 | Flush Kulite Individual Insert - Position 5a (Dwg 21) | SS 15-5PH H-1100 | 1 |

| ITEM NO. | PART NUMBER | MATERIAL | QTY. |
|---|---|---|---|
| 41 | Flush Kulite Individual Insert - Position 6a (Dwg 21) | SS 15-5PH H-1100 | 1 |
| 42 | Flush Kulite Individual Insert - Position 7a (Dwg 21) | SS 15-5PH H-1100 | 1 |
| 43 | Flush Kulite Individual Insert - Position 8a (Dwg 21) | SS 15-5PH H-1100 | 1 |
| 44 | Static Pressure Tap Insert - Position 6 (a & b) (Dwg 27) | SS 15-5PH H-1100 | 2 |
| 45 | Leveling Cut (Dwg 30) | AL 6061 | 1 |
| 46 | Ø .250 x 1/2 Dowels | SS 18-8 | 26 |
| 47 | 8-32 Brass Tipped Set Screws | Alloy Steel | 4 |
| 48 | 2-56 UNC x 3/16 Socket Head Cap Screw | Alloy Steel | 35 |
| 49 | 2-56 UNC x 5/16 Socket Head Cap Screw | Alloy Steel | 35 |
| 50 | #2 Washers, .026 Thick | Alloy Steel | 70 |
| 51 | 4-40 UNC x 5/16 Socket Head Cap Screw | Alloy Steel | 20 |
| 52 | #4 Washers, .025 Thick | Alloy Steel | 20 |
| 53 | 8-32 UNC x 1/2 Unbrako Socket Head Cap Screw | Alloy Steel | 40 |
| 54 | 8-32 UNC x 3/4 Unbrako Socket Head Cap Screw | Alloy Steel | 24 |
| 55 | 8-32 UNC x 1-3/4 Unbrako Socket Head Cap Screw | Alloy Steel | 24 |
| 56 | Tubing, 0.063 OD, .032 ID (Dwg 27) | Tubing | 5" |
| 57 | 4-inch Base Cone Rib B (Dwg 12b) | SS 15-5PH H-1100 | 1 |

Make one blank insert per insert location
Make one set of flush Kulite inserts for positions 1a through 8a
Make one insert of each sensor mounting type at position 1a and position 8a
Make 3 static pressure taps, one at position 6a and one at position 6b

TITLE: Parts List

SIZE B | DWG. NO. 1 | REV 1

SHEET 3 OF 4

Figure B.3. Parts list

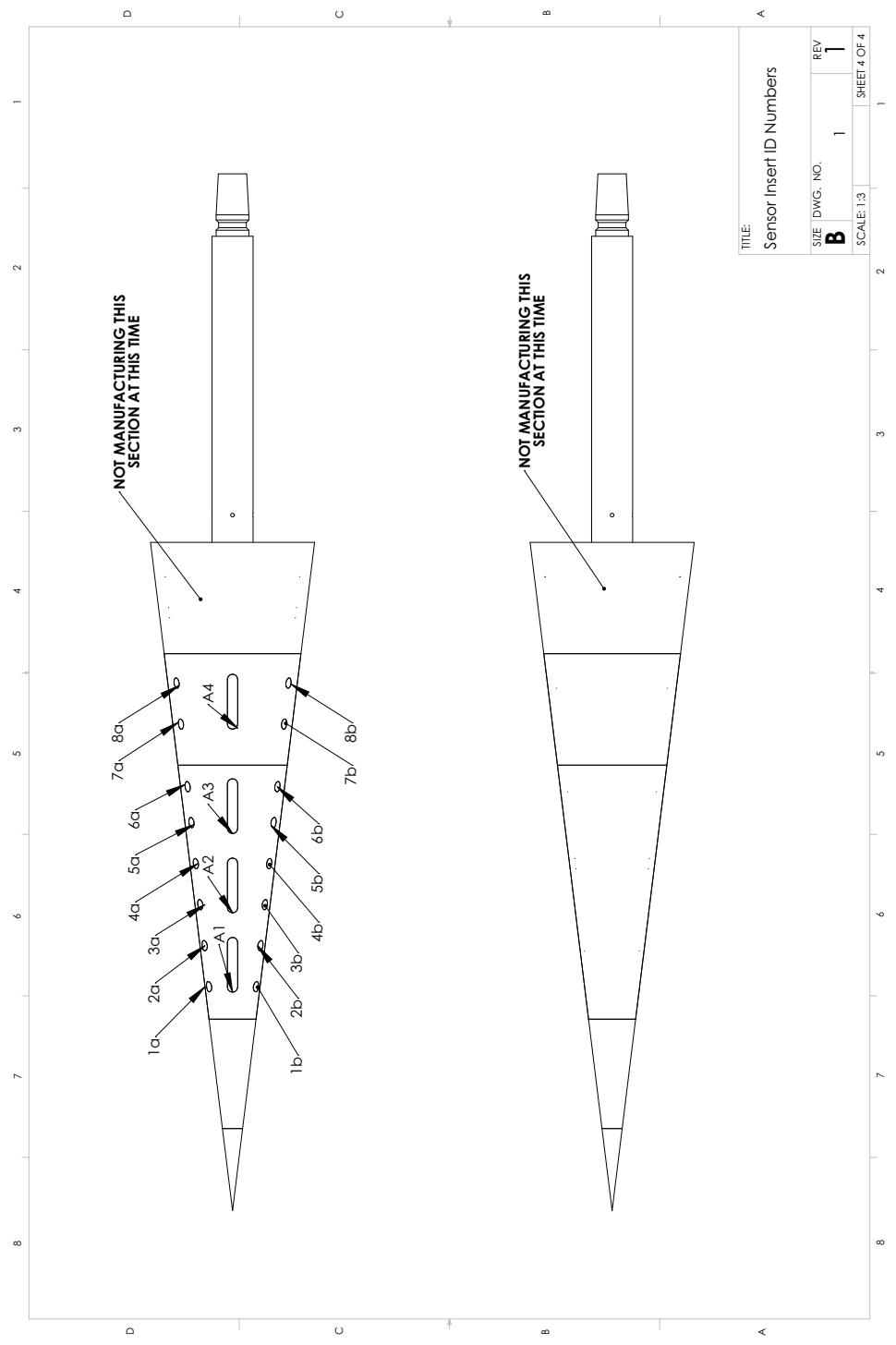


Figure B.4. Insert locations and position names

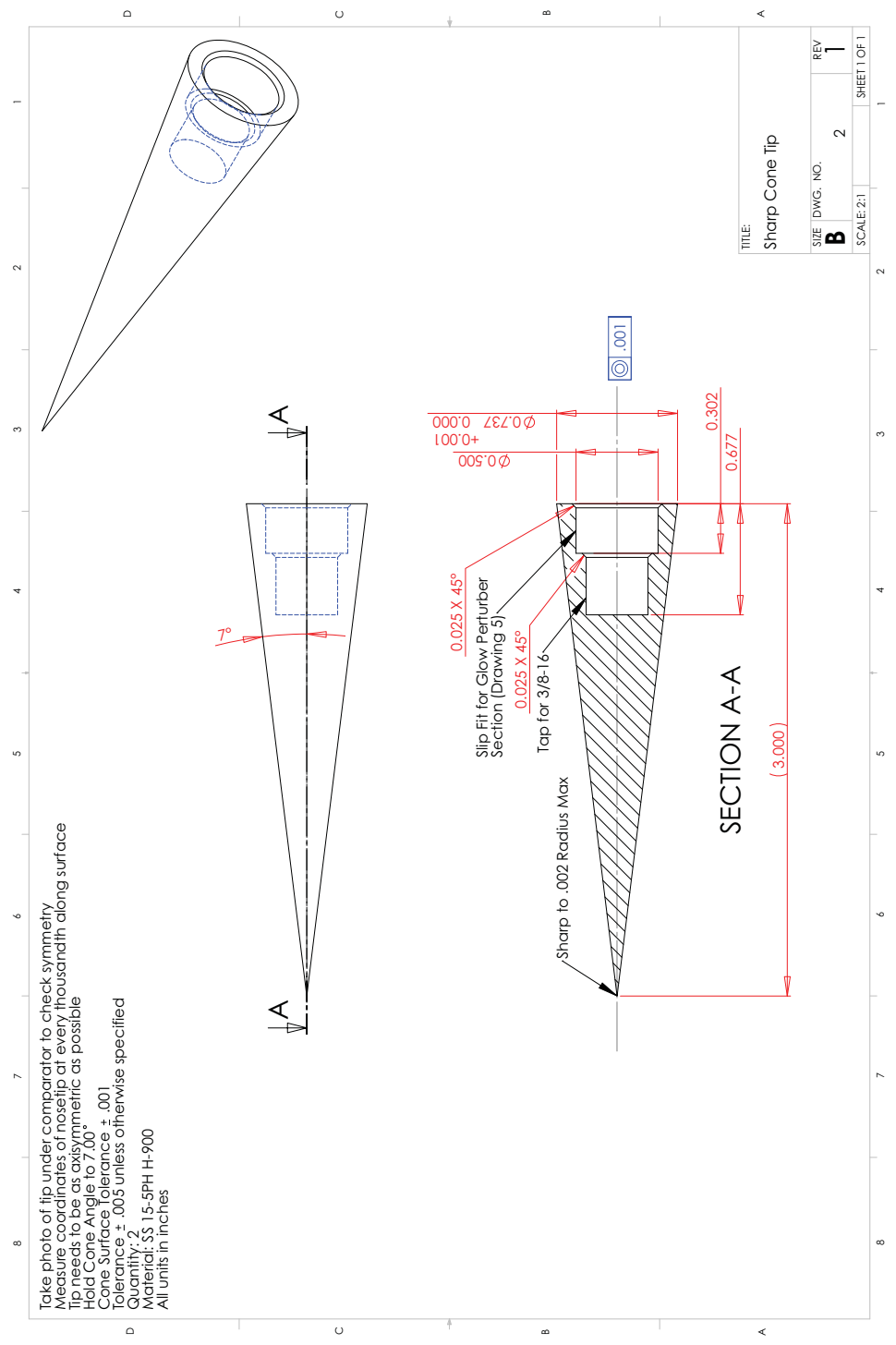


Figure B.5. Sharp nosetip

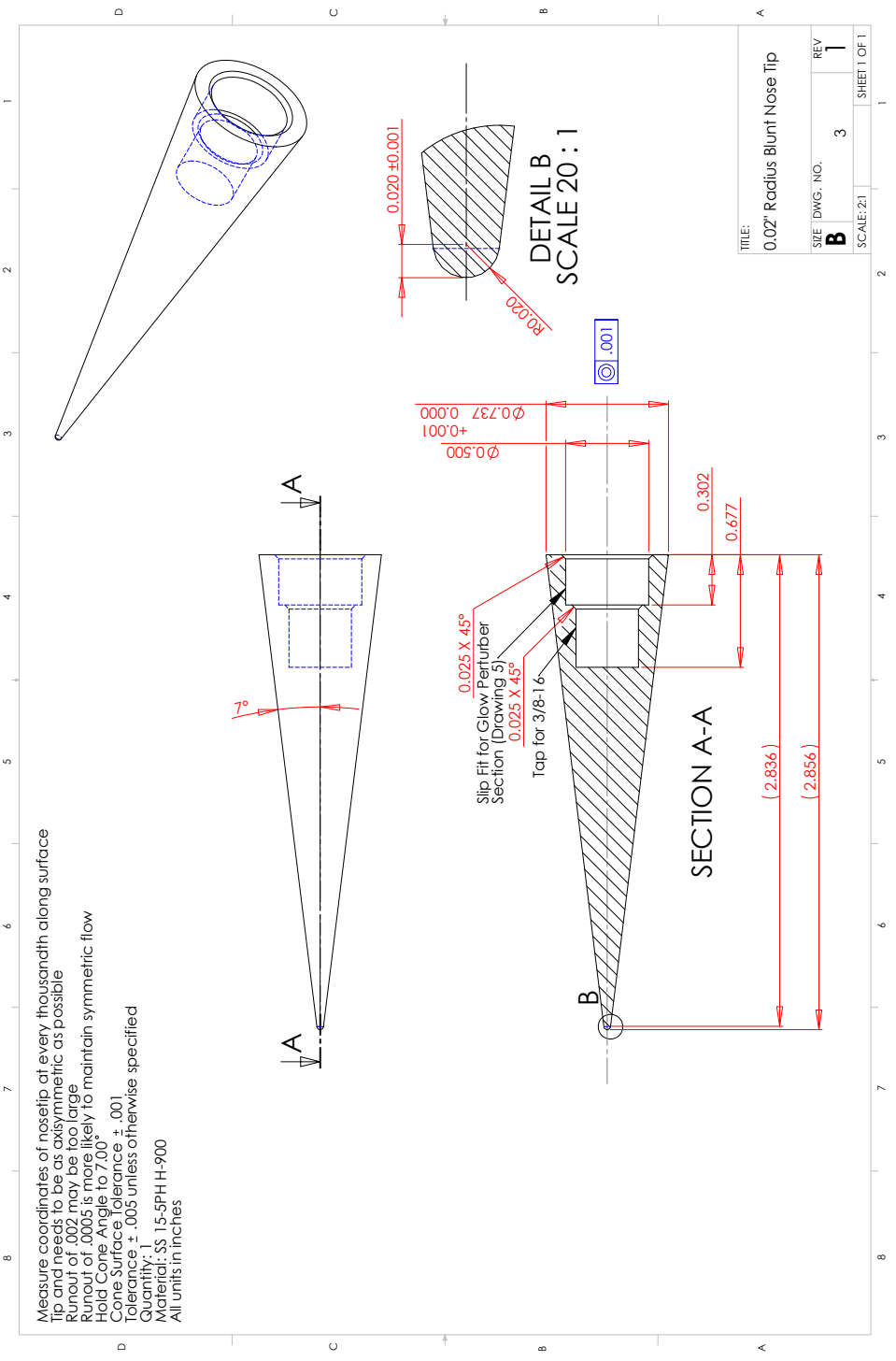


Figure B.6. 0.5-mm-radius blunt nosetip

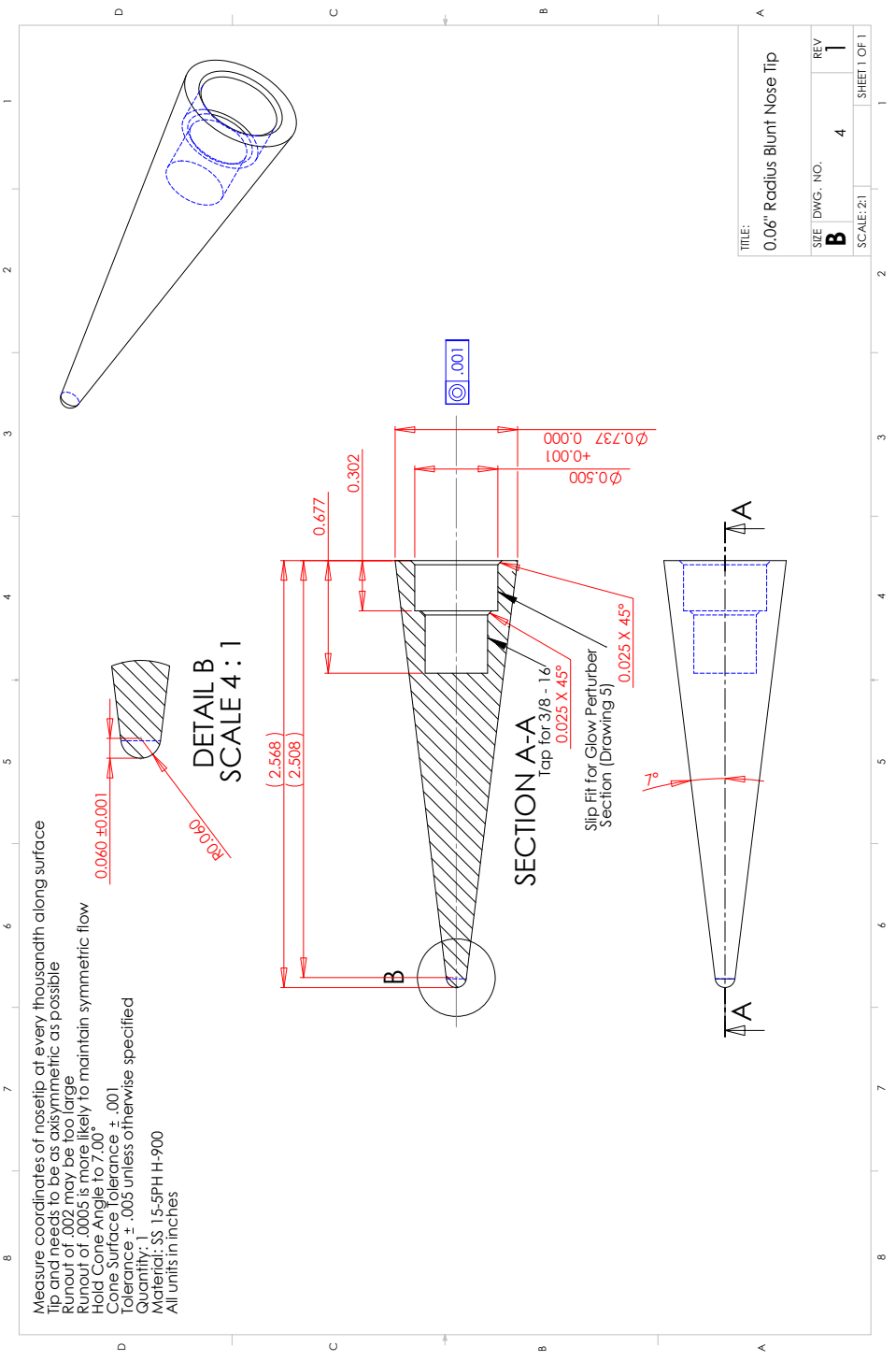


Figure B.7. 1.5-mm-radius blunt nosetip

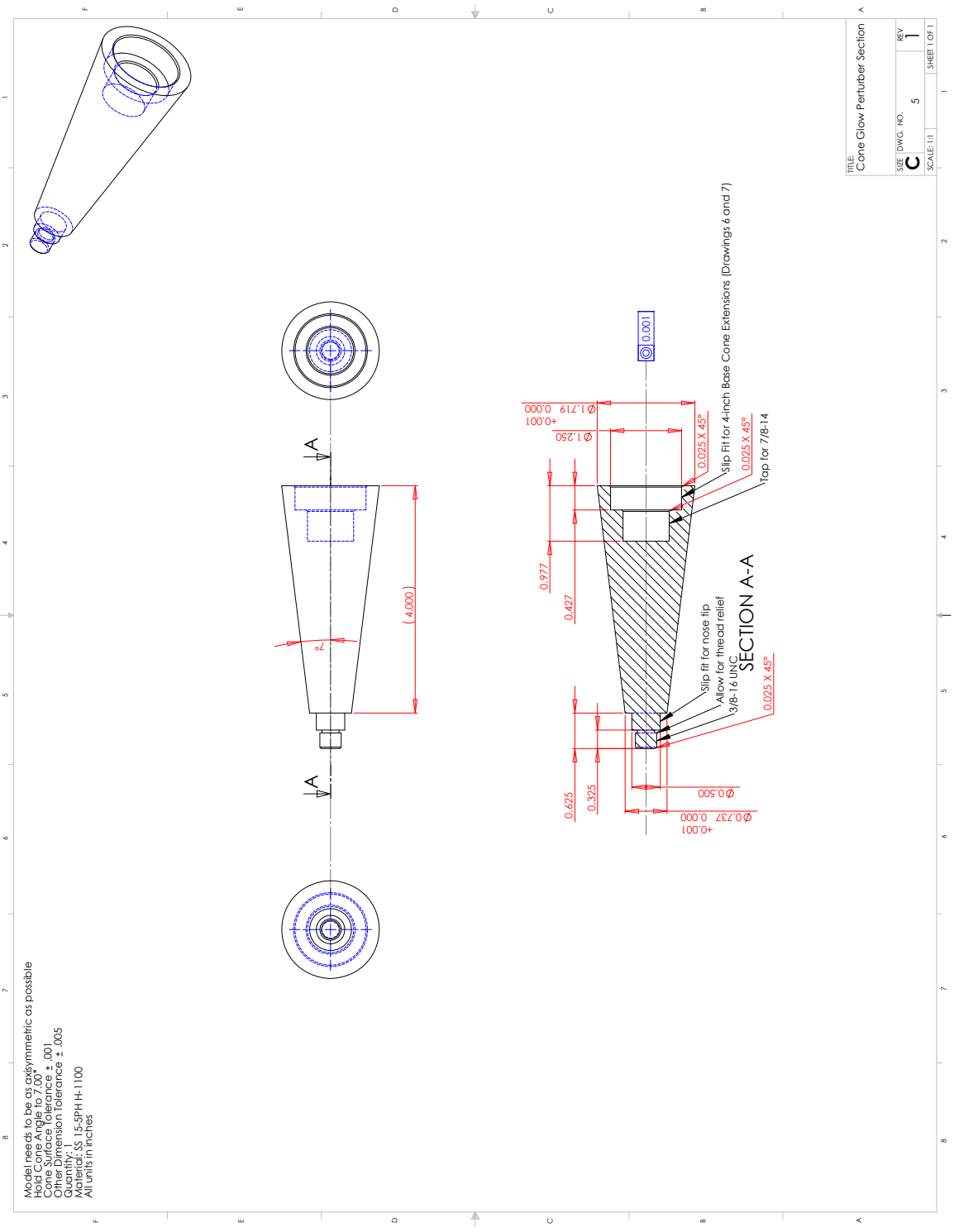


Figure B.8. Blank glow-perturber section

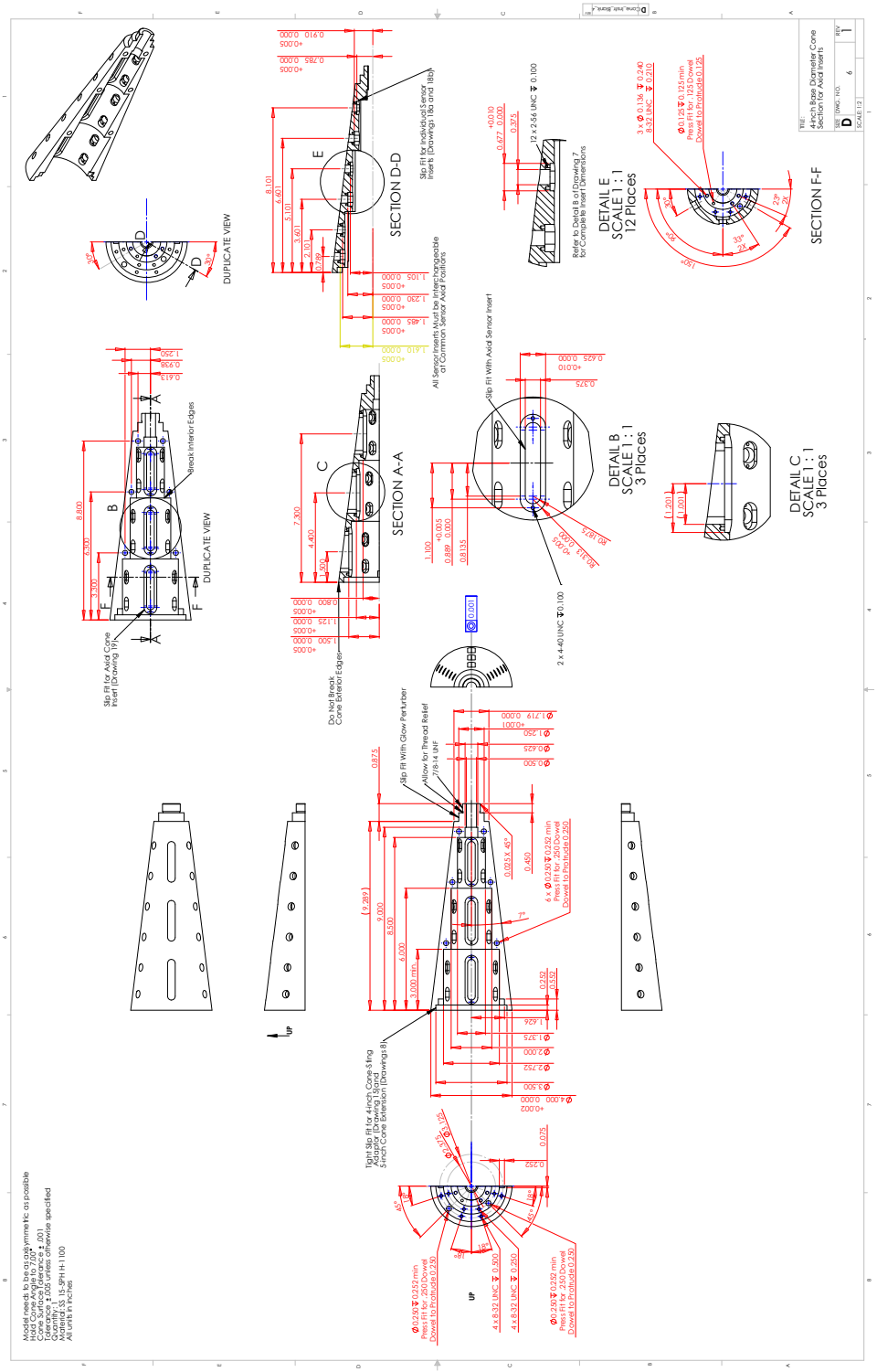

Figure B.9. 0.102-m base-diameter instrumentation section half

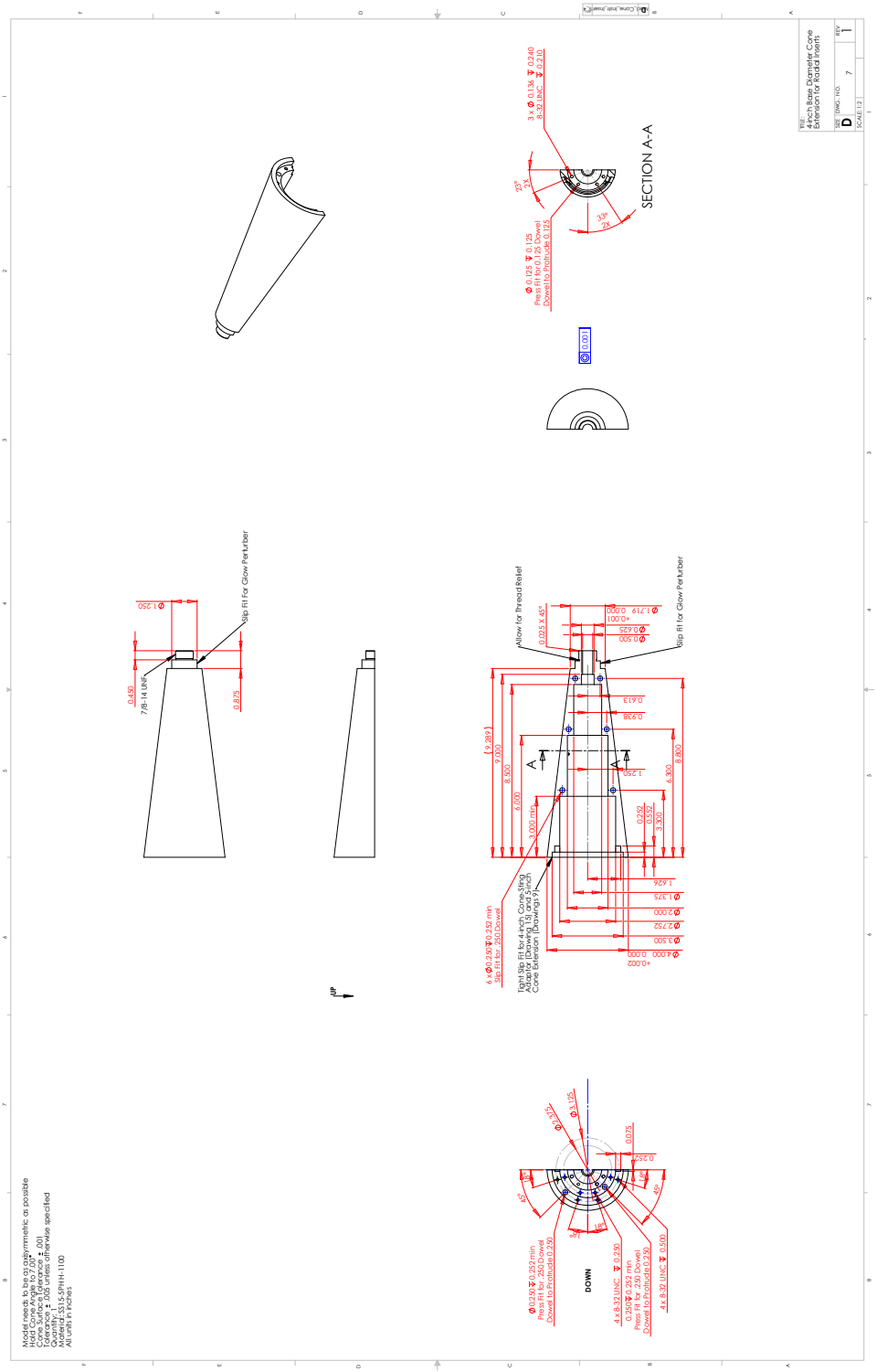


Figure B.10. Blank 0.102-m base-diameter section half

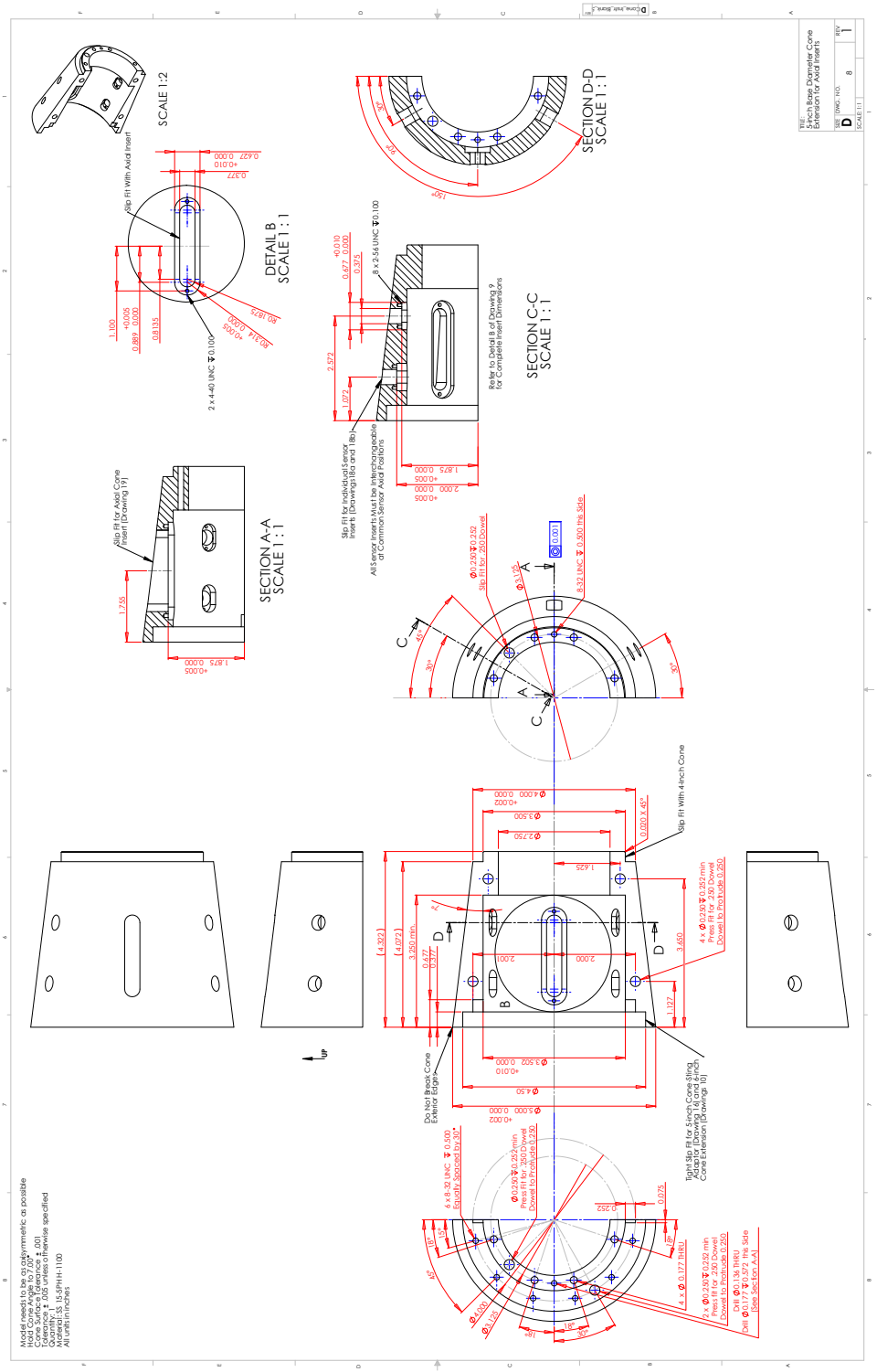


Figure B.11. 0.127-m base-diameter instrumentation section half

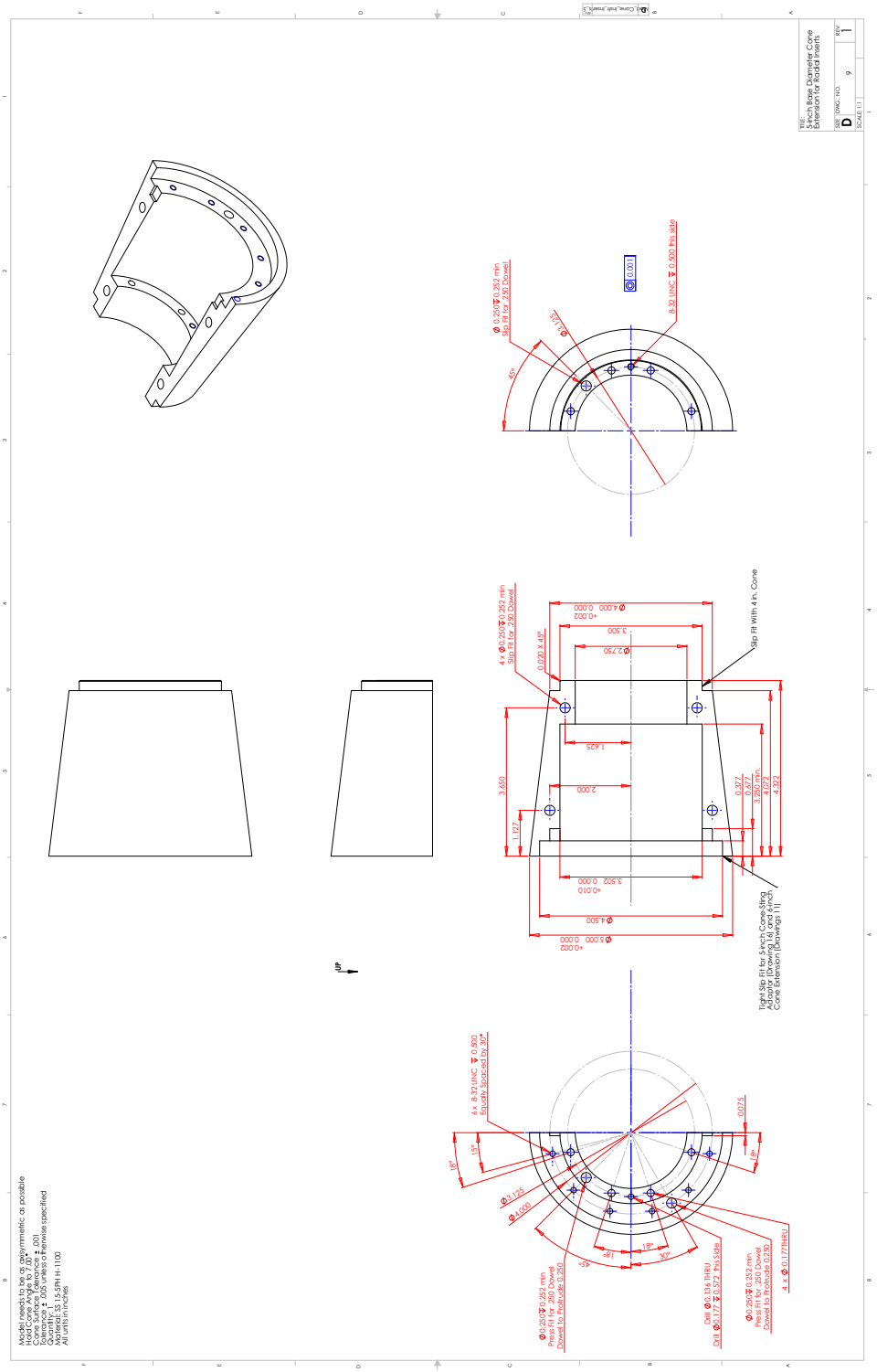


Figure B.12. Blank 0.127-m base-diameter section half

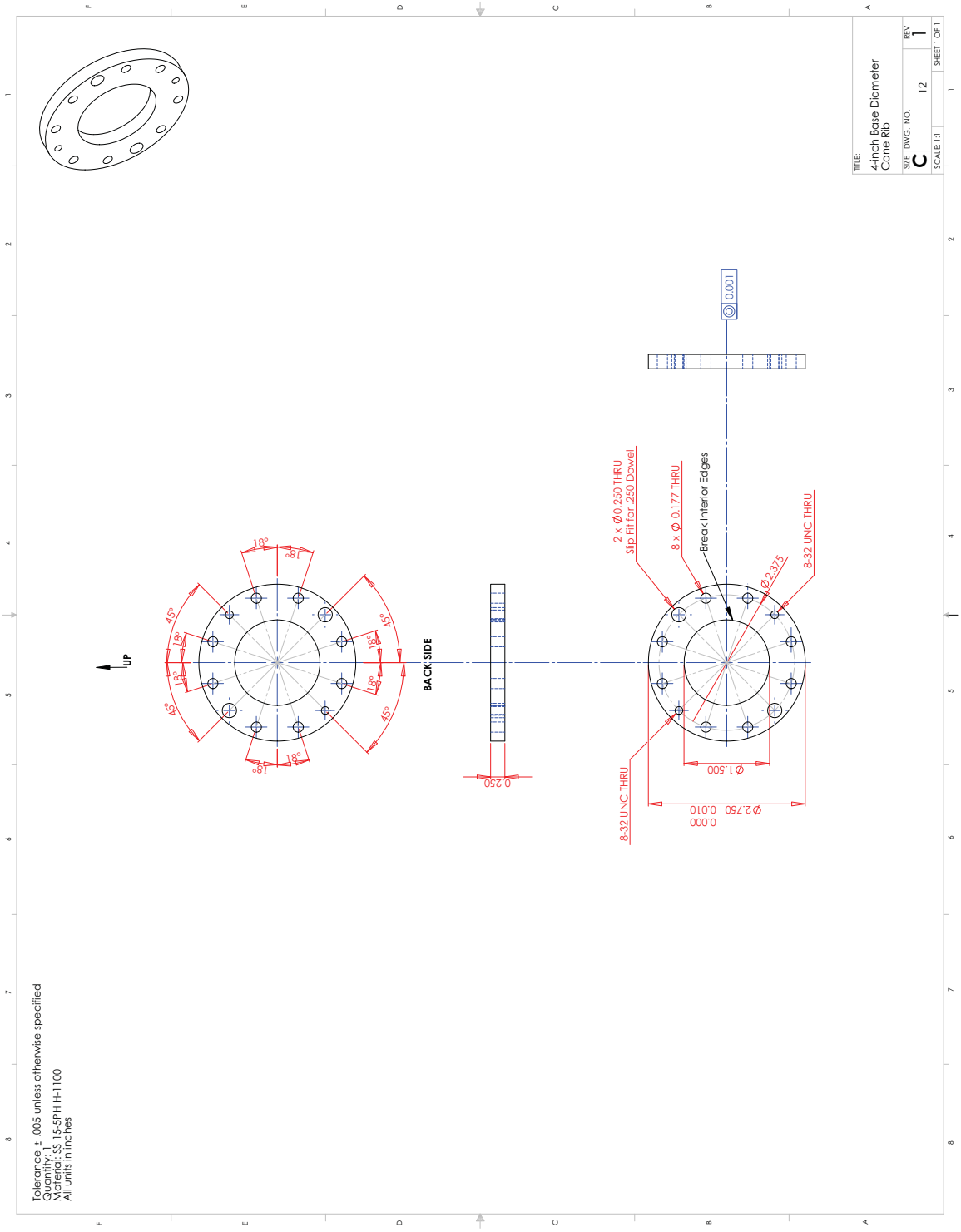


Figure B.13. 0.102-m base-diameter section rib

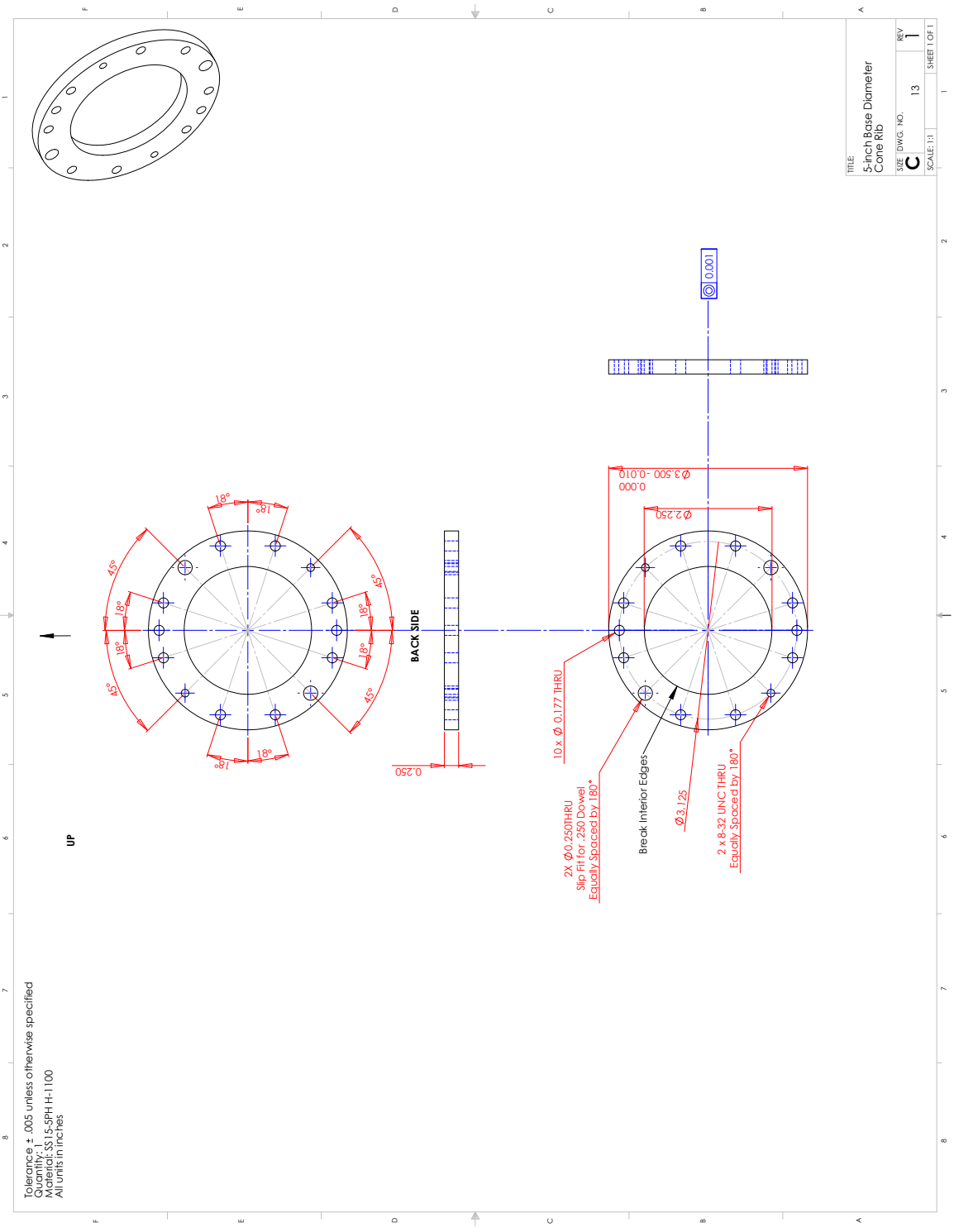


Figure B.14. 0.127-m base-diameter section rib

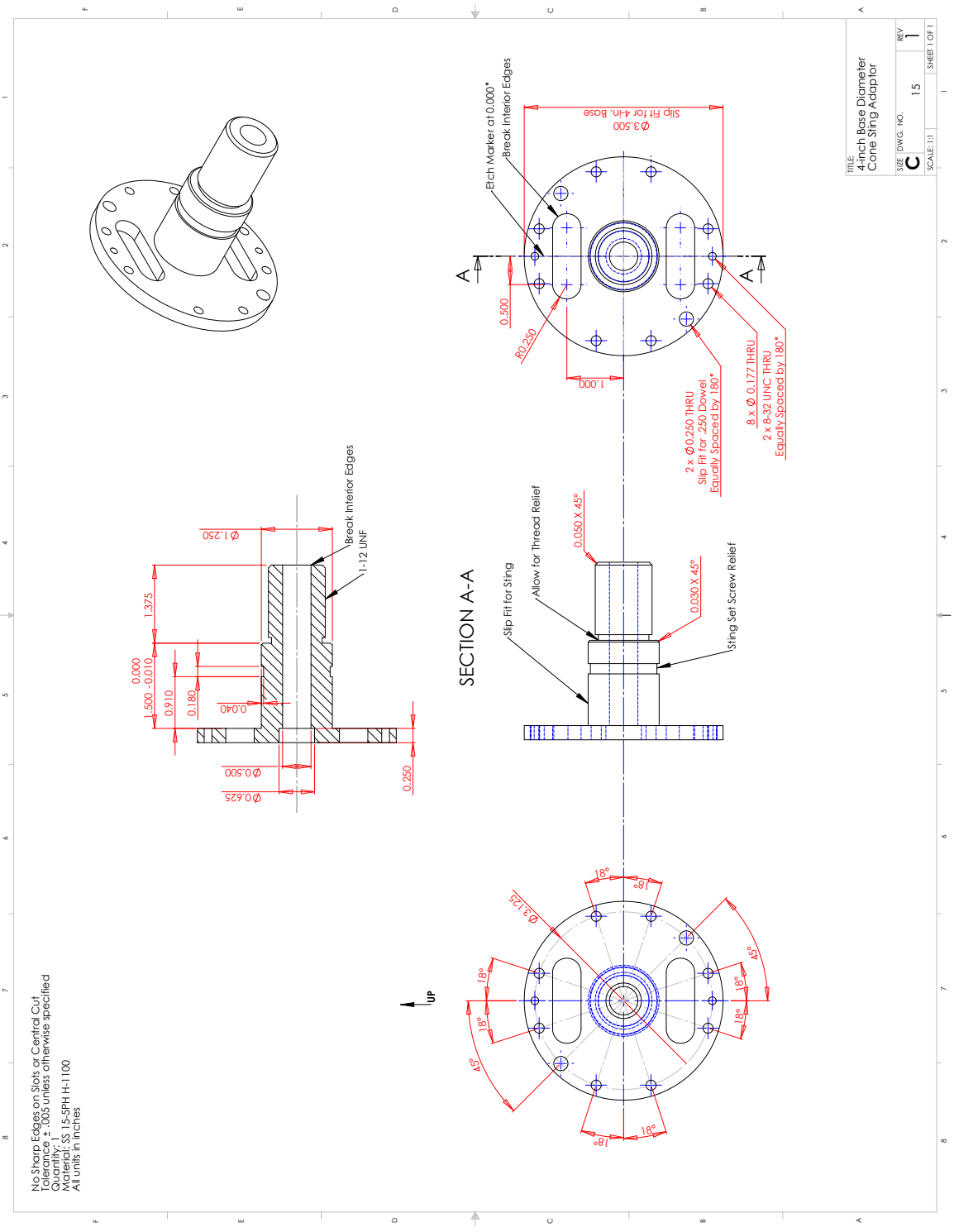


Figure B.15. 0.102-m base-diameter section sting adaptor

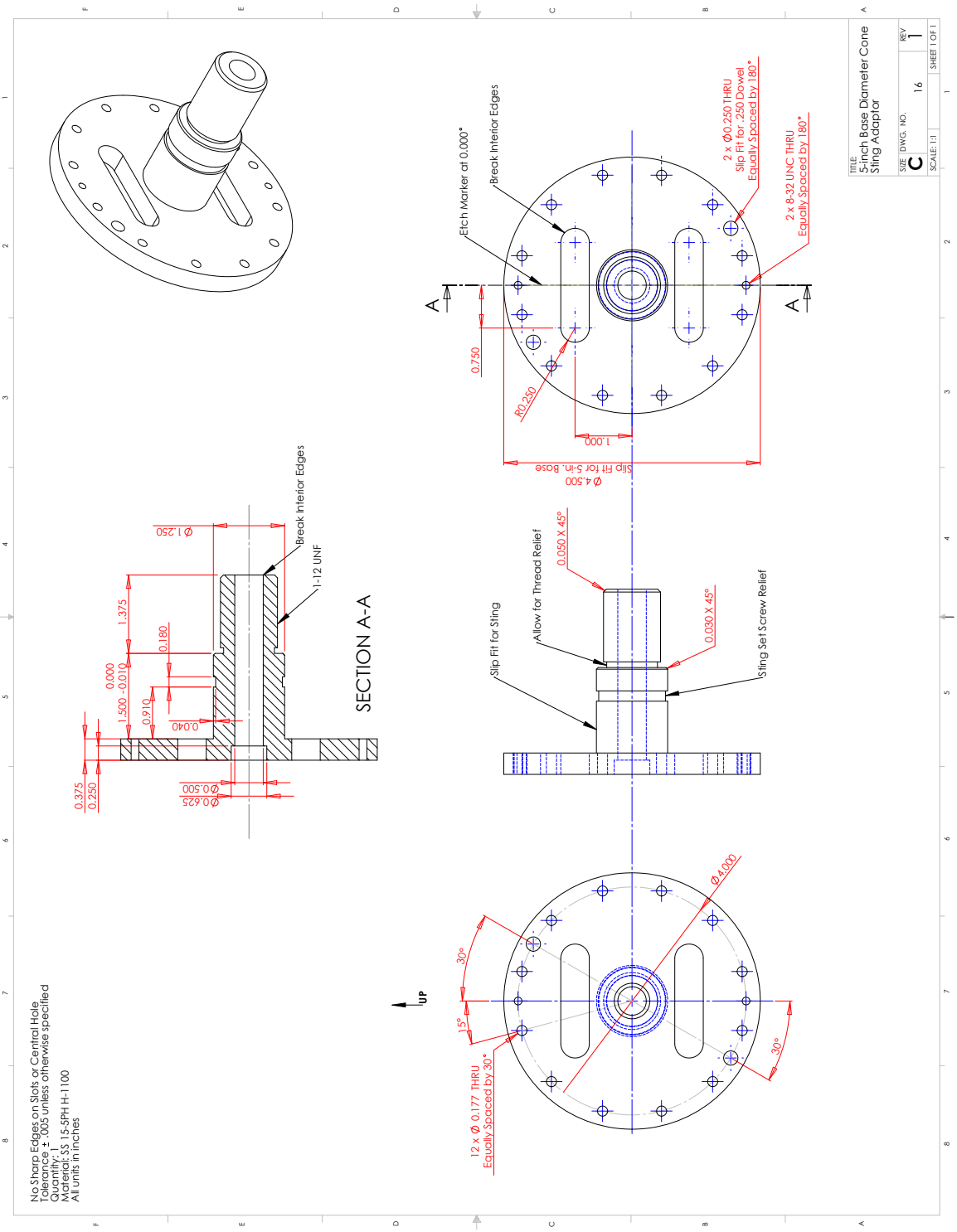


Figure B.16. 0.127-m base-diameter section sting adaptor

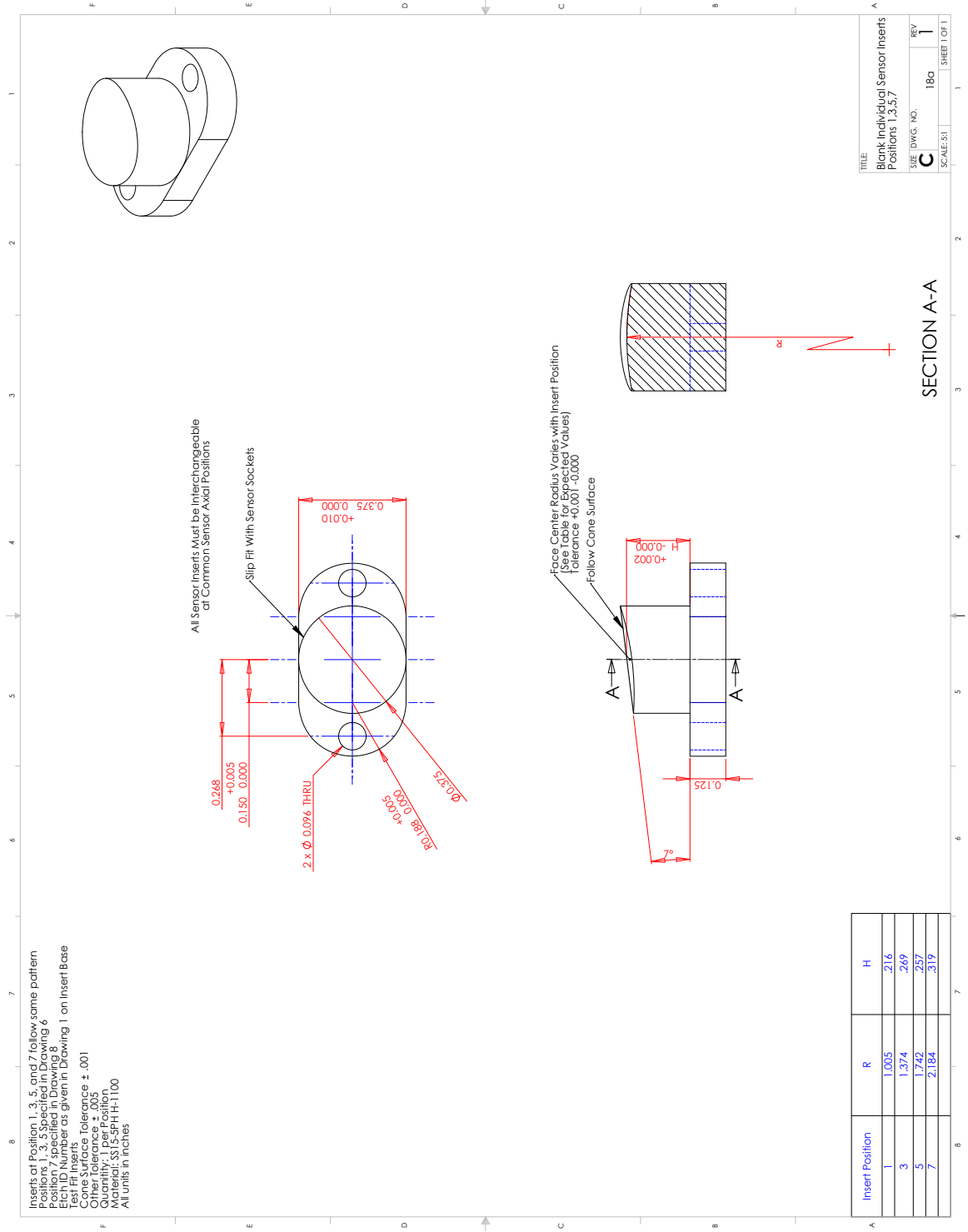


Figure B.17. Blank individual insert for positions 1, 3, 5, and 7

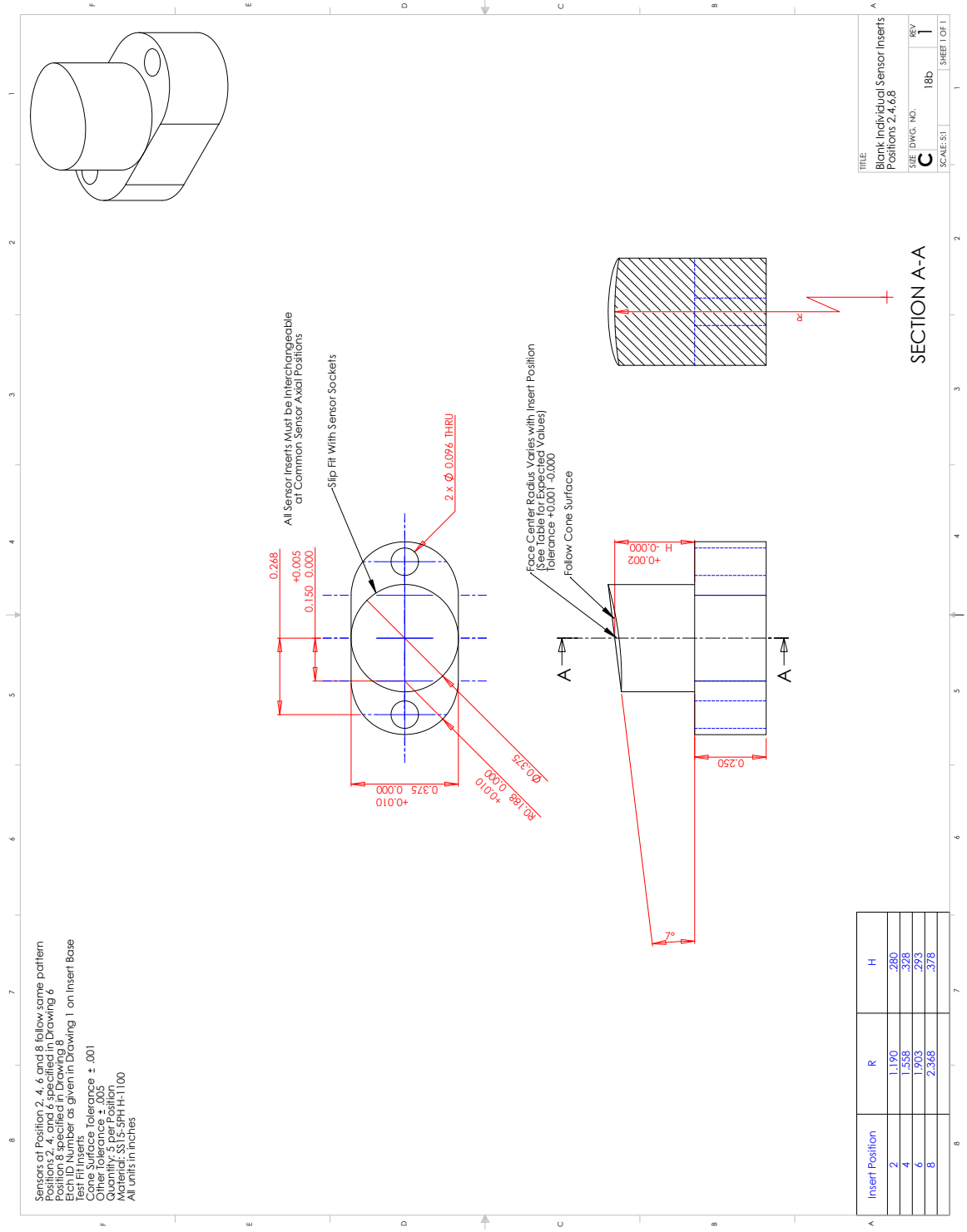


Figure B.18. Blank individual insert for positions 2, 4, 6, and 8

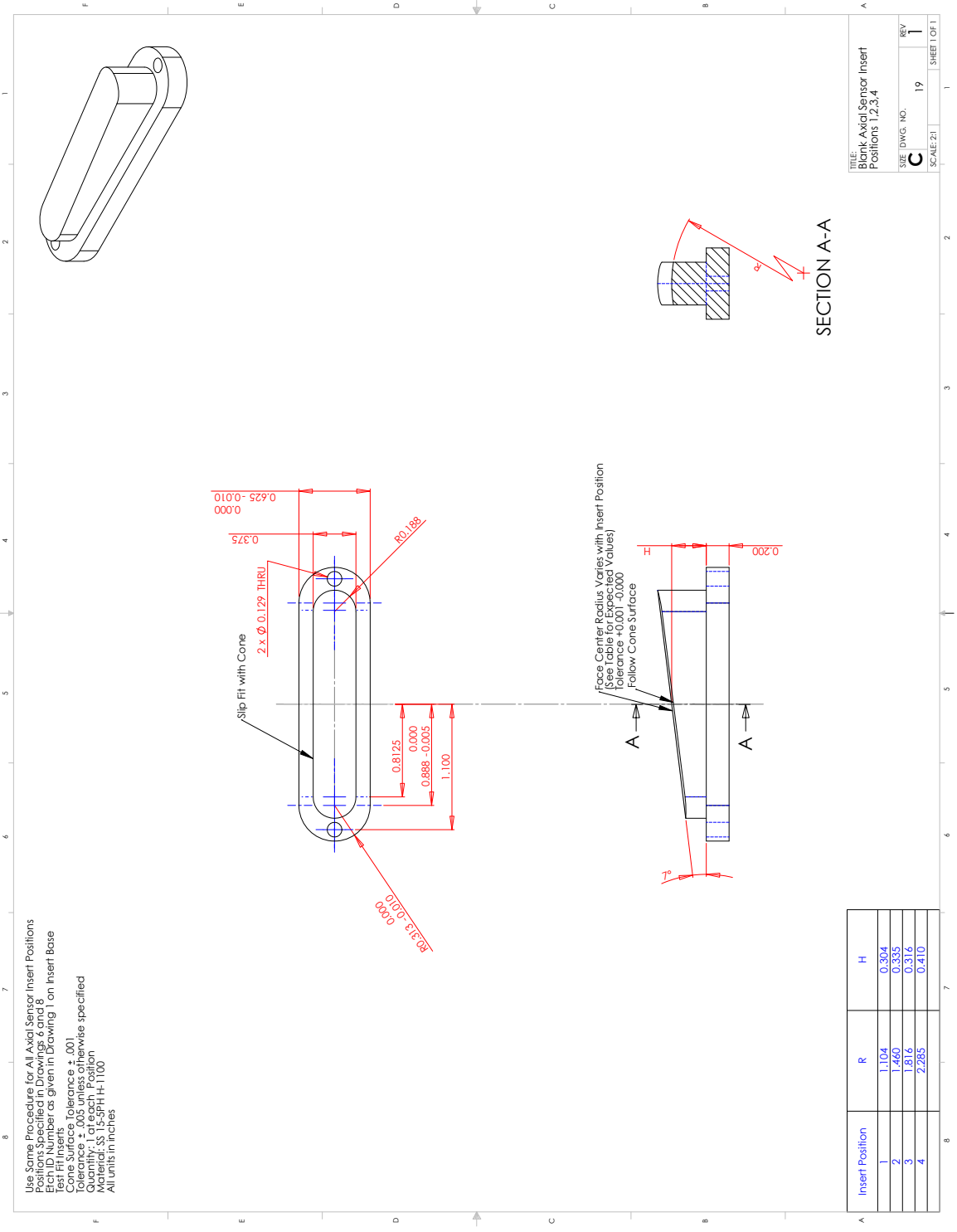


Figure B.19. Blank axial inserts for close spacing of sensors

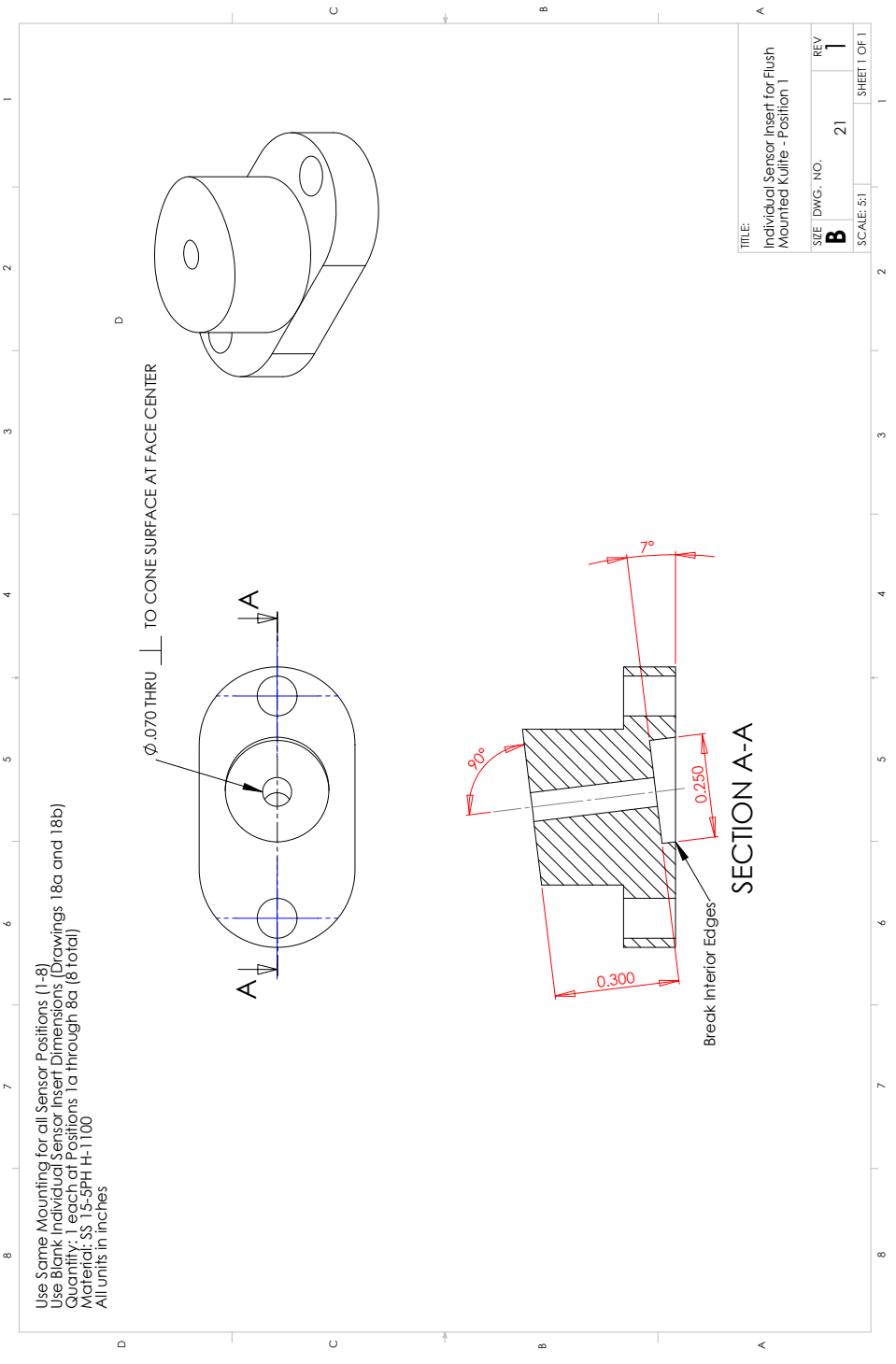


Figure B.20. Individual insert for flush-mounted Kulites

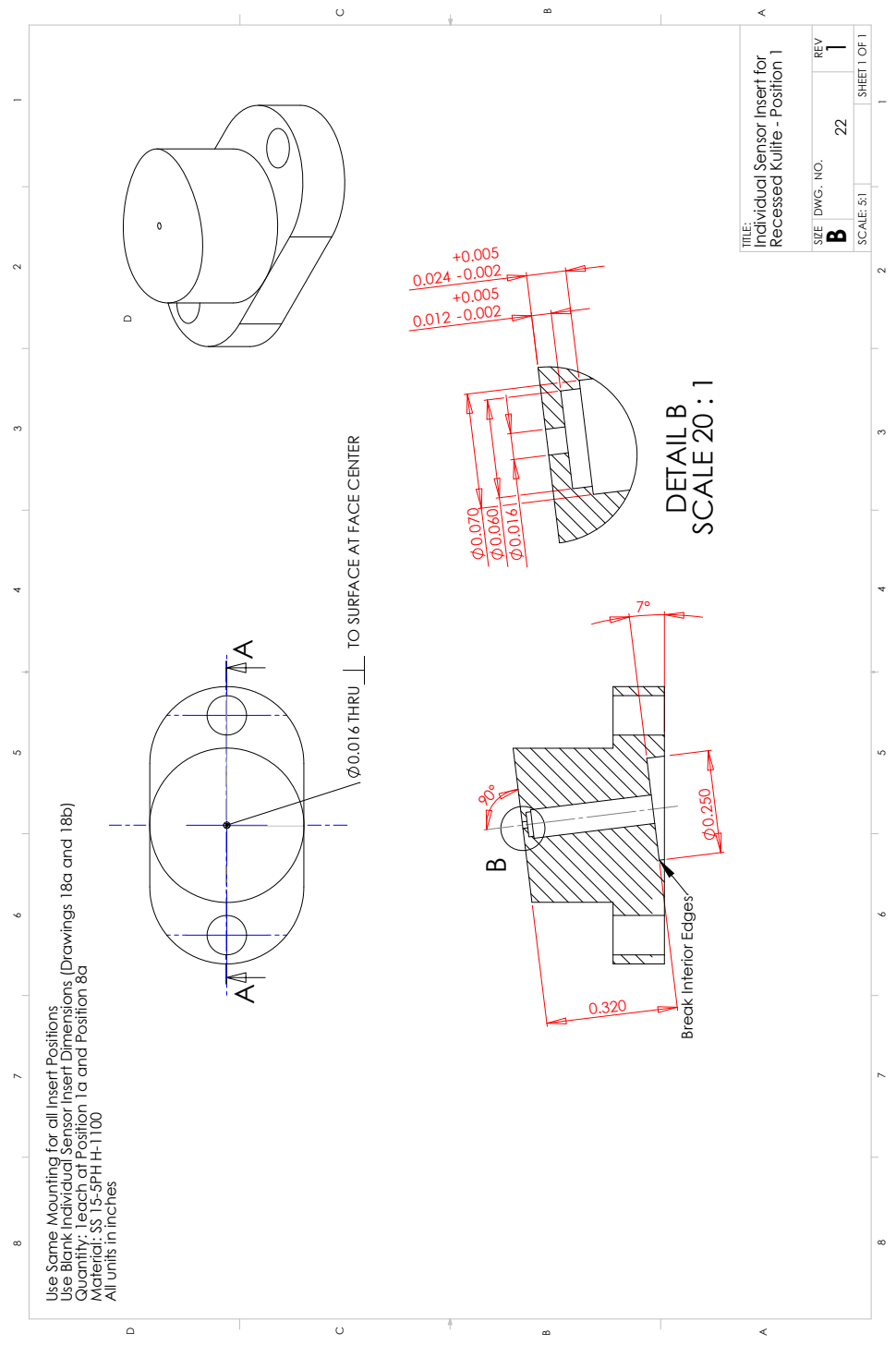


Figure B.21. Individual insert for recessed Kulites

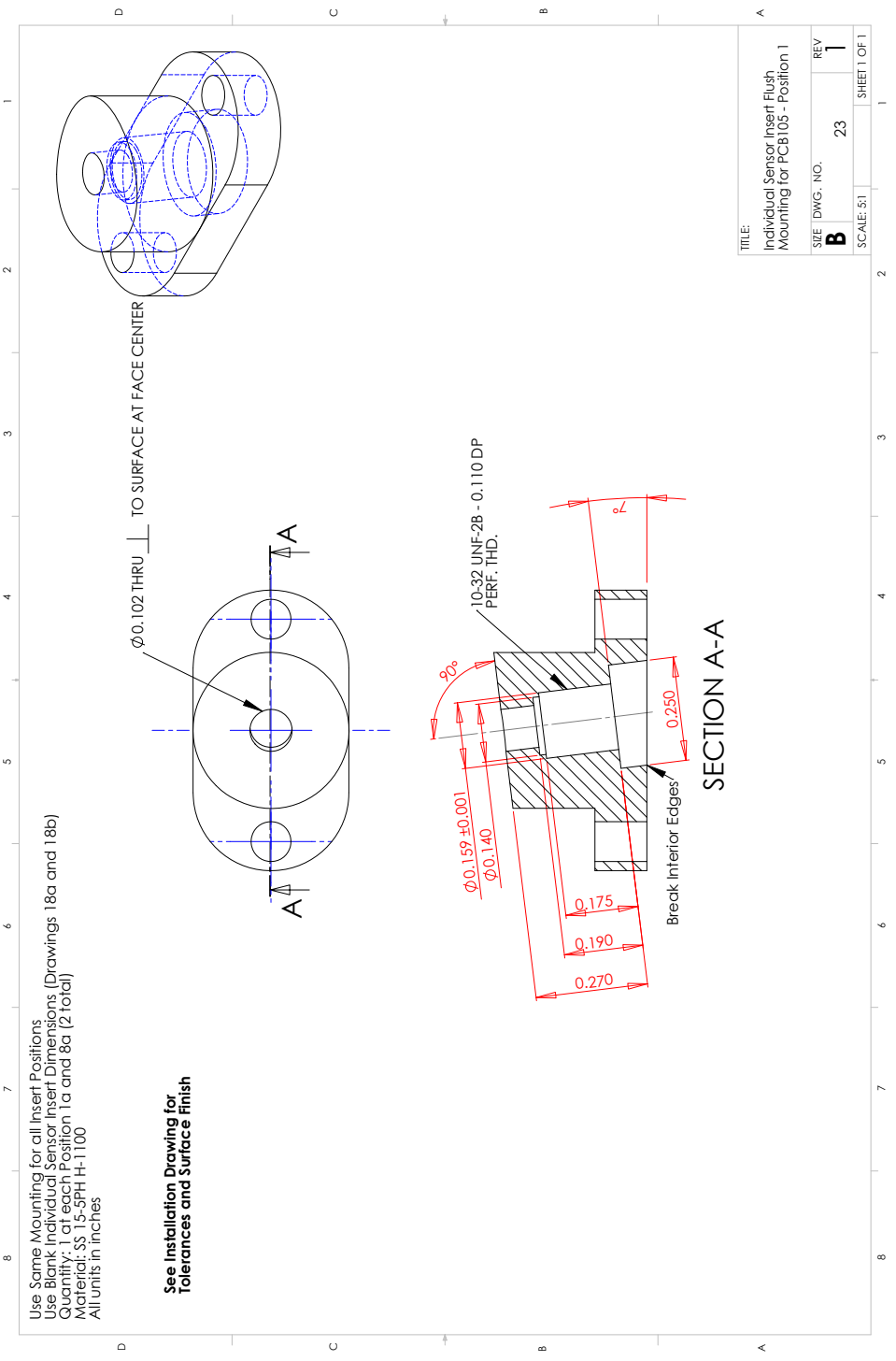


Figure B.22. Individual insert for flush-mounted PCB105 sensors

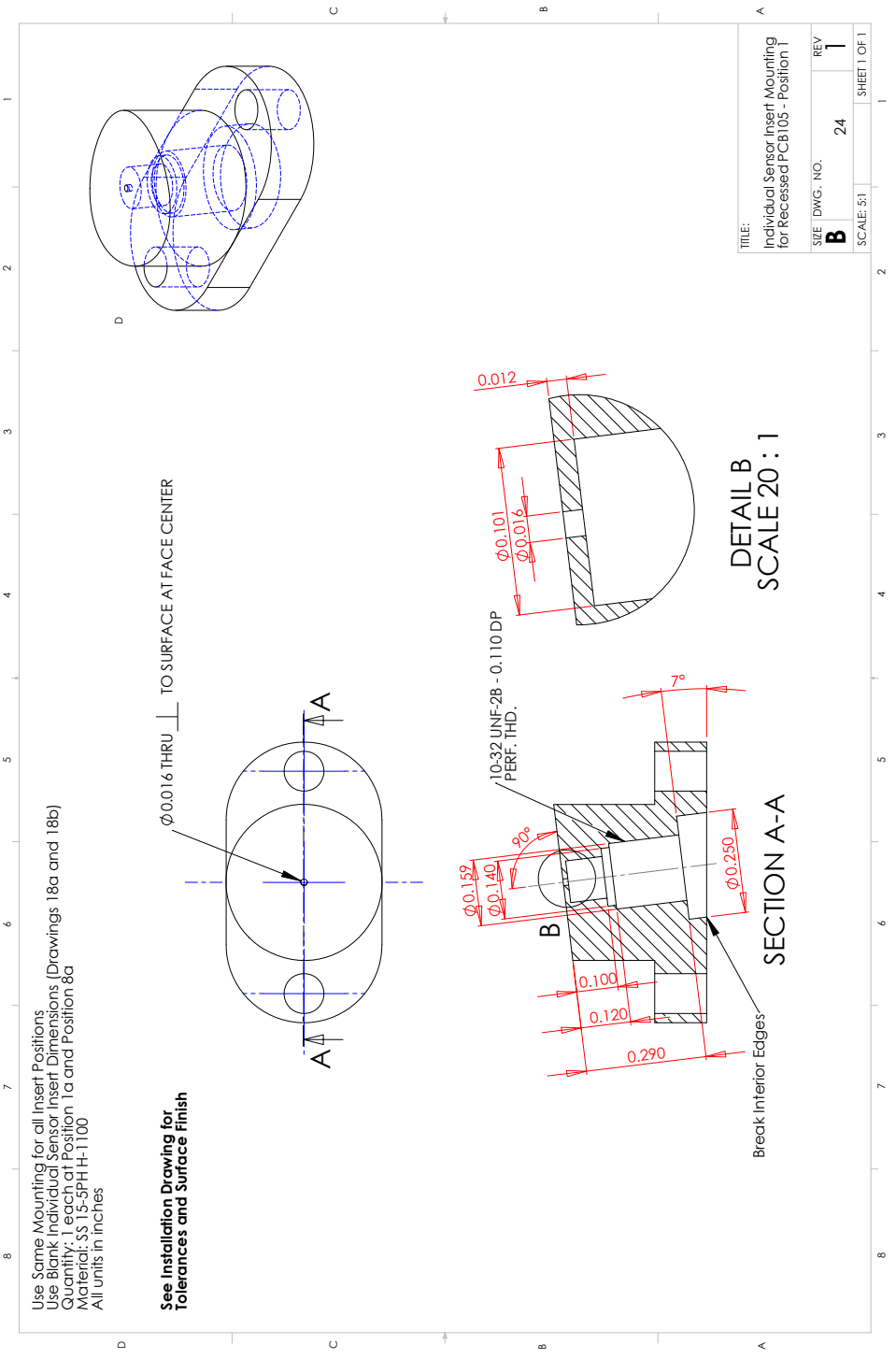


Figure B.23. Individual insert for recessed PCB105 sensors

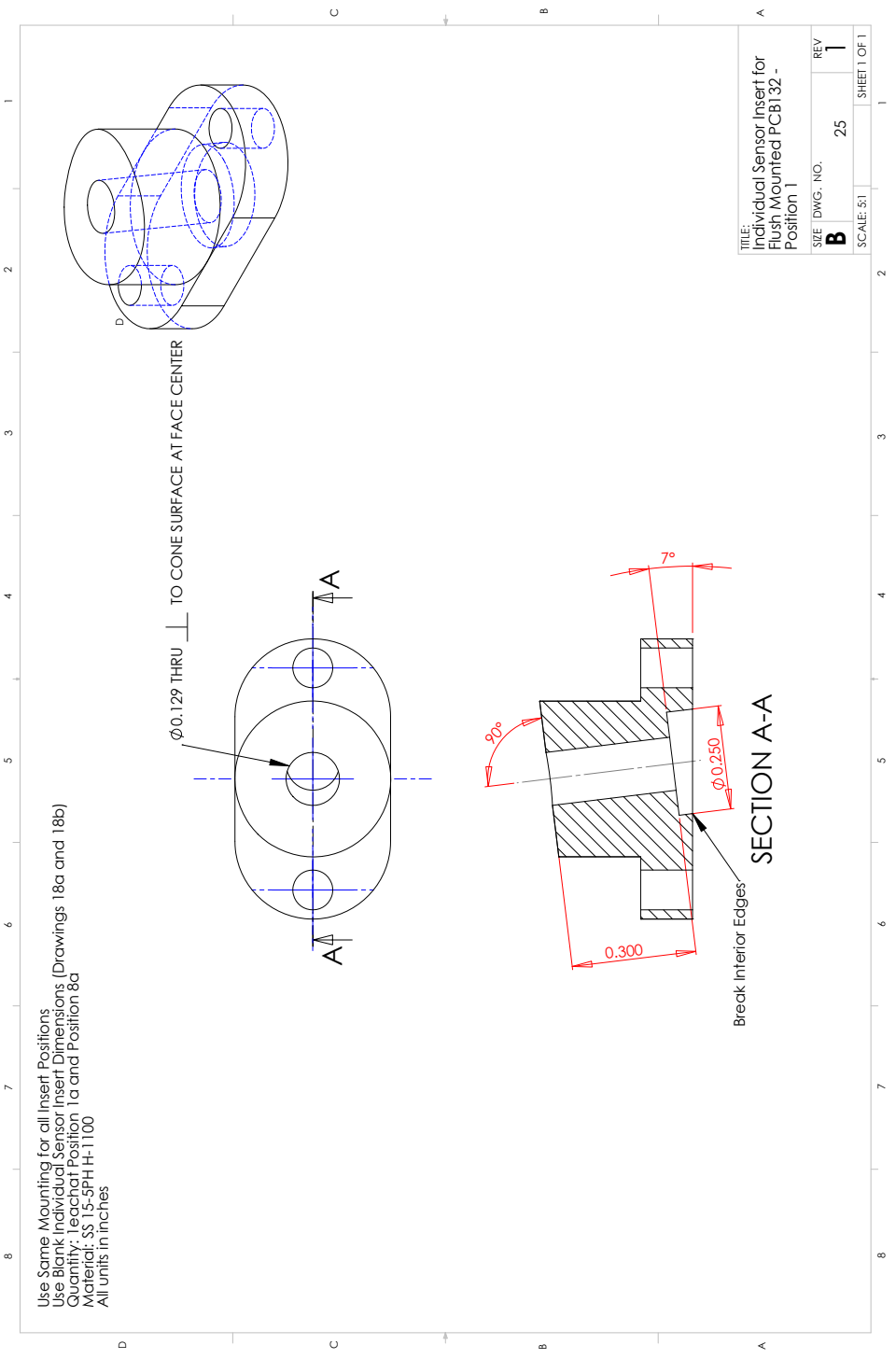


Figure B.24. Individual insert for flush-mounted PCB132 sensors

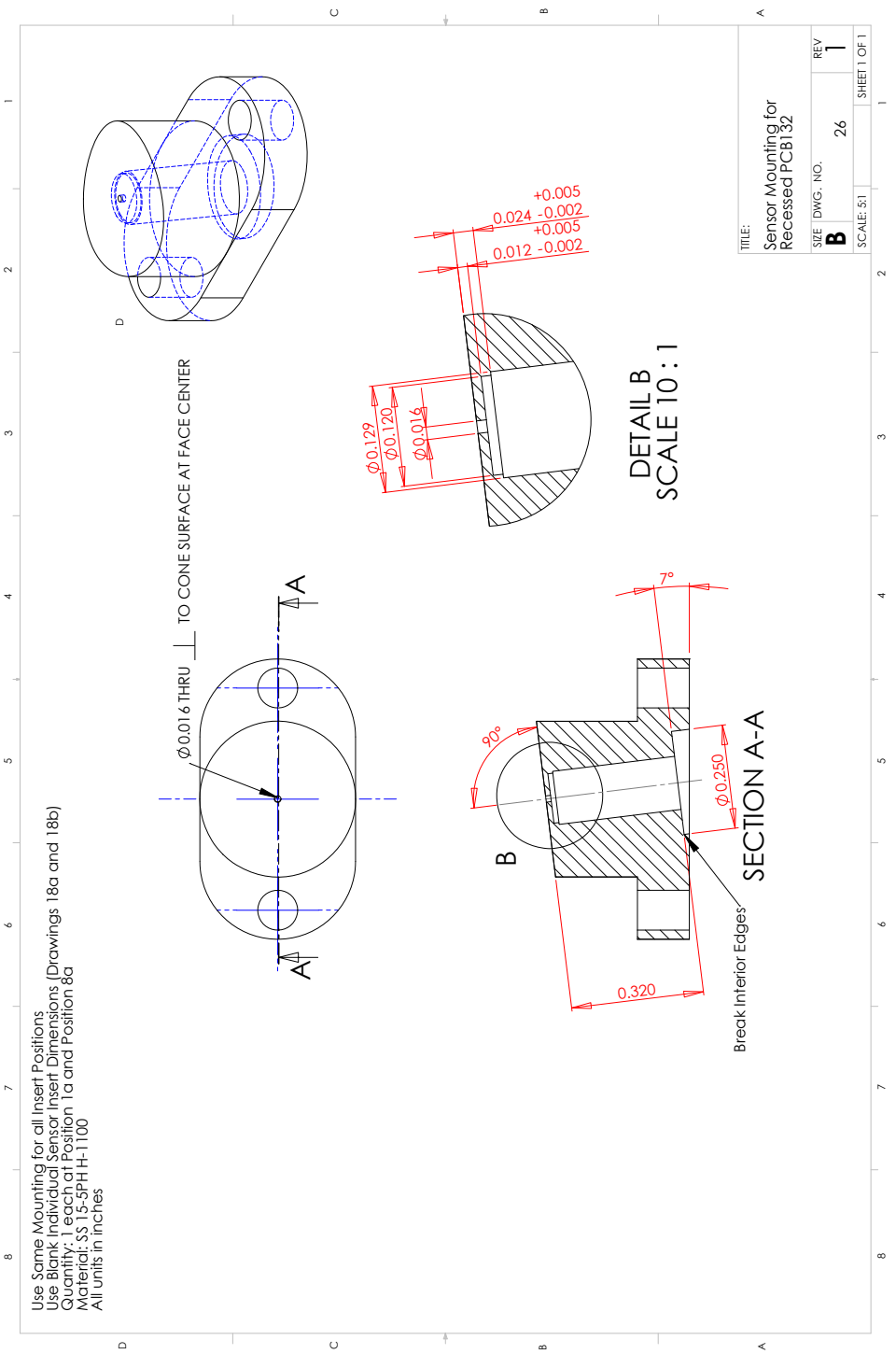


Figure B.25. Individual insert for recessed PCB132 sensors

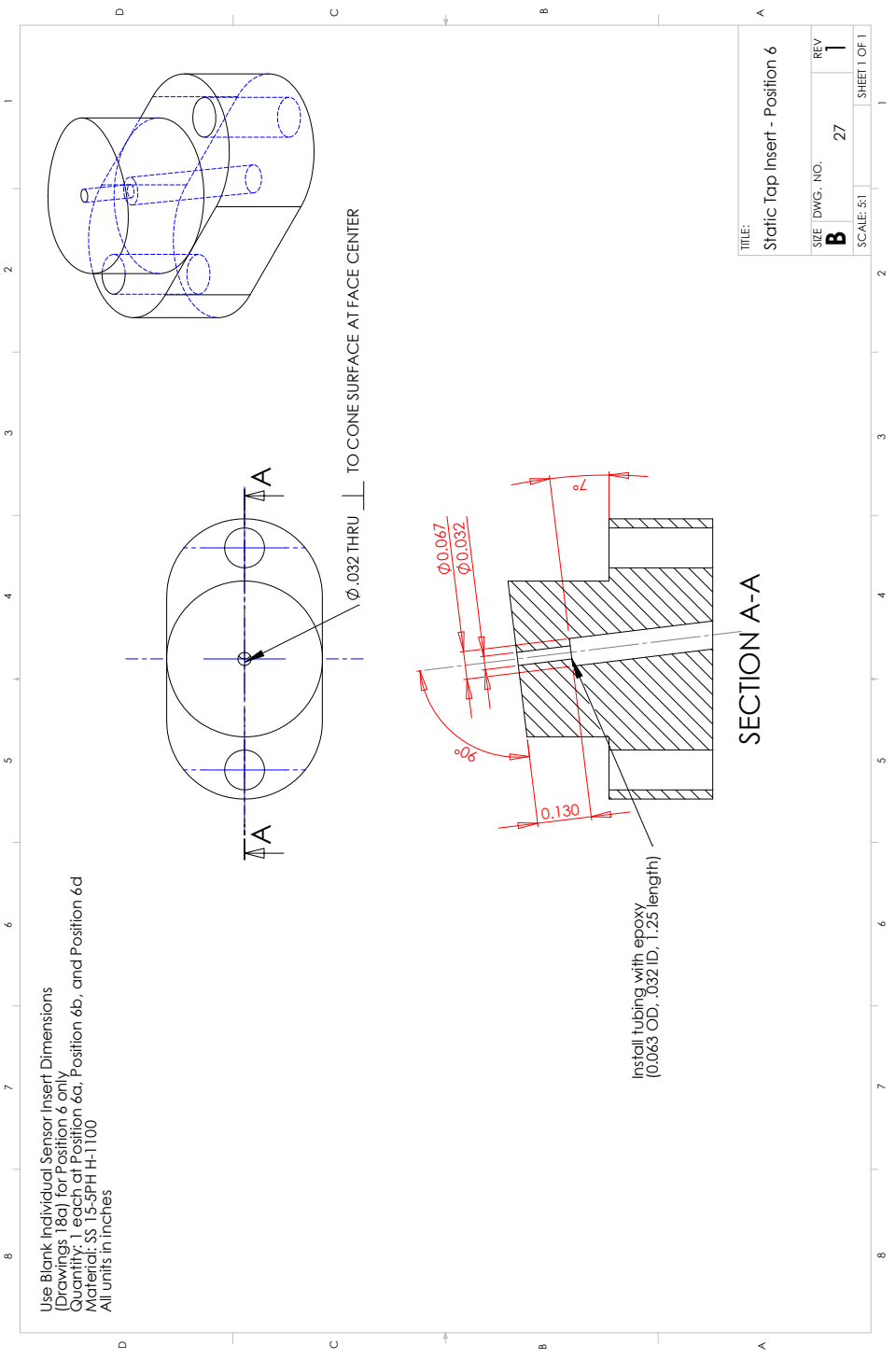


Figure B.26. Individual inserts for static pressure taps

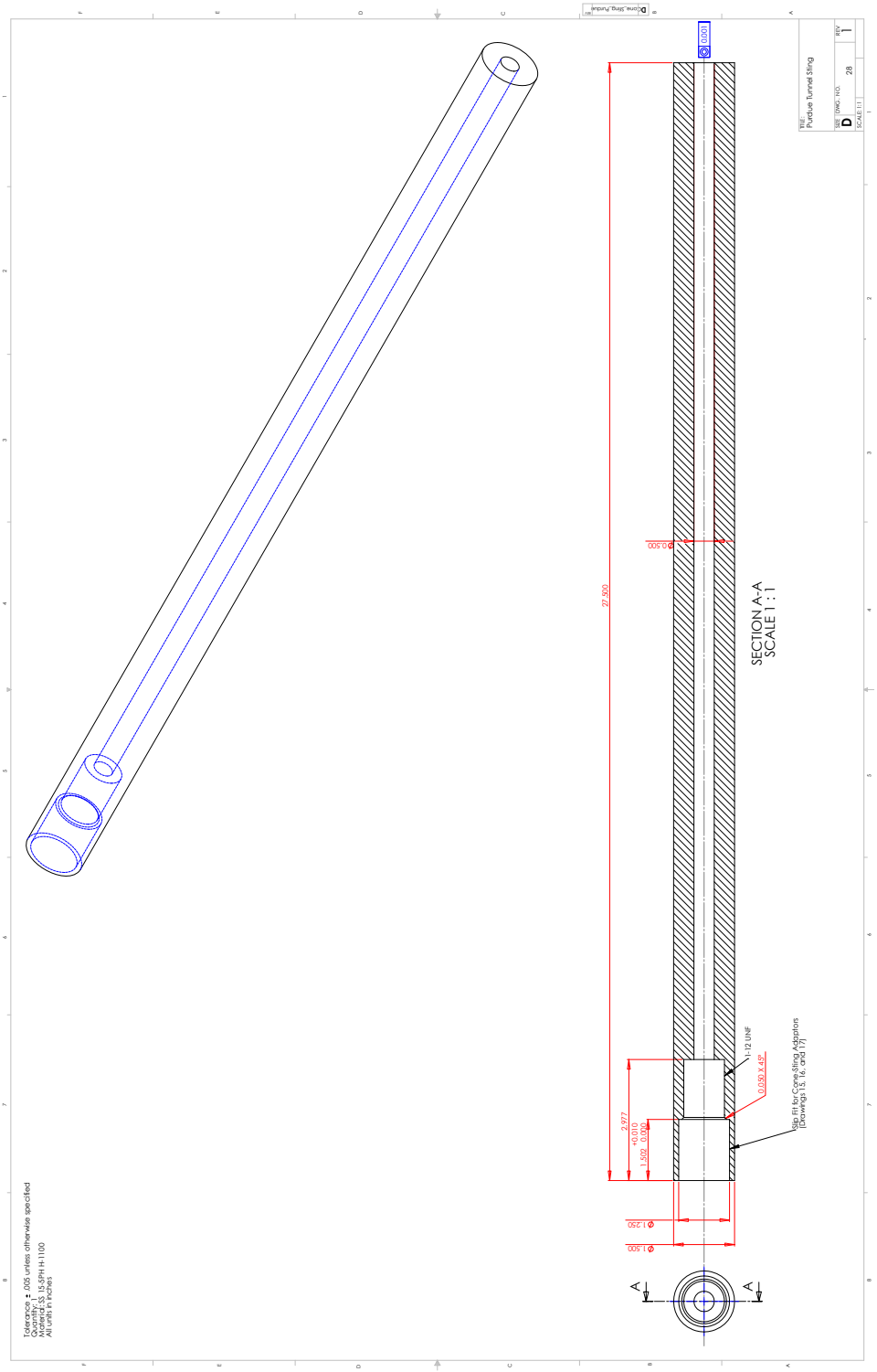


Figure B.27. BAM6QT sting

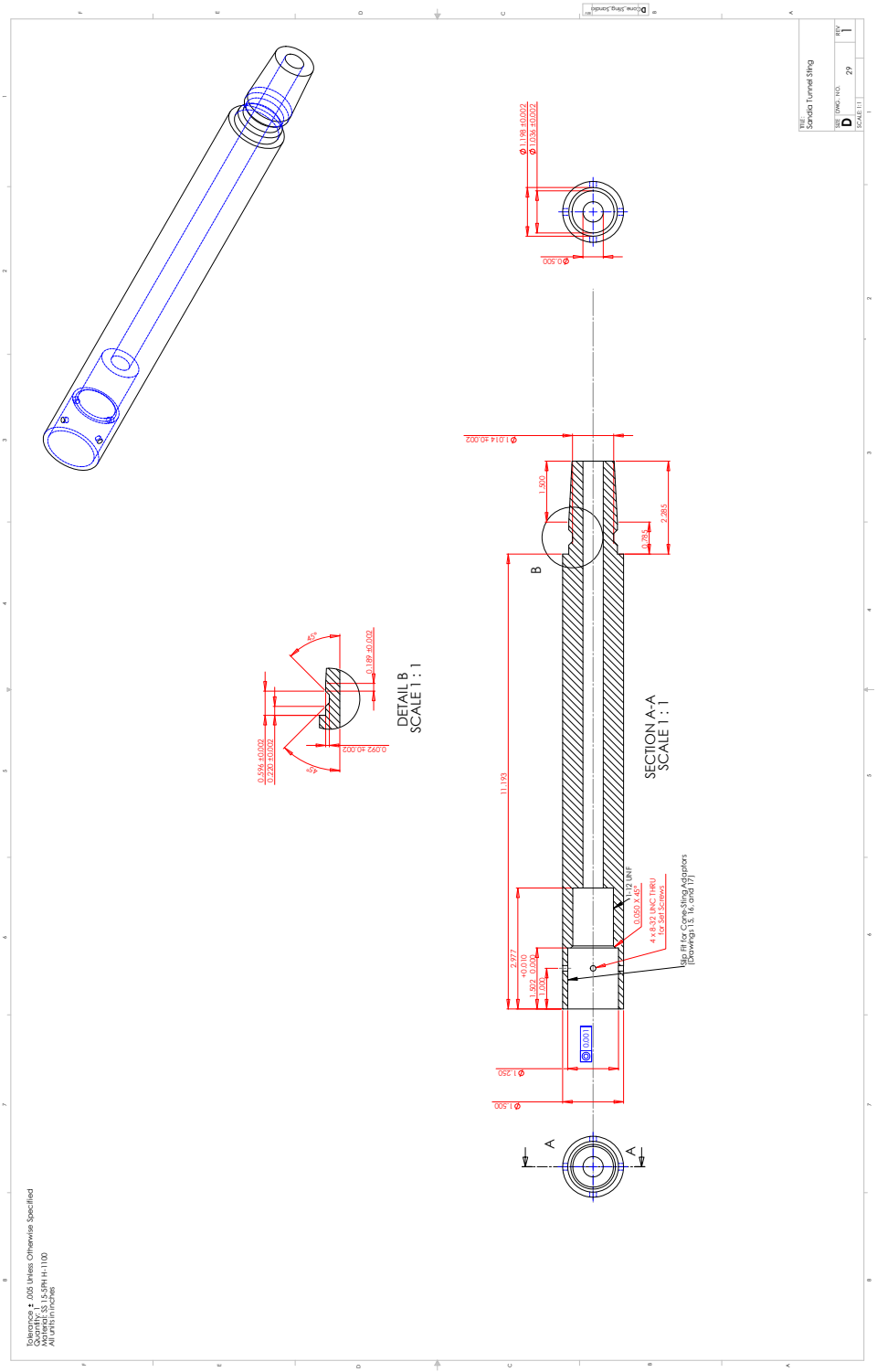


Figure B.28. HWT sting

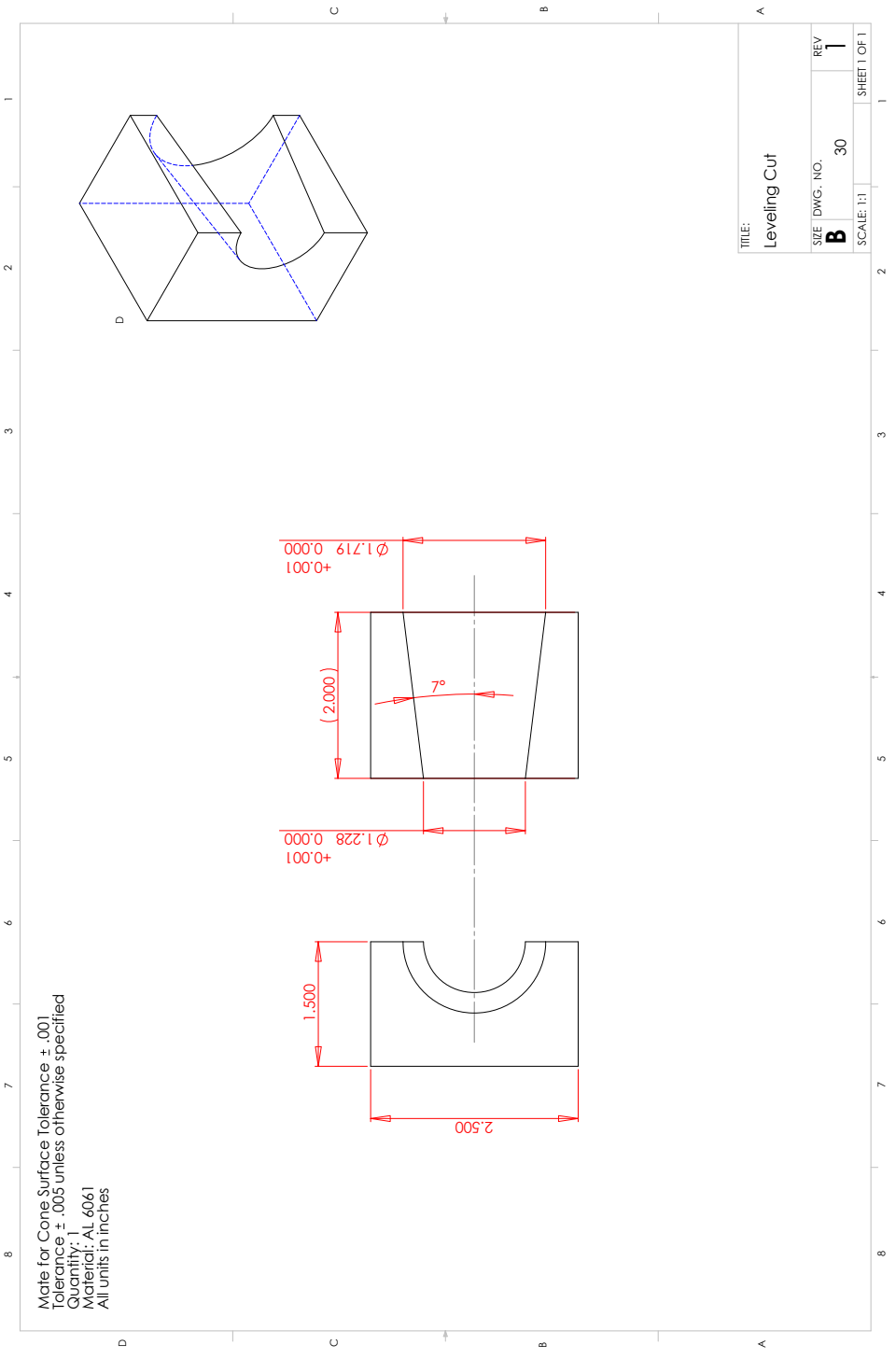


Figure B.29. Leveling cut

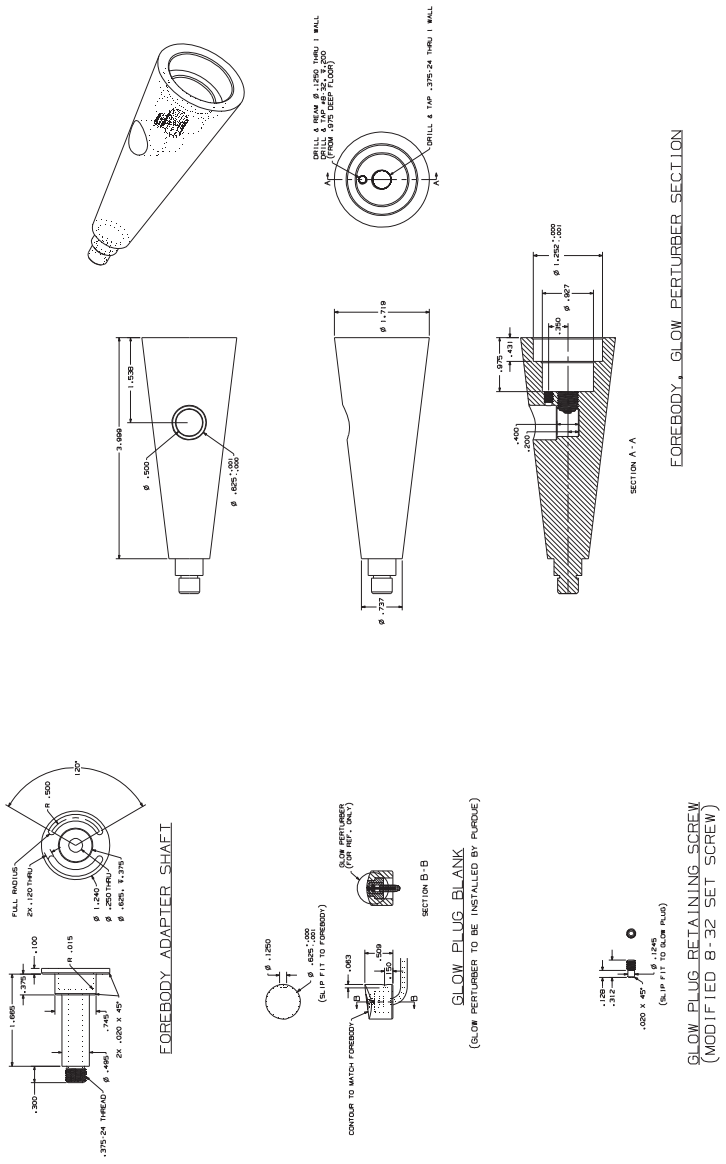


Figure B.30. Rotating glow-perturber section

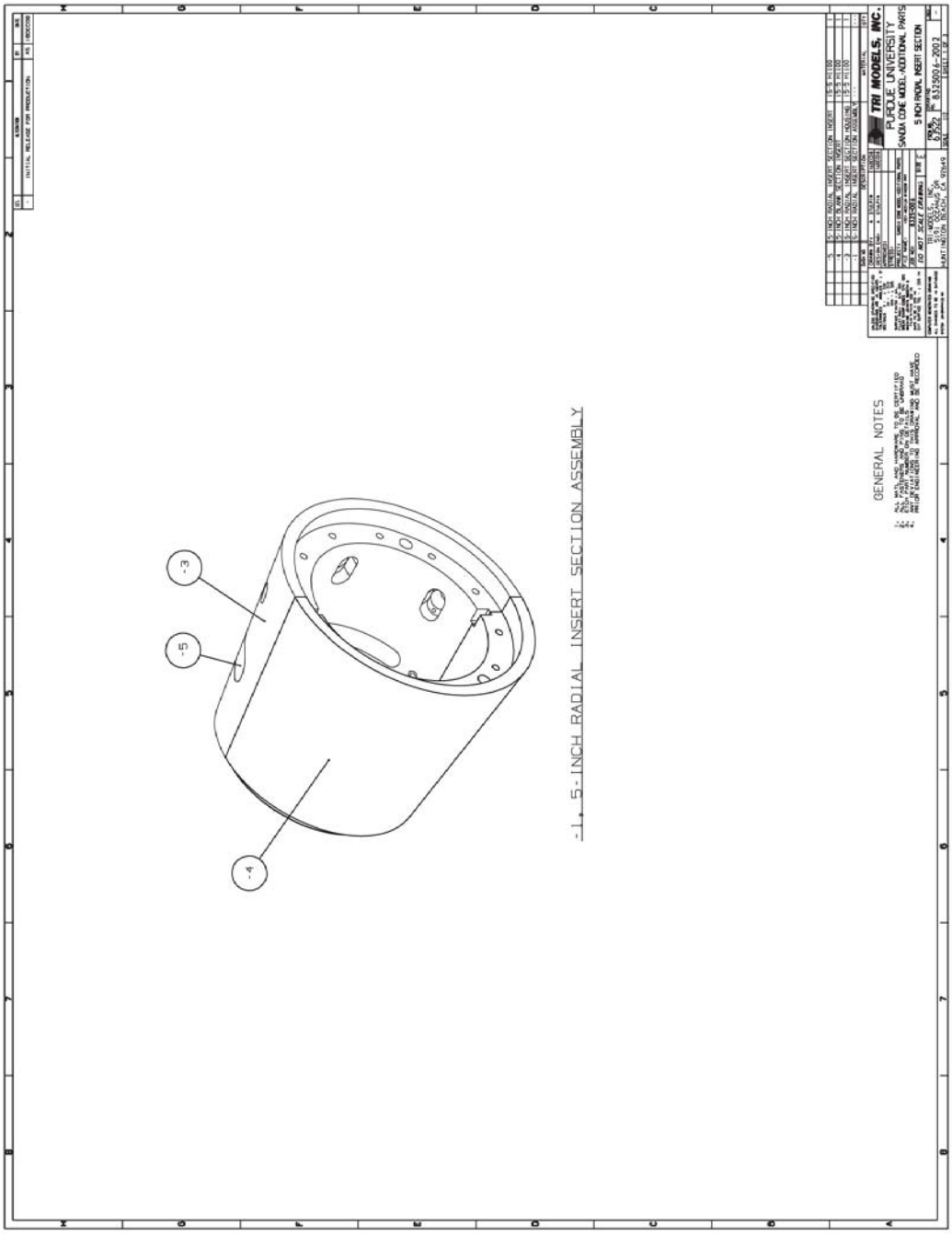


Figure B.31. 0.127-m base-diameter radial insert section assembly

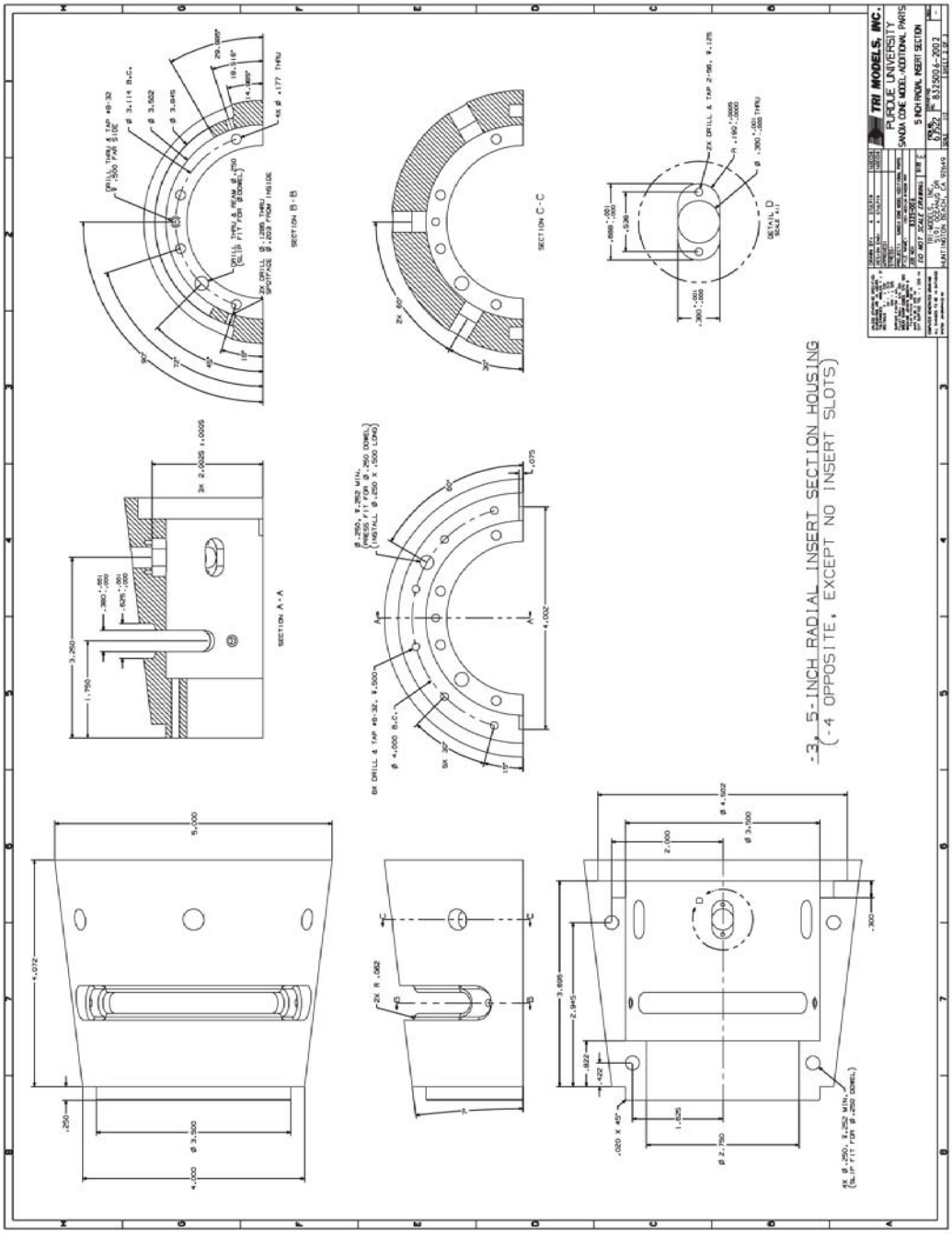


Figure B.32. 0.127-m base-diameter radial insert section

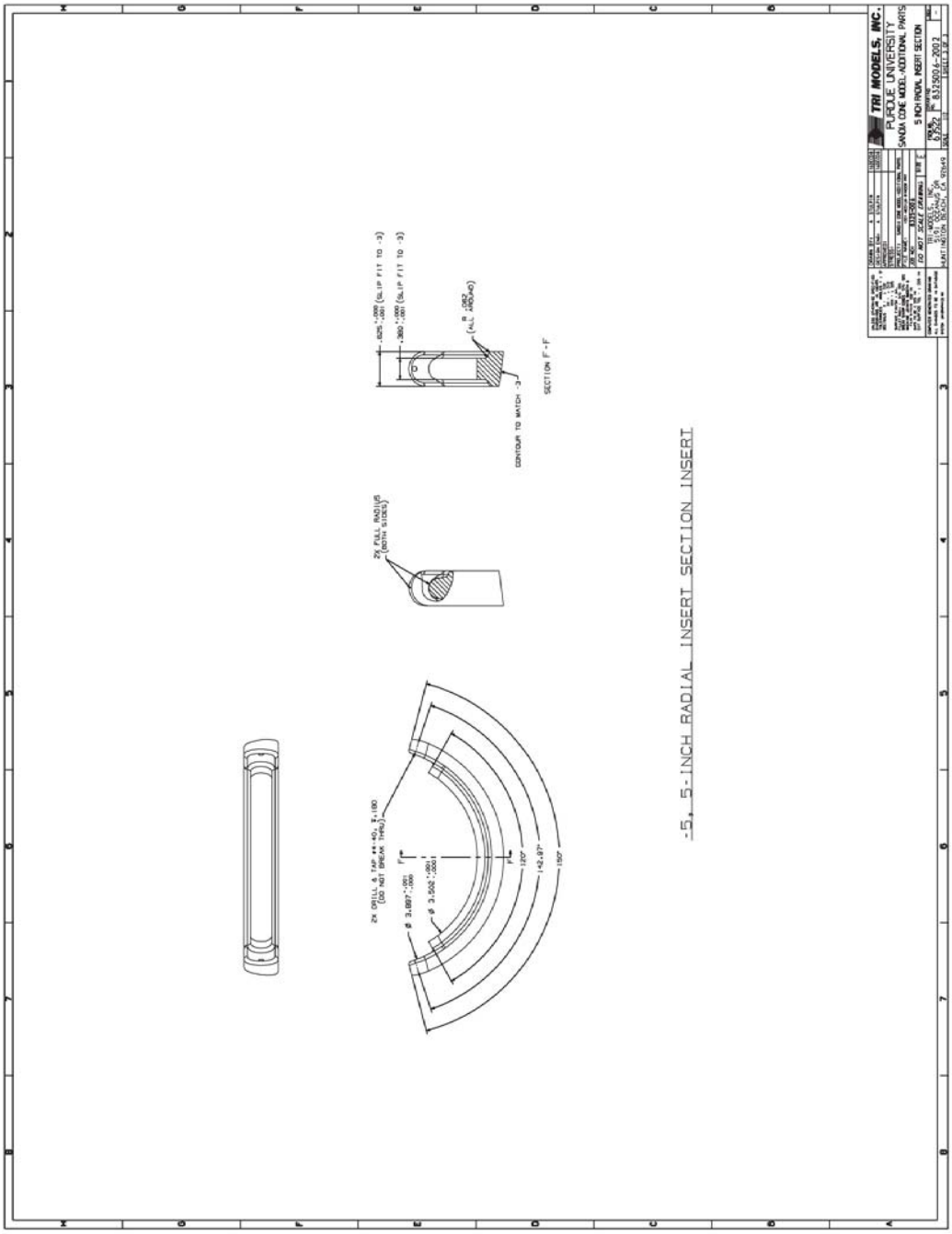


Figure B.33. Radial insert